UNIVERSITY OF OSLO

Francesco Pogliano

Nuclear astrophysics and the Oslo method

A study on experimental and theoretical radiative neutron-capture rates and their role in heavy-element nucleosynthesis

Thesis submitted for the degree of Philosophiae Doctor

Department of Physics
Faculty of Mathematics and Natural Sciences

2023

Deep in the human unconsciousness is a pervasive need for a logical universe that makes sense. But the real universe is always one step beyond logic.
– from "The Sayings of Muad'Dib" by the Princess Irulan

Frank Herbert, *Dune* (1965)

Acknowledgements

First I would like to thank my main supervisor Ann-Cecilie Larsen for giving me the opportunity to study and do research on this truly fascinating subject that is nuclear astrophysics. It is safe to say that my time as a PhD student would not have been nearly as pleasurable without your encouragement, useful advice, contagious curiosity and enthusiasm. Thank you for always being available when I needed it, regardless of your busy schedule.

To my co-advisor Sunniva Siem, thank you for the encouragement, support and good mood, and for holding the reins of this group through predictable and unpredictable times. To my second co-advisor Sijing Shen, thank you for teaching me about galactic chemical evolution.

This PhD adventure would not have been the same without all the amazing people I met along the way. Masha, thank you for accompanying me on Slovakian hikes, sharing obscenely expensive Swiss water, and of course for having the patience to help me out with all the data analysis questions I threw at you several times. You are the best office companion and travel buddy I could wish for, much better than a good colleague: a very good friend.

Thank you Wanja, for always being a positive presence around me through good and bad times. Thanks for all the bouldering, coffees and chats, amazing feedback and enthusiasm, Austrian snowshoe races and sleepy volcano hikes. You made the stressing times much more bearable and the fun times much more enjoyable.

I would also like to express my gratitude to the people in the nuclear physics group at UiO: Thank you Kevin for interesting discussions and for trusting me on adventures in Southern Italy. Thank you Andreas for amazing lectures and sharing your passion for nuclear structure. Magne, for your knowledge on the Oslo method and for the time teaching quantum physics. Eda, for always being in a good mood and for your support when writing proposals. To Frank, Line, Dorthea, Victor, Pawel and all the other people, it was a pleasure to get to know and work with you.

I would like to thank Ina for making me feel like at home during my stays in Brussels and for helping me out in understanding the subtleties of the r process. Thank you Stéphane for welcoming me in your group at ULB and giving me the opportunity to learn more on nucleosynthesis modelling, for the good discussions and for your lectures in nuclear astrophysics in South Africa. Arthur, thank you for your patience, for teaching me all you know about the i process and for sharing all the amazing Belgian beers with me.

Thank you to my family, whose love and support were central to the completion of this thesis. To my mother, for always believing in me, and to my father for giving me the passion for science that I still carry to this day.

Acknowledgements

Finally, I would like to thank all the beautiful people that I met in all the corners of the world and that I now have the honour of calling friends. Thank you Marthe and Terje Petter for the good times and adventures, Alf-Håkon for the beer brewing and philosophical discussions, Hanna and Karoline for all the dinners and hikes, and Heidi for sharing your passion for tango with me.

<div align="right">

Francesco Pogliano
Oslo, July 2023

</div>

Abstract

The subject of heavy-element nucleosynthesis still holds many mysteries. Part is due to the difficulty of simulating the astrophysical scenarios where it takes place, and part is because the relevant properties of the involved nuclei are mostly unknown for some of the main nucleosynthesis processes. Neutron-capture rates are one of these properties, and while described by theoretical models, these do not necessarily agree with each other or with experimental results. Experimental data are therefore central to both the correct simulation of heavy-element nucleosynthesis, and the development of more predictive models.

Experimental nuclear level densities and γ-ray strength functions are in this regard interesting quantities in the context of nuclear structure and because they provide the input for calculating neutron-capture rates for exotic, neutron-rich nuclei. These two quantities can be obtained by analyzing data from particle-γ experiments using the Oslo method. In this work, I present the results from three experiments carried out at the Oslo Cyclotron Laboratory: $^{124}\mathrm{Sn}(\alpha, p\gamma)^{127}\mathrm{Sb}$, $^{163}\mathrm{Dy}(\alpha, p\gamma)^{166}\mathrm{Ho}$ and $^{164}\mathrm{Dy}(\alpha, p\gamma)^{167}\mathrm{Ho}$, providing information on their nuclear structure as well as the neutron-capture rates of $^{126}\mathrm{Sb}$, $^{165}\mathrm{Ho}$ and $^{166}\mathrm{Ho}$. Finally, a sensitivity study of the rapid neutron-capture process using a model-consistent approach is presented.

Sammendrag

Dannelsen av tunge grunnstoff er et tema som fremdeles skjuler mange mysterier. Dette er delvis på grunn av de utfordringene man møter med å simulere de astrofysiske scenarioene hvor dette finner sted, og delvis på grunn av at de egenskapene til de involverte kjernene for det meste er ukjente for noen av hovedprosessene hvor tunge grunnstoff lages. Nøytroninnfangingsratene er en av disse egenskapene, og selv om disse beskrives av diverse teoretiske modeller, er ikke prediksjonene nødvendigvis innbyrdes konsistente eller i overenstemmelse med resultater fra eksperimenter. Eksperimentelle data er derfor sentrale for den korrekte simuleringen av nukleosyntesen, og for utviklingen av modeller med bedre evne til å forutsi disse egenskapene.

Eksperimentelle nivåtettheter og γ-styrkefunksjoner er i denne sammenhengen interessante størrelser, både når det gjelder forståelsen av kjernestruktur, og for å regne ut nøytroninnfangingsraten for eksotiske, nøytronrike kjerner. Disse to statistiske egenskapene kan bli målt ved å anvende Oslometoden til å analysere data fra partikkel-γ eksperimenter. I denne avhandlingen presenterer jeg resultatene fra tre eksperimenter utført ved Oslo Cyclotron Laboratory: ^{124}Sn$(\alpha, p\gamma)^{127}$Sb, ^{163}Dy$(\alpha, p\gamma)^{166}$Ho og ^{164}Dy$(\alpha, p\gamma)^{167}$Ho, som gir informasjon om deres nukleære struktur og i tillegg til nøytroninnfangningsratene til ^{126}Sb, ^{165}Ho og ^{166}Ho. Til slutt presenteres en studie om effekten av å bruke en modell-konsistent tilnærming i simuleringer for den raske nøytroninnfangningsprosessen.

List of Papers

Paper I

F. Pogliano, A. C. Larsen, F. L. Bello Garrote, M. M. Bjørøen, T. K. Eriksen, D. Gjestvang, A. Görgen, M. Guttormsen, K. C. W. Li, M. Markova, E. F. Matthews, W. Paulsen, L. G. Pedersen, S. Siem, T. Storebakken, T. G. Tornyi and J. E. Vevik "Indirect measurement of the $(n, \gamma)^{127}$Sb cross section". Published in: *Physical Review C.* Vol. 106, (2022), p. 015804. DOI: 10.1103/PhysRevC.106.015804.

Paper II

F. Pogliano, F. L. Bello Garrote, A. C. Larsen, H. C. Berg, D. Gjestvang, A. Görgen, M. Guttormsen, V. W. Ingeberg, T. W. Johansen, K. L. Malatji, E. F. Matthews, M. Markova, J. E. Midtbø, V. Modamio, L. G. Pedersen, E. Sahin, S. Siem, T. G. Tornyi and A. S. Voyles "Observation of a candidate for the $M1$ scissors resonance in odd-odd ^{166}Ho". Published in: *Physical Review C.* Vol. 107, (2023), p. 034605. DOI: 10.1103/PhysRevC.107.034605.

Paper III

F. Pogliano, A. C. Larsen, S. Goriely, L. Siess, M. Markova, A. Görgen, J. Heines, V. W. Ingeberg, R. G. Kjus, J. E. Larsson, K. C. W. Li, E. M. Martinsen, G. J. Owens-Fryar, L. G. Pedersen, S. Siem, G. S. Torvund, A. Tsantiri "Experimentally constrained ^{165,166}Ho(n, γ) rates and implications for the s process". Published in: *Physical Review C.* Vol. 107, (2023), p. 064614. DOI: 10.1103/PhysRevC.107.064614

Paper IV

F. Pogliano, A. C. Larsen "Impact of level densities and γ-strength functions on r-process simulations". Accepted to *Physical Review C.* arXiv: 2305.03664.

Contents

Contents

Chapter 1

Introduction

"*How was stuff made?*" is a very fascinating question. Together with "*What is stuff, anyway?*", it probably lists among the first philosophical questions humankind asked themselves when trying to explain the nature of everything. Indeed, one of the first attempts at guessing what stuff is made of in ancient Greek philosophy is due to Empedocles who, in the 5th century BCE, claimed that fire, wind, earth and water laid the basis for all existing matter. A few decades later Democritos would propose that everything was made of atoms: small, indivisible, fundamental blocks of existence. While we now know that atoms are indeed real (and divisible), the question on how these were made is yet not completely answered.

A good start for answering this dilemma is looking at the *proportions* elements present themselves. While planets (like Earth) may have different elemental abundances due to their formation history, a good representative for the solar system elemental proportions is the Sun. Our star consists of 99.87% of the solar system's total mass and its elemental composition was not altered in the same way as for the planets. By looking at spectral lines of the solar atmosphere we can infer its chemical composition, and this gives us a clue to the original elemental abundances for the solar system before if was fully formed.

What we call *elements* are atoms whose nuclei have a specific number of protons and, thus, a specific charge. For example, all carbon nuclei have 6 protons, and all tin nuclei have 50. This is also called their atomic number, charge number, or Z. When looking at the solar elemental abundances in Fig. 1.1, we notice different patterns. One is the high peak at $Z = 1$ and $Z = 2$, corresponding to H and He. The other feature is the iron peak at $Z = 26$, and the marked drop in abundances after that, together with a smudged, small double-peak at $Z \approx 53$ and a clearer double-peak at $Z \approx 78, 82$. These features hold the key to understand what the mechanisms behind the creation of elements in space are. They are the product of different astrophysical conditions and molded by the properties of the nuclei involved.

The origin of elements is a fascinatingly complicated topic, encompassing different fields of physics like astrophysics, thermodynamics, electrodynamics, fluid mechanics, special and general relativity, quantum physics in all of its shapes and forms (quantum chromodynamics, quantum electrodynamics, nuclear physics...), plasma physics, and the list goes on.

Specifically we may say that in order to study the subject of *nucleosynthesis*, we need to understand both the astrophysical phenomena where it takes place, and the working of the nuclei involved. In this work I will focus on the latter, and how experiments carried out at the Oslo Cyclotron Laboratory [2] may help us in getting a clearer picture of what happens up there.
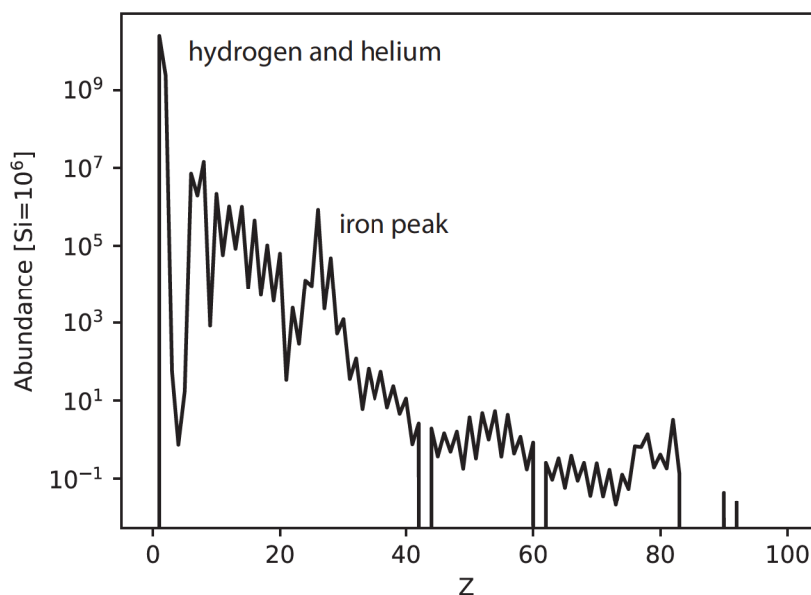
Figure 1.1: The solar elemental abundances from Lodders *et al.* [1]. The y-axis is logarithmic, and we see that hydrogen and helium at $Z = 1$ and 2 are the most abundant elements in the solar system. At $Z = 26$ we find the "iron peak", and at $Z \approx 53$ and $Z \approx 78, 82$ two small double-peaks in the heavy-element region. The first double-peak at $Z \approx 53$ is a bit unclear, but becomes more visible when the abundances are plotted against mass number, see Figure 2.1.

The thesis is structured in the following way: first, a short introduction to nuclear physics is given in the rest of this chapter. This will be useful in order to understand the following chapter on nucleosynthesis (Chapter 2), with a focus on neutron-capture processes. An introduction to nuclear theory for statistical nuclei is given in Chapter 3, and an overview of how experiments are done in Oslo and their contribution to nucleosynthesis studies in Chapter 4. This will lay the grounds to understand the four papers which make the second part of this work.

1.1   Nuclear physics in a nutshell

Atomic nuclei are quantum mechanical, dense objects consisting of neutrons and protons at the core of atoms. Although the existence of negatively charged electrons was already known by scientists in the beginning of the 20th century, the understanding of the structure of the atom was then still in its infancy. From the Dalton hard, electrically neutral "ball", the discovery of the electron allowed for the formulation of the so-called "plum pudding model" in 1904 by J. J. Thompson. In this model electrons are thought to be evenly embedded into a positively charged volume, like plums in a pudding. The first evidence that these charges were not evenly distributed is due to Ernest Rutherford, who between

1908 and 1913 carried out a series of experiments involving positively charged α particles on a thin gold foil target. From the way these particles scattered he was able to conclude that charge was not evenly distributed throughout the atom as Thompson's model suggested: the positive charge must be concentrated in a very small space in the center (the *nucleus*) while the negatively charged electrons were distributed on the outer part of the atom. Later, the picture of the atomic nucleus would become more and more complete with the discovery of the proton in 1920 again by Rutherford, and the discovery of the neutron by his former student James Chadwick in 1932 providing all the main building blocks of the nucleus.

As mentioned above, elements are characterized by their number of protons. Nuclei with the same amount of protons but different number of neutrons are called isotopes. By taking carbon as an example, we may have two different stable isotopes: one with 6 neutrons, and one with 7. The amount of neutrons is indicated by the letter N, while $A = Z + N$ indicates the sum of nucleons (meaning, protons and neutrons) and is called the *mass number*. These can be written using the $^{A}_{Z}X$ notation, where X indicates the elemental symbol, as $^{12}_{6}$C and $^{13}_{6}$C. Since the elemental symbol and Z convey the same information, the latter is often not written, leaving ^{12}C and ^{13}C.

Isotopes may be stable, or unstable. Unstable ones are *radioactive*, meaning that they will emit radiation in order to achieve stability. The main types of radiations are α, β and γ, where for example an α-unstable nucleus may α decay by emitting an α particle, and similarly for β and γ. In this context, the decaying nucleus is called *parent nucleus*, and the result of the decay the *daughter nucleus*. An α particle is the same as a ^{4}He nucleus, meaning a cluster of two protons and two neutrons. The daughter nucleus from α decay is the same as the parent, but with two protons and two neutrons less. What is collectively called β radiation may actually refer to either β^{-} or β^{+} radiation. The first is mediated by a W^{-} boson which rapidly disintegrates into an electron (e) and an antineutrino ($\bar{\nu}_e$). Since the W^{-} particle decays almost immediately and the antineutrino is rarely detected, the electron is for most purposes seen as the main β^{-}-decay product. The effect on the β^{-}-decaying nucleus is that a neutron is converted into a proton, and β^{-} decay is a common way for a neutron-rich nucleus to convert excess neutrons to protons and approach in this way stability. Similarly, β^{+} decay happens when proton-rich nuclei convert a proton to a neutron by emitting a W^{+} boson, which rapidly decays into a neutrino and a positron, the latter being the antiparticle of the electron and is positively charged. Lastly, γ decay corresponds to the emission of a γ ray as a way for it to decay to its ground state. While both α and β decays transform the nucleus into a different nucleus, γ decay leaves Z and N unchanged.

In order to understand why isotopes are stable or unstable, we need to consider the nuclear potential. The nucleus holds together even though it is constituted by neutral and positively charged particles, meaning that there must be another attracting force winning over the electrostatic repulsion. We call such a force the *strong nuclear force*, and it is responsible for trapping protons and neutrons in the *nuclear potential*. This potential may qualitatively

be approximated as a finite well. Even if its shape does not exactly correspond to that, this model provides useful insights. Neutron and protons are fermions with spin 1/2, meaning that only two of the same kind, but with opposite spin, may occupy the same energy state without breaking Pauli's exclusion principle.

In Figure 1.2 we see a sketch of the potential as seen by neutrons on the left, and as seen by protons on the right. The nucleus is in its ground state, meaning that all the lowest excited states are occupied. The energy difference called the neutron separation energy (or S_n) is the energy needed to strip one neutron out of the nucleus. Conversely, it would be the excitation energy of a nucleus if a free neutron with no kinetic energy were to be captured by the $A - 1$ nucleus. For protons the situation is different. They still feel the strong nuclear force, but its attractive effect is diminished by their electrostatic repulsion, meaning that the potential well for protons is slightly less deep than for neutrons. In addition, the electrostatic repulsion has a much wider range than the strong nuclear force, meaning that free protons are initially repelled by nuclei and they only have a meaningful chance to be captured by (or "fall into") the nucleus if they have enough energy to overcome (or at least tunnel through) the electrostatic (or *Coulomb*) barrier. Similarly, a positive electric charge inside a nucleus may have a chance to tunnel through the Coulomb barrier and escape, as long as energy conservation laws are respected. This is the case of α-decay, where the wave function of the α particle inside the nucleus leaks outside the barrier and has the chance of escaping.

Due to the Coulomb repulsion, the proton potential well is shallower, meaning that if we were to have similar separation energies for protons and neutrons ("wells filled up to about the same height") we would end up with having less
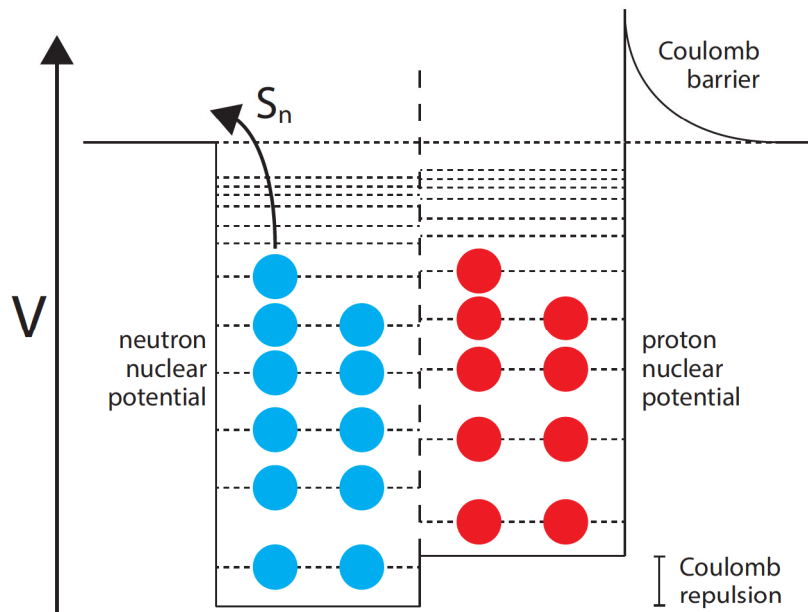

Figure 1.2: A qualitative description of the nuclear potential seen by neutrons and protons.

protons than neutrons. If we were to have more neutrons than this, it might be energetically favorable for the nucleus to convert one of these into a proton by β^- decay (see Figure 1.3). Correspondingly, β^+ decay will happen when there is a surplus of protons. If electrons are available, electron capture may also be a decay mechanism where a proton and an electron convert to a neutron and an electric neutrino.

In Figure 1.4 we see a *nuclide chart*, a way to organize and visualize all different nuclei and their favorite mode of decay. On the x-axis we have the number of neutrons, while on the y-axis we have the number of protons. The strip of black squares in the middle is called the *valley of β stability*, and represents the stable nuclei. To their right, neutron-rich nuclei will β-decay diagonally back to the black squares and thus stability, converting one neutron into a proton, and the proton-rich nuclei to the left will decay towards the valley in a similar way converting a proton to a neutron. The valley of stability bends slightly "downwards", favoring a higher number of neutrons than protons, in line with the discussion above. For heavier nuclei, α decay and even spontaneous fission become dominant, and beyond the valley of stability, separated by different unstable elements, we find thorium and uranium as the only known (almost) stable nuclei beyond lead.

When attempting to describe the structure of nuclei and the energy of their states, it was natural to compare the nucleus to atomic electrons, whose quantum-mechanical description was beginning to be well understood in the 1920's [5–7]. As for atoms, one expected to encounter certain numbers of protons and neutrons for which the nucleus was particularly strong bound, similarly as to noble gases for electrons. These numbers were eventually found not to be the same as for electrons, and they are called *magic numbers*. These are the same for protons and
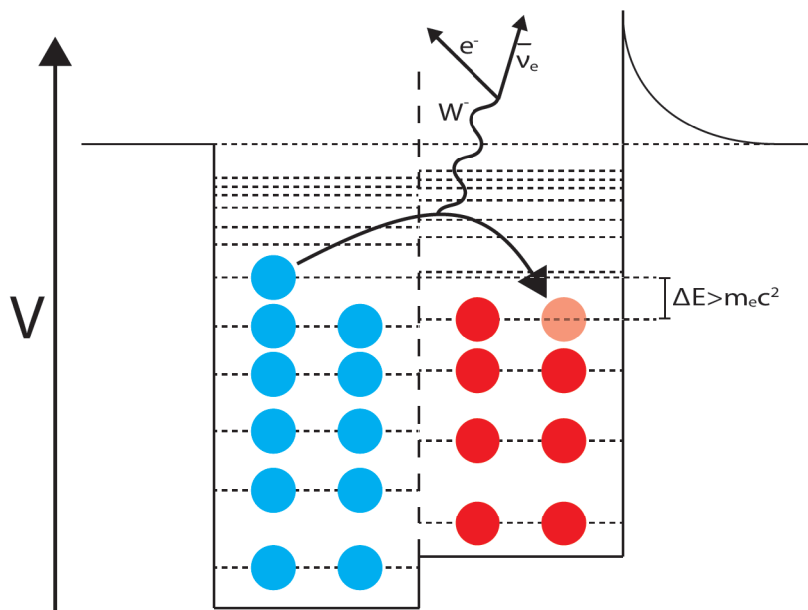

Figure 1.3: A schematic representation of the β^- decay.
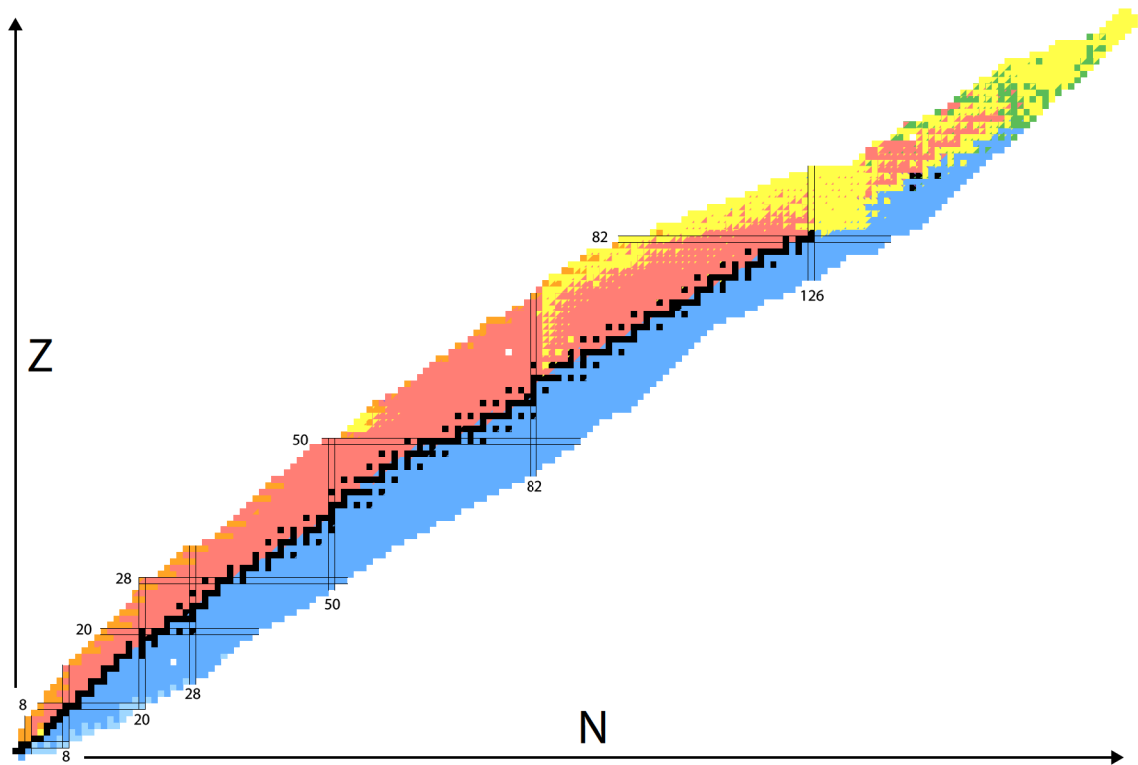
Figure 1.4: The nuclide chart. The black central squares represent the stable nuclei in the valley of β stability, and the color of all other squares represent their preferred way of decay, with yellow for α decay, red for β^+ decay, blue for β^- decay and green for spontaneous fission. The proton and neutron magic numbers are highlighted in black, solid lines. Two colors for the same square indicate that the nuclide may decay in two ways, and the probability is given by the area of the respective color. Drawn using the *Chart of nuclides drawer* [3], based on the data from the 2016 atomic mass evaluation [4].

neutrons: 2, 8, 20, 28, 50, 82, 126, and are illustrated as vertical and horizontal lines in the nuclide chart. Nuclei with this number of protons or neutrons are more tightly bound and will "resist change" to a larger degree than neighboring nuclei. With the introduction of the nuclear shell model by Maria Goeppert Mayer and Johannes Hans Daniel Jensen [8–10] this difference from the behavior of the electrons would be explained with the fundamental difference existing between the Coulomb and the strong nuclear interaction, where the latter has a much stronger dependence on spin and angular momentum than the former.

With this rudimentary introduction to nuclei and nuclear physics, we are ready to explore the field of nuclear astrophysics and the mechanisms behind the creation of elements in space in the next chapter.

Chapter 2

Nucleosynthesis

Nucleosynthesis is the term used to refer to the different processes responsible for the formation of new elements in the universe. These processes are both astrophysical and nuclear in nature, since they happen in specific locations in the universe, and their accurate description requires the knowledge of the properties of all the nuclei involved.

2.1 History

The history of nucleosynthesis is connected to another important question physicists were trying to answer between the end of the 1800s and the first half of the 1900s, and that is: What is the energy source of the Sun, and the other stars?

One of the first attempts at answering this question was by Lord Kelvin in 1862 [11]. In his hypothesis, the heat of the Sun was generated by countless meteorites falling on its surface, attracted by its strong gravitational pull. According to him, this must have been the only possible explanation as the only other conceivable alternative at the time was chemical reactions, and these are too weak to explain the longevity of the Sun. There are numerous problems with this theory, among others the fact that we should be able to see all these falling meteorites, and that the Earth's orbit should be influenced by the accretion of the Sun's mass.

It would go more than 50 years before someone would propose a different explanation. William D. Harkins and Ernest D. Wilson in 1915 [12] and Jean B. Perrin in 1919 [13] independently tried to explain why the measured mass of helium was slightly less than four times the mass of hydrogen [14]. They suggested that hydrogen could "condense" into helium and that the mass difference could power the sun when converted to energy using Einstein's famous relation $E = mc^2$.

In 1919 Ernest Rutherford produced the first man-made nuclear reaction in a laboratory, where α particles reacted with the nitrogen in the air creating oxygen and hydrogen [15]. This can be written as $\alpha + {}^{14}\text{N} \rightarrow {}^{17}\text{O} + p$, or ${}^{14}\text{N}(\alpha,p){}^{17}\text{O}$ using a more compact notation. These were productive years for nuclear physics (and physics in general), as 1920 was also the year Rutherford announced the results of his gold foil experiment, demonstrating the existence of the nucleus. All of these threads would be collected by Hans Bethe in 1939, where using measured cross sections he could theorize a way to create helium from hydrogen, using carbon as a catalyst [16].

The creation of helium was a step in the right direction. After the discovery of the neutron, George Gamow was quick to suggest in 1935 that neutrons could as

well play a role in nucleosynthesis, since they do not feel any Coulomb repulsion and are more easily captured by nuclei. Not so long after, Ralph Alpher, Hans Bethe and George Gamow[1] would suggest that the creation of heavier elements would take place by consecutive neutron captures during the Big Bang [18] (and thus proposing the Big Bang as a cosmogenesis theory for the first time). The explanation of the origin of heavier elements by consecutive capture of protons or neutrons met a problem in the lack of stable isotopes with mass 5 or 8, posing a big challenge when trying to explain the creation of nuclei heavier than ^{4}He.

This would be solved by Fred Hoyle when in 1953 he suggested the existence of a resonance at 7.7 MeV in ^{12}C [19] (called later as the *Hoyle state*) able to increase the rate of the $3\alpha \to {}^{12}$C reaction dramatically. Just the year before, in 1952, technetium lines were observed in the spectra of evolved giant stars [20]. Technetium is an unstable element whose longest living isotope has a half-life of about 4 million years, a time so short by astronomical standards that the only way to explain its presence in these stars was to assume that it was created there. When the Hoyle state was later observed in experiments in 1953 [21] the idea that heavier elements were created in stars, where this triple-α reaction could happen, started to gain traction.

In 1956 a review of elemental solar abundances was published by Suess and Urey [22] showing double-peaks close to where nuclei were supposed to have a magic number of neutrons, according to the nuclear shell model developed and published in 1949 by Goeppert Mayer and Jensen [8–10]. The idea of neutron capture as the main mechanism for the creation of heavy elements was put forward, and just one year later the seminal B2FH paper by Margaret Burbidge, Geoffrey Burbidge, William A. Fowler and Fred Hoyle [23] was published, together with the work from Alastair Graham Walter Cameron [24], listing a total of eight mechanisms for which elements could be created. Elements between ^{12}C and ^{56}Fe would be created in charged reactions during different life stages of a star, while heavy elements would be mainly created by neutron capture beyond iron.

2.2 Abundances

Figure 1.1 shows the elemental abundances in the sun. Another way to plot solar abundances is to order nuclides by mass number A. This requires information on the abundances of the different isotopes, something not possible to extract from spectral lines in the solar atmosphere. Fortunately, meteoric CI1 carbonaceous chondrites provide samples of primitive solar matter in its original composition

---

[1]The inclusion of Hans Bethe in this work was an idea of George Gamow so that the authors' names would read like the Greek letters $\alpha\beta\gamma$. "*It seemed unfair to the Greek alphabet to have the article signed by Alpher and Gamow only*", wrote Gamow in his book *The creation of the universe* [17]. This would have been a careless violation of the Vancouver recommendations for co-authorship, had not the Vancouver group only convened thirty years later, in 1978. Although Hans Bethe would later provide useful insights to the discussion, his inclusion did not please the then-PhD student Ralph Alpher, who feared his merit would be drowned by the fame of the two other well-established scientists. Alpher would then fight for recognition of his research for much of his career.
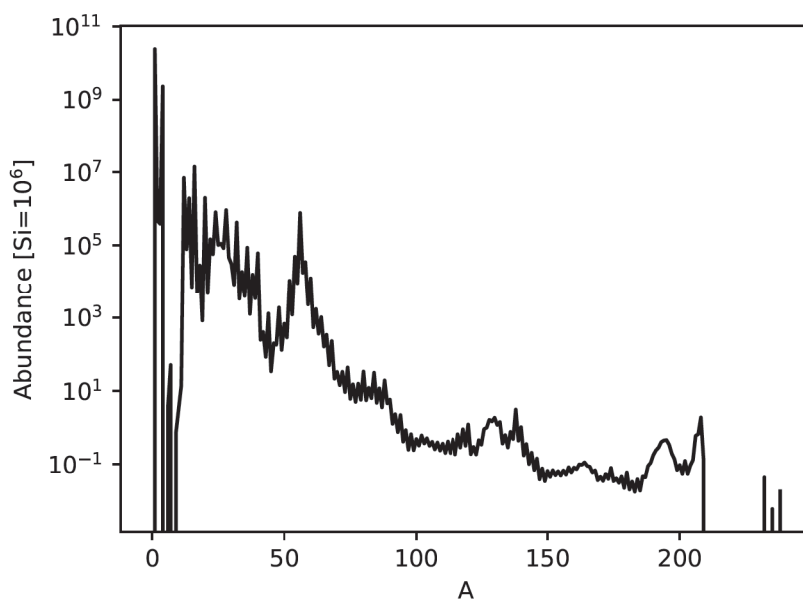
Figure 2.1: The solar abundances as a function of the mass number A from Lodders *et al.* [1]. Hydrogen and helium are now between $A = 1$ and 4, and the iron peak at $A = 56$. The two double-peaks in the heavy elements region are now more clearly distinguishable at $A \approx 130, 138$ and $A \approx 195, 208$.

where isotopic information can be extracted. The isotopic abundance plot in Figure 2.1 can be divided into three approximate regions, according to the nature of the processes that lead to the formation of these nuclei. The first part is taken by H and He ($A = 1$ to 4), the two lightest elements, and the only ones created during the Big Bang nucleosynthesis (along with some traces of Li). Some hundreds of millions of years later stars formed, and this allowed more helium to be synthesized by nuclear fusion in their cores. This reaction produces an internal outward pressure keeping the star from collapsing under its own gravity, but after enough hydrogen is depleted the reaction alone cannot support the star's gravitational pressure, which implodes. This implosion produces higher temperatures and densities in the star's core, allowing for other fusion reactions to happen. The second region includes nuclei created by stellar nucleosynthesis, it starts at He and stops at around $A = 56$ (the "iron peak").

The most likely nuclear reaction capable to increase a nucleus' mass in the third and last region ($A > 56$) is neutron-capture. Neutrons are neutral, and can just fall into the nuclear potential without having to tunnel through a Coulomb barrier[2]. By separating the slow and the rapid neutron-capture processes, we can explain the double-peaks in the abundance plot of Figure 2.1.

The two processes, shortened to s process and r process, are each responsible

---

[2]There might still be a "centrifugal" potential barrier for neutrons adding or subtracting angular momentum to the nucleus, called p-wave neutrons. For this reason, s-wave neutrons, with no angular momentum, are favored in neutron-capture reactions.

for the creation of about 50% of the elements heavier than iron in our solar system, and each yields a specific abundance pattern (see e.g. [23, 25]). Together with the p process, responsible for the creation of some proton-rich nuclei not achievable by neutron-capture [26], they can explain the origin of the elements in the solar system.

Although our solar system is enriched almost in the same proportions by the s and the r processes, this is not necessarily the case for other stars. Spectral lines from a star's atmosphere may help us to understand its elemental composition, and the presence of certain elements or elemental ratios in it can tell us which process was most responsible for its enrichment. For example, the r process contributes to 80-100% of the Eu abundance in the solar system, and the s to 70-100% of the Ba abundances, and for this reason the relative abundance of these elements to e.g. Fe can be used to trace the origin of chemical composition of stars [25]. Some are enriched only by s or r process elements, some others, like our sun, are enriched by both. By analyzing and mapping these stars we can understand not only their origin, but also the history of our galaxy.

Several observations moreover indicate the presence of another, minor process, called intermediate neutron-capture process (or i process). Its introduction has been deemed necessary to explain the abundances of a certain kind of stars presenting patterns typical for both the s and the r processes, but old enough to exclude the possibility of them being enriched by multiple sources. A description of all of these processes will be given in this chapter.

Simulations of these nucleosynthesis processes are invaluable tools when investigating their nature. Not only they provide an insight into how they work in astrophysical environments, but they also give indications to experimentalists about which nuclei or which mass regions are most important to extract nuclear properties from. This kind of studies are called sensitivity studies, and in Section 2.5.4 I will give a short overview about them as an introduction to Paper IV [27].

2.3   Big Bang nucleosynthesis

When Alpher, Bethe and Gamow presented their Big Bang theory in the 1940s [18], what they actually proposed was an explanation to the origin of elements. This would happen by successive neutron captures and β decays until all the elements were created. Although we now know that the Big Bang is only responsible for the formation of H, He and Li (see e.g. Ref. [28] for a review) the theory predicted a remaining background radiation from these nucleosynthesis processes. When the Cosmic Microwave Background radiation was observed in 1965 [29], it further solidified the Big Bang theory as the leading cosmological theory about the beginning of the universe.

The process behind the creation of primordial hydrogen, helium and lithium in the universe is called Big Bang nucleosynthesis. Protons and neutrons could form about $t = 0.5$ s after the Big Bang, when temperatures decreased to below $T \approx 15$ GK. It was not until after $t \sim 200$ s that temperatures became low

enough to allow nuclei to form without being immediately destroyed. At this time the neutron-to-proton ratio was about 1/7. As ^{4}He is the most tightly bound light nucleus, most of the neutrons ended up forming helium, and because of the 1/7 ratio the predicted mass fraction of helium compared to hydrogen is 0.25, very close to the one observed [30].

As the mean lifetime of free neutrons is $\tau = 880.1 \pm 1.1$ s [31], Big Bang nucleosynthesis ended after about 1000 s, as the universe continued to expand. In order to create heavier nuclei, we would have to wait until the creation of stars.

2.4 Stellar nucleosynthesis

The period following Big Bang nucleosynthesis is called the Dark Ages of the universe as stars did not form before some 100-400 Myr, or million years (theoretically 75 Myr [32], while one of the oldest observed stars in our galaxy is as old as 13.53 Gyr, forming some 400 Myr after the Big Bang [33]). Stars begin as big clouds of hydrogen collapsing upon themselves because of gravity, and can be understood as continuous explosions where the pressure from the nuclear reactions in their core is balanced by the one from their own gravity. Because of this, we say that these objects are in hydrostatic equilibrium as long as the internal pressure can be regarded as constant.

In this section I will present a qualitative overview of stellar nucleosynthesis, this being the process of element creation by nuclear fusion happening in the star up until and during its last explosion. The material in this section is based on Chapters 1 and 5 in *Nuclear physics of stars* by Christian Iliadis [34] (see also e.g. Refs. [35–37] for stellar models with different initial masses).

The first stars consisted of just H and He. When pressure and temperature are high enough in their core, four hydrogen nuclei may be converted into a He nucleus, releasing energy in the process. This process consists of several steps, and the collection of these is called the *pp-chain*. As long as the star has enough hydrogen to burn[3], the internal pressure is held practically constant and it may continue undisturbed for millions or billions of years, depending on the initial mass of the star (generally, the higher the initial mass, the shorter the lifetime). When the fuel is not enough to balance gravity, the core contracts increasing both its temperature and pressure. Depending on the initial mass of the star, this may unlock different burning stages during the lifetime of the star. If the star is larger than 0.4 $M_\odot$ (where $M_\odot$ represents the mass of the Sun), then these higher temperatures and pressures may allow the star to use He as a fuel for nuclear fusion in a new equilibrium stage. Helium will also exhaust after a while, and the core will contract and start another equilibrium stage burning now a different nucleus, when the mass is high enough and the conditions are right. This series of phases will continue until a last contraction will trigger an explosion which releases the envelope of the star into space, and leaves the

---

[3] By "burning" here and in the rest of the chapter we refer to nuclear fusion and not to the chemical reaction.

remaining core as either a white dwarf, a neutron star or a black hole. This is the death of the star.

When it comes to stellar nucleosynthesis, the different phases of a star's lifetime create different elements.

The first and longest phase is called H-burning, where hydrogen is combined into helium through the pp-chain, or if the star was formed from the remnants of another star and has enough carbon and high enough mass, the CNO-cycle where ^{12}C nuclei act as catalysts for forming He from H. For this last reaction cycle we have a bottleneck at the ^{14}N(p, γ) reaction, meaning that when hydrogen exhausts, the most abundant remaining nuclei will be ^{4}He and ^{14}N. If high enough pressures and temperatures are reached after the core's contraction, a new phase of He-burning becomes possible in the core, where ^{12}C is produced through the triple-α reaction and ^{22}Ne is produced by the reaction chain ^{14}N$(\alpha, \gamma)^{18}$F$(\beta^+)^{18}$O$(\alpha, \gamma)^{22}$Ne.

While He-burning happens in the inner part of the star, H-burning may still happen in an outer layer where lower pressures and temperatures are found. For each hydrostatic burning phase, we must imagine the star as some kind of onion, where the nuclear burning needing the highest temperatures and pressures happens in the center, while the previous burning process still happens, but in an outer shell where the physical conditions and presence of reactants are just right.

The H-burning and the He-burning phases are important both for low, intermediate mass stars ($M \lesssim 8-10M_\odot$) as well as massive stars ($M \gtrsim 8-10M_\odot$), but whereas low and intermediate mass stars usually stop at He-burning, massive stars will continue with different phases until their death. After He-burning we have C-burning. Its main reaction is ^{12}C$(^{12}$C,$\alpha)^{20}$Ne where neon, important for the subsequent Ne-burning phase, is produced. Here temperatures are so high that both nuclear fusion and photo-disintegration (a nuclear process where a nucleus is split by an incoming high-energy photon, or γ ray) happen, and oxygen and silicon are created with the ^{20}Ne$(\gamma, \alpha)^{16}$O and the ^{20}Ne$(\alpha, \gamma)^{24}$Mg$(\alpha, \gamma)^{28}$Si reaction chains. The oxygen created during the Ne-burning phase is then used to create more silicon in the O-burning phase via the reaction ^{16}O$(^{16}$O,$\alpha)^{28}$Si. The reactions listed so far are not the only ones happening during their respective phases, but merely the most important ones, and by the start of the final Si-burning phase we have a distribution light nuclei.

All of these burning stages last for less time the more advanced they are and where the H-burning phase may last for millions of years even for very massive stars, the Si-burning phase may last for a few days [38]. The duration of the burning stages for two stars of masses 1 and 15 $M_\odot$ is given in Table 2.1.

During the Si-burning stage the densities and temperatures are high, but not enough to fuse silicon with itself, given the very high Coulomb barrier. Instead, the weakest bound nuclei are photo-disintegrated, and the fragments may fuse with each other resulting in a chemical equilibrium of isotopes, meaning that the rate they are produced is the same as the rate of their destruction. This equilibrium is called *nuclear statistical equilibrium*, or NSE, and the abundance Y_i for any nucleus i is only determined by the temperature, the density, the binding

Burning stage	1 $M_\odot$ star	15 $M_\odot$ star
H-burning	11 Gyr	11.1 Myr
He-burning	1.1 Gyr	1.97 Myr
C-burning	-	2030 y
Ne-burning	-	0.732 y
O-burning	-	2.58 y
Si-burning	-	18.3 d

Table 2.1: Duration of the different burning stages for two stars of 1 and 15 $M_\odot$ solar masses, respectively. Whereas a 1 $M_\odot$ massive star will only manage to burn H and He, a more massive star will be able to go through all the burning stages up until Si-burning. Data gathered from Ref. [38].

energy B_i and charge conservation. The resulting products of the Si-burning phase is an abundance distribution centered around iron. All of these new nuclei are then spread in the subsequent supernova, ready to form new stars.

Elements heavier than He are called *metals* in astrophysics, and stars formed from the remnants of a previous stellar nucleosynthesis will have a higher *metallicity*. This will not only influence the life cycle of the star (by for example possibly enhancing energy production during the H-burning phase with the presence of ^{12}C and the CNO-cycle), but the now abundant nuclei of the iron peak will serve as seed nuclei for neutron-capture nucleosynthesis, responsible for the formation of heavy elements.

2.5 Neutron-capture nucleosynthesis

We have seen that silicon fusion is not a viable mechanism to create heavier elements even with the temperatures and densities of the Si-burning stage of stellar evolution, and this is because of the increasingly higher Coulomb barrier and of NSE becoming the main mechanism of nucleon reconfiguration. NSE yields an abundance distribution centered about ^{56}Ni, the nucleus with the most binding energy per nucleon, which eventually β-decays to stable ^{56}Fe forming the so-called iron-peak. The existence of nuclei as heavy as lead and uranium indicates that there must be another mechanism at play, and neutron-capture has been an attractive candidate for heavy-element nucleosynthesis ever since the discovery of the neutron. After the observation of double-peaks in the solar abundance of heavy elements in the vicinity of neutron magic numbers where the capture cross section is smaller, it became clear that at least two different neutron-capture processes were involved in their creation, later baptized in the B2FH paper [23] as *s process* and *r process*, standing for slow and rapid neutron-capture process, respectively.

Neutron-capture nucleosynthesis happens when seed nuclei find themselves in an environment with free neutrons. Neutrons are unstable particles with a half-life of minutes, meaning that this kind of nucleosynthesis can only happen

57Cu 196.3ms ε=100.00%	58Cu 3.204s ε=100.00%	59Cu 81.5s ε=100.00%	60Cu 23.7m ε=100.00%	61Cu 3.339h ε=100.00%	62Cu 9.673m ε=100.00%	63Cu STABLE 69.15%	64Cu 12.701h ε=61.50% β=38.50%
56Ni 6.075d ε=100.00%	57Ni 35.60h ε=100.00%	58Ni STABLE 68.077%	59Ni 7.6 10⁴y ε=100.00%	60Ni STABLE 26.223%	61Ni STABLE 1.1399%	62Ni STABLE 3.6346%	63Ni 101.2y β=100.00%
55Co 17.53h ε=100.00%	56Co 77.236d ε=100.00%	57Co 271.74d ε=100.00%	58Co 70.86d ε=100.00%	59Co STABLE 100%	60Co 5.28d β=100.00%	61Co 1.649h β=100.00%	62Co 1.50m β=100.00%
54Fe STABLE 5.845%	55Fe 2.744y ε=100.00%	56Fe STABLE 91.754%	57Fe STABLE 2.119%	58Fe STABLE 0.282%	59Fe 44.495d β=100.00%	60Fe 2.62 10⁶y β=100.00%	61Fe 5.98m β=100.00%
53Mn 3.74 10⁶y ε=100.00%	54Mn 312.20d ε=100.00% β −9.3 10⁸	55Mn STABLE 100%	56Mn 2.5789h β=100.00%	57Mn 85.4s β=100.00%	58Mn 3.0s β=100.00%	59Mn 4.59s β=100.00%	60Mn 0.28s β=100.00%
52Cr STABLE 83.789%	53Cr STABLE 9.501%	54Cr STABLE 2.365%	55Cr 3.497m β=100.00%	56Cr 5.94m β=100.00%	57Cr 21.1s β=100.00%	58Cr 7.0s β=100.00%	59Cr 1.05s β=100.00%

Figure 2.2: A schematic picture of neutron-capture nucleosynthesis for low neutron densities, starting from ^{56}Fe. Neutron-capture corresponds to a step in the right direction, while β^- decay occurs when the isotope obtained by neutron capture is unstable, and is represented by an oblique step in the upper-left direction. The background chart was drawn using the *Chart of nuclides drawer* [3], based on the data from the 2016 atomic mass evaluation [4].

where these are created. As we will see in the next section, some reactions in the He-burning shell may luckily just create neutrons as a byproduct, and together with explosive environments such as supernovae and neutron star mergers they are the astrophysical sites where such neutron-capture processes take place (see e.g. [39] and references therein for a review). In these sites seed nuclei may capture neutrons and become heavier isotopes of the same element (e.g. from ^{56}Fe we would obtain ^{57}Fe, see Figure 2.2). If the isotope is stable this process may repeat, but if it is β unstable and its β-decay rate is faster than its neutron-capture rate or photo-disintegration rate, then it will β decay transforming a neutron into a proton and thus creating a new element (in our case, Co from Fe). Neutron-capture nucleosynthesis is then able to climb the nuclide chart from lower Z nuclei up to Pb or even U. Here I will explain the main differences between the s and the r process, together with a description of a minor, but still important, process called the *i process*, standing for intermediate neutron-capture process.

2.5.1　The s process

The s process involves neutron densities of $N_n \leq 10^{10}$ cm^{-3} [40] and may last for many thousands of years, in 20 to 50 cycles of some 10 kyr each, and may happen in low to intermediate mass stars during their asymptotic giant branch (AGB) phase, and in massive stars during their core He-burning stage [41, 42]. During this process the stable seed nuclei capture free neutrons, but neutron densities are low enough to allow for most β-unstable nuclei to decay to stability before capturing another neutron. This means that the nucleosynthesis flow will closely follow the valley of stability up to Pb and Bi (in a similar fashion as Figure 2.2), but it will not be able to synthesize elements like Th or U. While climbing up the nuclear chart, the neutron-capture flow will cross certain areas of low neutron-capture rates at neutron shell closures. These will act as bottlenecks for the s-process nucleosynthesis and lead to a pile-up of elements at $A \approx 138$ and 209, which correspond to the right peaks of the two double-peaked structures in Figure 2.1.

For certain nuclei the β-decay rate is comparable to the neutron-capture rate, and the path they take may influence the final abundances. These are called branching points. The branching ratio tells us to which degree the s process will follow one path or another and it is sensible to the correct measurement of the neutron-capture cross section as well as the astrophysical conditions such as temperature and neutron densities. Some of the most famous branching points are ^{85}Kr and ^{151}Sm [43], and one minor one is ^{166}Ho, which has an isomer with a lifetime of 1200 years that may or may not decay to ^{166}Er before capturing a neutron. These considerations are further discussed in Paper III [44].

The observation of Tc on the surface of AGB stars [20] confirms that the s process indeed takes place in their interior. The nature of the s process changes depending on the mass of the star. Generally, we may distinguish low-mass stars ($M \lesssim 3 M_\odot$) from massive stars ($M \gtrsim 8 - 10 M_\odot$). In low-mass stars the AGB phase of stellar evolution happens during its He-burning phase, where an inert C and O core is covered by an intershell consisting mainly of He and ^{12}C, then a H-burning shell and finally a convective zone. These stars go through a pulsing phase because of thermal instability: H-burning and He-burning do not necessarily operate in a constant way or at the same time in their relative shells [30, 43]. Generally H-burning provides most of the energy and adds mass to the intershell below, increasing pressure and temperature until these are high enough to ignite He-burning at the bottom of the intershell. The energy produced here at a certain point becomes so high that it cannot be dissipated by radiation alone, and a thermal pulse seeks to release it by convection, mixing the above layers in the process. The H-burning shell is extinguished and protons from the former convective zone are brought down to the intershell, allowing for the creation of ^{13}C via the reaction chain ^{12}C$(p, \gamma)^{13}$N$(\beta^+)^{13}$C. After the pulse, the star contracts again and the H-burning shell reignites, starting the cycle again. A star may go through several thermal pulses before exiting the AGB phase. When temperatures reach $T = 0.09$ GK in between pulses, ^{13}C$(\alpha, n)^{16}$O becomes possible in the intershell and releases neutrons ready to be captured by

seed nuclei and fuel the s process. During a pulse, higher temperatures in the H-shell also allow for the $^{14}\text{N}(\alpha,\gamma)^{18}\text{F}(\beta^+)^{18}\text{O}(\alpha,\gamma)^{22}\text{Ne}$ reaction chain, where for a few years a stronger, but shorter neutron source is generated from the resulting ^{22}Ne via the $^{22}\text{Ne}(\alpha,n)^{25}\text{Mg}$ reaction, and this is able to overcome certain branching points. All these new elements will later be brought to the surface after the next thermal pulse. As the H-burning shell extinguishes and the convective zone lowers, not only protons from this upper zone mix with the intershell below, but the elements created during the nuclear fusion and the s process are mixed and brought to the surface. This mixing is also referred as *third dredge-up* for this reason[4].

This is the mechanism behind the *main s process*, responsible for most of the s-process abundances. The *weak s process* is another minor mechanism present in massive stars, where ^{14}N from the CNO cycle is transformed to ^{22}Ne as described above. The latter is responsible for the creation of nuclei in the $A \lesssim 90$ mass region [30, 42].

The s process is responsible for the creation of about 50% of the elements heavier than iron in the solar system and explains the right peak in both double-peaked regions in the isotopic abundance plot (Figure 2.1). In order to explain the other half and the left peaks, a different neutron-capture process must be invoked, called the r process.

2.5.2 The r process

The r process is more mysterious than the s process as it involves very exotic nuclei and the astrophysical sites where it is thought to take place are difficult to observe, study and simulate [23, 24]. The process involves neutron densities above 10^{20} cm^{-3} and lasts only for a few seconds (see e.g. Refs. [45, 46] for recent reviews of the r process). The high neutron densities allow for a capture-rate so high that the unstable, neutron-rich nuclei do not have time to β decay or be photo-disintegrated before they capture a new neutron, and thus end up very far in the neutron-rich side of the nuclear chart, where these reaction can balance. When the neutron flux is extinguished the nuclei are allowed to decay back to stability creating an abundance pattern different than that for the s process. Since we have very neutron-rich nuclei we may end up with nuclei with high Z such as Th and U when neutrons are converted into protons in the β decay, nuclei not otherwise reachable by the s process. Moreover, the bottlenecks corresponding to the neutron magic numbers are met at a lower Z, and thus lower A (See Figure 2.3). These bottlenecks allow for pileups in abundances similar to the s process, but being at a lower A, the peaks will be slightly shifted to the left. This explains the left peaks in the double-peaked structures in the

---

[4]The *first dredge-up* also happens at an earlier stage of the star, while the *second dredge-up* may only happen in more massive stars. These are two different processes with the only common feature of bringing the results of nuclear reactions from the interior to the surface of the star. The names are somewhat confusing and do not imply that they should occur subsequently to each other.
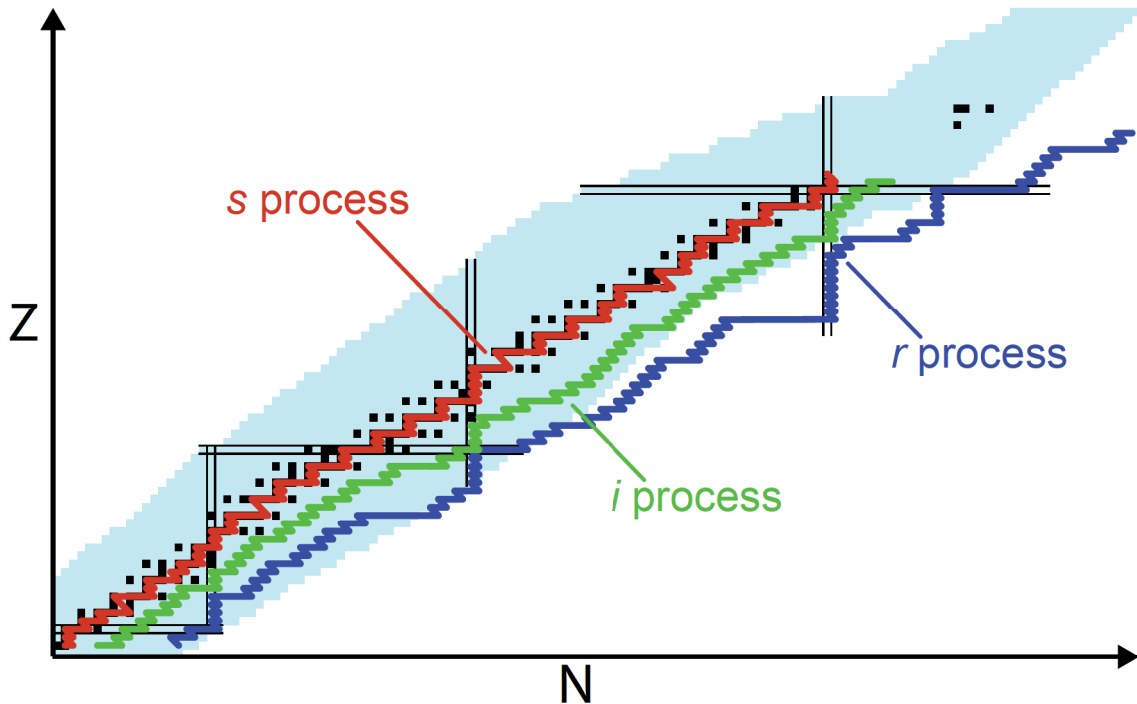
Figure 2.3: The qualitative nucleosynthesis paths for the s, i and r processes. While the s process closely follows the valley of stability, the r process generally involves very exotic, neutron-rich nuclei. The i process will find itself somewhere in the middle, about 5 neutrons away from stability. At the neutron magic numbers 82 and 126 all processes will experience pile-ups and bottlenecks.

abundance plot in Figure 2.1. The decomposed solar system abundances can be seen in Figure 2.4.

The huge amount of neutrons needed to drive the r process are thought to be created in cataclysmic explosions in space. There are many proposed sites for the r process, but the only one confirmed up to now are neutron star mergers (NSM). The observation of the gravitational waves from the GW170817 merger [47] and the associated electromagnetic signal showed nucleosynthesis activity matching the one expected for the r process [48]. The r process from NSM is expected to be strong enough to create all the heavy elements, reach the actinides and even allow for *fission recycling*, where superheavy elements fission and provide new seed nuclei for the r process from the fragments (see e.g. Refs. [46, 49, 50] and references therein).

Another, actual site for the r process are core-collapse supernovae (CCSN) with a mechanism called *neutrino-driven wind*. CCSNs may happen when a star of initial mass of $\gtrsim 10 M_\odot$ goes through all the burning stages and ends up with an iron core in NSE equilibrium [39, 41]. When the iron core collapses, matter neutronizes and a proto-neutron star is formed. The infalling material outside the core "bounces" on the hard proto-neutron star surface and explodes as a CCSN. The neutronization of the core matter releases a huge amount of energy in the form of neutrinos. These in turn will heat up the neutronized matter just

outside the proto-neutron star and drive it into the slower shock front from the bounce, fueling the supernova in the process [30]. This is the neutrino-driven wind, and although at first considered a promising scenario for the r process to happen, it later lost appeal when better simulations of supernovae could not attain the desired conditions. It may still be the location of the *weak r process*, creating nuclei up to $A \approx 130$ [51, 52].

2.5.3 The i process

Both the s and the r processes produce specific abundance patterns that can be recognized in stars. The abundances of Eu, Ba and Fe on star surfaces can be measured from their spectral lines, and their ratios can indicate whether a star has been enriched by s or r elements, or both. Many young stars for example show signs of enrichment from both, while old stars may present only one if any, as matter from both had not yet had time to mix by the time of their formation. This is the case of carbon-enhanced, metal poor stars (or CEMPs) in the galactic halo. These may be further categorized into CEMP-s, CEMP-r and CEMP-no, where the first category presents an enrichment of s elements, the second of r elements and the third no particular enrichment. There is though a fourth kind of CEMPs, called CEMP-s/r, that presents elements from both nucleosynthesis processes. This is difficult to explain in terms of s and r process alone, as these are thought to occur in completely different astrophysical sites, and matter from them had not the time to mix before the formation of CEMP-s/r [53]. Moreover, the ratio between s and r elements tends to be similar for all CEMP-s/r, pointing to a singular origin for their heavy element enrichment [54].

The i process is a neutron-capture process involving neutron densities of about 10^{15} cm^{-3}, and was first proposed by Cowan and Rose in 1977 [55] due to the ^{12}C$(p, \gamma)^{13}$N$(\beta^+)^{13}$C$(\alpha, n)^{16}$O reaction. It came recently to relevance as a possible explanation to such observed s/r abundance patterns, and some simulations seem to confirm this [53]. As for the s process, the i process requires the ingestion of protons in a He-burning shell, but given its relatively high neutron densities the ingestion has to be bigger, and the astrophysical conditions different.

AGB stars are again expected to be candidates for such a process to occur (see e.g. Refs. [53, 56] and references within), and although there are some ideas on how it may happen, the i process is still mysterious because it involves neutron-rich, exotic nuclei. Low metallicity in stars may make the mixing of H and He-burning shells easier, allowing for higher numbers of protons to mix during convective episodes due to thermal pulses. There are many candidates for the site where the i process is thought to occur. Among these are: low- to zero-metallicity AGB stars during their early stage (see e.g. [57]); post-AGB stars in the late thermal pulses (see e.g. [58]); low- to zero-metallicity massive stars during their C-burning stage (see e.g. [59]); the core He-flash of low-metallicity, low-mass stars (see e.g. [60]). Another possible scenario is in rapidly accreting white dwarfs, where the white dwarf captures hydrogen from the envelope of a companion star, H and He burning occur near the surface, and the ingestion of
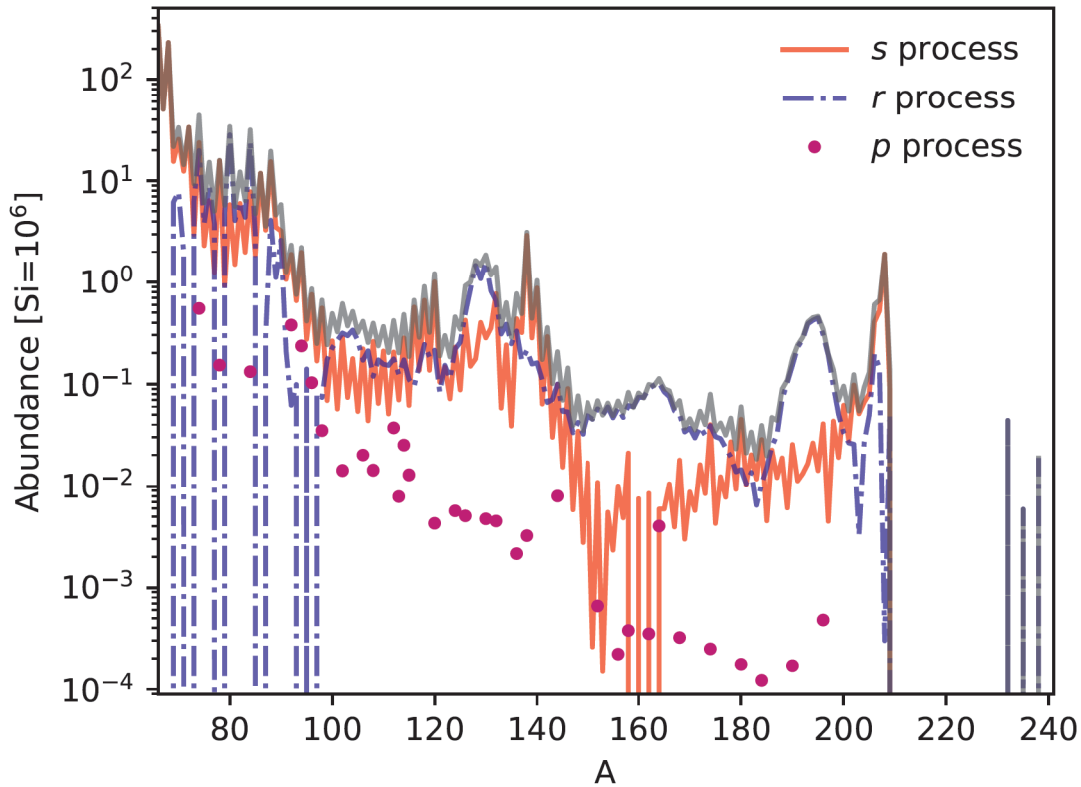
Figure 2.4: The solar isotopic abundances for trans-iron elements decomposed between p, s and r-process elements. The total abundances are from Lodders *et al.* [1], while the r-process abundances are from Goriely *et al.* [62] and the p-process abundances from Arnould *et al.* [26]. The two double-peaks are decomposed between the r-process peaks on the left, and the s-process peaks on the right.

surface hydrogen into the He-burning shell may trigger the i process [61]. For all these potential sites, see e.g. Ref. [56] and references therein.

2.5.4 Astrophysical modeling and sensitivity studies

In order to investigate all of these processes (s, r and i) we need a correct description of the astrophysical sites where they occur, and the knowledge of the properties of the nuclei involved. When it comes to the astrophysical site, great uncertainty has long shrouded the r process, and in this section I will present an overview of the models used in order to simulate its conditions. The material here is largely based on the review papers from Arnould *et al.* [25] and Mumpower *et al.* [63].

One of the first models started from the assumption that supernovae were the main host for the r process, where temperatures are high enough ($T \gtrsim 2$ GK) to permit $(n, \gamma) \rightleftharpoons (\gamma, n)$ equilibrium. For each element, isotopes are in thermal

equilibrium between neutron-capture and photo-disintegration, while a certain ratio is allowed to β-decay and create another element. Only a few nuclear properties are relevant at this stage: neutron separation energies, β decay rates and information about the energies and spins of ground and excited states. This simple model is called *canonical r process* (CAR) with the waiting point approximation. While the model was not able to reproduce the correct abundances, it could qualitatively predict the expected features and provided a good starting point for more sophisticated models. The CAR model includes a series of simplifications, such as only having ^{56}Fe as a seed nucleus (a reasonable assumption when talking about CCSN), a constant neutron flux and temperatures high enough to sustain the $(n, \gamma) \rightleftharpoons (\gamma, n)$ equilibrium for the timescale of the process. In order to give a broader picture, the r process was modeled as the superposition of different *canonical events* (CEV) models, meaning simulations with different sets of initial astrophysical conditions (in this case the temperature, the neutron density and the timescale). This is the multi-event r-process (MER) model. When dealing with a *cold r* process, the waiting-point approximation is not valid anymore and the astrophysical and nuclear parts become more complicated, as neutron capture has to compete with β decay and both rates are dependent on temperature. In addition, fission recycling may complicate things for very high neutron-density environments.

An attempt to go beyond CAR models was the introduction of dynamical models (DYR), where the r process is modeled as a "bubble" of nuclear material in NSE (and thus providing different seed nuclei than just iron) with a certain electron abundance Y_e and entropy per nucleon s[5], expanding at a certain rate, cooling down and breaking the thermal equilibrium. Here, nucleosynthesis is governed by a network of nuclear reactions influenced by a varying neutron density and temperature. This bubble may be part of the ejecta of a neutron star merger or a supernova, and different parts of these phenomena may have different starting conditions, so the MER treatment is relevant for dynamical models as well.

When it comes to s and i-process simulations, the situation is somewhat similar. Both processes happen at temperatures of about 0.25 GK, well under the $(n, \gamma) \rightleftharpoons (\gamma, n)$ temperature threshold. A nuclear network calculation is necessary, but a dynamical approach is no longer valid as both processes happen in (relatively) stable environments. Nonetheless, a correct description of the astrophysical site is still necessary, as the conditions for both the s and i processes are tightly connected to star dynamics such as the third dredge-up (for both processes) and proton ingestion episodes (for the i process in particular), as well as the metallicity of the star (see e.g. Ref. [64] for the s process, and Refs. [56, 65] for the i process). In this regard AGB-star simulations may be set up where the radius is divided into shells where network calculations are allowed to run

---

[5]low Y_e and high s together can be qualitatively understood as the quantity of free neutrons available for capture, as electric neutrality impose that the more electrons we have, the more protons we need to balance their charge up, and entropy tells us the amount of free neutrons that are released by photodissociation. Thus, the smaller the Y_e, and the higher the entropy s, the more strong and neutron rich the r process is.

in each of them, and also allow for mixing between shells and convection where convection conditions are met. These are called multi-zone simulations, and they may be 1D (only radial direction), 2D or 3D, where more sophisticated convection dynamics such as turbulence may be taken into account.

The nuclear network calculations behind the descriptions of the s, i and r processes are all dependent on the correct estimation of nuclear properties such as masses, β-decay rates and neutron-capture rates. Although important, I will not discuss masses and β-decay uncertainties, and I will focus mostly on neutron-capture rates. This quantity relates to the ability of a nucleus to capture a free neutron, releasing one or more γ rays. It may be measured directly for stable nuclei, and this greatly helped s process simulations by having access to most of the needed cross sections experimentally. This direct approach is however often unfeasible for unstable nuclei, where indirect methods such as the Oslo method (see Chapter 4) may help. For nuclei further away from stability we are dependent on theoretical estimates of their neutron-capture rates, and these may vary a lot from model to model making final abundance predictions uncertain for the i and r processes.

The experimental measurement of capture rates of every involved nucleus would be extremely time consuming, even assuming it was possible. Sensitivity studies are made in this regard in order to pinpoint the capture rate of which nucleus or nuclear chart region has the most impact on the final abundances. These sensitivity studies are carried out by using the abundance pattern from some astrophysical scenario (say, a neutron star merger) as a baseline. Then neutron-capture rates are varied, and the simulation is run again. The final abundances from these new simulations are then compared to the baseline, and conclusions are drawn from which neutron-capture rate variation produced the biggest abundance change[6]. There are two schools of thought regarding how these rates should be varied. One involves modifying the neutron-capture rates one nucleus at a time, for example by a factor up to 100. By then comparing every new simulation to the baseline, one may find out which single nucleus has the most impact on the final abundances. This method is used among others by Surman *et al.* [66], Mumpower *et al.* [63] and Vescovi *et al.* [67] for the r process and McKay *et al.* [68] for the i process. It is a powerful method as it is conservative in its estimation of uncertainties for the involved nuclear properties, but it suffers from the problem that by changing them one nucleus at a time it disregards the correlations we know exist between neighboring nuclei. For example, a nucleus with an odd number of neutrons will usually have a larger neutron-capture rate than a neighboring one with an even number. This approach is computationally expensive since many simulations have to be run, and simpler one-zone models that reproduce results from more sophisticated, heavier multi-zone simulations are used (with a notable exception by Denissenkov *et al.* [69]). This may also be a drawback since the importance of one specific nucleus in a particular zone may be washed out by the output from the other

---

[6]Similar sensitivity studies are made for all uncertain nuclear properties, such as β-decay rates or masses.

present "zones" in the astrophysical scenario.

The second school tries to solve many of the problems from the first by simulating the whole astrophysical site (may it be an AGB star or a neutron star merger) and vary the input *models* for some of the nuclear properties at once (see e.g. Kullmann *et al.* [70] for the r process and Goriely *et al.* [65] for the i process). This method is more rigorous on the physics side, as the astrophysical environment is well accounted for and nuclear correlations are included, but conclusions may be more vague (although not necessarily incorrect for that reason) pointing at important regions instead of single nuclei. Another problem with this approach is that it may underestimate nuclear uncertainties as none of these nuclear models provide confidence intervals. In Paper IV [27] these two approaches are compared in the context of the r process.

Chapter 3

Nuclear properties

The atomic nucleus is a quantum many-body system governed by the laws of quantum mechanics. Its constituents interact with the weak and the strong nuclear forces as well as the electromagnetic force. The peculiarity of atomic nuclei is that its particles create the potential they themselves are influenced by. This is in contrast to the nuclear Coulomb potential influencing the motion of the surrounding electrons. In order to simplify this problem, one often models the nuclear potential as a *mean field*. Here, the interaction felt by a nucleon from the other $A-1$ nucleons is modeled as an independent, common potential that affects all particles in the nucleus. The shape of this potential resembles a mix between the finite well and the harmonic oscillator potential, and it gives rise to a behavior similar to that of electrons in an atom, with some interesting twists. One obvious common trait is that both systems are quantum mechanical, meaning that as long as particles are bound in a potential, their wave functions will only be able to organize in certain *quantum states*, each with their own characteristic quantum numbers. Nucleons are fermions, and this means that no two identical particles may occupy the same quantum state at the same time. Another common trait is that the nucleus interacts with the electromagnetic force, and nucleons may excite or de-excite between energy levels by absorbing or emitting photons. One difference is though that the energy difference between levels is often in the order of MeV instead of eV as for electrons, so photons emitted by a nucleus are often called γ rays, and electromagnetic (EM) nuclear decay called γ radiation. EM decay may be understood both classically and quantum-mechanically, and for a mesoscopic system such as the atomic nucleus both approaches may be useful, depending on what kind of phenomenon we want to describe.

3.1   Electromagnetic properties

As the nucleus consists of charges and currents, its electromagnetic field may be described in terms of static multipole moments. The expansion in multipole moments is a useful mathematical tool to decompose functions dependent on two angles, such as the polar and azimuthal for spherical surfaces, and is analogous to the decomposition of functions into Taylor or Fourier series. The static electric monopole moment would be the first term in the expansion and corresponds to the isotropic field from a point charge. The second term is the electric dipole moment and corresponds to two charges q and $-q$ separated by a distance z. While no magnetic monopole has been observed, the magnetic dipole is the magnetic field formed by a current I encircling an area A. Monopole and dipole are the first terms in the multipole expansion, and because these fields arise from

simple charge and current distributions, nuclear EM fields are conventionally described in terms of these moments.

The time variation of these fields gives rise to *EM radiation fields*, and γ decay can also be decomposed into its multipole moments. We may now introduce some notation. While the radiation character X may be electric (E) or magnetic (M), the multipolarity L may be monopole (0, only for electric radiation) dipole (1), quadrupole (2) and so on. For example, we may call a variation in the dipole electric field as $E1$ radiation. We exclude from this discussion monopole transitions, as this would correspond to variations in the electric charge, and this cannot be accomplished by electrically neutral photons.

EM fields may also have positive or negative *parity*, describing how their operator transforms a quantum state when acting upon it. For example, the electric dipole momentum operator for a charge q moving a distance $\mathbf{r}$ is $q\mathbf{r}$, and when calculating the amplitude for the transition from ψ_2 to ψ_1 we would write $\int d\mathbf{x}\psi_1 q\mathbf{r}\psi_2$. Since the $\mathbf{r}$ term is odd, the two wavefunctions must have opposite parity in order for the integral to be nonzero. Electric and magnetic fields of the same multipolarity have always opposite parities, meaning that the *magnetic* dipole radiation will have even parity. For quadrupole radiation the situation is reversed: the electric dipole operator will have a term in r^2 keeping the symmetry unvaried (*even parity*) while this will not be the case for the magnetic quadrupole moment (*odd parity*).

A γ decay corresponds to the transition from a state $|i\rangle$ of excitation energy E_i to a state $|f\rangle$ of excitation energy E_f. These states are characterized by their energy, angular momentum and parity. Radiation of multipolarity L carries angular momentum $\mathbf{L}$, and the transition between two states of angular momentum $\mathbf{I}_i$ and $\mathbf{I}_f$ will only allow radiation of multipolarity between $|I_i - I_f|$ and $I_i + I_f$ in integer steps because of angular momentum conservation. Parity may also change. If it does, only $E1, M2, E3...$ transitions will be allowed (odd electric, even magnetic), while if it remains unvaried only $M1, E2, M3...$ are allowed (odd magnetic, even electric). The collection of these instructions on allowed and not allowed transitions are called *selection rules* for the EM nuclear interaction (may it be γ decay, or absorption).

Knowing this, we may express a transition of EM character X and multipolarity L from a state $|i\rangle$ to another state $|f\rangle$ as

$$\mathcal{O}_{fi}(XL) = \langle f|\hat{\mathcal{O}}(XL)|i\rangle, \tag{3.1}$$

where we call $\mathcal{O}_{fi}(XL)$ the *matrix element*, and $\hat{\mathcal{O}}(XL)$ the multipole operator. The matrix element can be understood as the overlap between the $|f\rangle$ state and the $|i\rangle$ state transformed by the multipole operator, meaning it tells us "how much" of the initial state ends up in the final state when undergoing a XL transition. Indeed, the squared matrix element can be used to find the rate for a certain transition (meaning "probability per second") by

$$\lambda^{XL\mu} = \frac{8\pi(L+1)}{L\hbar[(2L+1)!!]^2}\left(\frac{E_\gamma}{\hbar c}\right)^{2L+1}|\langle fm_f|\hat{\mathcal{O}}(XL\mu)|im_i\rangle|^2, \tag{3.2}$$

where $(2L + 1)!! = 1 \cdot 3 \cdot ...(2L + 1)$. A state with angular momentum $\mathbf{L}$ may have different magnetic substates characterized by the quantum number m, corresponding to the z component of $\mathbf{L}$. This means that the outgoing radiation will have an angular momentum L with a projection along the z axis of $\mu = m_f - m_i$.

What we are often interested in is the probability of going from one energy level to another, regardless of the substates m_i and m_f. We may then introduce the *reduced transition probability* $B(XL; J_i \rightarrow J_f)$, where we modify the matrix element by taking an average of the m_i possible substates and summing over the final m_f substates:

$$B(XL; J_i \rightarrow J_f) = \frac{1}{2J_i + 1} \sum_{m_i, m_f} |\langle f|\hat{\mathcal{O}}(XL\mu)|i\rangle|^2. \tag{3.3}$$

The rate in Eq. (3.2) becomes

$$\lambda^{XL} = \frac{8\pi(L+1)}{\hbar L[(2L+1)!!]^2} \left(\frac{E_\gamma}{\hbar c}\right)^{2L+1} B(XL), \tag{3.4}$$

or, alternatively,

$$\Gamma^{XL}(E_\gamma) = \frac{8\pi(L+1)}{L[(2L+1)!!]^2} \left(\frac{E_\gamma}{\hbar c}\right)^{2L+1} B(XL) \tag{3.5}$$

using the relation $\Gamma = \hbar\lambda$, where Γ is the decay width. $\Gamma_i^{XL}(E_\gamma)$ is called the *partial decay width* and it tells us to which degree a level at excitation energy E_i, angular momentum J_i and parity m_i will decay by emitting XL radiation of energy E_γ. The total decay width of a level, defined by $\Gamma_{i,\text{tot}} = \sum_{E_\gamma, XL} \Gamma_i^{XL}(E_\gamma)$, give us information on the lifetime of the excited level i. Conversely, we might obtain the branching ratio of a decay by $\Gamma/\Gamma_{\text{tot}}$, telling us the probability an excited level has to decay by emitting energy E_γ compared to the other possible decay modes.

Levels, matrix elements, transition probabilities, level widths and branching ratios are all useful quantities when talking about levels that can be well distinguished from each other. This is indeed the case for low excitation energies and for light nuclei, but the higher we go in excitation energy, the more levels we find and these will be closer and closer to each other. Generally, we may separate between three different regions in the excitation energy: the *discrete*, the *quasi-continuum* and the *continuum* regions. The discrete region is the lowest one, it includes the ground state and the first excited levels, and the energy levels are well separated and distinguishable from each other. When the density of levels becomes higher than $\approx$200 per MeV bin, we have reached the quasi-continuum region. Although levels here are still separable in principle, detector resolutions make the task either impractical or outright impossible. For this reason the region is best described by statistical quantities such as the *nuclear level density* and the *γ-ray strength function*. The quasi-continuum ends where the wave-functions begin to overlap, and levels are not separable from

each other anymore. As much of the astrophysics involving neutron capture happens in the quasi-continuum, the nuclear level density and the γ-ray strength function are a central topic of this thesis. In the rest of this chapter, the theory behind these two quantities will be discussed, together with the optical model potential and the role these have in describing neutron-capture rates through the compound nucleus picture and the Wolfenstein-Hauser-Feshbach formalism [71, 72].

3.2 The nuclear level density

As we leave the discrete excitation energy region and we move into the quasi-continuum, the best way to count quantized energy levels becomes using the nuclear level density instead of treating them as discrete entities. As the name suggests, the nuclear level density (NLD, $\rho(E_x)$) is the number of accessible levels within a certain excitation energy bin. In this work, we will mostly talk about the number of levels per MeV bin, and the NLD will have units of MeV^{-1}.

When considering the nucleus as a mean field potential where bound fermions move freely within, it is tempting to describe the system as a Fermi gas. This was the first approach used by Hans Bethe in 1936 [73], who found an exponential increase in the NLD with respect to the square root of the excitation energy E_x. Experimentally, the NLD is indeed found to increase exponentially in a qualitative sense, but the Fermi gas model does not consider effects such as pair breaking, shell effects or any collective behavior. These are taken into account in the Gilbert & Cameron formula [74] where, broadly speaking, the energy E_x is replaced with $U = E_x - \Delta_p - \Delta_n$, the last two being the pairing energies for protons and neutrons, respectively. Also, a dependency on the spin-cutoff parameter $\sigma(E_x)$ is introduced, telling us the expectation value for the angular momenta for levels at at a certain E_x. In the same paper Gilbert & Cameron make use of the model by Ericson [75] and propose a different model for the NLD, this being the constant temperature (CT) model. This uses a different approach than the Fermi gas one, where instead of treating the system firstly as a quantum system of fermions, it considers the nucleus as a thermodynamic system of paired nucleons, where the transfer of energy breaks the pairs analogously as what heat does to melting objects. During this phase transition, the temperature is held constant, and the NLD increases exponentially with E_x:

$$\rho_{\mathrm{CT}}(E_x) = \frac{1}{T_{\mathrm{CT}}} \exp[(E_x - E_0)/T_{\mathrm{CT}}], \qquad (3.6)$$

where T_{CT} and E_0 are both parameters to fit to experimental data, making the CT model phenomenological.

A more phenomenological variant of the Gilbert & Cameron Fermi gas model was also proposed by von Egidy in 1988 [76], called the back-shifted Fermi gas model (BSFG). In 2005, von Egidy & Bucurescu [77, 78] compiled the different parameters fitting the experimental data for a collection of nuclei between ^{19}F

and ^{251}Cf for both the CT formula in Eq. (3.6) and the BSFG formula:

$$\rho_{\mathrm{BSFG}}(E_x) = \frac{\exp[2\sqrt{a(E_x - E_1)}]}{12\sqrt{2}\sigma(E_x)a^{1/4}(E_x - E_1)^{5/4}}, \tag{3.7}$$

where, again, σ is the spin-cutoff parameter. We see that apart from the dependence on the NLD parameter a and backshift E_1, the BSFG formula depends on the spin-cutoff parameter and its E_x dependence.

The spin-cutoff parameter σ[1] is a parameter identifiable with the expectation value for the spin distribution $\langle J \rangle$ at a certain E_x [79]. The NLD may be decomposed into partial level densities, each describing the density of levels of a certain spin J and parity π:

$$\rho(E_x) = \sum_{J,\pi} \rho(E_x, J, \pi). \tag{3.8}$$

It is custom to assume a balanced distribution of parities, $\rho(E_x, J, \pi) \approx \rho(E_x, J)/2$, while spins are distributed as $g(E_x, J)$:

$$\rho(E_x, J) = g(E_x, J)\rho(E_x). \tag{3.9}$$

The spin distribution $g(E_x, J)$ is normalized, meaning $\sum_J g(E_x, J) = 1$, and is assumed to be distributed as [73, 75]:

$$g(E_x, J) = \exp\left(\frac{-J^2}{2\sigma^2(E_x)}\right) - \exp\left(\frac{-(J+1)^2}{2\sigma^2(E_x)}\right), \tag{3.10}$$

which is governed by the choice of spin-cutoff parameter function. In the articles included in this thesis, three different spin-cutoff parameter functions are considered. The first one is the one proposed by Gilbert & Cameron [74]

$$\sigma^2(E_x) = 0.0888A^{2/3}a\sqrt{(E_x - E_1)/a}, \tag{3.11}$$

and the second the one proposed by von Egidy & Bucurescu [77, 78]

$$\sigma^2(E_x) = 0.0146A^{5/3}\frac{1 + \sqrt{1 + 4a(E_x - E_1)}}{2a} \tag{3.12}$$

where both include the same parameters a and E_1 as for the BSFG NLD formula. The second model is frequently called the rigid-body moment of inertia (RMI) model, as it idealizes the nucleus as a rigid body, and for this reason frequently yields higher spin-cutoff parameters than the Gilbert & Cameron formula, the latter referred as the FG model for spin distribution. A third, simpler model is the one used e.g. by Guttormsen *et al.* [80] which models the distribution linearly in E_x:

$$\sigma^2(E_x) = \sigma_d^2 + \frac{E_x - E_d}{S_n - E_d}[\sigma^2(S_n) - \sigma_d^2], \tag{3.13}$$

---

[1]Sometimes I will refer to σ and other times to σ^2 as the spin-cutoff parameter. It should be clear from the context which form I am referring to.

where σ_d^2 is the spin-cutoff parameter at some discrete exitation energy E_d, while $\sigma^2(S_n)$ at S_n is used as the second point.

Both the CT and the BSFG models are phenomenological, meaning that their free parameters must be found from a fit to experimental data. This makes them good tools for describing existing data, but leads to poor predictive power for nuclei far from the valley of stability, where experimental data are scarce or non-existing. Microscopic models instead try to calculate the NLD from the underlying quantum mechanical laws and are, in principle, expected to have better prediction capabilities. Examples of microscopic models are the Hartree-Fock calculations from Ref. [81], the Skyrme-Hartree-Fock model [82] and the temperature-dependent Gogny-Hartree-Fock-Bogolyubov model [83], all implemented in the reaction code TALYS [84][2]. Their predictions will be compared to the experimental data for ^{127}Sb and ^{166,167}Ho obtained with the Oslo method in Paper I [85], Paper II [86] and Paper III [44] (more about the Oslo method in Section 4.2).

3.3 The γ-ray strength function

Where the NLD is the statistical equivalent of counting discrete states, the γ-ray strength function (GSF[3]) is the quasi-continuum version of the reduced transition probabilities. It may be interpreted as the average electromagnetic response of the nucleus, and it is defined as [87]

$$f^{XL}(E_\gamma, E_i, J_i, \pi_i) = \frac{\langle \Gamma_i^{XL} \rangle (E_\gamma, E_i, J_i, \pi_i)}{E_\gamma^{2L+1}} \rho(E_i, J_i, \pi_i) \qquad (3.14)$$

where Γ_i^{XL} is the partial decay width as defined in Eq. (3.5) and ρ the partial level density as found in Eq. (3.8). $\langle \Gamma_i^{XL} \rangle$ indicates the average partial decay width for initial energies in the vicinity of E_i making a transition of an energy close to E_γ. Although we may have strength functions for all multipolarities L, dipole radiation is the one dominating [88]. For this reason, from now on we will only consider dipole radiation. In particular, we may write

$$f(E_\gamma, E_i, J_i, \pi_i) \approx f^{E1}(E_\gamma, E_i, J_i, \pi_i) + f^{M1}(E_\gamma, E_i, J_i, \pi_i). \qquad (3.15)$$

The GSF as it stands in Eqs. (3.14) and (3.15) depends on four variables, these being the initial excitation energy E_i, the transition energy E_γ, and the spin and parity of the initial state, J_i and π_i. From here, we can do a series of simplifications. The GSF is in principle defined differently for photo-excitation (*upward*) and γ decay (*downward*). However, using arguments of detailed balance, we may say that these two are equal provided that the same states are populated regardless of direction. In addition one may assume that the

---

[2]These are to be considered more as semi-microscopic rather than pure microscopic models, as they also have free parameters to be fitted to experimental data.

[3]The GSF is also known as "photon strength function" or "radiative strength function" and the shorthands γSF, PSF, RSF.

GSF is independent of the initial excitation energy, angular momentum and parity, so that $f(E_\gamma, E_i, J_i, \pi_i) \approx f(E_\gamma)$. This series of simplification is referred to as the generalized Brink-Axis hypothesis [89, 90], and it is central for the application of the Oslo method. Although having been observed to hold for many nuclei [91–94], this feature is not universal and care should be applied.

3.3.1 Structures in the GSF

The GSF may shed light onto nuclear collective behaviors. Its features can be found in many nuclei, and a stylized drawing of known structures in the GSF is shown in Figure 3.1. The most prominent and regular one is the giant electric dipole resonance (GEDR). As the name suggests, it has $E1$ character and is a large, Lorentzian-shaped structure centered at about $E_\gamma \approx 15$ MeV, it is doubly-peaked for deformed nuclei, and may be interpreted in a macroscopic picture as protons and neutrons oscillating against each other [95, 96]. Although the GEDR usually dominates the GSF, other structures may be observed on its lower tail. The giant magnetic dipole resonance (also called the spin-flip $M1$ resonance, or spin Gamow-Teller resonance) is a weaker structure usually observed around $E_\gamma \approx 6 - 8$ MeV for deformed nuclei (around 10 MeV for spherical) and is microscopically understood as transitions between single-particle levels with $j = l + 1/2$ and $j = l - 1/2$ spins and same parity [97] The pygmy dipole resonance (PDR) is an $E1$ structure also centered at about $E_\gamma \approx$ 6-8 MeV and present in many neutron-rich nuclei [98, 99]. Although macroscopically understood as a core of $Z = N$ nucleons oscillating against the neutron excess, this interpretation is in conflict with the fact that it is often quite fragmented and difficult to fit with a Lorentzian function, and should probably be understood microscopically (see e.g. [100, 85]). Similar is the situation for the scissors resonance (SR, also called scissors mode). This is a small structure consisting of $M1$ radiation and centered around $E_\gamma \approx 3$ MeV, observed in deformed nuclei and originally interpreted as protons and neutrons oscillating against each other in a motion similar to a pair of scissors opening and closing. This behavior is now predicted to be at $E_\gamma \approx 20$ MeV, called the "true scissors resonance". The one at 3 MeV can be understood from the Nilsson model as coherent single-particle transitions between split magnetic substates in deformed nuclei ($\Delta j = 1$, same parity) [97]. Finally, a structure at low E_γ called the upbend (or "low energy enhancement", LEE) was discovered in ^{56,56}Fe [101] and has recently been observed in several nuclei [102]. Although its electromagnetic character still remains a mystery, shell model calculations suggest that it might have an $M1$ nature (see e.g. Ref. [102]).

3.4 The compound nucleus picture

Knowledge about the NLD and GSF is useful because it may uncover unknown properties of the nucleus and help us understand more of the behavior of this complicated, mesoscopic quantum many-particle system. Another use is
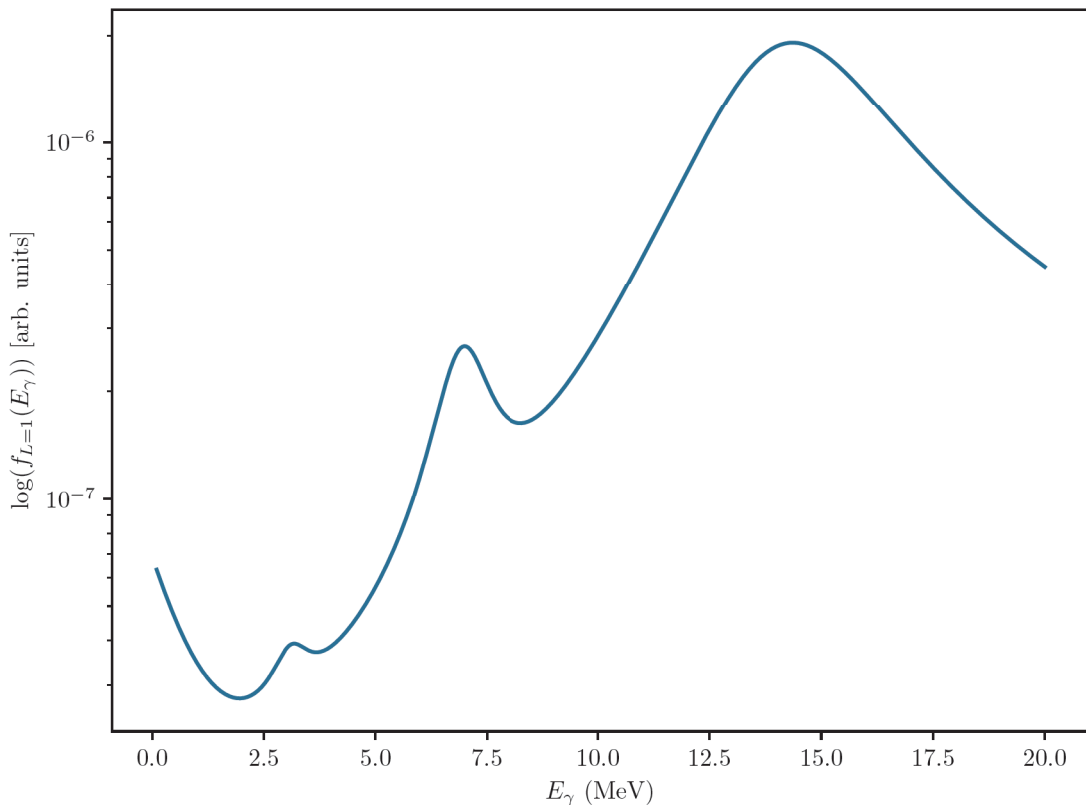
Figure 3.1: A qualitative depiction of the low end of the GSF (in unspecified units), where we can see the structure described in Section 3.3.1: The dominating giant dipole resonance centered at about $E_\gamma \approx 15$ MeV, the pygmy resonance at $E_\gamma \approx 7.5$ MeV, the scissors resonance at ≈ 3 MeV and the upbend at lower E_γ. The spin-flip resonance is usually hidden below the pygmy dipole resonance and is not shown in the above drawing.

within the Wolfenstein-Hauser-Feshbach framework [71, 72]. By exploiting the compound nucleus picture of Niels Bohr [103], we are able to describe compound reactions taking place in astrophysical scenarios. Compound reactions are one of three ways one may categorize how nuclei can interact with each other or with other nucleons, the other two being direct and pre-equilibrium reactions. Direct reactions have a very short timescale on the order of the time an incoming particle would take to travel a distance comparable to the target nucleus' diameter, about 10^{-18}-10^{-22} s [75]. Only a few nucleons partake in this reaction and the scattering is not isotropic, meaning that the angle between the incoming particle and the outgoing ejectile will be related. On the other hand, compound reactions take much longer times, about 10^{-15} s, and work in a qualitatively different way. The incoming particle will be absorbed by the target and the nucleus will have time to thermalize, meaning that the energy will be evenly distributed among the nucleons. When this happens, the nucleus will "forget" how it was made, its decay will be isotropic (no angle correlations between incoming and outgoing

particle) and its decay will only follow spin, parity and energy conservation laws. Pre-equilibrium reactions do not quite reach thermal equilibrium and present features of both kind of reactions.

Generally, we may describe a compound reaction as

$$\sigma_{a,b} = \sigma_a^{\mathrm{CN}} P_b \tag{3.16}$$

where the cross section $\sigma_{a,b}$ for a reaction with incoming channel a and outgoing channel b is given by the cross section for a-capture σ_a^{CN} multiplied by the probability for decay via the b channel.

We will mostly talk about radiative neutron-capture in the context of astrophysics. This involves thermalized neutrons as projectiles against heavier nuclei with energies spread as a Maxwell-Boltzmann distribution with expectation values in the order of tens of keV. In this regime, the compound nucleus picture is applicable, and we may rewrite Eq. (3.16) as

$$\sigma_{n,\gamma}(E_x) = \sum_{J,\pi} \sigma_n^{\mathrm{CN}}(E_x, J, \pi) P_\gamma(E_x, J, \pi), \tag{3.17}$$

where the first term $\sigma_n^{\mathrm{CN}}(E_x, J, \pi)$ describes the possibility for a free neutron to end up forming an excited nucleus of excitation energy E_x, spin J and parity π. This may in turn be separated into

$$\sigma_n^{\mathrm{CN}}(E_x, J, \pi) = \frac{\pi}{k_n^2} \mathcal{T}_n(E_x, J, \pi), \tag{3.18}$$

where k_n and $\mathcal{T}_n$ are the incoming neutron's wave number and transmission coefficient, respectively. Qualitatively, we understand that the higher the wave number, the faster the neutron is and thus the shorter the time it will be able to interact with the nucleus, making the cross section smaller. The neutron-transmission coefficient is calculated from the optical model potential of the target nucleus. The second term of Eq. (3.17), P_γ, may be expressed as

$$P_\gamma(E_x, J, \pi) = \frac{\mathcal{T}_\gamma(E_x, J, \pi)}{\mathcal{T}_{\mathrm{tot}}(E_x, J, \pi)}, \tag{3.19}$$

meaning that the probability for a nucleus to γ-decay (and thus absorb the neutron) is given by the ratio between the γ-transmission coefficient $\mathcal{T}_\gamma$ and all the ways the nucleus may decay. In astrophysical settings, neutron energies will usually not go beyond 1 MeV (see Section 4.3), meaning that the excitation energy of the compound nucleus will be maximum $E_x \lesssim S_n + 1$ MeV. Often, the only two ways the nucleus will decay will be by γ or n emission, so that $\mathcal{T}_{\mathrm{tot}} = \mathcal{T}_\gamma + \mathcal{T}_n$. Joining Eqs. (3.18) and (3.19) into Eq. (3.17) we obtain

$$\sigma_{n,\gamma}(E_x) = \frac{\pi}{k_n^2} \sum_{J,\pi} \frac{\mathcal{T}_n(E_x, J, \pi)\mathcal{T}_\gamma(E_x, J, \pi)}{\mathcal{T}_n(E_x, J, \pi) + \mathcal{T}_\gamma(E_x, J, \pi)}. \tag{3.20}$$

For high energies, the neutron decay channel dominates, so that $\mathcal{T}_n \approx \mathcal{T}_{\text{tot}}$ and we may rewrite Eq. (3.20) as

$$\sigma_{n,\gamma}(E_x) \approx \frac{\pi}{k_n^2} \sum_{J,\pi} \mathcal{T}_\gamma(E_x, J, \pi) = \frac{\pi}{k_n^2} \mathcal{T}_\gamma(E_x), \tag{3.21}$$

where the choice of optical model potential (OMP) has no longer any influence on the capture cross section. This is typically the case for energies associated with the r process. The OMP has to be taken into account for s-process neutron energies of ≈ 30 keV though, as its impact to the capture cross section may still be appreciable. For both cases the partial γ-transmission coefficient $\mathcal{T}_\gamma(E_x, J, \pi)$ is an important ingredient. This is given as

$$\mathcal{T}_\gamma(E_x, J, \pi) = \sum_{X,L} \int_0^{E_x} \mathcal{T}^{XL}(E_\gamma) \rho(E_x - E_\gamma, J, \pi) \mathrm{d}E_\gamma \tag{3.22}$$

where $\mathcal{T}^{XL}(E_\gamma)$ is directly related to the GSF as

$$\mathcal{T}^{XL}(E_\gamma) = 2\pi E^{2L+1} f^{XL}(E_\gamma) \tag{3.23}$$

and $\rho(E_x - E_\gamma, J, \pi)$ is the partial level density as seen in Eq. (3.8).

3.5 Nuclear physics in astrophysics

As explained in chapter 2, the s, i and r processes all happen in astrophysical scenarios where temperatures are high enough to allow for the mechanisms that create the necessary neutrons. For the s and i processes these temperatures are at $T \approx 0.25$ GK, while for the r process they may go up to the $(n, \gamma) \rightleftharpoons (\gamma, n)$ equilibrium temperature threshold of $T \approx 1.5 - 2.0$ GK and beyond. In these hot environments, we have to consider two things. First, neutron incident energies will follow a Maxwell-Boltzmann distribution

$$f_E(T) = \frac{1}{v_T} \sqrt{\frac{8}{\widetilde{m}\pi}} \left(\frac{1}{k_B T}\right)^{3/2} \int_0^\infty E \exp\left(-\frac{E}{k_B T}\right) \mathrm{d}E, \tag{3.24}$$

where $v_T = \sqrt{2E/\widetilde{m}}$ is the thermal velocity, $\widetilde{m}$ is the reduced mass, k_B is the Boltzmann constant and T the temperature. Second, nuclei may very well be excited themselves. In this case the cross section will be a sum of all the cross sections $\sigma_{n\gamma}^\mu$ built on the different excited states μ[4], each weighted down for their relative population:

$$\sigma_{n\gamma} = \sum_\mu P_\mu \sigma_{n\gamma}^\mu. \tag{3.25}$$

---

[4]Here again the Brink-Axel hypothesis, in its original formulation, may come to the rescue and set these cross sections to be the same as the one on the ground state [89, 90].

The population of each level will be thermalized, meaning that the probability of finding the nucleus excited to the level μ will be [30]

$$P_\mu = \frac{(J_\mu + 1)e^{-E_\mu k_B}}{\sum_\mu (J_\mu + 1)e^{-E_\mu k_B}} = \frac{1}{G(T)} \frac{(J_\mu + 1)}{(J_0 + 1)} e^{-E_\mu k_B} \qquad (3.26)$$

where J_0 and J_μ refer to the ground state and the μ excited state spins, E_μ to the μ excited state energy, and we have defined the partition function as

$$G(T) \equiv \sum_\mu \frac{(J_\mu + 1)}{(J_0 + 1)} e^{-E_\mu k_B}. \qquad (3.27)$$

Putting all together, we may convolute the cross sections with the Maxwell-Boltzmann distribution, obtaining the Maxwellian-averaged cross section (MACS):

$$\langle\sigma\rangle_T(T) = \frac{1}{v_T} \left(\frac{8}{\pi\widetilde{m}}\right)^{1/2} \frac{1}{(k_B T)^{3/2} \, G(T)} \times$$
$$\int_0^\infty \sum_\mu \frac{2J_t^\mu + 1}{2J_t^0 + 1} \sigma_{n\gamma}^\mu(E) E \exp\left[-\frac{E + E_\mu}{k_B T}\right] \mathrm{d}E. \qquad (3.28)$$

Equivalent to the MACS, the neutron-capture rate $N_A\langle\sigma v\rangle_T$ [5] may be given in the literature. These two quantities are closely related by

$$N_A\langle\sigma v\rangle_T = N_A v_T \langle\sigma\rangle_T, \qquad (3.29)$$

where N_A is Avogadro's number.

The equations for the MACS and the neutron-capture rate work as long as the thermalization argument in Eq. (3.26) holds. This is the case for many nuclei, but sometimes the process of thermalization may be too slow even considering the timescales of the s process. This may happen when selection rules of spin and parity make communication between low lying levels difficult, so that if a nucleus becomes stuck in a high-spin isomeric level, for example, it will not be able to decay to the ground state even in hot stellar environments. This is for example the case of ^{166}Ho for temperatures below $k_B T = 7$ keV [104], where the first excited state at $E_x \approx 6$ keV is 7^- and cannot decay to the 0^- ground state unless going through intermediate levels at higher excitations, something unlikely at cold temperatures. This case is discussed in Paper III [44].

The MACS and the neutron-capture rate are temperature-dependent quantities telling us the degree they will be able to capture a neutron. For astrophysical simulations of the nucleosynthesis processes, libraries of these rates may be found. JINA REACLIB [105] is a widely used one built on the NONSMOKER formula [106], and BRUSLIB [107] is another.

---

[5]The notation here is a bit confusing, as this is not a *rate* in the meaning of e.g. Eq. (3.4), but *reactivity*. This quantity is nevertheless often referred to as neutron-capture *rate* in the literature.

In this chapter we have seen how starting from the NLD and GSF we may calculate the MACS and the neutron-capture rate using the compound nucleus picture. How can one find the NLD and GSF of a nucleus, though? In the next chapter I will go through the Oslo method, a set of analytical techniques able to extract precisely these two quantities from particle-γ coincidence experiments.

Chapter 4

Experiments and the Oslo method

We have seen in the previous two chapters how the origin of the elements heavier than iron depends on astrophysical neutron-capture processes, and how these both rely on the proper simulation of these nucleosynthesis events and the correct nuclear inputs. One of the most useful inputs in this regard is the neutron-capture rate, telling us to which degree an (n, γ) reaction on a specific nucleus is likely to happen. This is in turn important because it will create heavier isotopes of the same element, which will eventually β decay and climb up the nuclide chart. As we saw in Section 3.5 the neutron-capture rate can be derived from the nuclear level density and the γ-ray strength function of the $N + 1$ nucleus, exploiting the compound nucleus picture [103] and the Wolfenstein-Hauser-Feshbach formalism [71, 72]. The two average statistical quantities can be extracted from particle-γ coincidences using a data-analysis procedure called the Oslo method. In this chapter I will describe the experimental setup at the core of the experiments analyzed in Papers I, II and III, how we can extract the nuclear level density (NLD) and the γ-ray strength function (GSF) from the data, and finally connect all the steps that lead us from laboratories on Earth to the nucleosynthesis in the cosmos.

4.1 The experiments

The three experimental papers included in this thesis are all based on the data from the Oslo Cyclotron Laboratory (OCL, [2]). The three experiments analyzed are ^{124}Sn$(\alpha, p\gamma)^{127}$Sb (Paper I), ^{163}Dy$(\alpha, p\gamma)^{166}$Ho (Paper II) and ^{164}Dy$(\alpha, p\gamma)^{167}$Ho (Paper III). All three experiments involved α-beams impinged on self-supporting stable targets. In the first experiment a 24 MeV beam was impinged on a 0.47 mg/cm^2 thick ^{124}Sn target of 95.3% enrichment, in the second a 26 MeV α beam on a 2.00 mg/cm^2 thick ^{163}Dy target of 98.5% enrichment, and in the third again a 26 MeV α beam, but now on a 1.73 mg/cm^2 thick ^{164}Dy target of 98.5% enrichment. For all of these the same beam was impinged on a ^{12}C target for calibration purposes.

Figure 4.1 shows a sketch of the laboratory. Charged α particles are produced by ionizing ^{4}He gas and accelerated by the MC-35 Scanditronix cyclotron. Different steering magnets are then used to focus the beam on the target inside the Silicon Ring (SiRi, Figure 4.2) and the Oslo Scintillator Array (OSCAR, Figure 4.3), where particle-γ coincidences are measured and stored. Experiments varied in duration between under a day as for ^{167}Ho, or six days for ^{166}Ho.

The beam reacts with the target in the center of the detectors, emitting a particle first, followed by a γ cascade[1]. SiRi [108] is a particle detector array in

---

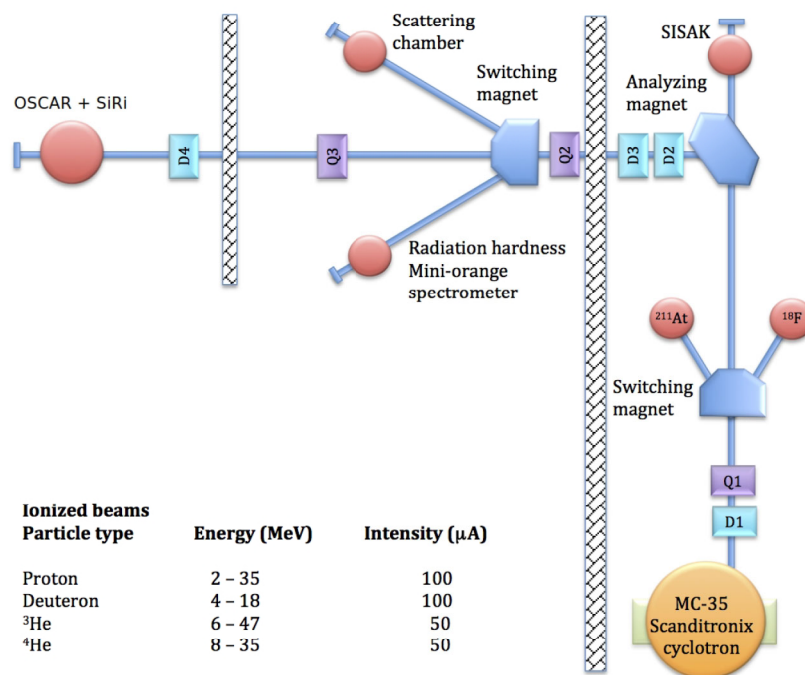[1]When excited well above the neutron separation energy, a nucleus will much rather decay

Figure 4.1: A sketch of OCL. Beams of α, ^{3}He, d or p particles are produced in the MC-35 Scanditronix cyclotron by ionizing helium or hydrogen gas, and accelerated to the desired energy. Steering magnets direct and focus the beam on the target inside the OSCAR and SiRi detector arrays. From https://www.mn.uio.no/fysikk/english/research/about/infrastructure/ocl/index.html.

charge of telling us the type and the energy of the outgoing particles. This is achieved by having a thin detector in front (130 µm, called ΔE) and a thicker one in the back (1550 µm called E). Faster particles spend less time in the thinner detector and deposit less energy there and more in the rear one. Slower particles will deposit relatively more energy on the thin detector for the same reasons. In addition, lighter particles (such as p) will be faster than heavier ones (such as d, t etc.) for the same total kinetic energy, and will again leave less energy in the front detector and more in the back compared to the heavy ones. Charge influences the amount of energy deposited as well since ultimately it is the Coulomb force that is responsible for the working of the particle detector. All of these factors help us discriminate between the different types of emissions and measure their energy. In a ΔE-E plot they will appear like bows (also called "bananas", see Figure4.4). In this way we are able to only select (to "gate on") the ejectiles for the reaction we are interested in. This is called the ΔE-E technique.

SiRi consists of eight E detectors in a ring covering 126°-140° in backward angles, and in front of each of them there are eight strips of ΔE detectors, forming an array of 64 detectors altogether. It may be placed in forward or

---

with a neutron than a γ ray. The "leftover" energy in the nucleus will then be released by EM radiation.
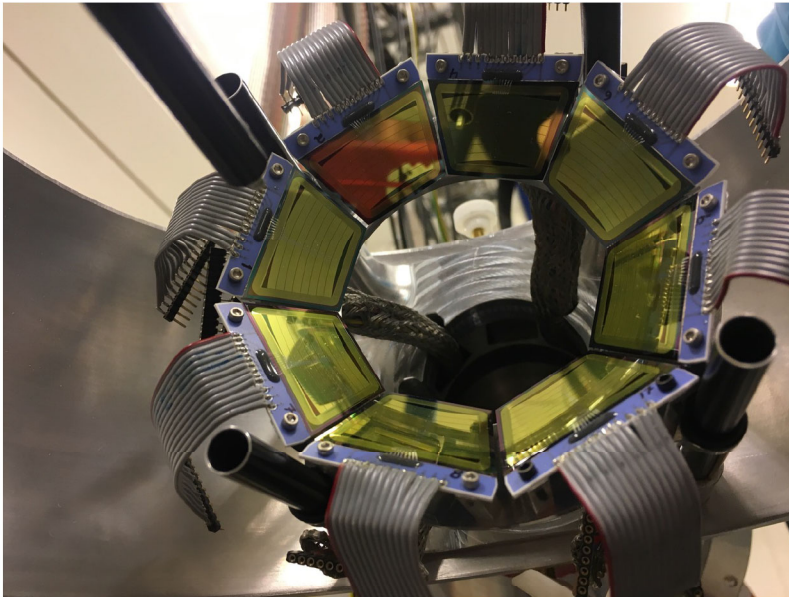
Figure 4.2: The SiRi particle detector array.

Figure 4.3: The OSCAR γ-ray detector array.

backward angles, and for our three experiments the latter was chosen to minimize the impact of elastic scattering.

OSCAR [109] is the detector array responsible for recording γ radiation. It consists of 30 cylindrical LaBr3(Ce) detectors build on a icosahedron frame around the target. Events recorded by OSCAR and SiRi are timestamped so that they may be associated in particle-γ coincidences. Knowing then the energy of the beam, the Q value of the reaction and the energy of the ejectile (from SiRi) we are able to calculate the energy E_x the product nucleus is left in before the γ cascade. OSCAR provides information on the γ de-excitation of the nucleus. After calibrating the detectors with runs on well known targets (in our case ^{12}C), and subtracting background events, we obtain the E_x-E_γ coincidence matrix, also known as the *raw matrix*. This is the starting point for the Oslo method.
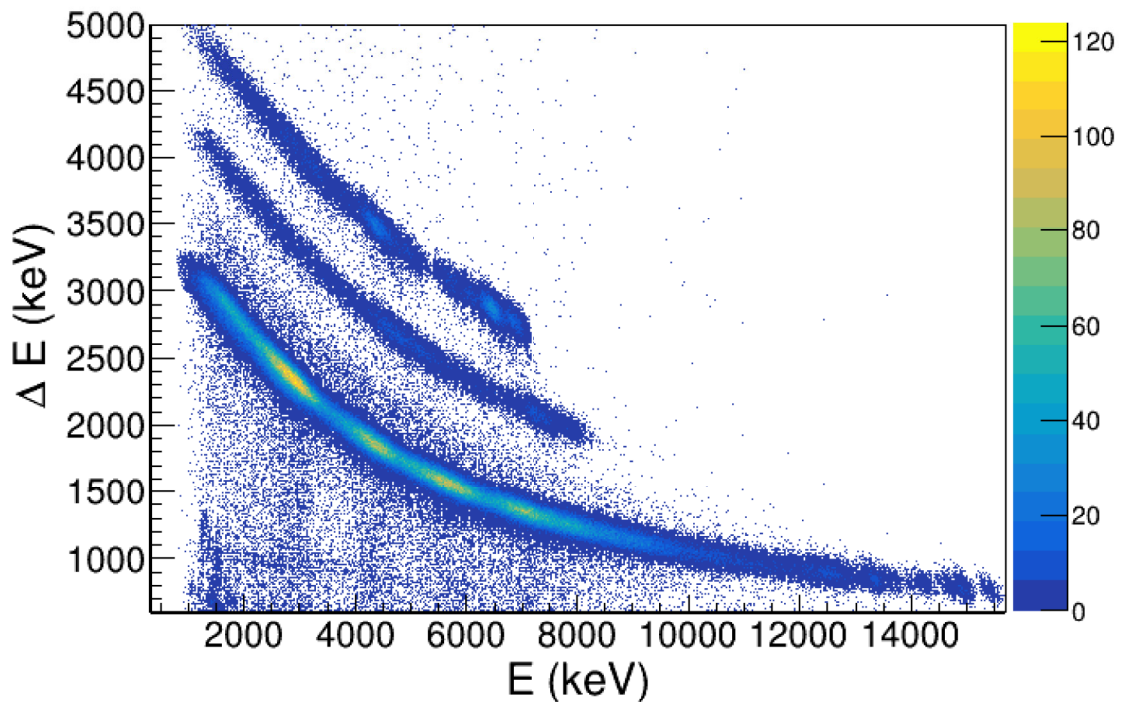
Figure 4.4: The ΔE-E "banana" plot for the ^{124}Sn$(\alpha, p\gamma)^{127}$Sb experiment, taken from Paper I [85]. The lower bow corresponds to protons, the middle bow to deuterons and the upper to tritons. The α bow is also detected in the experiment, but is outside the limits of the plot. Using this plotting technique, we are able to gate on the p decay channel and only select the $(\alpha, p\gamma)$ reaction for our analysis.

4.2 The Oslo method

The Oslo method is an analysis technique that allows us to simultaneously extract the NLD and the GSF from the E_x-E_γ matrix. The raw matrix obtained

from the calibrated SiRi and OSCAR data need to be corrected for the detector response in a process called *unfolding*, and in order to only select the first γ rays in the de-excitation cascade the *first generation method* is applied. The next step is to select the region in the resulting *first generation matrix* corresponding to the quasi-continuum, and extract the functional shape of the NLD and GSF. Finally, a normalization procedure can be employed in order to anchor the functional shapes of these two functions to external experimental data.
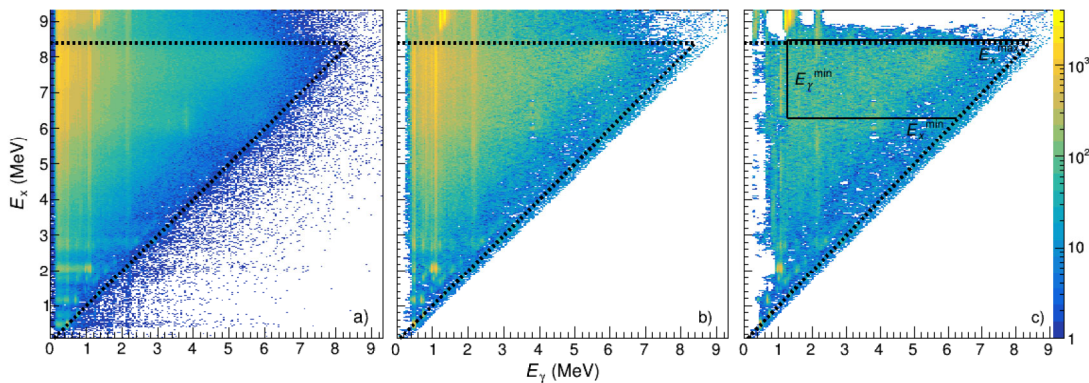
Figure 4.5: The a) *raw*, b) *unfolded* and c) *first-generation* matrices for the ^{124}Sn$(\alpha, p\gamma)^{127}$Sb experiment taken from Paper I [85]. The diagonal, black, dotted line in the three matrices indicates where $E_x = E_\gamma$, meaning the highest energy the nucleus may decay with for a given excitation energy. The horizontal, black dotted line indicates the neutron-separation energy S_n. In the c) panel the selected region for the extraction of the NLD and GSF is shown inside the black, solid line. See text for more explanation of the matrices and the Oslo method.

4.2.1 The unfolding

The matrix we obtain from the two detector arrays does not correspond to the true signal from the experiment. This has to do with the fact that we have to expect some "noise" and distortions from the detectors. Some high-energy photons may interact with the detector crystals and produce an electron-positron pair, which creates photons that may escape detection. If we are then to expect a γ ray with energy E_γ, what we would also see are two small peaks with $E_\gamma - m_e c^2 \approx E_\gamma - 511$ keV and $E_\gamma - 2m_e c^2 \approx E_\gamma - 1022$ keV in the spectrum, called *single* and *double escape*, respectively. Together with these, Compton scattering may be responsible for the transfer of only some of the photon energy to electrons, producing a low "ridge" at $E < E_\gamma$ and the rest of the energy escaping detection. Finally, we would also expect a peak at 511 keV due to photons from electron-positron annihilations. All of these spurious signals should be filtered out, and this is done by using the response function of the OSCAR detector to de-convolute (or *unfold*) the experimental data.

Mathematically we may describe the problem as the true signal $U(E_\gamma)$ being folded by the response matrix $P(E'_\gamma, E_\gamma)$ into the folded signal $F(E'_\gamma)$:

$$F(E'_\gamma) = \int P(E'_\gamma, E_\gamma)U(E_\gamma)\mathrm{d}E_\gamma. \qquad (4.1)$$

Since we work with 2D histograms, we may describe the problem with matrices as

$$f = Pu, \qquad (4.2)$$

where f and u are column vectors of length N representing a γ spectrum at E_x, and P being the $N \times N$ response matrix. Although it would be tempting to just invert P into P^{-1} and calculate u from f with it, this produces large fluctuations in u and does not yield the desired result. To address this problem the unfolding procedure developed by Guttormsen et $al.$ [110] uses a different approach and approximates the true signal iteratively. One starts with a trial true spectrum u_0, which is taken to be equal to the measured spectrum r. This is folded into f_0 using Eq. (4.2). One then takes the difference between the measured r and the folded f_0, and add it to the trial matrix u_0 to obtain the new trial spectrum u_1:

$$u_1 = u_0 + (r - f_0). \qquad (4.3)$$

The newly obtained u_1 will then take the place of u_0 and repeat the above procedure until the n-th folded trial matrix corresponds to the raw matrix within the experimental fluctuations. In addition, the Compton subtraction is used to avoid spurious fluctuations. Finally, the "true" signal is multiplied up so to retain the original number of counts. In Figure 4.5 one can observe the raw and the unfolded matrix for ^{127}Sb as published in Paper I [85].

4.2.2 First-generation γ rays

The matrix obtained from the unfolding procedure is the collection of γ spectra from each measured excitation energy. We are only interested in the $first$ γ rays coming out from the nucleus at that specific excitation energy, but the decay is generally too fast to detect which γ ray comes first. This means that the spectra include the whole γ cascades from the excited level to the ground state. The $first$-$generation$ $method$ is a subtraction technique developed at OCL with the aim to extract only the first γ rays from each cascade. It is described in detail in Ref. [111], and I will explain the idea behind the method here.

Imagine that all excitation levels E_x are populated with equal probability. Then the full γ spectrum $a(E_\gamma)_{E_x}$ of a specific excitation energy E_x can be thought as its first-generation spectrum $f(E_\gamma)_{E_x}$, plus a weighted sum of all the full spectra at $E'_x < E_x$:

$$a(E_\gamma) = f(E_\gamma)_{E_x} + \sum_{E'_x < E_x} w(E'_x)_{E_x} a(E_\gamma)_{E'_x}, \qquad (4.4)$$

where $w(E'_x)_{E_x}$ are the weighing factors telling us "how much of the E'_x-level full spectrum we have in the E_x-level full spectrum". In other words, $w(E'_x)_{E_x}$ can

be considered the branching ratio from a level at E_x to one at E'_x. Unfortunately, the assumption of equal population is not necessarily valid, and the sum has to be adjusted by a normalization parameter $n(E'_x)_{E_x}$ accounting for the different level population cross sections:

$$a(E_\gamma) = f(E_\gamma)_{E_x} + \sum_{E'_x < E_x} n(E'_x)_{E_x} w(E'_x)_{E_x} a(E_\gamma)_{E'_x}. \qquad (4.5)$$

The good news is that we can calculate $n(E'_x)_{E_x}$. This normalization factor is nothing more than the ratio between the cross sections of E'_x-level and the E_x-level. Since we usually have enough statistics, this ratio may be found by dividing the number of times we populate the level at E'_x by the corresponding number for E_x or, equivalently, dividing the number of cascades originating from E'_x by the number originating from E_x. The number of cascades may be calculated by summing the energy from all the photons coming out from an excited level E'_x and dividing by the number of photons N, obtaining the average energy of each photon in the spectrum, $\langle E_\gamma \rangle_{E'_x}$. Knowing that each cascade leads to the ground state, dividing E'_x by this number we obtain the average number of photons per cascade, this being the average multiplicity $\langle M \rangle_{E'_x}$. Thus, we may divide the total number of photons by the average multiplicity, to obtain the number of cascades. Repeating for E_x and taking the ratio, we obtain $n(E'_x)_{E_x}$:

$$n(E'_x)_{E_x} = \frac{N_{E'_x}/\langle M \rangle_{E'_x}}{N_{E_x}/\langle M \rangle_{E_x}}. \qquad (4.6)$$

As anticipated, $w(E'_x)_{E_x}$ may be understood as the branching ratio for γ decay between E_x and E'_x. This is nothing more than the normalized first-generation spectrum for the level at E_x:

$$w(E'_x)_{E_x} = \frac{f(E_x - E'_x)_{E_x}}{\sum_{E'_\gamma < E_x} f(E'_\gamma)_{E_x}}. \qquad (4.7)$$

Pulling all the threads together, we may write Eq. (4.5) as

$$f(E_\gamma)_{E_x} = a(E_\gamma)_{E_x} - \sum_{E'_x < E_x} \frac{N_{E'_x}/\langle M \rangle_{E'_x}}{N_{E_x}/\langle M \rangle_{E_x}} \frac{f(E_x - E'_x)_{E_x}}{\sum_{E'_\gamma < E_x} f(E'_\gamma)_{E_x}} a(E_\gamma)_{E'_x}. \qquad (4.8)$$

This creates a system of equations that may be solved iteratively by picking trial functions for $f(E_\gamma)_{E_x}$ like unity and run until convergence. The resulting first-generation matrix for ^{127}Sb is shown in figure 4.5c).

4.2.3 Decomposition of the NLD and GSF functionals

Fermi's golden rule [112, 113] states that the probability of a transition is proportional to the density of states at the final energy level, times the squared matrix element (and a constant):

$$\lambda = \frac{2\pi}{\hbar} |\langle f|H'|i \rangle|^2 \rho(E_f), \qquad (4.9)$$

for an initial state i, a final state f, a perturbation operator H' and a state density ρ at final excitation energy E_f. The same idea may be applied in our case, where the γ-transmission coefficient $\mathcal{T}_\gamma(E_\gamma)$ can interpreted as the quasi-continuum equivalent of what the matrix element is for discrete states, and the NLD as the equivalent for the number of states at final excitation energy. $\mathcal{T}_\gamma$ here does not depend on initial or final energies, meaning that by doing this substitution we are assuming the Brink-Axel hypothesis. From this idea we may build the relation[2] [115]

$$P(E_\gamma, E_x) \propto \mathcal{T}_\gamma(E_\gamma)\rho(E_x - E_\gamma), \tag{4.10}$$

where $P(E_\gamma, E_x)$ are the first-generation spectra for each excitation energy E_x, representing the probability of decay by E_γ energy from an excited state E_x. This is the first-generation matrix, when only statistical decay is selected. The selection is done by picking a lower limit of E_γ ensuring that we do not include leftover decay from discrete states, and a lower and upper limit on E_x keeping sure that we hold ourselves inside the quasi-continuum region and below S_n. A theoretical normalized first-generation matrix can be formulated as

$$P_t(E_\gamma, E_x) = \frac{\mathcal{T}_\gamma(E_\gamma)\rho(E_x - E_\gamma)}{\sum_{E_\gamma = E_\gamma^{\min}}^{E_x} \mathcal{T}_\gamma(E_\gamma)\rho(E_x - E_\gamma)}, \tag{4.11}$$

which can be used in a χ^2 minimization with the experimental $P(E_\gamma, E_x)$ as

$$\chi^2 = \sum_{E_\gamma, E_x} \left(\frac{P(E_\gamma, E_x) - P_t(E_\gamma, E_x)}{\Delta P(E_\gamma, E_x)} \right)^2, \tag{4.12}$$

where $\Delta P(E_\gamma, E_x)$ are the uncertainties connected to the first-generation matrix.

From this minimization procedure we are only able to extract the functional shapes of the NLD $\tilde{\rho}(E_x - E_\gamma)$ and the γ-transmission coefficient $\tilde{\mathcal{T}}_\gamma(E_\gamma)$. It can be shown [115] that these are related by three free parameters A, B and α as:

$$\tilde{\rho}(E_x - E_\gamma) = Ae^{\alpha(E_x - E_\gamma)}\rho(E_x - E_\gamma), \tag{4.13a}$$

$$\tilde{\mathcal{T}}_\gamma(E_\gamma) = Be^{\alpha E_\gamma}\mathcal{T}_\gamma(E_\gamma). \tag{4.13b}$$

Any choice of these three parameters reproduces the first-generation matrix, so that we have infinite solutions for this minimization. These parameters may be fixed by fitting them to known physical quantities through *normalization*.

4.2.4 Normalization

The values of two parameters (A and α) have to be found in order to fix the NLD. Since we already know its functional shape, we only need two anchor points

---

[2]If this explanation seems hand-wavy, it is because it is. For a thorough derivation from Fermi's golden rule to this relation (and an interesting discussion on its validity) I refer to Dr. Midtbø's doctoral thesis [114].

in order to find the physical $\rho(E_x)$, and preferably we would want these two points to be known experimentally. The first point is actually a region of points, and it is the NLD at low excitation energy. Data on the lowermost discrete energy levels are usually available, and may be used to calculate the NLD and fit our function to it. The second point corresponds to the NLD at the neutron separation energy, $\rho(S_n)$. This may be found by [115]

$$\rho(S_n) = \frac{2\sigma^2}{D_0} \frac{1}{(I_t + 1)\exp[-(I_t + 1)^2/2\sigma^2] + \exp[-I_t^2/2\sigma^2]}. \qquad (4.14)$$

Here, s-wave (or p-wave) neutron resonance spacings D_0 (D_1) are usually available for stable targets [116, 117], σ^2 is the spin-cutoff parameter at S_n and I_t is the spin of the target nucleus. The spin-cutoff parameter must be chosen from either the RMI or the FG model as discussed in Section 3.2, and the choice introduces the first model dependence in the normalization procedure. When selecting the quasi-continuum region from the first-generation matrix, the first or first couple of MeV in transition energy ($E_\gamma^{\min}$) are left out since they correspond to discrete transitions from the lowermost excited states. Assuming then that the selected excitation energy region goes up to the neutron separation energy S_n, NLD data will only reach up to about $E_x = S_n - E_\gamma^{\min}$. This means that we will have to extrapolate our data up to S_n in order to normalize it. This is done by using either the BSFG model or the CT model, both discussed in Section 3.2. The choice of extrapolation model can impact the normalization results in a considerable way if the gap in E_x between $S_n - E_\gamma^{\min}$ and S_n is large. This introduces the second model dependence in the normalization procedure. In order to minimize this, one may pick the model that fits the existing data best, as done in by Guttormsen *et al.* [118] and my two Ho papers (Paper II [86] and Paper III [44]).

Once the NLD is normalized, the α parameter may be used for the γ-transmission coefficient $\mathcal{T}_\gamma(E_\gamma)$, and we are left with the last free parameter B. This may be fixed with the help of the average total radiative width at the neutron separation energy $\langle \Gamma_\gamma(S_n) \rangle$. In the case of the target spin being 0^+ and considering s-wave capture, we get the relation

$$\langle \Gamma_{\gamma 0}(S_n, I_t + 1/2, \pi_t) \rangle = B \frac{D_0}{4\pi} \int_0^{S_n} dE_\gamma \mathcal{T}_\gamma(E_\gamma)$$

$$\times \sum_{J=0}^{+1} \rho(S_n - E_\gamma, I_t \pm 1/2 + J, \pi_t), \quad (4.15)$$

where $I_t = 0$ is the target spin and $\pi_t = +$ is the target spin parity, and J is the difference in angular momentum between the initial and final level. This expression assumes equal parity distribution and dominance of dipole transitions and is based on Equation (3.1) of Kopecky and Uhl [88].

When D_0 or $\langle \Gamma_\gamma \rangle$ are not provided (as it usually is the case for unstable nuclei that cannot be reached by (n, γ) experiments), these values can be extracted by systematics, meaning comparing to known values for neighboring, measured

nuclei. This is done for ^{127}Sb in Paper I [85], where an example of this procedure can be found.

4.2.5 Other experimental techniques

In this section we have covered the Oslo method, from the data collection during the experiments, to the extraction of the NLD and GSF. The Oslo method requires a stable, solid target to be employed. On one hand, this allows for the easy collection of a lot of data (leading to small statistical errors) and usually the possibility to use experimental data for the normalization procedure; on the other hand it is limited to the study of nuclei that are reachable using p, d, ^{3}He or α probes, meaning close to or at stability. Although the study of these nuclei is important both from a nuclear structure perspective and an for the extraction of neutron-capture rates and Maxwellian-averaged cross sections for the s and partially the i process, (see Sections 3.5 and 4.3), many nuclei involved in the latter and especially in the r process are unreachable by this kind of experiments.

In order to solve this problem, variations of the Oslo-method have been developed to study more exotic nuclei far from stability. The *Oslo method in inverse kinematics* [119] is one of these variations. It retains most of the elements of the original Oslo method, but instead of light projectiles impinging on a heavy target, radioactive heavy isotopes are produced by spallation are accelerated towards a light target, this usually being a deuterated carbon compound, allowing for (d, p) experiments. These radioactive isotopes are usually much further into the neutron-rich side of the nuclear chart, and by recording particle-γ coincidences one may employ the Oslo method in order to extract the NLD and GSF of the desired nucleus. A limitation to the Oslo method in inverse kinematics is that the production of the desired isotope and its reaction cross section with the light target may lead to limited data, increasing the statistical errors. Another is usually the lack of experimental data to be used for the normalization procedure, increasing the systematic errors. A different approach is the β-*Oslo method* [120], which instead of exciting a nucleus by a nuclear reaction, it does it by β decay. For many neutron-rich nuclei produced in radioactive beams, the β-decay Q-value is in fact comparable to the neutron-separation energy S_n, and this allows for the population of a wide range of energies in the daughter nucleus. The electron from the β-decay is tagged, and the associated γ rays from the de-excitation cascade provide information on E_γ, and E_x when summed. This method allows for a faster data collection than with the "inverse kinematics" method as it does not deal with reaction cross sections, and more data leads to smaller statistical errors. Nevertheless, the lack of experimental data in the exotic nuclear region leads to difficulties for the normalization procedure just as for the Oslo method in inverse kinematics. In addition, correcting for the narrow spin-population by the β decay into the daughter nucleus can be difficult when there is little or no information on the spin of its parent.

4.3 Calculating the Maxwellian-avaraged cross section

Knowing the NLD and the GSF and assuming an optical model potential (OMP), we are able to calculate what is the neutron-capture cross section exploiting the Wolfenstein-Hauser-Feshbach formalism, as explained in Section 3.4. In a sense, we are saying "since the excited compound nucleus forgets how it was made, we can pretend it was formed by neutron capture instead of (α, p). By studying nucleus A's γ de-excitation, we can then calculate the chance that nucleus $A - 1$ will radiatively capture a neutron". Starting from the cross section, the Maxwellian-averaged cross section (MACS) and the neutron-capture rate can be calculated with the equations shown in Section 3.5. This is usually done using the reaction code TALYS [84]. Some more data have to be provided before such a calculation can be undertaken. First, we have to think about neutron energies. As temperatures will vary between about 0.25 in AGB stars to 1.5-2 GK in the r process after a broken $(n, \gamma) \leftrightharpoons (\gamma, n)$ equilibrium, neutron energies will follow a Maxwell-Boltzmann distribution centered somewhere between 30 and 200 keV, meaning that the most energetic neutrons may have energies in the order of ≈ 1 MeV. When a neutron with energy E_n is captured, the new compound nucleus will have an excitation energy of $E_x = S_n + E_n$. In our best case scenario, the GSF data stop at $E_\gamma = S_n$, while for the NLD it actually falls short of S_n by one or two MeV. NLD and GSF data are seldom available above S_n for unstable nuclei, and this means that we depend on extrapolations in order to calculate such cross sections of interest for astrophysics. For the GSF, this can usually be done by fitting to known data from other neighboring nuclei, or by extrapolating it with a model beyond $E_\gamma = S_n$. This is usually sufficient since the GEDR does not peak before $E_\gamma \approx 15$ MeV, well above the typical neutron energy, but care should be taken anyway. For the NLD the model used to extrapolate it up to S_n may be used to extrapolate further.

4.4 Error propagation

While obtaining experimental data for the NLD and the GSF, as well as when calculating the MACS, we encounter different sources of errors. Some of them are of statistical nature, such as the ones related to the finite experimental data. The propagation of this kind of errors is challenging and its correct quantification still has not been achieved. Nevertheless, major steps in that direction have been taken by the treatment of uncertainties by ensembles as done by Midtbø *et al.* with their software package OMpy [121]. Nevertheless, some challenges still remain when it comes to error propagation through the unfolding procedure, where work is currently underway. Other errors are connected to the choice of model for the spin-cutoff parameter and the NLD extrapolation, and others are connected to the physical quantities used in the normalization of the NLD and GSF functionals. These are a combination of statistical and systematic errors that influence the final uncertainties of the two quantities. Finally, we have the choice of OMP model used to calculate the MACS and the neutron-capture rate,

especially relevant for nuclei partaking in the s and i processes.

The error sources related to normalization have been a focus of mine during my PhD period, and were first published in Paper I [85] and refined when used for the data analysis in Papers II [86] and III [44]. In the following subsections I will go through a procedure developed to quantify these errors and propagate them in the most correct way in order to provide the best experimental uncertainty constraints to the MACS. The analysis codes for each paper were written in Python and can be found as distinct repositories on my Github https://github.com/Cyangray.

4.4.1   NLD and GSF

The normalization of the NLD depends on the fitting to the known low excitation energy levels and its value at S_n. The match between the experimental data and the low lying levels is usually not perfect, since the available level scheme may not be complete and the experimental data includes statistical uncertainties. For this reason only the region in E_x that matches the experimental data the most is selected for the fit. The value of $\rho(S_n)$ is calculated from D_0 values and the choice of spin-cutoff parameter model. Normally, then, the normalization procedure for the NLD is done by choosing an E_x interval for the low excitation level fit, and by picking a model for the spin-cutoff parameter to use with D_0 in order to calculate the second anchor point at $\rho(S_n)$. From this point, a χ^2 minimization is done to find the best fit between the functional and the anchor points, and a "correct" NLD is provided. The associated systematic uncertainties from this method are only the ones related to the error in D_0, usually (but not always) provided in the literature, and not the ones connected to the choice of E_x interval or spin-cutoff parameter. In order to address this problem I developed a method to propagate also this kind of uncertainties. The procedure may be simply described as doing something similar to a "grid search": Several fitting simulations as described above are run with slightly different parameters, such as the choice of low-E_x region and spin-cutoff parameter. Then we evaluate the χ^2 score between every simulation and the "well fitting" low-lying E_x level region as well as the assumed $\rho(S_n)$ calculated using Eq. (4.14). Then for every simulation n we evaluate a χ^2 score as:

$$\chi^2_{\mathrm{NLD},n} = \sum_i \frac{(\rho_n(E_i) - \rho_k(E_i))^2}{\Delta\rho_n(E_i)^2} + \chi^2_{S_n,n}, \qquad (4.16)$$

where the sum runs over a wide, low excitation energy region considered to have a complete level scheme[3], $\rho_n(E_i)$ and $\Delta\rho_n(E_i)$ are the n-th NLD simulation evaluated at E_i and its respective uncertainty, and $\rho_k(E_i)$ is the NLD from the known level scheme. The value of $\chi^2_{S_n,n}$ represents the χ^2 score of the fit between the n-th simulation's $\rho(S_n)$ and a chosen probability distribution for the $\rho(S_n)$ error. This last probability distribution may be chosen to be Gaussian centered

---

[3]The NLD is technically a histogram, so we are summing over bins instead of integrating over an energy interval.

around a value. This would be the case when we have strong arguments for choosing a spin-cutoff parameter model above the another. In this case $\chi^2_{S_n,n}$ may be calculated as

$$\chi^2_{S_n,n} = \frac{(\rho_n(S_n) - \rho(S_n))^2}{\Delta\rho(S_n)^2} \tag{4.17}$$

where $\rho(S_n)$ is calculated as in Eq. (4.14), and $\Delta\rho(S_n)$ is calculated from the given uncertainties in σ^2 and D_0 as

$$\Delta\rho(S_n) = \rho(S_n)\sqrt{\left(\frac{\Delta D_0}{D_0}\right)^2 + \left(\frac{\Delta 4\sigma\Delta\sigma}{2\sigma^2}\right)^2\left(1 - \frac{z_1}{z_2 2\sigma^2}\right)^2} \tag{4.18}$$

where

$$z_1 = I_t^3 \exp\left(\frac{I_t^2}{2\sigma^2}\right) + (I_t + 1)^3 \exp\left(\frac{(I_t + 1)^2}{2\sigma^2}\right) \tag{4.19a}$$

$$z_2 = I_t \exp\left(\frac{I_t^2}{2\sigma^2}\right) + (I_t + 1) \exp\left(\frac{(I_t + 1)^2}{2\sigma^2}\right), \tag{4.19b}$$

and I_t is as usual the target spin in the neutron-resonance experiment. Oftentimes though we cannot make a strong argument for choosing the RMI model over the FG one, or vice versa. In this case, we may decide to let the probability distribution not prefer any of the two values by holding it flat between them. Our $\chi^2_{S_n,n}$ will then be[4]

$$\chi^2_{S_n,n} = \begin{cases} \frac{(\rho_n(S_n) - \rho_{\text{FG}})^2}{\Delta\rho(S_n)}, & \text{if } \rho_n(S_n) < \rho_{\text{FG}} \\ 0, & \text{if } \rho_{\text{FG}} \leq \rho_n(S_n) \leq \rho_{\text{RMI}} \\ \frac{(\rho_n(S_n) - \rho_{\text{RMI}})^2}{\Delta\rho(S_n)}, & \text{if } \rho_n(S_n) > \rho_{\text{RMI}}, \end{cases} \tag{4.20}$$

where ρ_{FG} and ρ_{RMI} are the NLDs estimated with the FG and the RMI spin-cutoff parameters respectively, and $\Delta\rho(S_n)$ is calculated as in Eq. (4.18).

If all errors going in Eq. (4.16) are Gaussian distributed, then the χ^2 scores will draw a parabola for every i energy bin. The lowest χ^2 ($\chi^2_{\min}$) will be our middle value, while the points where the parabola crosses the $\chi^2_{\min} + 1$ horizontal line will decide the uncertainty for every evaluated point. This evaluation can be done graphically (see Figure 4.6)

If we choose the flat distribution for $\chi^2_{S_n}$, the parabola-shape will also have a flat region in the middle, as can be seen in Figure 4.7. This does not stop us from finding where the parabola-like shape crosses the $\chi^2_{\min} + 1$ line and evaluating the systematic errors this way.

When it comes to the GSF error propagation, we use a similar strategy. Its normalization is carried out by using the α parameter from the NLD normalization, and fixing B using $\langle\Gamma_\gamma\rangle$. This last quantity usually has an uncertainty $\Delta\langle\Gamma_\gamma\rangle$ associated, so that we may calculate the GSF χ^2 score by

---

[4]Usually the FG model ends up giving a lower value for the spin-cutoff parameter at S_n and is thus chosen to be the lower bound.
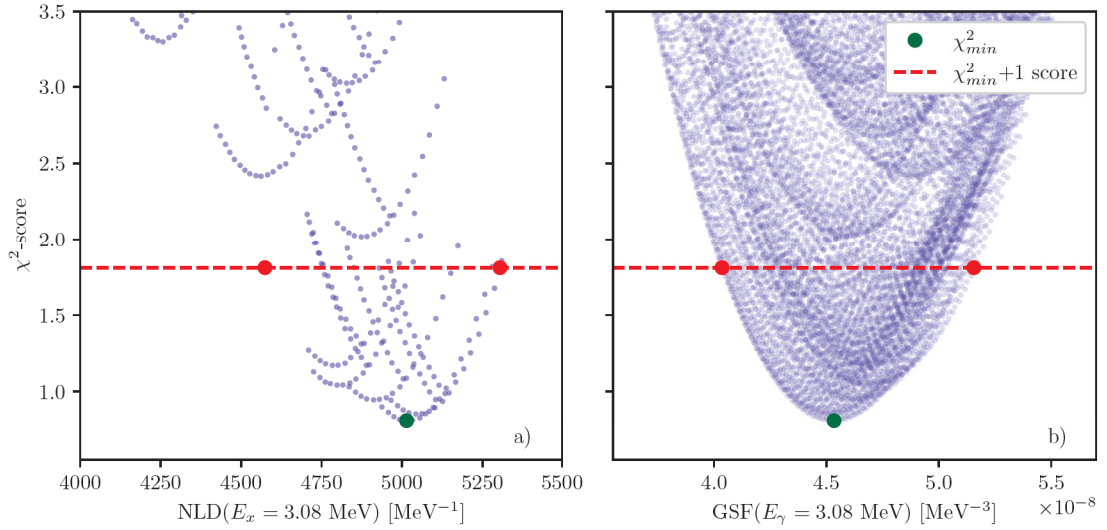
Figure 4.6: For each energy bin for the NLD and the GSF, the middle value is chosen as the one with the least χ^2-score, and the uncertainty by checking graphically where the parabola-like shape crosses the $\chi^2_{\min} + 1$ line. Here is shown an example for the bins at $E_x = 3.08$ MeV and $E_\gamma = 3.08$ MeV for the NLD and the GSF of ^{167}Ho, respectively.
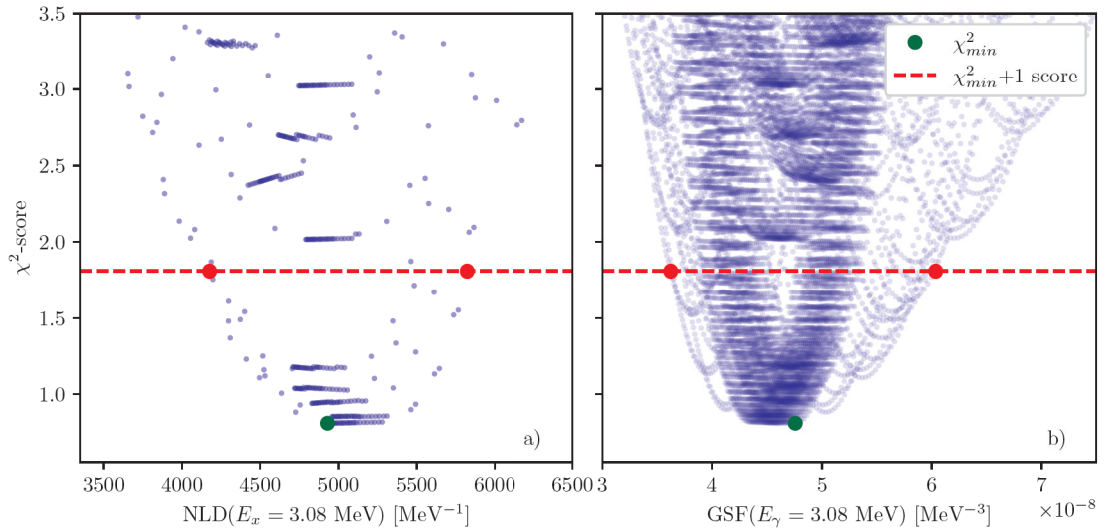

Figure 4.7: Same χ^2-score plots as for Figure 4.6, but where a flat probability distribution is chosen between the $\rho(S_n)$ values calculated with the FG and RMI spin-cutoff parameter formulas. In this way the parabola-shape is slightly distorted and the errors less symmetric about the value at $\chi^2_{\min}$, but we are less bound to a specific spin-cutoff model.

running different simulations varying $\langle \Gamma_\gamma \rangle_m$ around the suggested value, and calculating an array of $\chi^2_{\text{GSF},nm}$ as

$$\chi^2_{\text{GSF},nm} = \chi^2_{\text{NLD},n} + \frac{(\langle \Gamma_\gamma \rangle_m - \langle \Gamma_\gamma \rangle)^2}{\Delta \langle \Gamma_\gamma \rangle^2}. \tag{4.21}$$

Again the uncertainty will be where the $\chi^2_{\text{min}} + 1$ line crosses the parabola (or flat-parabola) shape for every E_γ bin.

4.4.2 The MACS

Maxwellian-averaged cross sections may be calculated from experimental NLDs and GSFs as explained earlier. In order to propagate the experimental systematic errors to the MACS, we calculate a MACS for every NLD and GSF pair, and associate the same χ^2 score as for the GSF employed in the calculation,

$$\chi^2_{\text{MACS},sys,nm} = \chi^2_{\text{GSF},nm}, \tag{4.22}$$

and again evaluating where the $\chi^2_{\text{MACS},sys,nm}$ parabola (or flat-parabola) for every energy bin E_i crosses the $\chi^2_{\text{min}} + 1$ line (see Figure 4.8).

This only propagates the systematic errors from the normalization procedure, though. When it comes to the statistical ones, they are propagated by calculating four MACS with every combination of $\rho_{\text{max}}(E_x) = \rho_{\chi^2_{\text{min}}}(E_x) \pm \Delta\rho_{\chi^2_{\text{min}}}(E_x)$ and $f_{\text{max}}(E_\gamma) = f_{\chi^2_{\text{min}}}(E_\gamma) \pm \Delta f_{\chi^2_{\text{min}}}(E_\gamma)$, and selecting the maximum and minimum MACS values for every bin. The lower error may then be calculated as

$$\Delta_{\text{lower}}\langle\sigma\rangle_T = \sqrt{\Delta_{\text{sys, lower}}\langle\sigma\rangle_T^2 + \Delta_{\text{stat, lower}}\langle\sigma\rangle_T^2} \tag{4.23}$$

and similarly for the upper error. This last part is not a rigorous uncertainty propagation, and tends to overestimate the error band. Nevertheless, this is probably the best choice as the OMP model used for the MACS calculation usually does not provide uncertainties, and it is safer to stay on the conservative side. The experimentally constrained uncertainties in the MACS are usually smaller than the ones provided by combining all the available NLD and GSF models in nuclear reaction software such as TALYS (about one order of magnitude difference for ^{126}Sb and ^{166}Ho in Papers I and III, see tables in the Appendix. See also Fig. 2 in Paper IV for an overview of the TALYS theoretical neutron-capture rate uncertainty span for all the neutron-rich nuclei), and certainly smaller than the factor 10 or 100 used for different sensitivity studied for the i and r processes (see Section 2.5.4). This is true even when considering variations in the choice of OMP model as seen for ^{166}Ho(n, γ) in Paper III [44] (Figure 6b in the paper, see also Appendix A.3). Even with conservative error estimation, experimentally constrained MACS using the Oslo method may still provide useful input for nucleosynthesis network calculations.
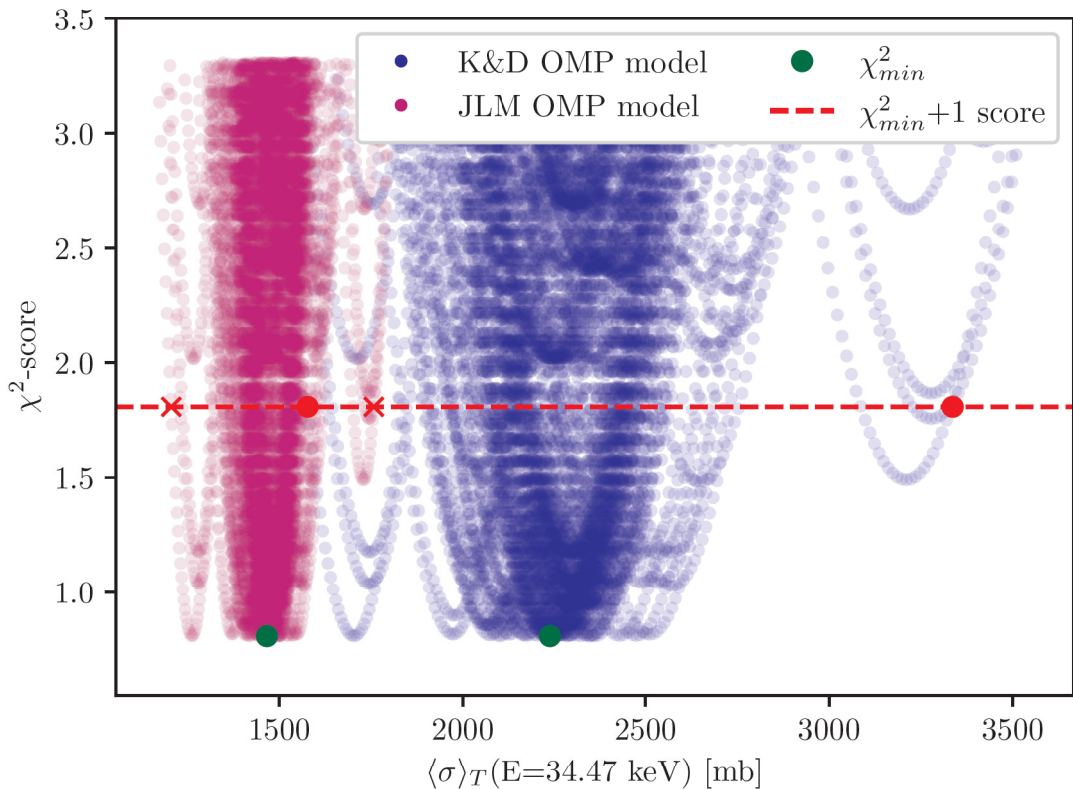
Figure 4.8: From every NLD and GSF pair we may calculate the MACS, and each MACS calculated inherits the χ^2-score of the used GSF. From these χ^2-scores we can use the same procedure for the uncertainty evaluation as for the NLD and GSF by finding graphically where the "flat-parabola" crosses the $\chi^2_{\min} + 1$ line for every energy bin. Here the MACS for $(n,\gamma)^{167}$Ho evaluated at $E = 34.47$ keV is shown. The two colors represent the MACS calculated using the Koning & Delaroche (K&D) OMP model [122] and the Jeukenne-Lejeune-Mahaux (JLM) OMP model [123]. The whole MACS may be observed in Figure 6b in Paper III [44]. For data on all the calculated MACS for all the papers included in this thesis, see Appendix.

Chapter 5

Summary and outlook

In the first part of this thesis I presented an overview of nuclear physics in the context of astrophysics. The overarching question of *How elements are made in the universe* involves different disciplines, and I chose to give a short summary of basic nuclear physics in Chapter 1 and then Chapter 2 begins from the very place where nucleosynthesis takes place, namely the cosmos. Here we see how the Big Bang first, then stars and finally their dying phase with explosions and mergers stand behind the creation of elements from hydrogen, through carbon, iron, lead and up to the heaviest isotope of uranium. Neutron-capture nucleosynthesis was given the main focus, and can be divided into three processes: the slow, the intermediate and the rapid neutron-capture process. Correct simulations of the astrophysical phenomena where these processes happen is paramount to their proper description, and this means having the correct nuclear inputs. In chapter 3 I went through the theoretical foundation that lets us calculate the neutron-capture rate from two average statistical quantities of the nucleus: the nuclear level density and the γ-ray strength function. These can be extracted from experiments carried out at the Oslo Cyclotron Laboratory and analyzed using the Oslo method. This was explained in Chapter 4 together with a novel error propagation procedure developed by me.

This foundation allows us to get into the papers forming the second part of this thesis. These touch all three neutron-capture processes, although in different ways and with different focuses. Paper I [85] looks into the role that ^{127}Sb plays in the i process, and the following two (Paper II [86] and Paper III [44]) analyze the scissors resonance in rare-earth nuclei ^{166}Ho and ^{167}Ho, and the role of the ^{166}Ho 1200-years isomeric state at 6 keV in the s process. Paper I was my first published article where the above mentioned error propagation procedure (used also in Papers II and III) is described. The constrained neutron-capture rate of ^{126}Sb represents the first step into the analysis of the ^{135}I region, relevant to the i process, and tabulated data can be found in Appendix A.1. The paper also provides information on the pygmy resonance and the upbend in the region, features still not well understood and whose impact on the nucleosynthesis should be further investigated. Similarly for Papers II and Paper III not only the experimentally constrained neutron-capture rates are provided (tabulated data again in Appendix A.2 and A.3), but also information on the evolution of the scissors resonance, relevant to deformed, rare-earth nuclei. Again, data on the behavior of these features of the γ-ray strength function may prove very useful to theoreticians aiming to develop more predictive nuclear models for the exotic region of the nuclear chart, which is key to the correct simulation of the i and r processes. Finally, Paper IV [27] touches upon the problems with simulating the r process, and how different strategies used to evaluate the errors

in the nuclear input (the neutron-capture rate in our case) may give different predictions. Whereas other groups choose to vary these quantities from nucleus to nucleus independently from each other, it can be argued that this method loses the correlations we know exist between neighboring nuclei, and that a model-consistent approach should be used. Nevertheless, as also discussed earlier in Section 2.5.4, both methods have their own strengths and weaknesses.

New insights on the behavior of the pygmy resonance in elements around cadmium, tin, antimony and tellurium would give a better picture not only of the nuclear physics surrounding this mysterious structure, but also useful data to be used in nucleosynthesis network calculations. Secondly, a proper study of the transition strengths and branching ratios of ^{166}Ho would give us a correct picture of this nucleus and possibly answer if this indeed is thermalized or not at s-process temperatures, and if not, whether the long-lived, 1200-years isomer plays a role in shaping the final s-process abundances. Finally, new methods to propagate nuclear uncertainties (especially for neutron-capture rates) in i-process and r-process nucleosynthesis are needed. These new methods should have the ability to consider both the uncertainty in the model predictions for exotic nuclear properties, and to embed these in proper, multi-zone simulations of the astrophysical environments. In this way we would obtain more precise information on which nuclei are most important to study, and help uncovering the mysteries in these two processes.

Heavy-element nucleosynthesis is a vast subject, and even after four years of doctoral studies I feel like I only scraped its surface. However, I hope that the results included in this work may help move the limits of knowledge towards a better and more complete understanding of this field.

Chapter 6

Summary of papers

6.1 Paper I: Indirect measurement of the $(n, \gamma)^{127}$Sb cross section

In this paper I analyze the results of the ^{124}Sn$(\alpha, p\gamma)^{127}$Sb experiment carried out at the Oslo Cyclotron Laboratory. The motivation behind this experiment was investigating the nuclide chart region near ^{135}I. According to Hampel *et al.* [53], ^{135}I acts as a bottleneck for the astrophysical i process, and more knowledge on the neutron-capture rates in the region could help in the correct modeling of this nucleosynthesis event. From the ^{124}Sn$(\alpha, p\gamma)^{127}$Sb experiment we are able to extract the nuclear level density and the γ-ray strength function, which are then used to calculate the Maxwellian-averaged cross section (MACS) of ^{126}Sb, which is easily translatable to the neutron-capture rate. The level density follows a constant-temperature model, while the strength function presents an upbend, together with a possibly split pygmy resonance and a small structure at $E_\gamma \approx 3$ MeV. The calculated MACS is found to be in agreement with the libraries commonly used for astrophysical calculations such as JINA REACLIB [105], TENDL [124] and BRUSLIB [107], but less with other libraries such as ENDF/B-VIII.0 [125] (see Fig. 6.1). In this paper the error propagation procedure described in Section 4.4 is presented, and will lay the basis for the same procedure to be used in Papers II and III.
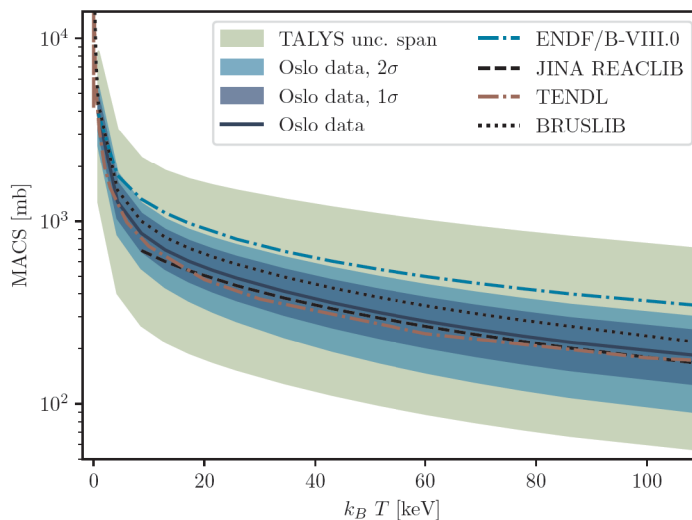
Figure 6.1: The experimental MACS for ^{126}Sb obtained in Paper I, compared to the rates from known libraries. See Fig. 8 in Paper I and discussion for references and details. Appendix A.1 for tabulated data.

6.2 Paper II: Observation of a candidate for the *M1* scissors resonance in odd-odd ^{166}Ho

The focus of this article is on the scissors resonance (SR). This structure has been presented in Section 3.3.1 and is a resonance-like "bump" in the γ-ray strength function at $E_\gamma \approx 3$ MeV present in deformed rare-earth nuclei (and other nuclei as well). Here, ^{166}Ho is obtained via the ^{163}Dy$(\alpha, p\gamma)^{166}$Ho reaction, and again the NLD and the GSF are extracted using the Oslo method. The scissors resonance is an $M1$ feature, and experiments at OCL cannot distinguish between $E1$ and $M1$ radiation. We know however enough about the expected structures in the GSF to be able to make an educated guess. Indeed, a "bump" at $E_\gamma \approx 3$ MeV is found, strongly indicating the presence of the scissors resonance. This is the first observation of the SR in an odd-odd nucleus such as ^{166}Ho using the Oslo method analysis. Much of the paper goes through the different methods one may use to separate the observed structure from the $E1$ background strength, and compares the results from these methods with each other and with the results from other experiments for similar nuclei in the rare-earth region (see Fig. 6.2).
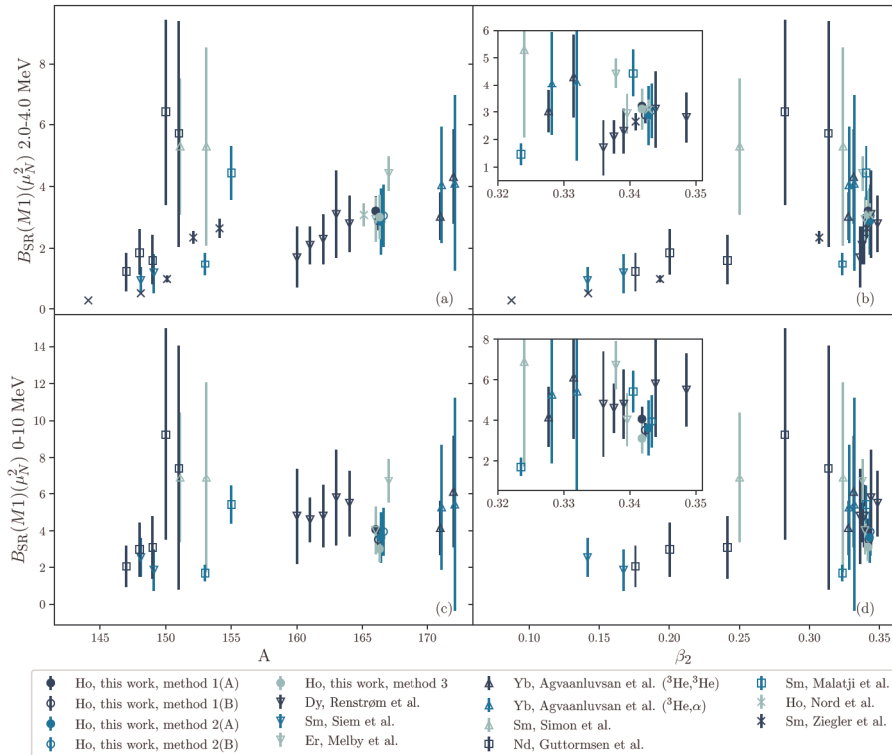
Figure 6.2: The $B_{\mathrm{SR}}(M1)$ strength for the scissors resonance plotted against the mass number A and the deformation β_2 for many nuclei in the rare-earth region, included the values calculated with different methods for ^{166}Ho. See Fig. 7 in Paper II and its discussion for references and details about the data.

6.3   Paper III: Experimentally constrained ^{165,166}Ho(n,γ) rates and implications for the s process

This paper is a natural continuation of Paper II, where the ^{166}Ho NLD and GSF obtained from the ^{163}Dy$(\alpha, p\gamma)^{166}$Ho reaction are used to find the corresponding MACS for ^{165}Ho(n,γ). Similarly, the data from the ^{164}Dy$(\alpha, p\gamma)^{167}$Ho experiment are analyzed and the ^{166}Ho(n,γ) MACS is calculated. The motivation for this is the interesting nature of ^{166}Ho, which has a 0^- ground state with a half-life of 27-h and a longer lived 7^- isomer at $E_x \approx 6$ keV with a half-life of about 1200 years, which is comparable to the timescale of the s process. Experimentally constrained (n,γ) rates for ^{165}Ho and ^{166}Ho may first impact on how much ^{165}Ho is made, and second on whether ^{165}Ho manages to capture two neutrons, to become ^{167}Ho and β-decay to ^{167}Er impacting the ^{166}Er/^{167}Er final abundance ratio. Apart from constraining s-process abundance uncertainties for ^{165}Ho, our results do not show a big impact on the Er final abundances because of the short ^{166}Ho lifetime in astrophysical environments due to its thermalization. The question of the thermalization of ^{166}Ho is still open though, as many of the transition probabilities and branching ratios used to find out about this are only estimates [104]. I collaborated with the Brussels group (S. Goriely and L. Siess) on the astrophysical part of this work.
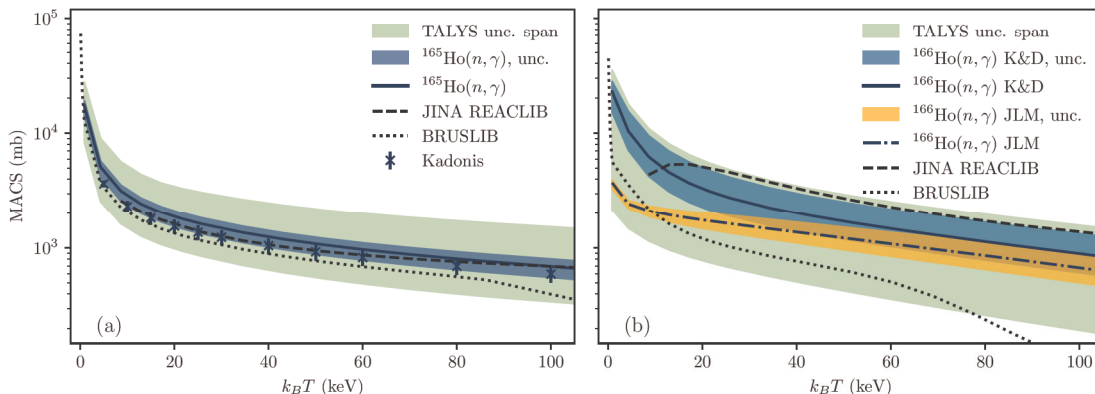
Figure 6.3: The MACS obtained with the ^{166,167}Ho NLD and GSF extracted from the ^{163}Dy$(\alpha, p\gamma)^{166}$Ho experiment from Paper II, and the ^{164}Dy$(\alpha, p\gamma)^{167}$Ho from Paper III. Here again the MACS is compared to existing reaction rate libraries. See Fig. 6 in Paper III and discussion for references and details. Appendix A.2 and A.3 for tabulated data.

6.4 Paper IV: Model-consistent study of level densities and γ-strength functions for r-process simulations

In this paper we describe the two main approaches employed in r-process sensitivity studies to propagate nuclear uncertainties to the final abundances. The first, dubbed the "statistical approach", attempts to estimate these uncertainties by assuming a confidence interval in the predictions of a model, and running many one-zone, r-process simulations in order to show the impact these have on the final abundances. The second approach, dubbed "model-consistent approach", instead uses different nuclear models as inputs. Both of these methods have strengths and weaknesses. The study only focuses on neutron-capture rates, and uses five different trajectories (a trajectory being the density and temperature time evolutions for a "bubble" of expanding stellar ejecta where the r process takes place) and 49 different neutron-capture rate models. The r-process simulations were run on the nuclear reaction network SkyNet [126] and the rates are those of JINA REACLIB [105] plus 48 models obtained by combining the six level density with the eight γ-strength function models available in TALYS 1.95 [124, 127]. One of the main takeaways of the study is that shell effects and pairing correlations between neighboring N-even and N-odd nuclei are not correctly taken into account in the statistical approach, and that their inclusion produces a staggering effect in the rare-earth peak final abundances that is not reproduced in the statistical approach, see Fig. 6.4.
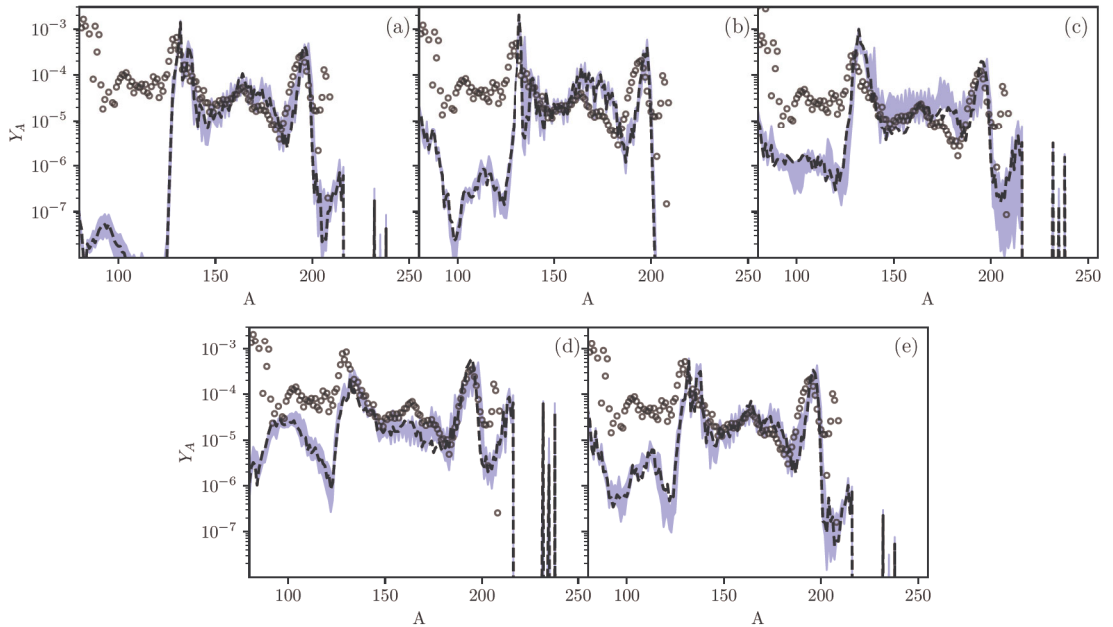
Figure 6.4: The final abundances from the five trajectories used in the sensitivity study in Paper IV. The blue band represents the prediction span from using the 48 neutron-capture rate models, and the black dashed line the abundances obtained by using the rates from JINA REACLIB [105]. See Fig. 7 in Paper IV for more details.

Papers

Paper I

Indirect measurement of the $(n, \gamma)^{127}$Sb cross section
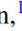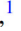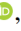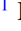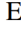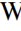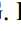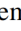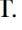
I

Indirect measurement of the $(n, \gamma)\,^{127}$Sb cross section

F. Pogliano[1,*] A. C. Larsen[1,†] F. L. Bello Garrote[1] M. M. Bjørøen[1] T. K. Eriksen[1] D. Gjestvang[1] A. Görgen[1] M. Guttormsen[1] K. C. W. Li[1] M. Markova[1] E. F. Matthews[2] W. Paulsen[1] L. G. Pedersen[1] S. Siem[1] T. Storebakken[1] T. G. Tornyi[1] and J. E. Vevik[1]

[1]*Department of Physics, University of Oslo, N-0316 Oslo, Norway*
[2]*Department of Nuclear Engineering, University of California, Berkeley, California 94720, USA*

Nuclei in the ^{135}I region have been identified as being a possible bottleneck for the i process. Here we present an indirect measurement for the Maxwellian-averaged cross section of ^{126}Sb(n, γ). The nuclear level density and the γ-ray strength function of ^{127}Sb have been extracted from ^{124}Sn$(\alpha, p\gamma)\,^{127}$Sb data using the Oslo method. The level density in the low-excitation-energy region agrees well with known discrete levels, and the higher-excitation-energy region follows an exponential curve compatible with the constant-temperature model. The strength function between $E_\gamma \approx 1.5$–8.0 MeV presents several features, such as an upbend and a possibly double-peaked pygmy-like structure. None of the theoretical models included in the nuclear reaction code TALYS seem to reproduce the experimental data. The Maxwellian-averaged cross section for the ^{126}Sb$(n, \gamma)\,^{127}$Sb reaction has been experimentally constrained by using our level-density and strength-function data as input to TALYS. We observe a good agreement with the JINA REACLIB, TENDL, and BRUSLIB libraries, while the ENDF/B-VIII.0 library predicts a significantly higher rate than our results.

I. INTRODUCTION

The origin of elements heavier than iron in our universe is a hot topic of research among nuclear and astrophysicists, and is regarded as being one of the *Eleven Science Questions for the New Century* [1]. Since the seminal paper of Burbidge *et al.* [2], neutron-capture reactions have been identified as the main mechanism for which heavy-element nucleosynthesis take place in stars. Now we know that two processes are mainly responsible for the abundances of heavier-than-iron elements in the universe: the s process and the r process, standing for the slow and rapid neutron-capture processes, respectively. These two processes produce different abundance patterns, and the relative abundances of Ba, La, and Eu on a star's surface may indicate whether the elemental abundance of the star follows an s or r process distribution (see, e.g., [3]).

One particularly interesting case is the one of carbon-enhanced metal-poor stars (CEMPs). These are old stars in the galactic halo and may be enriched in either r process elements [4], s process elements, or both [5]. CEMPs enriched in both s and r process elements present a huge challenge. Since the two processes are thought to happen in very different astrophysical sites, the mixing of the interstellar medium prior to the formation of the star cannot be the reason behind this peculiar abundance pattern. A possible explanation is the presence of an *intermediate* neutron-capture process (the

i process) with neutron densities between that of the s and r processes [6]. By assuming that the i process is taking place, both one-zone models and more complex star simulations are able to reasonably reproduce the observed abundances in these stars (see, e.g., [6–8]). However, all these studies conclude that more accurate estimates of fundamental nuclear properties are needed for a better understanding of the i process. In particular, neutron-capture rates are of great importance.

Experimental studies of nuclei in the ^{135}I region are interesting for two reasons. First, this region is thought to act as a bottleneck for the i process in CEMP-r/s stars according to Hampel *et al.* [6]. However, to say how significant this bottleneck might be, one needs information on the neutron-capture rates for the involved nuclei. Second, experimental data on fundamental properties of neutron-rich nuclei will help us to develop better and more predictive theoretical models, which both i and r process simulations heavily rely on.

As neutron-capture rates are extremely hard to measure directly on unstable nuclei, one relies on indirect techniques to constrain these rates. At the Oslo Cyclotron Laboratory (OCL), an experimental method has been developed to measure nuclear statistical properties, namely, the γ-ray strength function (GSF) and the nuclear level density (NLD). These two quantities can in turn be used to calculate an experimentally constrained (n, γ) cross section (see [9] and references therein). In this work, we present new data on ^{127}Sb, produced by the ^{124}Sn$(\alpha, p\gamma)\,^{127}$Sb reaction. This is the first experiment of a new experimental campaign where neutron-rich nuclei are made by bombarding the most neutron-rich, stable nucleus in an isotopic chain with α particles. The ^{127}Sb nucleus is part of the ^{135}I region, and using our measured GSF and NLD

*francesco.pogliano@fys.uio.no
†a.c.larsen@fys.uio.no

of ^{127}Sb we can provide a data-constrained ^{126}Sb(n, γ) ^{127}Sb reaction rate for the first time.

The article is structured as follows: The experimental setup will be described in Sec. II, and the Oslo method will be presented in Sec. III. The uncertainty analysis and quantification will be discussed in Sec. IV and a discussion on the resulting calculation of the neutron-capture rate in Sec. V. Finally, a summary and an outlook are given in Sec. VI.

II. EXPERIMENTAL SETUP

The experiment was carried out in November 2020 at the OCL, using an α beam of 24 MeV and ≈ 6 nA intensity produced by the MC-35 Scanditronix cyclotron. The beam impinged on a ^{124}Sn self-supporting target of 0.47 mg/cm^2 thickness and 95.3% enrichment for a period of six days. A short run with a 1-mg/cm^2-thick ^{12}C target was performed for calibration purposes.

As we were interested in the particle-γ coincidences from the $(\alpha, p\gamma)$ reaction, the Oslo SCintillator ARray (OSCAR) and the Silicon Ring (SiRi) detector arrays were used. The targets were placed inside OSCAR [10], an array of 30 cylindrical (3.5″ × 8.0″) LaBr$_3$(Ce) γ-ray detectors mounted on a truncated icosahedron frame. The distance between the front of the detectors and the center of the target was 16 cm. OSCAR has an energy resolution of 2.7% at $E_\gamma = 662$ keV, and fast timing properties with a typical resolution of the prompt timing peak of ≈ 1–5 ns. SiRi [11] is a ΔE-E particle telescope consisting of a ring of eight silicon-telescope modules covering 126°–140° in backward angles (corresponding to 6% of 4π). Each module consists of a thick (1550 μm) E back detector, with a thin (130 μm) ΔE detector in the front. The ΔE detector is divided into eight strips covering about 2° each, all together forming a system of 64 detectors. To separate the various reaction channels and select only the (α, p) data, we used the ΔE-E technique, plotting the deposited energy in the back detector versus the deposited energy in the front strip
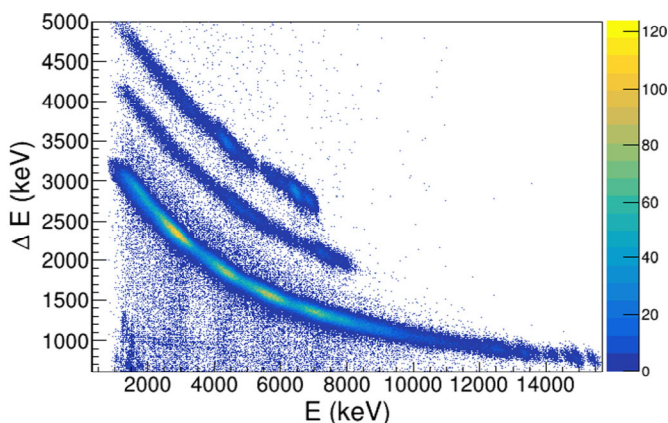

FIG. 1. The ΔE-E plot, or "banana" plot, where the energy deposited on the front strip of SiRi (ΔE) is plotted against the one deposited on the back detector (E). From bottom to top, we see three bands where the lowest one shows the energies deposited by ejected protons in the ^{124}Sn(α, p) ^{127}Sb reaction, the second deuterons from the ^{124}Sn(α, d) ^{126}Sb reaction, and the third tritons from the ^{124}Sn(α, t) ^{125}Sb reaction.

("banana" plots; see Fig. 1). The recently installed XiA digital electronics were applied for the data acquisition.

For the energy calibration of OSCAR, we used the 4.439 MeV γ transition from the first-excited state of ^{12}C, together with the 511 keV annihilation peak. To calibrate SiRi, we used the ground-state peak of ^{127}Sb in the proton "banana" and the ground-state peak of ^{125}Sb in the triton "banana."

Using the reaction kinematics, we mapped the measured ejectile's energy to excitation energy of the recoiled nucleus, thus providing an excitation energy vs γ-ray energy 2D spectrum called the "raw" coincidence matrix. Both the excitation energy and γ-ray energy calibration were then fine-tuned using the known low-lying excited states of ^{127}Sb, their decay energy, and the nucleus's neutron-separation energy.

III. THE OSLO METHOD

The Oslo method is a set of techniques developed at the OCL to extract the GSF and the NLD from the first-generation γ-ray matrix [12–14]. To obtain the first-generation matrix, we start from the calibrated raw matrix shown in Fig. 2(a), which must first be unfolded. By unfolding, we mean the process of deconvolution; i.e., we estimate the "true" signal that was distorted due to the detector response. The algorithm is explained in detail in Ref. [12]. In brief, it is an iterative technique exploiting the fact that folding is a very fast procedure. Starting out with a trial function for the "true" spectrum, the trial function is folded with the known detector response matrix and compared to the observed spectrum. The trial function is then updated accordingly and the process is repeated until good agreement with the observed spectrum is found. The unfolding procedure is regularized in two ways: First, the Compton subtraction method is used to preserve the experimental fluctuations bin-by-bin. Second, the "goodness-of-fit" is weighted with the experimental fluctuations in addition to the usual χ^2 result. Here we use the OSCAR response function [10,15], and the unfolded matrix is presented in Fig. 2(b).

An excited nucleus may decay directly to the ground state or go through a γ-ray cascade, involving one or more lower-lying excited levels, before reaching the ground state. To extract the NLD and GSF, we need the *first-generation* (or *primary*) γ rays, meaning the first γ rays from a cascade. These can be extracted by the iterative subtraction method described in Ref. [13]. The main assumption behind this method is that the γ spectra are the same whether an excitation-energy bin was populated directly through the reaction, or by γ decay from above-lying E_x bins. The resulting first-generation matrix is shown in Fig. 2(c).

The NLD and GSF are average, statistical quantities describing the nucleus in the quasicontinuum, and are the equivalent of levels and reduced transition probabilities in the discrete region. In the quasicontinuum region, the energy levels are still separable, in principle, as the mean level spacing, D, is bigger than the level width, Γ. However, in practice, it is very hard to measure each level and its decay properties, and so it is more useful to describe the nucleus using the NLD and GSF in the quasicontinuum region. This excitation-energy region is chosen in the first-generation
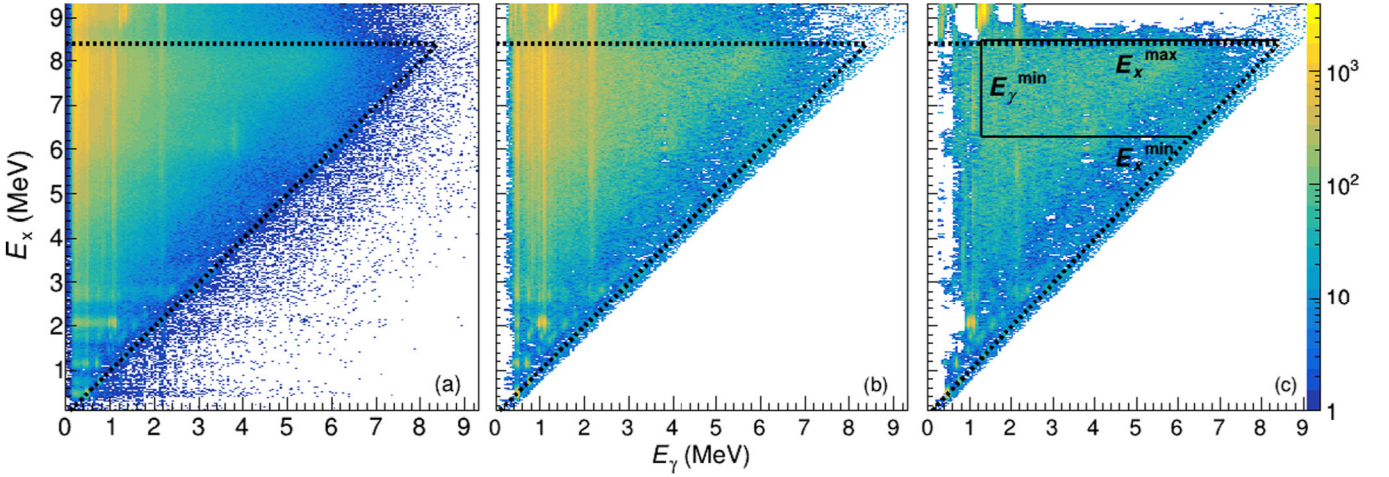
FIG. 2. The (a) raw, (b) unfolded, and (c) first-generation matrices used in the Oslo method analysis. On all matrices, the x axis indicates the γ-ray energy, E_γ, and the y axis the excitation energy E_x. Displayed on all three panels are the $E_x = E_\gamma$ lines and the neutron-separation energy $S_n = 8.383$ MeV.

matrix to extract the NLD and the GSF [14], as shown in Fig. 2(c).

The GSF is defined as [16]

$$f^{XL}(E_x, E_\gamma, J, \pi) = \frac{\langle \Gamma_\gamma^{XL}(E_x, E_\gamma, J, \pi) \rangle}{D(E_x, E_\gamma, J, \pi) E_\gamma^{2L+1}}, \quad (1)$$

where f^{XL} is the GSF for electromagnetic character X and multipolarity L for a transition energy E_γ, $\langle \Gamma_\gamma^{XL} \rangle$ is the average partial γ decay width, and D is the mean level spacing. In principle, the GSF may depend on excitation energy E_x, spin J, and parity π. The GSF is directly related to the γ transmission coefficient by

$$f^{XL}(E_x, E_\gamma, J, \pi) = \frac{\mathcal{T}^{XL}(E_x, E_\gamma, J, \pi)}{2\pi E_\gamma^{2L+1}}. \quad (2)$$

The generalized Brink-Axel hypothesis [17,18] states that we can average out the dependence on E_x, J, and π, allowing us to simplify this expression. This hypothesis, central to the Oslo method, is shown to hold for neighboring nuclei of tin [19], and we assume this is the case also for ^{127}Sb. Using this hypothesis, and considering the dipole radiation ($L = 1$) to be dominant, we obtain

$$f(E_\gamma) = \frac{\mathcal{T}(E_\gamma)}{2\pi E_\gamma^3}. \quad (3)$$

From Fermi's golden rule [20,21], we know that the decay probability is proportional to both the square of the matrix element between the initial and final state, and the number of states available in the final excitation-energy bin. This is applied in the following ansatz [14]:

$$P(E_\gamma, E_x) \propto \mathcal{T}(E_\gamma) \rho(E_x - E_\gamma); \quad (4)$$

i.e., the first-generation matrix $P(E_\gamma, E_x)$ is proportional to the product of the two vectors of $\mathcal{T}(E_\gamma)$ and $\rho(E_x - E_\gamma)$, where the latter is the NLD at excitation energy $E_x - E_\gamma$. This holds as long as we deal with statistical decay: the decay is independent of the way the compound nucleus was originally

created. Therefore, we must make cuts in the first-generation matrix to ensure that this is fulfilled.

For ^{127}Sb, we choose the following limits: $E_x^{min} = 6.3$ MeV, $E_x^{max} = 8.5$ MeV, and $E_\gamma^{min} = 1.3$ MeV. These limits ensure that the excitation energy is high enough for statistical decay to be dominant. The upper E_x limit is just above the neutron-separation energy, so that the spectra are not contaminated with neutron signals. The limit on E_γ is necessary to prevent the possible inclusion of transitions originating from higher-generation γ rays with low transition energies, in particular the strong 1095 keV transition originating from the $(11/2^+)$ level at $E_x = 1095$ keV [see Fig. 2(a)]. Applying these limits on $P(E_\gamma, E_x)$, we estimate the experimental first-generation matrix by [14]

$$P(E_\gamma, E_x) = \frac{\mathcal{T}(E_\gamma) \rho(E_x - E_\gamma)}{\sum_{E_\gamma = E_\gamma^{min}}^{E_x} \mathcal{T}(E_\gamma) \rho(E_x - E_\gamma)}. \quad (5)$$

The simultaneous extraction of $\mathcal{T}(E_\gamma)$ [and thus $f(E_\gamma)$ by Eq. (3)] and $\rho(E_x - E_\gamma)$ happens by normalizing the first-generation matrix, $P(E_\gamma, E_x)$, at each excitation energy E_x, i.e.,

$$\sum_{E_\gamma = E_\gamma^{min}}^{E_\gamma} P(E_\gamma, E_x) = 1, \quad (6)$$

and running a χ^2 minimization of Eq. (5) [14] to extract two solutions for $\tilde{f}(E_\gamma)$ and $\tilde{\rho}(E_f)$. If one solution is found, it can be shown [14] that any solution of the form

$$\tilde{\rho}(E_x - E_\gamma) = Ae^{\alpha(E_x - E_\gamma)} \rho(E_x - E_\gamma), \quad (7a)$$

$$\tilde{\mathcal{T}}(E_\gamma) = Be^{\alpha E_\gamma} \mathcal{T}(E_\gamma) \quad (7b)$$

also satisfies Eq. (5) for any three parameters A, B, and α. These are to be determined from experimental data. Normally, the number of levels at low excitation energies, the s-wave level spacing at the neutron-separation energy, D_0, and the average total radiative width, $\langle \Gamma_\gamma \rangle$, would be used. However, such data are typically not available for nuclei far
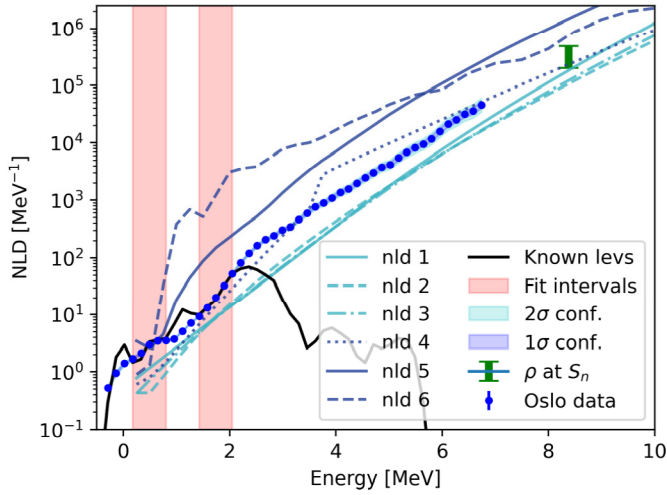
63

FIG. 3. Normalization of the NLD (see text) together with the theoretical level density models `nld` (shorthand for `ldmodel` 1 to 6) used in TALYS [31,32]. The uncertainties in the data points include statistical uncertainties and systematic uncertainties from unfolding and the first-generation method. The total uncertainty band includes also systematic errors from the normalization.

from stability and ^{127}Sb is no exception. We will discuss the normalization of the functions ρ and $\mathcal{T}$ in the following section.

IV. NORMALIZATION AND UNCERTAINTY PROPAGATION

A. Normalization of the NLD

The parameters A and α from Eq. (7a) are needed for the normalization of the NLD. To constrain these would require two anchor points at low and high excitation energy. We normalize our data points in the low-energy region by a fit to known, discrete levels taken from Ref. [22]. By comparing our data points to the known levels smoothed with our experimental resolution, we observe that the experimental NLD fits very well in the E_x region between ≈ 0.2 and 0.8 MeV, as well as between ≈ 1.4 and 2.1 MeV (shaded regions in Fig. 3). The apparent "bump" in between these intervals could be due to levels in the database that we do not observe in our experiment. We also normalize our experimental $\rho(E_x)$ to the level density at the neutron-separation energy. This can be calculated from the measured level spacing D_0 of s-wave neutron resonances at separation energy with [14]

$$\rho(S_n) = \frac{2\sigma_I^2}{D_0[(I_t+1)e^{-(I_t+1)^2/2\sigma_I^2} + I_t e^{-I_t^2/2\sigma_I^2}]}, \quad (8)$$

where I_t is the spin of the target nucleus and σ_I is the spin-cutoff parameter. The use of this formula introduces a model dependence by requiring the estimation of σ_I for the spin distribution at the separation energy. This is done by assuming a rigid-body moment of inertia:

$$\sigma_{I,\mathrm{RMI}}^2(S_n) = 0.00146 A^{5/3} \frac{1 + \sqrt{1+4aU_n}}{2a}, \quad (9)$$

where $U_n = S_n - E_1$, $E_1 = -0.45$ MeV is the excitation-energy shift and $a = 12.35$ MeV^{-1} is the level-density parameter, calculated according to the formalism of Ref. [23]. The observed experimental values of $\rho(E_x)$ do not reach the separation energy due to the lower limit $E_\gamma^{\min}$, which means the highest E_x is given by $E_x^{\max} - E_\gamma^{\min}$. To perform a fit to the $\rho(S_n)$ value, the data must be extrapolated up to $E_x = S_n$. This extrapolation introduces another model dependence as one has to assume some model for $\rho(E_x)$ in the gap between our data points and $\rho(S_n)$. A commonly used model is the constant-temperature (CT) model, given by the formula [24,25]

$$\rho_{\mathrm{CT}}(E_x) = \frac{1}{T_{\mathrm{CT}}} \exp\left(\frac{E_x - E_0}{T_{\mathrm{CT}}}\right), \quad (10)$$

where the energy shift, E_0, and the nuclear temperature, T_{CT}, are parameters to be found from fitting to data. Using another model, such as the back-shifted Fermi gas model, gives essentially the same results in the case where the gap between our data and $\rho(S_n)$ is not too large (see Ref. [26]).

Experimental D_0 values are typically available for stable nuclei, from which $\rho(S_n)$ can be derived using Eq. (8). For unstable nuclei, the value of $\rho(S_n)$ must be obtained by other means. In this work, we compare theoretical values to the semiexperimental values for nuclei in the same mass region as ^{127}Sb. Thus, we apply a similar strategy to the one in Kullmann *et al.* [27], where D_0 values for the neighboring isotopes of Sn, Sb, and Te (corresponding to $Z = 50, 51$, and 52, respectively) from both the *Atlas of Neutron Resonances* [28] and the *Reference Input Parameter Library* [29] were used to calculate $\rho(S_n)$. These values are then compared to the theoretical $\rho(S_n)$ estimates using the global parametrization of Ref. [23] to evaluate how well they agree. From this, $\rho_{\mathrm{EB}}(S_n) = 376 \times 10^3$ MeV^{-1} is obtained for ^{127}Sb.

A conservative estimate of the uncertainty of $\rho(S_n)$ for ^{127}Sb from this evaluation would be a flat probability distribution between $0.53\rho_{\mathrm{EB}}$ and $1.28\rho_{\mathrm{EB}}$, where the edges of the distribution are smoothed with a Gaussian with a standard deviation of $\delta\rho = 90 \times 10^3$ MeV^{-1}. The probability distribution was chosen to be flat between the two values $0.53\rho_{\mathrm{EB}}$ and $1.28\rho_{\mathrm{EB}}$, as there is no clear reason to prefer one value over another within this range. The value of $\delta\rho$ is not straightforward to obtain. However, we believe that we have chosen a reasonable estimate, as it corresponds to what is obtained by translating the uncertainty in the value of D_0 for neighboring nuclei to $\rho(S_n)$ using Eq. (8).

Many different NLD normalizations were generated with the `counting.c` code from the Oslo method software [30] by varying the input parameters to the code. The code normalizes the experimental NLD by running a χ^2 minimization of the (unnormalized) experimental data fitting it to the known levels at low E_x, and to the CT model that goes through $\rho(S_n)$ at high E_x. The input parameters that are changed are the lower- and upper-energy bins constraining the fitting interval (L1 and L2) for the χ^2 minimization in the low-E_x region. Further, the ρ_{CT} formula in Eq. (10) is used to interpolate the level density between our data points and $\rho(S_n)$. The parameters E_0 and T_{CT} from Eq. (10) are determined in `counting.c` by

TABLE I. Values used for the normalization of the NLD. The parameters E_1 and a are the excitation-energy shift and the level-density parameter, respectively, used in the rigid-body moment of inertia formula in Eq. (9). E_0 and T_{CT} refer to the parameters used in the constant-temperature model in Eq. (10), while $\rho_f(S_n)$ and $\delta\rho(S_n)$ represent the limits for which the level density at neutron-separation energy is flat, and the width of the tapering outside these limits, respectively. Finally, σ_I is the spin-cutoff parameter calculated by Eq. (9) and D_0 is the range of level spacings of s-wave neutron resonances related to $\rho_f(S_n)$ by Eq. (8).

E_1 (MeV)	a (MeV^{-1})	E_0 (MeV)	T_{CT} (MeV)	$\rho_{EB}(S_n)$ (10^3 MeV^{-1})	$\rho_f(S_n)$ (10^3 MeV^{-1})	$\delta\rho(S_n)$ (10^3 MeV^{-1})	σ_I	D_0 (eV)
-0.45	12.35	$(-1.2, -1.9)^a$	0.8	376	199–481	90	6.45	58.8–24.3

[a]Varying according to the choice of $\rho_f(S_n)$.

providing a fitting interval to the data at high E_x and to the value of $\rho(S_n)$.

Above a given E_x, the level density becomes more smooth and the information about the known levels starts to become incomplete (in this case, where $E_x \gtrsim 3$ MeV). As the CT model is essentially an exponential function, and our data points display a very smooth trend where $E_x \approx 3$–6.5 MeV, the T_{CT} parameter was found to vary very little when choosing different data points for the fit. Therefore, these fitting points were kept fixed, using a temperature parameter of $T_{CT} = 0.8$ MeV. The E_0 parameter in the CT formula is the shift parameter, and for a fixed T_{CT}, this will change according to the choice of $\rho(S_n)$. The E_0 parameter was found to have values between $E_0 = -1.2$ MeV (for $0.53\rho_{EB}$) and $E_0 = -1.9$ MeV (for $1.28\rho_{EB}$). See Table I for an overview of all the parameters used in the NLD normalization.

The `counting.c` code was run with every L1 and L2 combination so that L1 $<$ L2 $\leqslant$ 22 (where bin 22 corresponds to $E_x = 2.68$ MeV), and a range of 50 values for $\rho(S_n)$ between $0.4\rho_{EB}$ and $1.4\rho_{EB}$, incorporating the smoothing of the edges as mentioned above. This range corresponds to 11 500 different parameter combinations, and thus differently normalized NLDs. For each of these combinations, we calculate a χ^2_{NLD} score through

$$\chi^2_{NLD} = \sum_i \frac{[\rho_n(E_i) - \rho_k(E_i)]^2}{\Delta\rho_n(E_i)^2} + \chi^2_{S_n}, \quad (11)$$

where the sum runs over the energy bins $i = \{6, 7, 8, 9, 10, 14, 15, 16, 17, 18\}$, where the results seem to agree the most with the known levels and are shown in the shaded regions of Fig. 3. $\rho_n(E_i)$ is the value at the ith energy bin of the normalized NLDs, $\Delta\rho_n(E_i)$ its associated statistical uncertainty from the experiment, and $\rho_k(E_i)$ the level density calculated from the smoothed known levels. Finally, $\chi^2_{S_n}$ keeps track of the uncertainty for the normalization tied to the choice of $\rho(S_n)$ and is calculated as

$$\chi^2_{S_n} = \begin{cases} \frac{[\rho_n(S_n) - 0.53\rho_{EB}]^2}{\rho_\sigma^2}, & \text{if } \rho_n(S_n)/\rho_{EB} < 0.53, \\ 0, & \text{if } 0.53 \leqslant \rho_n(S_n)/\rho_{EB} \leqslant 1.28, \\ \frac{[\rho_n(S_n) - 1.28\rho_{EB}]^2}{\rho_\sigma^2}, & \text{if } \rho_n(S_n)/\rho_{EB} > 1.28, \end{cases} \quad (12)$$

mimicking what a χ^2 score would look like for a flat distribution inside a range, and otherwise behaving as a normal distribution. With 11 500 different NLDs [and thus 11 500 $\rho(E_x)$ values for each energy bin], each with its own χ^2_{NLD},

we are able to find the mean value of each bin by choosing the value with the smallest χ^2_{NLD}. Then, for each E_i bin, the uncertainty was graphically determined by checking where the parabola-like $\chi^2_{NLD}(\rho(E_i))$ plot crossed the $\chi^2_{min} + 1$ line [see Fig. 4(a)].

We note that the NLD normalization is rather strongly constrained by the fit to the known levels in the two shaded regions shown in Fig. 3. Therefore, despite the large uncertainty in the normalization point $\rho_{EB}(S_n)$, the slope of the NLD data points (and thus the slope of the GSF) is quite well determined.

In Fig. 3, together with the experimental results, we show the six NLD models included in TALYS 1.95 [31,32]. Here `ldmodel` 1 combines a constant-temperature model with the Fermi gas model [25], `ldmodel` 2 is the back-shifted Fermi gas model [25], `ldmodel` 3 the generalized superfluid model [33,34], and `ldmodel` 4–6 are Hartree-Fock-based calculations. From Fig. 3 we can observe that most of the models fail at reproducing the experimental results, and do not even meet the conservative error estimate for $\rho(S_n)$, with the exception of `ldmodel` 4 that comes the closest to the Oslo data.
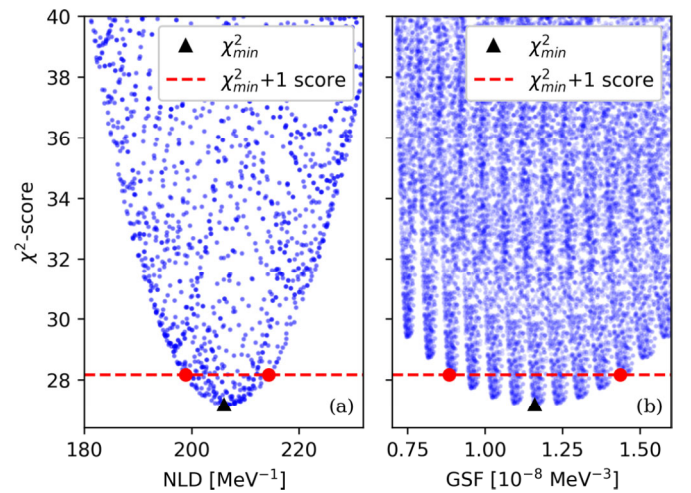

FIG. 4. The χ^2 scores of each calculated NLD (a) and GSF (b) for $E_x = 2.68$ MeV and $E_\gamma = 2.68$ MeV. Each E_x and E_γ bin has a similar, parabola-shaped distribution of χ^2 scores. From these we estimate the uncertainty of every bin by checking graphically where the parabola crosses the $\chi^2 + 1$ line (red points). The mean value is where $\chi^2 = \chi^2_{min}$ (black triangles).
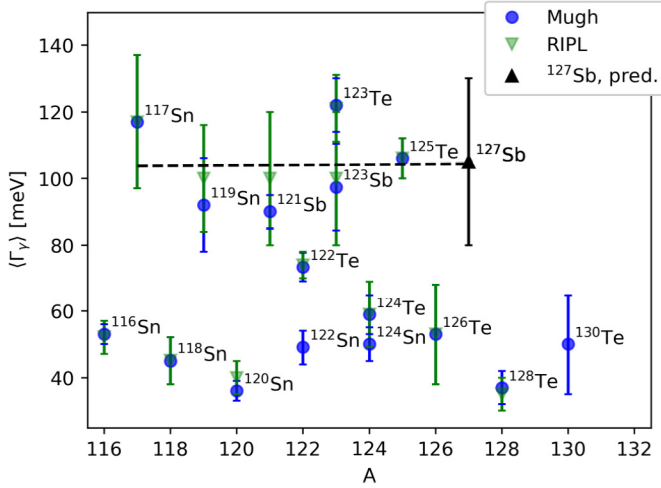
FIG. 5. Values of $\langle\Gamma_\gamma\rangle$ from Mughabghab [28] and RIPL [29] for the neighboring nuclei of ^{127}Sb. The black dashed line indicates the linear regression for the $\langle\Gamma_\gamma\rangle$ values of the odd-even nuclei.

B. GSF

The last free parameter in Eq. (7b) is B, responsible for the absolute normalization of the GSF. Since the average total radiative width, $\langle\Gamma_\gamma\rangle$, for ^{127}Sb is not known, it is again necessary to use systematics from neighboring nuclei to assess its value. In Fig. 5 we show the $\langle\Gamma_\gamma\rangle$ values for different nuclei in this mass region, gathered from Ref. [28]. Two patterns are observed, one for the even-even and one for the odd-even nuclei, respectively. As ^{127}Sb is odd-even, we use the data from the other odd-A nuclei to estimate $\langle\Gamma_\gamma\rangle$. Either an average or an extrapolation from linear regression could be used to predict the $\langle\Gamma_\gamma\rangle$ value for ^{127}Sb, and fortunately, both yield about the same values, rounded to $\langle\Gamma_\gamma\rangle_\mu = 105$ meV. The uncertainty is taken to be normally distributed and is kept conservatively to be $\langle\Gamma_\gamma\rangle_\sigma = 25$ meV (see Fig. 5).

To get the absolute normalization of the GSF, we use the script `normalization.c` [30], that takes as input the $\langle\Gamma_\gamma\rangle$ value, the estimated D_0 value which (with the given spin distribution) reproduces $\rho(S_n)$ used for the NLD data points, the normalized NLD, and the γ-ray transmission coefficient normalized in slope with the parameter α. By choosing 13 different $\langle\Gamma_\gamma\rangle$ values between $\langle\Gamma_\gamma\rangle = 65.5$–$142.5$ meV, we run `normalization.c` for each NLD obtained from `counting.c`. This gives us 149 500 different GSFs, 13 for each NLD. Each GSF inherits the $\chi^2_{\rm NLD}$ score from the associated NLD, and to assess the "goodness-of-fit" we add a term accounting for the deviation of the chosen $\langle\Gamma_\gamma\rangle_n$ from the mean value $\langle\Gamma_\gamma\rangle_\mu = 105$ meV:

$$\chi^2_{\rm GSF} = \chi^2_{\rm NLD} + \frac{(\langle\Gamma_\gamma\rangle_n - \langle\Gamma_\gamma\rangle_\mu)^2}{\langle\Gamma_\gamma\rangle_\sigma^2}. \quad (13)$$

Similarly to the NLD calculations, the GSF evaluated at each E_γ energy bin will have a mean value corresponding to where $\chi^2_{\rm GSF} = \chi^2_{\rm min}$, and an uncertainty where the $\chi^2_{\rm min}(f(E_\gamma)) + 1$ line crosses the parabola. This is shown for one specific bin ($i = 22$, where $E_i = 2.68$ MeV) in Fig. 4(b). The resulting GSF with the corresponding errors is displayed in Fig. 6.
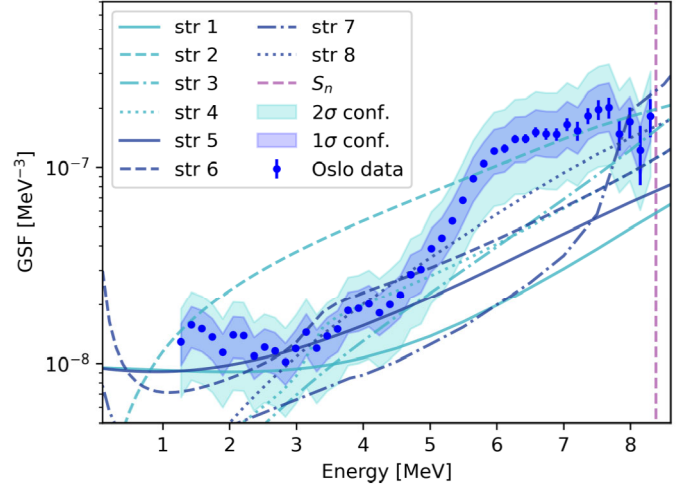

FIG. 6. The normalized GSF, together with the theoretical models `str` (shorthand for `strength` 1 to 8) used in TALYS [31,32]. The uncertainties in the data points include statistical uncertainties and systematic uncertainties from unfolding and the first-generation method. The total uncertainty band includes also systematic errors from the normalization.

C. Comparison with GSF models

We observe that the GSF shows similar features to the ones found in the neighboring nuclei—most prominently, a resonance-like peak at about $E_\gamma \approx 7$ MeV and a low-energy enhancement below $E_\gamma \approx 3$ MeV. These structures can be interpreted as the pygmy dipole resonance (PDR) and the upbend on top of the tail of the giant dipole resonance (GDR). Along with the experimental results, Fig. 6 shows the eight theoretical GSF models available from the reaction code TALYS 1.95 [31,32]. None of these seem to fit well, as none predict such a strong pygmy-like structure as observed in the data. Although the upbend is included in four of them (`strength` 1, 5, 6, and 7), none seem to give a fully correct behavior. The GFSs modeled by `strength` 1 and 2 are the generalized Lorentzian model [35] and the standard Lorentzian (Brink-Axel) model [18,36], respectively. These are phenomenological models, and are not expected to give good predictions for nuclei far from stability. All other models are microscopic, mostly based on the quasiparticle random-phase approximation. These models attempt to describe nuclei from the underlying physics rather than by phenomenology. However, none of them manage to predict the PDR for ^{127}Sb in a satisfying way; they all systematically underestimate the strength in the $E_\gamma = 5$–7 MeV region. This underestimate of the PDR may consequently lead to systematic underestimates of (n, γ) rates used in astrophysical applications.

The main feature of the GSF for transition energies below S_n is the tail of the GDR, and also the PDR. The GDR tail can be modeled by a generalized Lorentzian (GLO) [35],

$$f^{\rm GLO}(E_\gamma) = \frac{\sigma_0\Gamma_0}{3\pi^2\hbar^2c^2}\left(\frac{E_\gamma\Gamma_K}{\left(E_\gamma^2 - E_0^2\right)^2 + E_\gamma^2\Gamma_K^2} + 0.7\frac{\Gamma_{K,0}}{E_\gamma^3}\right), \quad (14)$$

66

TABLE II. Fitting parameters for the GLO of ^{126}Sn, ^{127}Sb, and ^{128}Te (see text).

Nucleus	T_f (MeV)	E_0 (MeV)	Γ_0 (MeV)	σ_0 (mb)
^{126}Sn	0.30(10)	15.3(3)	4.6(6)	265(22)
^{127}Sb	0.30(30)[a]	15.4(4)	5.4(10)	283(28)
^{128}Te	0.30(30)[a]	15.4(1)	6.1(4)	301(5)

[a]Estimated from tin isotopes.

where

$$\Gamma_K(E_\gamma, T_f) = \frac{\Gamma_0}{E_0^2}\left(E_\gamma^2 + 4\pi^2 T_f^2\right) \qquad (15)$$

and $\Gamma_{K,0} = \Gamma_K(0, T_f)$. σ_0, E_0, Γ_0, and T_f are considered free parameters, representing the peak cross section, the energy centroid, the width, and the temperature of the final levels, respectively. As there are no experimental photonuclear data of ^{127}Sb, we infer the GLO parameters by again comparing to data from neighboring nuclei. We choose the GLO parameters by averaging over the values of fitting the GDRs for ^{126}Sn and ^{128}Te, these being the nuclei directly below and above ^{127}Sb in the nuclear chart, respectively. As a proxy for the GDR of ^{128}Te, we sum over the ^{128}Te(γ, n) and ^{128}Te$(\gamma, 2n)$ cross sections from Lepretre *et al.* [37], while the GLO parameter values of ^{126}Sn are found by extrapolation from the lighter isotopes of tin [19,38,39]. These two approaches give GLOs quite similar in magnitude and shape, and we estimate the GLO parameters of σ_0, E_0, and Γ_0, for ^{127}Sb to be the mean of the corresponding values found for ^{126}Sn and ^{128}Te. However, in order to find an appropriate value for T_f, we need information on the low-energy tail (well below S_n), which is not available from photonuclear data as the data from Lepretre *et al.* [37] only probes the GSF from S_n and higher E_γ. We choose to use the same T_f as applied for the tin isotopes, with a large uncertainty. All parameters can be found in Table II.

Figure 7 shows two different attempts to decompose the GSF into its constituent structures. The GDR, the upbend and a pygmy-like structure at ≈ 7 MeV, and the spin-flip M1 resonances are included in both. The GDR was modeled with a GLO using the parameters in Table II, the upbend by an exponential function of the form

$$f^{\mathrm{up}}(E_\gamma) = C_{\mathrm{up}} e^{-a_{\mathrm{up}} E_\gamma}, \qquad (16)$$

and the spin-flip M1 resonances by a standard Lorentzian

$$f^{\mathrm{SLO}}(E_\gamma) = \frac{1}{3\pi^2\hbar^2 c^2}\frac{\sigma_s \Gamma_s^2 E_\gamma}{\left(E_\gamma^2 - E_s^2\right)^2 + E_\gamma^2 \Gamma_s^2}, \qquad (17)$$

where σ_s, Γ_s, and E_s are free parameters and correspond to the same quantities as for the GLO in Eq. (14). These parameters were determined by extrapolation of the fittings of the M1 strengths measured in lighter tin isotopes [39] similarly as what done with the GDR. In Fig. 7(a), a single Gaussian is employed to describe the pygmy structure, while in Fig. 7(b) two Gaussians are employed. The choice of employing Gaussians to model resonances is unorthodox, but gives a better fit
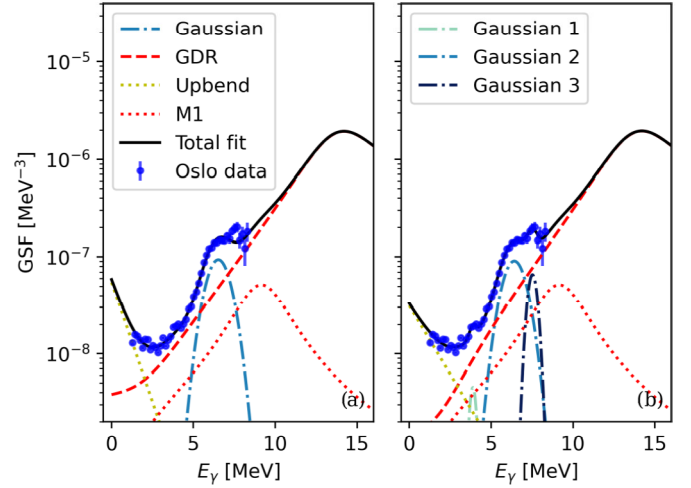

FIG. 7. Two possible decompositions of the GSF with one (a) and two (b) Gaussians for the PDR region (see discussion in text). The uncertainties in the data points correspond to the statistical uncertainty and systematic uncertainties from unfolding and the first-generation method.

than using a more conventional Lorentzian when applied to the PDR. This is as also observed for other nuclei (e.g., tin isotopes in Ref. [40]) and the reason for this is unknown. The Gaussian function is given by

$$f^{\mathrm{Gauss}}(E_\gamma) = \frac{1}{\sqrt{2\pi}\sigma_r} C \exp\left[-\frac{(E_\gamma - E_r)^2}{2\sigma_r^2}\right], \qquad (18)$$

where σ_r is the standard deviation, C is a normalization constant, and E_r is the centroid (expected value). A satisfying fit of the PDR is obtained with only one Gaussian function, although the data points at the highest E_γ are not fully reproduced. This fit gives an integrated, energy-weighted cross section of $\approx 0.7\%$ of the Thomas-Reiche-Kuhn energy-weighted sum rule (EWSR) [41–43]; see Table III. Three Gaussians are needed to reproduce all the visible structures as shown in Fig. 7(b), yielding $\approx 0.9\%$ of the sum rule; see Table IV. While the use of two Gaussians has been done in Ref. [40] to describe the PDR in tin isotopes, an additional, smaller structure is observed for ^{127}Sb at $E_\gamma \approx 4$ MeV. A similar feature is present in the ^{117}Sn GSF at $E_\gamma \approx 2.5$ MeV [38,44] and they might have the same origin. Although the energy region could coincide with that of the scissors mode, both tin and antimony with their respective proton numbers of 50 and 51 are known to be almost spherical nuclei, while the scissors mode is observed only in deformed nuclei.

Although it was found that the integrated, energy-weighted cross section of the pygmy-like structure is $\approx 0.8\%$ of the EWSR, it should be emphasized that this is a conservative estimate. In this work a fitted GLO "background" with a maximal

TABLE III. Parameters used for the Gaussian in Fig. 7(a).

Function	E_r (MeV)	σ_r (MeV)	C (10^{-9} MeV^{-2})	EWSR (%)
Gauss	6.52(5)	0.70(3)	164(9)	0.72(5)

TABLE IV. Parameters used for the three Gaussians in Fig. 7(b). The EWSR is calculated only for the second and third Gaussian, fitting the pygmy-like peak.

Function	E_r (MeV)	σ_r (MeV)	C $(10^{-9}$ MeV$^{-2})$	EWSR (%)
Gauss1	3.88(2)	0.19(3)	2.2(4)	–
Gauss2	6.41(7)	0.69(4)	157(15)	–
Gauss3	7.52(8)	0.28(9)	46(15)	–
Sum	–	–	–	0.9(2)[a]

[a]Calculated only for the last two Gaussians.

$E1$ strength is employed. Considering that theoretical models (e.g., those in TALYS) give a rather low GDR tail (see Fig. 6), the fraction could be considerably larger.

V. NEUTRON-CAPTURE CROSS SECTION

The radiative neutron-capture rate [or (n, γ)-rate] and the Maxwellian-averaged cross section (or MACS) are of particular interest for astrophysical applications such as nucleosynthesis network calculations. These quantities are closely related by [45]

$$N_A \langle \sigma \rangle = \frac{N_A \langle \sigma v \rangle}{v_T}, \tag{19}$$

where $N_A \langle \sigma v \rangle$ is the (n, γ) rate, $N_A \langle \sigma \rangle$ the MACS, N_A is Avogadro's number, and $v_T = \sqrt{2 k_B T / \tilde{m}}$ is the thermal speed. Further, k_B, T, and $\tilde{m}$ are the Boltzmann constant, the temperature, and the reduced mass of the neutron plus the target nucleus, respectively. The (n, γ) rate can then be calculated by (see, e.g., [3])

$$N_A \langle \sigma v \rangle (T) = \left(\frac{8}{\pi \tilde{m}} \right)^{1/2} \frac{N_A}{(k_B T)^{3/2} G_t(T)} \int_0^\infty \sum_\mu \frac{2 J_t^\mu + 1}{2 J_t^0 + 1}$$
$$\times \sigma_{n\gamma}^\mu(E) E \exp \left[-\frac{E + E_x^\mu}{k_B T} \right] dE, \tag{20}$$

where J_t^0 and J_t^μ are the spin for the ground state and the μth excited state, respectively, E_x^μ the energy of the μth excited state, E the relative energy between the neutron and the target nucleus, $\sigma_{n\gamma}^\mu$ the (n, γ) cross section for the target nucleus excited to the μth state, and $G_t(T)$ is the partition function given by

$$G_t(T) = \sum_\mu \frac{2 J_t^\mu + 1}{2 J_t^0 + 1} \exp \left[\frac{-E_x^\mu}{k_B T} \right]. \tag{21}$$

The radiative neutron-capture cross section $(\sigma_{n\gamma}^\mu)$ in Eq. (20) can be calculated from either theoretical or experimental values of the NLD and GSF for the compound nucleus in the Hauser-Feshbach framework [46]. Recommended theoretical values for either the (n, γ) rate, the MACS, or both can be found in libraries such as the JINA REACLIB rates [47], TENDL-19 [32], BRUSLIB [48], and ENDF/B-VIII.0 [49].

From the experimentally constrained NLD and GSF of ^{127}Sb, we calculate the (n, γ) rate and the MACS for ^{126}Sb, the latter shown in Fig. 8. This was done using TALYS [31,32].
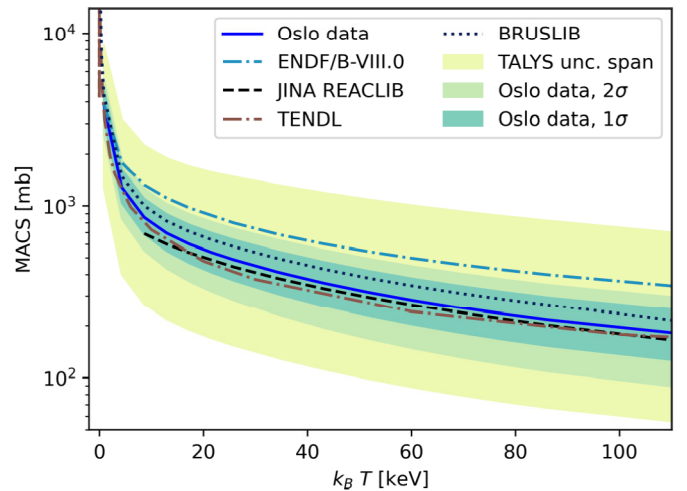

FIG. 8. The calculated experimentally constrained MACS for the ^{126}Sb(n, γ) reaction, together with theoretical values from JINA REACLIB [47], TENDL [32], BRUSLIB [48], and ENDF/B-VIII.0 [49].

By using each NLD-GSF pair as input, we propagate both the statistical and systematic uncertainties of the NLD and the GSF by letting the resulting MACS inherit the χ^2 score of the pair. From this, the uncertainty was found for each energy bin by graphically checking where the $\chi^2 + 1$ line would cross the parabola, similarly to what done before with the NLD and the GSF.

The experimentally constrained MACS is compared to different libraries such as JINA REACLIB, TENDL-19, ENDF/B-VIII.0, and BRUSLIB, together with the span of all TALYS predictions available from each theoretical NLD and GSF model combination, including both microscopic and macroscopic models (light yellow band in Fig. 8). We see that the MACS of both TENDL-19 and JINA REACLIB are inside the 1σ confidence band and the same is true for the BRUSLIB library. All of those libraries are compatible with our estimated MACS. However, the ENDF/B-VIII.0 library predicts a much higher rate (outside the experimental 2σ confidence), although it is still within the TALYS uncertainty band. It is not clear why ENDF/B-VIII.0 predicts a much higher MACS than the others, but probably it is due to significant differences in the input NLD and GSF used for the evaluation of the MACS.

The large variations in the NLD and GSF models are demonstrated in Figs. 3 and 6. The actual input models used in the libraries are not necessarily transparent, except for the BRUSLIB library which consequently uses the `ldmodel 5` and `strength 4` [48]. Therefore, it is hard to explain why some of the library MACS are within the 1σ band of the present work and some are not. To be able to conclude whether the i process can explain abundance observations, one needs to know the uncertainty in the (n, γ) rates of the nuclei involved in the i process. Moreover, the abundance sensitivity to nuclear input is often evaluated by varying the (n, γ) rates within some range. Unless known experimentally, the range might be determined from the variation in theoretical predictions using different NLD and GSF models (see, e.g., Refs. [7,50,51]), or by varying the rates of a library (such as JINA REACLIB) by a fixed factor (see, e.g., Ref. [52]). Both these methods

suffer from the problem that the models themselves usually do not provide parameter uncertainties. For a given rate, the uncertainty range might be too large, but also skewed, as the theoretical predictions are not necessarily normally distributed about the "true" value. Therefore, it is of utmost importance to (i) obtain as much experimental information as possible for nuclei relevant to the i process, and (ii) develop models of the NLD and GSF that are able to grasp the underlying physics, and at the same time provide reasonable estimates of existing experimental data.

VI. SUMMARY AND OUTLOOK

This work presents the measurement of the $^{124}\text{Sn}(\alpha, p\gamma)^{127}\text{Sb}$ reaction. We have experimentally extracted the NLD and GSF of ^{127}Sb. These quantities have allowed us to estimate the Maxwellian-averaged cross section for the $^{126}\text{Sb}(n, \gamma)^{127}\text{Sb}$ reaction, which is of interest for i process network calculations. The resulting MACS is in agreement with the estimates from the JINA REACLIB, BRUSLIB, and TENDL libraries. In contrast, a significant discrepancy was found with the ENDF/B-VIII.0 library.

It has been found that the GSF of ^{127}Sb displays an upbend and a pygmy-like resonance at about $E_\gamma = 7$ MeV. By fitting models to the data, we have estimated that the strength in the PDR region corresponds to about 0.7%–0.9% of the Thomas-Reiche-Kuhn energy-weighted sum rule. A small peaklike structure was observed at about $E_\gamma = 4$ MeV, which is difficult to explain with theoretical models. More precise measurements in this area, together with data of the GSF below 3 MeV and above the neutron-separation energy, would be desirable to better understand the behavior of these structures.

It is our hope that our data might inspire future developments of better theoretical models for the GSF. The impact of the data-constrained $(n, \gamma)^{127}\text{Sb}$ MACS on final i (and possibly r) process abundances will be addressed in a future work.

[1] N. R. Council, *Connecting Quarks with the Cosmos: Eleven Science Questions for the New Century* (National Academies Press, Washington, DC, 2003).

[2] E. M. Burbidge, G. R. Burbidge, W. A. Fowler, and F. Hoyle, Synthesis of the elements in stars, Rev. Mod. Phys. **29**, 547 (1957).

[3] M. Arnould, S. Goriely, and K. Takahashi, The r-process of stellar nucleosynthesis: Astrophysics and nuclear physics achievements and mysteries, Phys. Rep. **450**, 97 (2007).

[4] T. Hansen, C. J. Hansen, N. Christlieb, T. C. Beers, D. Yong, M. S. Bessell, A. Frebel, A. E. G. Pérez, V. M. Placco, J. E. Norris, and M. Asplund, An elemental assay of very, extremely, and ultra-metal-poor stars, Astrophys. J. **807**, 173 (2015).

[5] C. Sneden, J. J. Cowan, and R. Gallino, Neutron-capture elements in the early galaxy, Annu. Rev. Astron. Astrophys. **46**, 241 (2008).

[6] M. Hampel, R. J. Stancliffe, M. Lugaro, and B. S. Meyer, The intermediate neutron-capture process and carbon-enhanced metal-poor stars, Astrophys. J. **831**, 171 (2016).

[7] J. E. McKay, P. A. Denissenkov, F. Herwig, G. Perdikakis, and H. Schatz, The impact of (n,γ) reaction rate uncertainties on the predicted abundances of i-process elements with $32 \leqslant Z \leqslant 48$ in the metal-poor star HD94028, Mon. Not. R. Astron. Soc. **491**, 5179 (2020).

[8] S. Goriely, L. Siess, and A. Choplin, The intermediate neutron capture process, Astron. Astrophys. **654**, A129 (2021).

[9] A. Larsen, A. Spyrou, S. Liddick, and M. Guttormsen, Novel techniques for constraining neutron-capture rates relevant for r-process heavy-element nucleosynthesis, Prog. Part. Nucl. Phys. **107**, 69 (2019).

[10] F. Zeiser, G. Tveten, F. Bello Garrote, M. Guttormsen, A. Larsen, V. Ingeberg, A. Görgen, and S. Siem, The γ-ray energy response of the Oslo Scintillator Array OSCAR, Nucl. Instrum. Methods Phys. Res. Sect. A **985**, 164678 (2021).

[11] M. Guttormsen, A. Bürger, T. E. Hansen, and N. Lietaer, The SiRi particle-telescope system, Nucl. Instrum. Methods Phys. Res. Sect. A **648**, 168 (2011).

[12] M. Guttormsen, T. Tveter, L. Bergholt, F. Ingebretsen, and J. Rekstad, The unfolding of continuum γ-ray spectra, Nucl. Instrum. Methods Phys. Res. Sect. A **374**, 371 (1996).

[13] M. Guttormsen, T. Ramsøy, and J. Rekstad, The first generation of γ-rays from hot nuclei, Nucl. Instrum. Methods Phys. Res. Sect. A **255**, 518 (1987).

[14] A. Schiller, L. Bergholt, M. Guttormsen, E. Melby, J. Rekstad, and S. Siem, Extraction of level density and γ strength function from primary γ spectra, Nucl. Instrum. Methods Phys. Res. Sect. A **447**, 498 (2000).

[15] F. Zeiser and G. M. Tveten, oslocyclotronlab/OCL_GEANT4: Geant4 model of OSCAR, in *Nuclear Instruments and Methods in Physics Research Section A: Accelerators, Spectrometers, Detectors and Associated Equipment (v2.0.0.1, Vol. 985, p. 164678)*, Zenodo (2020), https://doi.org/10.5281/zenodo.4018494.

[16] G. A. Bartholomew, E. D. Earle, A. J. Ferguson, J. W. Knowles, and M. A. Lone, Gamma-ray strength functions, in *Advances in Nuclear Physics: Volume 7*, edited by M. Baranger and E. Vogt (Springer US, Boston, MA, 1973), p. 229.

[17] D. M. Brink, Some aspects of the interaction of fields with matter, Ph.D. thesis, Oxford University, 1955.

[18] P. Axel, Electric dipole ground-state transition width strength function and 7-Mev photon interactions, Phys. Rev. **126**, 671 (1962).

[19] M. Markova, P. von Neumann-Cosel, A. C. Larsen, S. Bassauer, A. Görgen, M. Guttormsen, F. L. Bello Garrote, H. C. Berg, M. M. Bjørøen, T. Dahl-Jacobsen, T. K. Eriksen, D. Gjestvang, J. Isaak, M. Mbabane, W. Paulsen, L. G. Pedersen, N. I. J. Pettersen, A. Richter, E. Sahin, P. Scholz *et al.*, Comprehensive Test of the Brink-Axel Hypothesis in the Energy Region of the Pygmy Dipole Resonance, Phys. Rev. Lett. **127**, 182501 (2021).

[20] P. A. M. Dirac, The quantum theory of the emission and absorption of radiation, Proc. R. Soc. London, Ser. A **114**, 243 (1927).

[21] E. Fermi, *Nuclear Physics* (University of Chicago Press, Chicago, 1950).

[22] National Nuclear Data Center, information extracted from the NuDat database, https://www.nndc.bnl.gov/nudat.

[23] T. von Egidy and D. Bucurescu, Systematics of nuclear level density parameters, Phys. Rev. C **72**, 044311 (2005).

[24] T. Ericson, The statistical model and nuclear level densities, Adv. Phys. **9**, 425 (1960).

[25] A. Gilbert and A. G. W. Cameron, A composite nuclear-level density formula with shell corrections, Can. J. Phys. **43**, 1446 (1965).

[26] H. K. Toft, A. C. Larsen, U. Agvaanluvsan, A. Bürger, M. Guttormsen, G. E. Mitchell, H. T. Nyhus, A. Schiller, S. Siem, N. U. H. Syed, and A. Voinov, Level densities and γ-ray strength functions in sn isotopes, Phys. Rev. C **81**, 064311 (2010).

[27] I. K. B. Kullmann, A. C. Larsen, T. Renstrøm, K. S. Beckmann, F. L. Bello Garrote, L. C. Campo, A. Görgen, M. Guttormsen, J. E. Midtbø, E. Sahin, S. Siem, G. M. Tveten, and F. Zeiser, First experimental constraint on the ^{191}Os(n, γ) reaction rate relevant to *s*-process nucleosynthesis, Phys. Rev. C **99**, 065806 (2019).

[28] S. F. Mughabghab, *Atlas of Neutron Resonances, Volume 2: Resonance Parameters and Thermal Cross Sections Z = 1–100* (Elsevier, Amsterdam, Netherlands, 2018).

[29] R. Capote, M. Herman, P. Obložinský, P. Young, S. Goriely, T. Belgya, A. Ignatyuk, A. Koning, S. Hilaire, V. Plujko, M. Avrigeanu, O. Bersillon, M. Chadwick, T. Fukahori, Z. Ge, Y. Han, S. Kailas, J. Kopecky, V. Maslov, G. Reffo *et al.*, RIPL—Reference Input Parameter Library for calculation of nuclear reactions and nuclear data evaluations, Nucl. Data Sheets **110**, 3107 (2009).

[30] M. Guttormsen, F. Zeiser, J. E. Midtbø, V. W. Ingeberg, and A.-C. Larsen, oslocyclotronlab/oslo-method-software: Oslo Method v1.1.5 (v1.1.5), Zenodo (2021), https://doi.org/10.5281/zenodo.5507864.

[31] A. Konig, S. Goriely, and S. Hilaire, TALYS-1.9, A nuclear reaction program, User manual, Tech. Rep., 2017, https://tendl.web.psi.ch/tendl_2019/talys.html.

[32] A. Koning, D. Rochman, J.-C. Sublet, N. Dzysiuk, M. Fleming, and S. van der Marck, TENDL: Complete nuclear data library for innovative nuclear science and technology, Nucl. Data Sheets **155**, 1 (2019).

[33] A. Ignatyuk, K. Istekov, and G. Smirenkin, Collective effects in the level density and the nuclear fission probability, Yad. Fiz. **30**, 1205 (1979).

[34] A. V. Ignatyuk, J. L. Weil, S. Raman, and S. Kahane, Density of discrete levels in ^{116}Sn, Phys. Rev. C **47**, 1504 (1993).

[35] J. Kopecky and M. Uhl, Test of gamma-ray strength functions in nuclear reaction model calculations, Phys. Rev. C **41**, 1941 (1990).

[36] D. Brink, Individual particle and collective aspects of the nuclear photoeffect, Nucl. Phys. **4**, 215 (1957).

[37] A. Leprêtre, H. Beil, R. Bergère, P. Carlos, J. Fagot, A. De Miniac, A. Veyssière, and H. Miyase, A study of the giant dipole resonance in doubly even tellurium and cerium isotopes, Nucl. Phys. A **258**, 350 (1976).

[38] H. K. Toft, A. C. Larsen, A. Bürger, M. Guttormsen, A. Görgen, H. T. Nyhus, T. Renstrøm, S. Siem, G. M. Tveten, and A. Voinov, Evolution of the pygmy dipole resonance in sn isotopes, Phys. Rev. C **83**, 044320 (2011).

[39] S. Bassauer, P. von Neumann-Cosel, P.-G. Reinhard, A. Tamii, S. Adachi, C. A. Bertulani, P. Y. Chan, A. D'Alessio, H. Fujioka, H. Fujita, Y. Fujita, G. Gey, M. Hilcker, T. H. Hoang, A. Inoue, J. Isaak, C. Iwamoto, T. Klaus, N. Kobayashi, Y. Maeda *et al.*, Electric and magnetic dipole strength in ^{112,114,116,118,120,124}Sn, Phys. Rev. C **102**, 034327 (2020).

[40] M. Markova, Experimental study of the pygmy dipole resonance in the $(p, p'\gamma)$ reaction on ^{124}Sn and its evolution in the Sn isotopic chain, Master's thesis, University of Oslo, 2020.

[41] W. Thomas, Über die Zahl der Dispersionselektronen, die einem stationren Zustande zugeordnet sind. (Vorläufige Mitteilung), Naturwissenschaften **13**, 627 (1925).

[42] F. Reiche and W. Thomas, Über die Zahl der Dispersionselektronen, die einem stationären Zustand zugeordnet sind, Z. Phys. **34**, 510 (1925).

[43] W. Kuhn, Über die Gesamtstärke der von einem Zustande ausgehenden Absorptionslinien, Z. Phys. **33**, 408 (1925).

[44] U. Agvaanluvsan, A. C. Larsen, R. Chankova, M. Guttormsen, G. E. Mitchell, A. Schiller, S. Siem, and A. Voinov, Enhanced Radiative Strength in the Quasicontinuum of ^{117}Sn, Phys. Rev. Lett. **102**, 162504 (2009).

[45] C. Iliadis, *Nuclear Physics of Stars* (Wiley-VCH, Weinheim, 2015).

[46] T. Rauscher and F.-K. Thielemann, Astrophysical reaction rates from statistical model calculations, At. Data Nucl. Data Tables **75**, 1 (2000).

[47] R. H. Cyburt, A. M. Amthor, R. Ferguson, Z. Meisel, K. Smith, S. Warren, A. Heger, R. D. Hoffman, T. Rauscher, A. Sakharuk, H. Schatz, F. K. Thielemann, and M. Wiescher, The JINA REACLIB database: Its recent updates and impact on type-I x-ray bursts, Astrophys. J. Suppl. Series **189**, 240 (2010).

[48] Y. Xu, S. Goriely, A. Jorissen, G. L. Chen, and M. Arnould, Databases and tools for nuclear astrophysics applications: BRUSsels nuclear LIBrary (BRUSLIB), Nuclear Astrophysics Compilation of REactions II (NACRE II) and nuclear NETwork GENerator (NETGEN), Astron. Astrophys. **549**, A106 (2013).

[49] D. Brown, M. Chadwick, R. Capote, A. Kahler, A. Trkov, M. Herman, A. Sonzogni, Y. Danon, A. Carlson, M. Dunn, D. Smith, G. Hale, G. Arbanas, R. Arcilla, C. Bates, B. Beck, B. Becker, F. Brown, R. Casperson, J. Conlin *et al.*, ENDF/B-VIII.0: The 8th major release of the nuclear reaction data library with CIELO-project cross sections, new standards and thermal scattering data, Nucl. Data Sheets **148**, 1 (2018).

70

[50] P. A. Denissenkov, F. Herwig, U. Battino, C. Ritter, M. Pignatari, S. Jones, and B. Paxton, i-process nucleosynthesis and mass retention efficiency in He-shell flash evolution of rapidly accreting white dwarfs, Astrophys. J. **834**, L10 (2017).

[51] B. Côté, P. Denissenkov, F. Herwig, A. J. Ruiter, C. Ritter, M. Pignatari, and K. Belczynski, ii/i-process contribution of rapidly accreting white dwarfs to the solar composition of first-peak neutron-capture elements, Astrophys. J. **854**, 105 (2018).

[52] R. Surman, M. Mumpower, J. Cass, I. Bentley, A. Aprahamian, and G. C. McLaughlin, Sensitivity studies for r-process nucleosynthesis in three astrophysical scenarios, EPJ Web Conf. **66**, 07024 (2014).

Correction: Typographical errors in Eqs. (2), (3), (19) and in the second sentence of the second paragraph of Sec. II have been fixed.
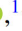
Paper II
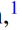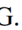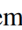
Observation of a candidate for the $M1$ scissors resonance in odd-odd ^{166}Ho

II

Observation of a candidate for the *M*1 scissors resonance in odd-odd ^{166}Ho

F. Pogliano [1,*] F. L. Bello Garrote,[1] A. C. Larsen,[1,†] H. C. Berg,[2,3,4] D. Gjestvang,[1] A. Görgen,[1]
M. Guttormsen,[1] V. W. Ingeberg,[1] T. W. Johansen,[1] K. L. Malatji,[5,6] E. F. Matthews,[7] M. Markova,[1] J. E. Midtbø,[1]
V. Modamio,[1] L. G. Pedersen,[1] E. Sahin,[1] S. Siem,[1] T. G. Tornyi,[1,8] and A. S. Voyles[7]

[1]*Department of Physics, University of Oslo, N-0316 Oslo, Norway*
[2]*Physics Department, Michigan State University, East Lansing, Michigan 48824, USA*
[3]*National Superconducting Cyclotron Laboratory, Michigan State University, East Lansing, Michigan 48824, USA*
[4]*Joint Institute for Nuclear Astrophysics Center for the Evolution of the Elements,*
University of Notre Dame, Notre Dame, Indiana 46556, USA
[5]*SSC Laboratory, iThemba LABS, P.O. Box 722, Somerset West 7129, South Africa*
[6]*Physics Department, Stellenbosch University, Matieland 7602, South Africa*
[7]*Department of Nuclear Engineering, University of California, Berkeley, California 94720, USA*
[8]*Institute for Nuclear Research (Atomki), 4026 Debrecen, Hungary*

The γ-strength function and the nuclear level density for the odd-odd, rare-earth nucleus ^{166}Ho have been extracted from ^{163}Dy$(\alpha, p\gamma)^{166}$Ho data using the Oslo method. A structure at ≈ 3 MeV in the γ-stren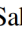gth function is interpreted as the *M*1 scissors resonance. By employing three different methods we find that its strength depends rather strongly on the modeling of the *E*1 strength, while its centroid does not. The ^{166}Ho scissors resonance parameters are consistent with previous results on other rare-earth nuclei.

I. INTRODUCTION

Our understanding of the response of rare-earth elements to electromagnetic radiation is far from complete. This region of the nuclear chart is interesting because of the variety in deformation (from close-to-spherical to well-deformed prolate shapes [1]), and it is an ideal region for studying nuclear statistical properties (see, e.g., Refs. [2–6]).

The *scissors resonance* (SR), also called the scissors mode, has received much attention over the years. The SR was originally predicted to be originating from neutrons and protons oscillating against each other like scissor blades in deformed, rotational nuclei [7], but is now understood as a coherent contribution from single-particle couplings between orbitals of the same angular momentum ℓ and j centered at around $E_\gamma = 3$ MeV [8]. While the SR has been observed in many even-even and odd-even nuclei (see, e.g., Refs. [6,8]), it has not yet been studied thoroughly in odd-odd ones, with the notable exception of the two-step cascade experiment on ^{160}Tb by Kroll *et al.* [9].

While many studies have been carried out using the nuclear resonance fluorescence (NRF) technique (see Ref. [8] and references within), this technique has usually been applied in the low excitation-energy region. Counting individual states and transitions becomes increasingly difficult when the density of energy levels increases. To account for the apparent

missing strength in odd-*A* nuclei, Huxel *et al.* [10] applied a statistical analysis in the case of ^{165}Ho and ^{169}Tm. With such an approach, they were able to obtain an integrated upwards $B(M1)\uparrow$ strength of ≈ 3 μ_N^2, in good agreement with previous NRF results on well-deformed even-even nuclei in the rare-earth region [11,12]. Also, Nord *et al.* [13] performed experiments with even better resolution on the same nuclei and thus an improved sensitivity for several odd-*A* rare-earth nuclei. When the number of energy levels per excitation energy bin $\rho(E_x)$ (or nuclear level density, NLD) becomes larger than ~ 50–100 levels per MeV, it is often more useful to consider the statistical properties of the nucleus instead of singular levels and decays. The nuclear excitation energy region between E_x for which $\rho(E_x) > 50$ MeV^{-1} and where particles are still bound is called the quasicontinuum, and two useful quantities here are the NLD and γ-strength function $f(E_\gamma)$, or GSF. The GSF is the statistical counterpart of transition probabilities for the discrete region; it gives us information on which γ energies the nucleus prefers to decay with, and thus an insight into its internal structure and collective modes. A puzzle that is still not fully solved is the seemingly conflicting results on the integrated strength of the SR obtained from different types of experiments. As already mentioned, NFR experiments have revealed a total strength of ≈ 3 μ_N^2 for well-deformed rare-earth nuclei. In contrast, experiments utilizing the two-step cascade method following neutron capture [14–16] have found about twice the integrated strength, which is also the case for data analyzed with the Oslo method [3,4,6,17–22]. One possible explanation for this discrepancy is related to the different moments of inertia the
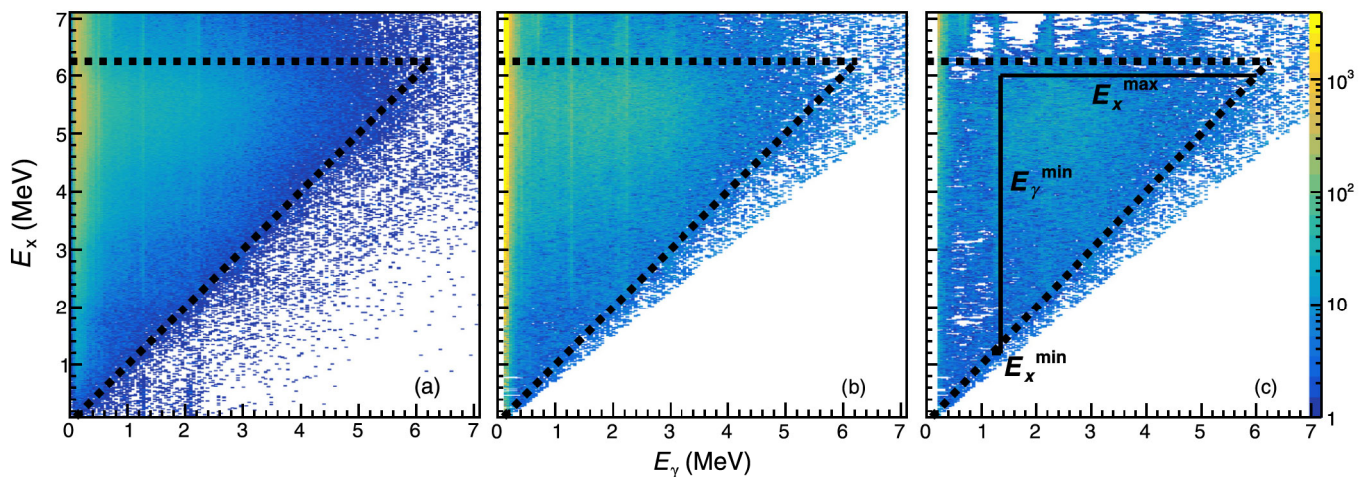
*francesco.pogliano@fys.uio.no
†a.c.larsen@fys.uio.no

FIG. 1. The (a) raw, (b) unfolded, and (c) first-generation matrices used in the Oslo method analysis. The x axis indicates the γ-ray energy E_γ, while the y axis indicates the excitation energy E_x. The stapled lines indicate the $E_x = E_\gamma$ diagonal and the neutron-separation energy $S_n = 6.244$ MeV.

nucleus attains for ground-state excitations and quasicontinuum decay (for which in the latter case, many quasiparticles are involved; see, e.g., Uhrenholt *et al.* [23]). If this is the case, it would mean that the Brink-Axel hypothesis [24,25] is not valid for the SR; i.e., its properties in the ground state are not the same as those for excited levels. However, as discussed in Ref. [6], there are many possible sources of uncertainties when extracting the integrated SR strength, and they are perhaps so significant that one should be careful making strong conclusions as of now.

This work aims to further investigate the SR in rare-earth, odd-odd nuclei through the data from the $^{163}\text{Dy}(\alpha, p\gamma)\,^{166}\text{Ho}$ experiment performed at the Oslo Cyclotron Laboratory (OCL). Using the Oslo method, it is possible to simultaneously extract the NLD and the GSF from particle-γ coincidences in charged reaction experiments. In this article, the experimental setup and data analysis are described in Secs. II and III, discussion on implications for scissors mode is given in Sec. IV and a summary is given in Sec. V.

II. EXPERIMENTAL METHOD

The experiment was carried out at the OCL in April 2018 for a period of 6 days, where an α beam of 26 MeV and $\approx$3-nA intensity was impinged on a ^{163}Dy self-supporting target of 2 mg/cm^2 thickness and 98.5% enrichment. The Oslo Scintillator Array (OSCAR) and the silicon ring (SiRi) detector arrays were used in order to detect the particle-γ coincidences from the $(\alpha, p\gamma)$ reaction. The γ rays were detected by placing the targets inside OSCAR [26], an array of 30 cylindrical (3.5"×8.5") LaBr$_3$(Ce) scintillator detectors mounted on a truncated icosahedron frame, where 28 were operational at the time of the experiment. OSCAR has an energy resolution of 2.7% at $E_\gamma = 662$ keV and a typical time resolution of the prompt timing peak of $\approx$1–5 ns. Particles were detected using SiRi [27], a $\Delta E\text{-}E$ particle telescope consisting of a ring of 8 silicon-telescope modules covering 126°–140° in backwards angles (corresponding to 6% of 4π).

Each of these modules consists of a thick (1550 μm) E back detector, and a thin (130 μm) ΔE strip detector segmented in 8 parts in the front covering about 2° each, together forming a system of 64 detectors. Using the $\Delta E\text{-}E$ technique, we collect particle energy and timing information and represent the event by plotting the deposited energy in the back detector versus the deposited energy in the front strip. This was used in order to separate the various reaction channels and select only the (α, p) data. Given the projectile and ejectile energies, together with the known Q values of the reaction, we are able to calculate the excitation energy of the residual nucleus using the reaction kinematics. With this, an excitation energy vs γ-ray energy matrix called the *raw* coincidence matrix is obtained [see Fig. 1(a)]. From the raw coincidence matrix, the primary γ-ray spectra for each excitation energy can be obtained using the established methodology of the Oslo method [28–30]. This is done by first deconvoluting [28] the raw matrix using the response function of Refs. [26,31] [see Fig. 1(b)] and then extracting the first-emitted γ rays in the decay cascades through a subtraction technique (Fig. 1(c), see Ref. [29]).

Assuming the validity of the generalized Brink-Axel hypothesis [24,25], stating that the GSF is independent of initial and final excitation energy, spin, and parity, we can extract the NLD and GSF from the *primary γ-ray* matrix, also known as the *first-generation γ-ray* matrix. The Brink-Axel hypothesis has been tested for neighboring nuclei of dysprosium [6,32] and is therefore expected to be applicable in this mass region. Fermi's Golden rule [33,34] allows us to apply the ansatz [30]

$$P(E_\gamma, E_x) \propto \mathcal{T}(E_\gamma)\rho(E_x - E_\gamma), \tag{1}$$

where P is the probability for the excited nucleus to decay from excitation energy E_x by emitting a γ ray with energy E_γ, $\rho(E_x - E_\gamma)$ is the level density in the final energy level, and $\mathcal{T}(E_\gamma)$ is the γ-transmission coefficient, from which one can derive the GSF, denoted by f^{XL}, through the relation

$$\mathcal{T}^{XL}(E_\gamma) = 2\pi E_\gamma^{2L+1} f^{XL}(E_\gamma), \tag{2}$$

for γ transitions of electromagnetic character X, multipolarity L, and γ energy E_γ. The GSF is defined as [35]

$$f^{XL}(E_x, E_\gamma, J, \pi) = \frac{\langle \Gamma_\gamma^{XL}(E_x, E_\gamma, J, \pi) \rangle}{D(E_x, E_\gamma, J, \pi) E_\gamma^{2L+1}}, \quad (3)$$

where $\langle \Gamma_\gamma^{XL} \rangle$ is the average partial γ-decay width and D is the mean level spacing. The average partial γ-decay width is also directly connected to the transmission coefficient by [36]

$$\langle \Gamma_\gamma^{XL}(E_x, E_\gamma, J, \pi) \rangle = \mathcal{T}^{XL}(E_x, E_\gamma, J, \pi) \frac{D(E_x, E_\gamma, J, \pi)}{2\pi}. \quad (4)$$

By then combining Eqs. (3) and (4), we obtain

$$f^{XL}(E_x, E_\gamma, J, \pi) = \frac{\mathcal{T}^{XL}(E_x, E_\gamma, J, \pi)}{2\pi E_\gamma^{2L+1}}. \quad (5)$$

By applying the generalized Brink-Axel hypothesis [24,25], the dependencies on E_x, J, and π are averaged out; i.e., the experimental γ-transmission coefficient represents an average transmission coefficient for all the spins accessible in the experiment, as well as for the excitation-energy range used in the extraction procedure. At high excitation energies, the γ transitions are dominantly of the dipole type ($L = 1$, see, e.g., Ref. [37]), and our experimental γ-transmission coefficient can be approximated by

$$\mathcal{T}(E_\gamma) \approx \mathcal{T}^{E1}(E_\gamma) + \mathcal{T}^{M1}(E_\gamma), \quad (6)$$

and thus we obtain the simplified expression

$$f(E_\gamma) = \frac{\mathcal{T}(E_\gamma)}{2\pi E_\gamma^3}, \quad (7)$$

where $f(E_\gamma)$ and $\mathcal{T}(E_\gamma)$ now represent the average total dipole GSF and γ-transmission coefficient, respectively. Using a χ^2-minimization technique [30], it is possible to extract simultaneously the NLD and GSF from the quasicontinuum region in the first-generation matrix. For ^{166}Ho, the region between $E_x^{\min} = 1200$ keV, $E_x^{\max} = 6000$ keV, and $E_\gamma^{\min} = 1350$ keV was selected. This minimization technique is able to determine the functional, un-normalized form of the NLD and the GSF,

$$\tilde{\rho}(E_x - E_\gamma) = A e^{\alpha(E_x - E_\gamma)} \rho(E_x - E_\gamma), \quad (8a)$$

$$\tilde{\mathcal{T}}(E_\gamma) = B e^{\alpha E_\gamma} \mathcal{T}(E_\gamma), \quad (8b)$$

meaning that any value combination for the parameters A, B, and α would give a NLD and GSF pair compatible with the experimental results [30]. In order to fix the values of these three parameters, we have to normalize the two physical quantities by using known experimental data.

III. NORMALIZATION AND UNCERTAINTY PROPAGATION

A. Level density

The unnormalized NLD has two free parameters, A and α, so we need at least two external data points in order for these to be determined. Experimental values for the low

TABLE I. Parameters used for the NLD normalization. σ_I^2 is calculated using either the RMI model of Eq. (10) or the FG model of Eq. (11), combined with the temperature expressions of either the CFG formula of Eq. (12) or the AFG formula of Eq. (13). For both, the values of $a = 18.277$ MeV^{-1} and $E_1 = -0.949$ MeV for ^{166}Ho from the global parametrization of Refs. [40,41] were used. Finally, $\rho(S_n)$ was calculated for each σ_I^2 using the expression given in Eq. (9) where $I_t = 7/2$ and $D_0 = 4.35(15)$ eV [39].

Model	σ_I^2	$\rho(S_n)$ ($\times 10^6$ MeV^{-1})
RMI + AFG	6.93	3.28
FG + CFG	5.55	2.32

excitation-energy region in ^{166}Ho can be obtained by using the known discrete excitation-energy levels from Ref. [38]. In our case we observe a good fit for the region between $E_x = 0.26$ and 0.74 MeV, which we use for our normalization. At high excitation energies, we can calculate the total NLD value at the neutron separation energy S_n by using the measured level spacing D_0 of s-wave neutron resonances from, e.g., *Atlas of Neutron Resonances* [39]. We calculate the total NLD at S_n by [30]

$$\rho(S_n) = \frac{2\sigma_I^2}{D_0 \left[(I_t + 1) e^{-(I_t+1)^2/2\sigma_I^2} + I_t e^{-I_t^2/2\sigma_I^2} \right]}, \quad (9)$$

where I_t is the spin of the target nucleus and σ_I is the spin cutoff parameter. The σ_I parameter must be estimated, which means we must assume a model for the spin distribution. Some well-known models include using the rigid-body moment of inertia (RMI) [40,41]

$$\sigma_I^2 = 0.0146 A^{5/3} T \quad (10)$$

and the Fermi gas (FG) model from Gilbert and Cameron [42],

$$\sigma_I^2 = 0.0888 A^{2/3} a T, \quad (11)$$

where A here is the nucleon number, a is the level density parameter, and T represents the nuclear temperature. The T parameter can be expressed by either the Gilbert and Cameron approach (CFG) [42],

$$T = \sqrt{U/a}, \quad (12)$$

or the formalism developed by von Egidy and Bucurescu (AFG) [40,41],

$$T = \frac{1 + \sqrt{1 + 4aU}}{2a}, \quad (13)$$

where in both cases $U = E_x - E_1$, where E_1 is a shift parameter. The parameters a and E_1 for ^{166}Ho are calculated using the prescription of Refs. [40,41]: $a = 18.277$ MeV^{-1} and $E_1 = -0.949$ MeV for both models of the T parameter. As we have no reason to prefer one model above the other, we allow σ_I^2 to vary between 5.55 and 6.93. These values are listed in Table I. The chosen σ_I^2 uncertainty limits are reasonable when compared to the results of Uhrenholt *et al.* [23], where a study on ^{162}Dy shows that the ratio between the spin cutoff parameter at S_n from their combinatorial method and

the one calculated using the RMI model is 0.9, compared to 0.8 and 1.0 corresponding to the lower and upper limits we have chosen for ^{166}Ho.

Since any value between the two limits for σ_I^2 is, in principle, equally possible, we assume that the $\rho(S_n)$ error is flatly distributed between the values obtained by using the two σ_I^2 values in Eq. (9), as shown in Table I. The edges of the flat distribution are then smoothed with a Gaussian with a standard deviation calculated by propagating the uncertainties in the D_0 parameter. We obtain thus a flatly distributed $\rho(S_n)$ between 2.32×10^6 and 3.28×10^6 MeV^{-1}, with a lower error of 0.08×10^6 MeV^{-1} and an upper error of 0.12×10^6 MeV^{-1}.

Further, we need to extrapolate the experimental $\rho(E_x)$ data to S_n. In order to do this, we have considered two models. The first one is the constant-temperature (CT) model [42,43]:

$$\rho_{CT}(E_x) = \frac{1}{T_{CT}} \exp\left(\frac{E_x - E_0}{T_{CT}}\right), \tag{14}$$

where E_0 and T_{CT} are parameters representing the energy shift and the nuclear temperature, respectively. The second is the back-shifted Fermi gas (BSFG) model [42,44]:

$$\rho_{FG}(E_x) = \frac{\exp(2\sqrt{aU})}{12\sqrt{2}a^{1/4}U^{5/4}\sigma_I}, \tag{15}$$

where σ_I is the spin cutoff parameter, a is the level-density parameter, and $U = E_x - E_1$, where E_1 is the back-shift parameter. For convenience, we introduce an additional scaling parameter η in order to make the model reproduce the experimentally derived $\rho(S_n)$. For the best fit, η was found to be 0.507. While the NLD normalization parameters A and α are determined through the normalization procedure, the choice between the CT or the BSFG model comes down to the functional form of the experimental NLD data. While the CT model has a simple, exponential shape, the BSFG model is somewhat more curved due to the $\sim\sqrt{E_x}$ dependence. In order to decide which NLD model describes the experimental data best, we use an approach similar to that used in Guttormsen *et al.* [45] for ^{164}Dy. Here we run a χ^2 test for each model, where the model parameters are allowed to vary in order to minimize the χ^2 score. While the parameter values and the magnitudes of the χ^2 scores depend on the choice of A and α, the relationship between the χ^2 scores for the two models should not change, as this only depends on the functional shape of the NLD. The test gives a better χ^2 for the BSFG model by a factor of 1.5; therefore, this model is chosen for the extrapolation in the normalization procedure. Using a technique similar to the one presented in Ref. [46], we can propagate the normalization uncertainties to the whole NLD. By generating different NLDs with different combinations of the A and α parameters, we evaluate their goodness-of-fit to the selected region at low excitation energy and the calculated $\rho(S_n)$ by estimating a χ^2 score. For each E_x bin, we have many different $\rho(E_x)$ values, each with an associated χ^2 score. By plotting the χ^2 scores against $\rho(E_x)$ for each E_x bin, we can observe a parabolalike shape, from which we can graphically estimate the mean value of $\rho(E_x)$ to be the one for which $\chi^2 = \chi^2_{\min}$, and the associated uncertainty where the $\chi^2 = \chi^2_{\min} + 1$ line crosses the parabola
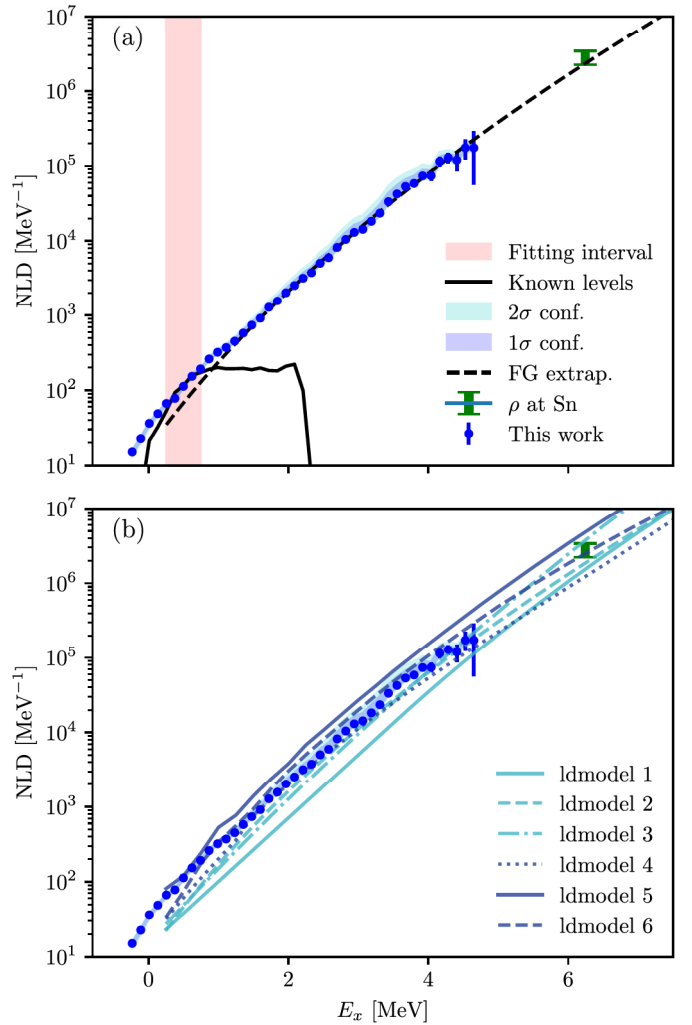
FIG. 2. The normalized NLD data points (see text). The uncertainties in the data points show the statistical and systematic uncertainties from the Oslo method analysis. In the total uncertainty band the systematic errors from the normalization are included. In panel (a), the normalized ^{166}Ho NLD is shown together with the fitting interval, the known levels, and the Fermi gas extrapolation to $\rho(S_n)$, while in panel (b) the same NLD is compared to the theoretical models from TALYS 1.95 [47,48]. The values are given as number of energy levels per MeV bin, where, e.g., the value at $E_x = 2$ MeV indicates the number of energy levels in the 1-MeV E_x interval between 1.5 and 2.5 MeV. This means that nonzero values for the NLD are expected down to $E_x = -0.5$ MeV, the last one including the ground-state level at $E_x = 0$ MeV.

(see Ref. [46] for details). The normalized NLD is shown in Fig. 2.

B. Gamma strength function

For the GSF, the parameter B in Eq. (8b) is found by normalizing it to the average total radiative width $\langle \Gamma_\gamma \rangle$ [32,49]. Experimental values for this quantity are available in Ref. [39], where for ^{166}Ho we find 84 ± 5 meV. The average total radiative width of s-wave neutron capture resonances with spins $I_t \pm 1/2$ expressed in terms of the

FIG. 3. The normalized GSF data points (see text). Here we include a comparison to the theoretical models (strength 1 to strength 8) used in TALYS 1.95 [47,48]. Uncertainties are displayed as in Fig. 2.

experimental $\mathcal{T}$ is given by

$$\langle \Gamma_\gamma (S_n, I_t \pm 1/2, \pi_t) \rangle$$

$$= \frac{B}{4\pi \rho(S_n, I_t \pm 1/2, \pi_t)} \int_{E_\gamma = 0}^{S_n} dE_\gamma \mathcal{T}(E_\gamma) \rho(S_n - E_\gamma)$$

$$\times \sum_{J=-1}^{1} g(S_n - E_\gamma, I_t \pm 1/2 + J), \qquad (16)$$

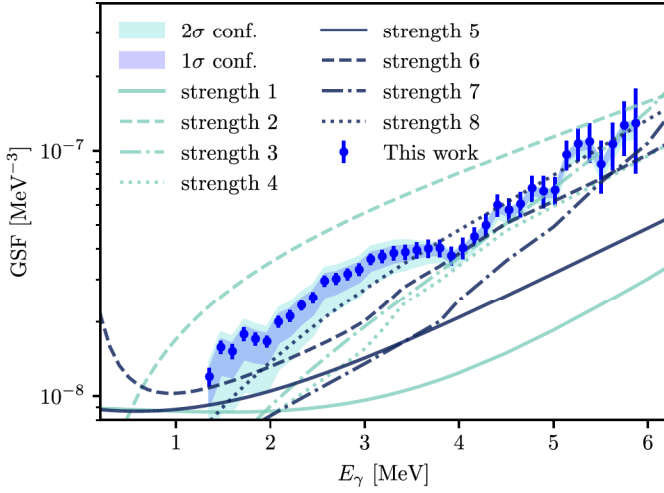where I_t and π_t are the spin and parity of the target nucleus in the (n, γ) reaction, and $\rho(S_n - E_\gamma)$ is the experimental level density. Here it is assumed that there are equally many accessible levels with positive and negative parity for any excitation energy and spin, and again that dipole radiation is the dominant decay mechanism. Note that the factor $1/\rho(S_n, I_t \pm 1/2, \pi_t)$ equals the neutron resonance spacing D_0. By assuming the uncertainty in $\langle \Gamma_\gamma \rangle$ to be normally distributed such that the given number represents one standard deviation from the mean, we can again use the same procedure as for the NLD used in Ref. [46] to propagate these uncertainties to the GSF. The results are shown in Fig. 3.

IV. RESULTS AND DISCUSSION

As anticipated from the NLD normalization discussed in Sec. III, the experimental ^{166}Ho NLD was found to be better described by the BSFG model than by the CT model. In Fig. 2 we present the normalized experimental NLD data together with the six theoretical models provided in TALYS 1.95 [47,48], where ldmodel 1, ldmodel 2, and ldmodel 3 are phenomenological models, and ldmodel 4, ldmodel 5, and ldmodel 6 are microscopical. For the three microscopical models the default values for c and δ were used, these being the two parameters for which the models can be adjusted to data. Although none of the models fits perfectly, we observe that the experimental data fall somewhat in the middle of the different suggested models. Overall, our data

points behave rather smoothly, as can be expected for an odd-odd nucleus with many available levels. In general, the GSF shows various features with different electromagnetic characters. Most notably for the energy region of this work ($E_\gamma \approx 1$ to 6 MeV), we expect the tail of the giant electric dipole resonance (GEDR, [50,51]), possibly the pygmy dipole resonance (PDR), (both of $E1$ character [52,53]), the spin-flip resonance, and the SR (both of $M1$ character [8]) to be present. As the Oslo method does not separate between $E1$ and $M1$ transitions, the GSF must be decomposed using models and/or auxiliary data. Figure 3 shows the GSF plotted together with the different theoretical models available in TALYS. Our data points are not well reproduced by any of the TALYS models, although an agreement when it comes to magnitude can be observed with the microscopic Gogny-HBF+QRPA model strength 8 [54]. Most of the models fail in predicting enough strength to match the experimental results, and none of them are able to describe properly the broad bump centered around $E_\gamma \approx 3$ MeV. The GSF in the $E_\gamma < S_n$ region is expected to be dominated by the tails of the GEDR and the PDR, as observed in the neighboring dysprosium isotopes [6]. Another interesting feature is the broad, resonancelike structure centered around $E_\gamma \approx 3$ MeV, which is a good candidate for the $M1$ scissors mode. This is the first observation of the mode in an odd-odd rare-earth nucleus with the Oslo method. In order to quantify the observed structures, the experimental GSF was decomposed into its constituent features. As for Dy isotopes and other deformed, rare-earth nuclei, we expect the GEDR of ^{166}Ho to be double-peaked [50,51]. Experimental GSF data for $E_\gamma > S_n$ for ^{166}Ho are not available, so data on ^{165}Ho have been used. There are data in the literature for this energy region from Berman *et al.* [55] and Bergère *et al.* [56], but their measured cross sections differ considerably. In order to resolve this conflict, a reanalysis of the two experiments has been carried out by Varlamov *et al.* [57], and the data from this re-evaluation have been used to model the $E1$ strength due to the GEDR. In order to fit the GEDR, a generalized Lorentzian (GLO) [37] is used:

$$f^{\mathrm{GLO}}(E_\gamma) = \frac{\sigma_0 \Gamma_0}{3\pi^2 \hbar^2 c^2} \left(\frac{E_\gamma \Gamma_K}{\left(E_\gamma^2 - E_0^2\right)^2 + E_\gamma^2 \Gamma_K^2} + 0.7 \frac{\Gamma_{K,0}}{E_\gamma^3} \right), \qquad (17)$$

where

$$\Gamma_K(E_\gamma, T_f) = \frac{\Gamma_0}{E_0^2} \left(E_\gamma^2 + 4\pi^2 T_f^2\right) \qquad (18)$$

and $\Gamma_{K,0} = \Gamma_K(0, T_f)$. E_0, Γ_0, σ_0, and T_f are fit parameters representing the energy centroid, the width, the peak cross section, and the temperature of the final levels, respectively. The PDR and the scissors mode are fitted using a standard Lorentzian (SLO),

$$f^{\mathrm{SLO}}(E_\gamma) = \frac{1}{3\pi^2 \hbar^2 c^2} \frac{\sigma_s \Gamma_s^2 E_\gamma}{\left(E_\gamma^2 - E_s^2\right)^2 + E_\gamma^2 \Gamma_s^2}, \qquad (19)$$

where E_s, Γ_s, and σ_s are again free parameters corresponding to the same quantities as for Eq. (17). In some other studies of the rare-earth region (see, e.g., Ref. [6]), a second $E1$ PDR was included in the fit, as well as the spin-flip $M1$ resonance.

The GLO already gives us a good fit of the GEDR without having to include these two structures, whose contribution is only noticeable in the $E_\gamma \approx 10$ MeV energy region, well beyond the range of this experiment. Our choice of fit functions reduces considerably the number of free parameters used in the fit.

Another interesting quantity to calculate is the experimental, integrated upward SR strength B_{SR}, defined as

$$B_{SR} = \frac{(3\hbar c)^3}{16\pi} \int f_{SR}(E_\gamma)dE_\gamma, \qquad (20)$$

where f_{SR} is expressed by the fitted SLO in Eq. (19) to the broad structure at $E_\gamma \approx 3$ MeV. The result of the integration depends on the chosen limits, which should vary according to which work or experimental technique the result is to be compared with. Many NRF experiments have limited E_γ range and thus a smaller summed B_{SR}. When it comes to Oslo-method-like analyses, the decomposition of the GSF into two GEDR peaks (henceforth GEDR1 and GEDR2), a PDR and an SR, involves a series of challenges not only due to the high number of parameters involved but also because of the fact that OCL data cannot directly distinguish between $E1$ and $M1$ radiation. This is a particular problem for the SR, as its fit result is sensitive to the fitting parameters of the underlying $E1$ strength. In this work we show how we can attempt to solve these problems using three different methods. This provides us with a comparison of the different methods, as well as a tool in order to evaluate the uncertainties for the resulting B_{SR}. The first method (the "simultaneous fit") is to fit all of the structures (the two peaks of the GEDR, the PDR and the SR) simultaneously. This gives the least χ^2 score, but also potentially underestimates the $E1$ strength yielding a potentially too big B_{SR}. The second method (the "two-step fit") involves a fit of the GEDR first and a subsequent fit of the PDR and the SR by holding the newly found GEDR parameters fixed. This gives a higher χ^2 score, but a B_{SR} closer to previously determined values in this mass region. One of the most sensible parameters in the fit is the temperature T_0. In both methods, the fit was run by holding the temperature fixed to either $T = 0.59$ MeV or $T = 0.66$ MeV, these corresponding to the calculated values from von Egidy and Bucurescu [40] for the CT and BSFG models, respectively. The resulting parameters from the first two fitting methods are shown in Table II, where method 1 corresponds to the simultaneous fit, method 2 corresponds to the two-steps fit, and (A) and (B) both indicate whether the CT value or the BSFG value for the temperature parameter was used. Figure 4 shows the obtained decomposition using method 2(A) as an example.

The third method (the "exponential background fit"), used among others by Nyhus *et al.* [4], Malatji *et al.* [60], and Agvaanluvsan *et al.* [19] involves approximating the $E1$ strength "background" as an exponential function of the form Ae^{cE_γ}, where A and c are parameters to be tuned to make the function go through the two points estimated to be the end points of the SR. When the background is subtracted, the excess strength can be integrated numerically to find B_{SR} (see Fig. 5). This last method does not involve a fit to the SR and thus gives no E_s, Γ_s, and σ_s parameters to compare to other works, but it

TABLE II. The parameters for the functions fitting the ^{166}Ho GSF (see text) Method 1 refers to the "simultaneous fit," while Method 2 refers to the "two-step fit." The labels (A) and (B) refer to the different choices in temperature.

Method	Function	T_0 (MeV)	$E_{0,s}$ (MeV)	$\Gamma_{0,s}$ (MeV)	$\sigma_{0,s}$ (mb)
1(A)	GEDR1	0.59	12.359(1)	3.35(3)	324(1)
	GEDR2	0.59	14.78(1)	1.89(3)	189(2)
	PDR		5.92(8)	1.96(12)	4.4(3)
	SR		3.14(7)	0.98(9)	0.43(3)
1(B)	GEDR1	0.66	12.341(1)	3.22(3)	330(1)
	GEDR2	0.66	14.78(1)	1.89(3)	195(2)
	PDR		5.58(40)	1.40(10)	3.8(3)
	SR		3.18(7)	0.80(4)	0.44(3)
2(A)	GEDR1	0.59	12.40(12)	3.50(4)	323(3)
	GEDR2	0.59	14.80(15)	1.82(2)	183(2)
	PDR		6.07(11)	1.89(3)	5.0(2)
	SR		3.20(12)	1.00(30)	0.40(8)
2(B)	GEDR1	0.66	12.38(12)	3.37(3)	330(3)
	GEDR2	0.66	14.79(15)	1.82(2)	188(2)
	PDR		5.48(17)	1.06(2)	4.1(9)
	SR		3.29(12)	0.98(26)	0.43(8)

gives perhaps the most reasonable estimate for the lowest limit of B_{SR}. An argument in support of this third approach is that the $E1$ modeling is not dependent on the description of the GEDR peaks and the PDR, and also because an SLO fit may not always be the best tool to describe a structure that is often fragmented and not necessarily resonance-shaped. However, the resulting integrated SR strength is indeed dependent on the choice of the two points enclosing the SR structure used
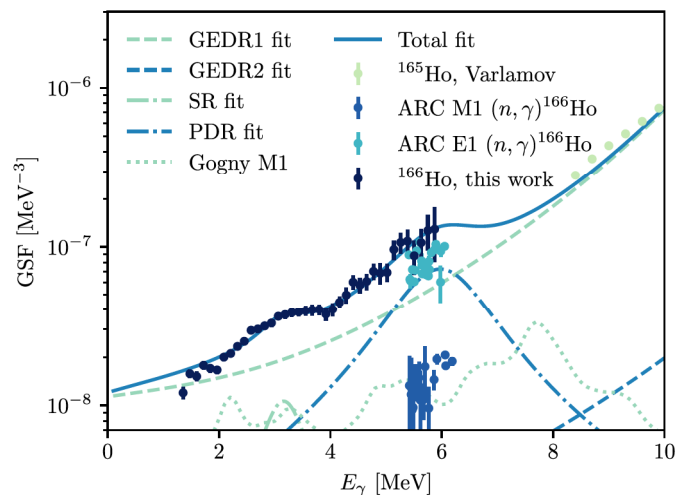
FIG. 4. Decomposition of the GSF into its underlying structures, using method 2(A), where the ^{165}Ho data for $E_\gamma > 6$ MeV from Varlamov *et al.* [57] were used to fit the double-peaked GEDR. The dotted line is the theoretical prediction from the deformed-basis QRPA calculations for $M1$ excitations on the ground state [58] and is compared to the average resonance capture (ARC) data from Ref. [59] for both $E1$ and $M1$ transitions.
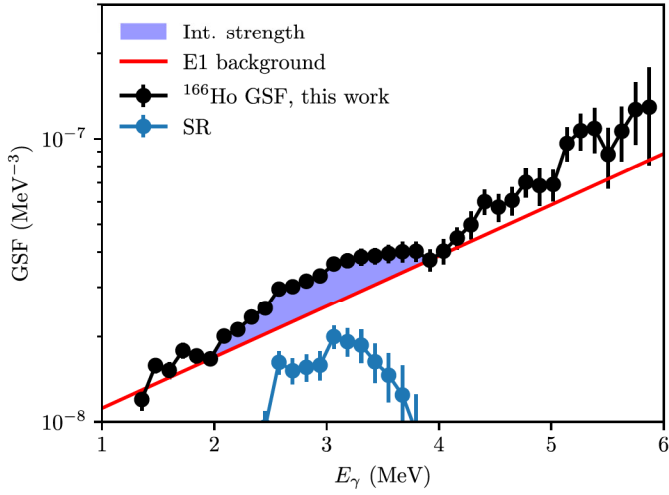
FIG. 5. The SR integrated strength evaluated by selecting the energy range of the SR and modeling the $E1$ background as an exponential going through the two outermost GSF points (see text). Shown in black are the data from the present work, in red (dark gray) the modeled $E1$ background as an exponential, and in blue (lighter gray) the residual strength obtained by subtracting the $E1$ component from the GSF data. This plot corresponds to the $E1$ fitting for method 3(B).

to fit the exponential background. Although the choice for the upper limit might fall naturally in the "kink" of the GSF at about $E_\gamma \approx 4$ MeV, the lower limit is more difficult to determine unambiguously. In order to reflect this uncertainty, we have calculated B_{SR} using two different exponential "background" fits, one choosing the first fitting point to be at $E_\gamma = 1.6$ MeV and the other at $E_\gamma = 2.0$ MeV. We denote these two variants of the third method as method 3(A) and method 3(B), respectively.

In Table III the fitting parameters for the different fits of the SR are shown, together with the calculated summed strengths B_{SR} for both the integration range $E_\gamma = 2.0$–4.0 MeV (comparable to the one used in NRF experiments) and the integration range $E_\gamma = 0.0$–10.0 MeV (for a more complete B_{SR} integration).

These results can be compared to those for neighboring isotopes. As many other nuclei have been analyzed using the Oslo method, we have the possibility to systematically study the different centroids, widths, and peak cross sections of the SR fitted by SLOs for the rare-earth region. In Fig. 6 are collected the results for Nd [63], Sm [18,60–62,64], Dy [6],

TABLE III. The integrated SR strengths for both the $E_\gamma = 2.0$–4.0 MeV range and the $E_\gamma = 0.0$–10.0 MeV range (see text).

Method	$B_{SR}^{2.0-4.0}$ (μ_N^2)	$B_{SR}^{0.0-10.0}$ (μ_N^2)
1(A)	3.3(4)	4.2(5)
1(B)	2.9(2)	3.5(3)
2(A)	3.1(15)	4.0(15)
2(B)	3.2(10)	4.1(14)
3(A)	2.9(5)	3.0(6)
3(B)	3.1(6)	3.2(6)
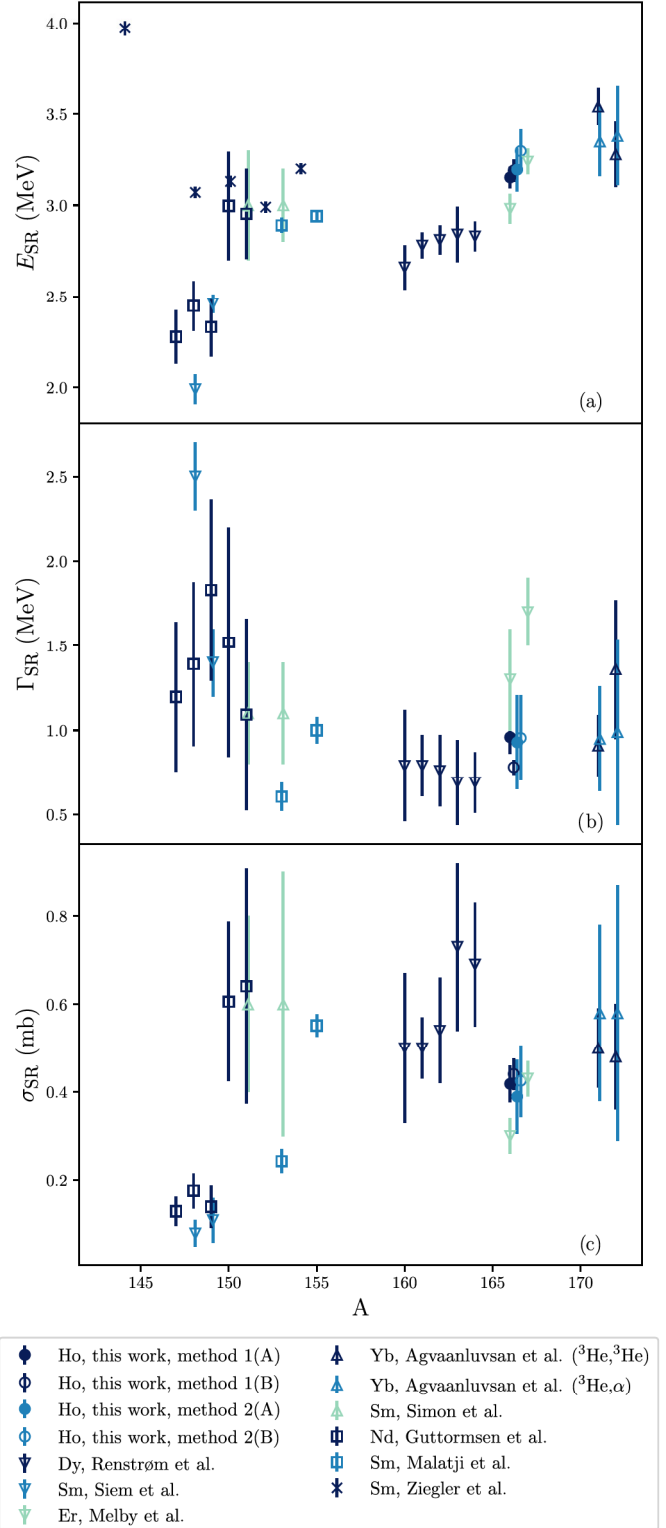
FIG. 6. Plot showing the values of the SLO fitting parameters for the SR collected for different deformed rare-earth nuclei (Refs. [6,17–19,60–64]), where panel (a) shows the centroids, panel (b) shows the widths, and panel (c) show the cross sections. Data obtained using the Oslo method are shown with triangles and squares, while a cross indicates another experiment modality (e.g., NRF). The results from the present work are shown with empty and solid circles.
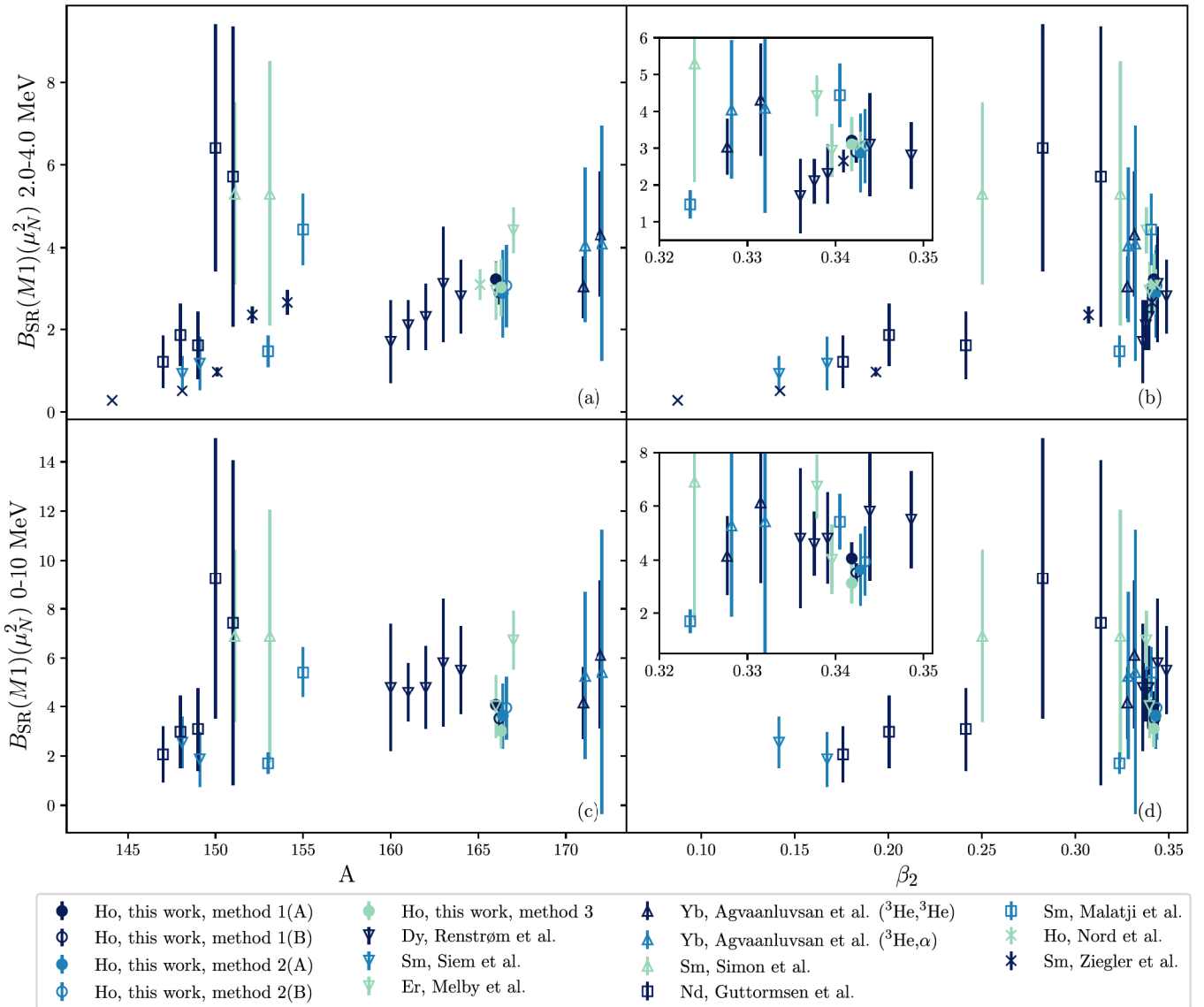
FIG. 7. In these graphs the SR strength B_{SR} collected from Refs. [6,13,17–19,60,62–64] is integrated between two regions: $E_\gamma = 2.0$–4.0 MeV in panels (a) and (b), and $E_\gamma = 0.0$–10.0 MeV in panels (c) and (d), and is plotted against the mass number in panels (a) and (c) and against the deformation parameter β_2 in panels (b) and (d) (region where $0.32 \leqslant \beta_2 \leqslant 0.35$ in the smaller inset plots). Circles, triangles, and squares indicate Oslo method data, and crosses indicate other experimental or analytical techniques (e.g., NRF). The data from Ziegler *et al.* [64] are integrated between 0 and 5 MeV.

Er [17], and Yb [19], where the results from Ziegler *et al.* [64] are results from a NRF experiment and only provide the energy centroid information. Together with these, the results for ^{166}Ho from the present work are included. There is no very clear pattern emerging from the plots in Fig. 6, as the results generally seem to be scattered. Nevertheless, in Fig. 6(a) we observe that the values for E_{SR} increase until $A \approx 150$, then remain constant, and finally increase again from about $E_{SR} \approx 2.7$ MeV for ^{160}Dy to $E_{SR} \approx 3.4$ MeV for ^{172}Yb. The results from this work fit nicely between those for dysprosium by Renstrøm *et al.* [6], erbium by Melby *et al.* [17], and ytterbium by Agvaanluvsan *et al.* [19]. This pattern does not correspond to what we would expect from the study by Enders *et al.* [12], which describes a constant or slowly decreasing value for E_{SR} between 3 and 3.5 MeV. Theoretical predictions for E_{SR} can

be obtained using the sum-rule approach [65], following the procedure in Ref. [12] replacing the ground-state moment of inertia with the rigid-body moment of inertia (following the same steps as in Guttormsen *et al.* [21]). From this approach a value of $E_{SR} = 2.89$ MeV is found by using $\beta_2 = 0.342$ as a value for the deformation, the average of those listed for ^{164}Dy and ^{168}Er in Ref. [66]. This is close but lower than the evaluated errors for all four values listed in Table II. Using the value from the FRDM evaluation by Möller *et al.* [67], $\beta_2 = 0.296$, we obtain an even lower value of $E_{SR} = 2.55$ MeV. The width Γ_{SR} and the peak cross section σ_{SR} are also plotted in Figs. 6(b) and 6(c), respectively. Here results are more scattered, although a possibly decreasing trend could be noticed for Γ_{SR}, and a possibly increasing one could be noticed for σ_{SR}.

In Fig. 7 are shown the SR strengths for two different integration intervals: $E_\gamma = 2.0$–4.0 MeV and $E_\gamma = 0.0$–10.0 MeV) calculated by means of Eq. (20). These are in turn plotted against the mass number A and the deformation parameter β_2 retrieved from the evaluations in the *Atomic Data and Nuclear Data Tables* of Ref. [66]. The data for odd nuclei were obtained by averaging between neighboring even-even nuclei. These values were preferred to the FRDM evaluation by Möller *et al.* [67] as the latter tends to systematically undervalue the values calculated from $B(E2)$ experimental values. In Fig. 7 the calculated data from ^{166}Ho are plotted in five solid or empty circles, where the value for method 3 is the average of (A) and (B) (see Table III). Again we can compare to the plots in Enders *et al.* [12], where in Fig. 4 we notice how B_{SR} increases sharply at $A \approx 150$ from 1 to $3.5\,\mu_N^2$, remains somewhat constant until $A \approx 170$ when it starts to slowly diminish. The data collected in Enders *et al.* [12] have a limited integration range (2.5 to 4.0 MeV), so it is best compared to Fig. 7(a). Although one might argue that the data may show an increase at around $A = 150$, these go all the way up to $6\,\mu_N^2$ for Nd and Sm isotopes, and no flat or diminishing pattern is observed afterwards. Figure 7(c) shows the whole integrated SR strength, and again, although the pattern may seem similar to Fig. 4 in Enders *et al.* [12], the values are much larger. A different pattern appears when B_{SR} is plotted against deformation in Figs. 7(b) and 7(d). In both, and more clearly in Fig. 7(d), we notice how the strength increases gradually with deformation and reaches an apparent top at $\beta_2 \approx 0.28$, before decreasing. Many of the collected data sets agree in the value of B_{SR} at $\beta_2 \approx 0.34$. The experimental B_{SR} for ^{166}Ho can be again compared to the theoretical one obtained with the sum-rule approach, from which we obtain a value of $B_{SR} = 7.9\mu_N^2$ using $\beta_2 = 0.342$ from Ref. [66], a value above the upper error limit for all methods. The same conclusion is reached by using the possibly undervalued evaluated deformation $\beta_2 = 0.296$ from Ref. [67], where the value $B_{SR} = 6.9\mu_N^2$ is obtained.

V. SUMMARY

In this work the data from the ^{163}Dy$(\alpha, p\gamma)\,^{166}$Ho experiment were analyzed using the Oslo method, and the NLD and GSF for ^{166}Ho were extracted. The resulting GSF presents typical features of a rare-earth, deformed, neutron-rich nucleus, such as a pygmy resonance at $E_\gamma \approx 6$ MeV and a peak compatible to the $M1$ scissors resonance at 3 MeV. This is the first time such a structure has been observed in an odd-odd nucleus with the Oslo method, confirming previous observations in ^{160}Tb where the two-step cascade method was used [9]. The SR strength has been extracted using three different methods, and while there is a spread in the measured values, they all yield results compatible to nuclei of similar mass number, and even more so to nuclei of similar deformation.

[1] J. P. Delaroche, M. Girod, J. Libert, H. Goutte, S. Hilaire, S. Péru, N. Pillet, and G. F. Bertsch, Structure of even-even nuclei using a mapped collective Hamiltonian and the D1S Gogny interaction, Phys. Rev. C **81**, 014303 (2010).

[2] M. Guttormsen, J. Rekstad, A. Henriquez, F. Ingebretsen, and T. F. Thorsteinsen, Nonstatistical Cooling of the Highly Excited ^{161}Dy Nucleus, Phys. Rev. Lett. **52**, 102 (1984).

[3] M. Guttormsen, A. Bagheri, R. Chankova, J. Rekstad, S. Siem, A. Schiller, and A. Voinov, Thermal properties and radiative strengths in ^{160,161,162}Dy, Phys. Rev. C **68**, 064306 (2003).

[4] H. T. Nyhus, S. Siem, M. Guttormsen, A. C. Larsen, A. Bürger, N. U. H. Syed, G. M. Tveten, and A. Voinov, Radiative strength functions in ^{163,164}Dy, Phys. Rev. C **81**, 024325 (2010).

[5] H. T. Nyhus, S. Siem, M. Guttormsen, A. C. Larsen, A. Bürger, N. U. H. Syed, H. K. Toft, G. M. Tveten, and A. Voinov, Level density and thermodynamic properties of dysprosium isotopes, Phys. Rev. C **85**, 014323 (2012).

[6] T. Renstrøm, H. Utsunomiya, H. T. Nyhus, A. C. Larsen, M. Guttormsen, G. M. Tveten, D. M. Filipescu, I. Gheorghe, S. Goriely, S. Hilaire, Y.-W. Lui, J. E. Midtbø, S. Péru, T. Shima, S. Siem, and O. Tesileanu, Verification of detailed balance for γ absorption and emission in Dy isotopes, Phys. Rev. C **98**, 054310 (2018).

[7] N. Lo Iudice and F. Palumbo, New Isovector Collective Modes in Deformed Nuclei, Phys. Rev. Lett. **41**, 1532 (1978).

[8] K. Heyde, P. von Neumann-Cosel, and A. Richter, Magnetic dipole excitations in nuclei: Elementary modes of nucleonic motion, Rev. Mod. Phys. **82**, 2365 (2010).

[9] J. Kroll, F. Bečvář, M. Krtička, and I. Tomandl, Photon strength functions of ^{160}Tb from the two-step gamma cascade measurement, Int. J. Mod. Phys. E **20**, 526 (2011).

[10] N. Huxel, P. von Brentano, J. Eberth, J. Enders, R.-D. Herzberg, P. von Neumann-Cosel, N. Nicolay, N. Pietralla, H. Prade, C. Rangacharyulu, J. Reif, A. Richter, C. Schlegel, R. Schwengner, S. Skoda, H. G. Thomas, I. Wiedenhöver, G. Winter, and A. Zilges, Complete scissors mode strength in heavy deformed odd-mass nuclei: a case study of ^{165}Ho and ^{169}Tm, Nucl. Phys. A **645**, 239 (1999).

[11] N. Pietralla, P. von Brentano, R.-D. Herzberg, U. Kneissl, N. Lo Iudice, H. Maser, H. H. Pitz, and A. Zilges, Systematics of the excitation energy of the 1^+ scissors mode and its empirical dependence on the nuclear deformation parameter, Phys. Rev. C **58**, 184 (1998).

[12] J. Enders, P. von Neumann-Cosel, C. Rangacharyulu, and A. Richter, Parameter-free description of orbital magnetic dipole strength, Phys. Rev. C **71**, 014306 (2005).

[13] A. Nord, J. Enders, A. E. de Almeida Pinto, D. Belic, P. von Brentano, C. Fransen, U. Kneissl, C. Kohstall, A. Linnemann, P. von Neumann-Cosel, N. Pietralla, H. H. Pitz, A. Richter, F. Stedile, and V. Werner, Low-energy photon scattering experiments of ^{151,153}Eu, ^{163}Dy, and ^{165}Ho and the systematics of the *M*1 scissors mode in odd-mass rare-earth nuclei, Phys. Rev. C **67**, 034307 (2003).

[14] M. Krtička, F. Bečvář, J. Honzátko, I. Tomandl, M. Heil, F. Käppeler, R. Reifarth, F. Voss, and K. Wisshak, Evidence for *M*1 Scissors Resonances Built on the Levels in the Quasicontinuum of ^{163}Dy, Phys. Rev. Lett. **92**, 172501 (2004).

[15] A. Schiller, A. Voinov, E. Algin, J. Becker, L. Bernstein, P. Garrett, M. Guttormsen, R. Nelson, J. Rekstad, and S. Siem, Low-energy *M*1 excitation mode in 172Yb, Phys. Lett. B **633**, 225 (2006).

[16] S. Valenta, B. Baramsai, T. A. Bredeweg, A. Couture, A. Chyzh, M. Jandel, J. Kroll, M. Krtička, G. E. Mitchell, J. M. O'Donnell, G. Rusev, J. L. Ullmann, and C. L. Walker, Examination of photon strength functions for ^{162,164}Dy from radiative capture of resonance neutrons, Phys. Rev. C **96**, 054315 (2017).

[17] E. Melby, M. Guttormsen, J. Rekstad, A. Schiller, S. Siem, and A. Voinov, Thermal and electromagnetic properties of ^{166}Er and ^{167}Er, Phys. Rev. C **63**, 044309 (2001).

[18] S. Siem, M. Guttormsen, K. Ingeberg, E. Melby, J. Rekstad, A. Schiller, and A. Voinov, Level densities and γ-strength functions in ^{148,149}Sm, Phys. Rev. C **65**, 044318 (2002).

[19] U. Agvaanluvsan, A. Schiller, J. A. Becker, L. A. Bernstein, P. E. Garrett, M. Guttormsen, G. E. Mitchell, J. Rekstad, S. Siem, A. Voinov, and W. Younes, Level densities and γ-ray strength functions in ^{170,171,172}Yb, Phys. Rev. C **70**, 054611 (2004).

[20] M. Guttormsen, L. A. Bernstein, A. Bürger, A. Görgen, F. Gunsing, T. W. Hagen, A. C. Larsen, T. Renstrøm, S. Siem, M. Wiedeking, and J. N. Wilson, Observation of Large Scissors Resonance Strength in Actinides, Phys. Rev. Lett. **109**, 162503 (2012).

[21] M. Guttormsen, L. A. Bernstein, A. Görgen, B. Jurado, S. Siem, M. Aiche, Q. Ducasse, F. Giacoppo, F. Gunsing, T. W. Hagen, A. C. Larsen, M. Lebois, B. Leniau, T. Renstrøm, S. J. Rose, T. G. Tornyi, G. M. Tveten, M. Wiedeking, and J. N. Wilson, Scissors resonance in the quasicontinuum of Th, Pa, and U isotopes, Phys. Rev. C **89**, 014302 (2014).

[22] T. G. Tornyi, M. Guttormsen, T. K. Eriksen, A. Görgen, F. Giacoppo, T. W. Hagen, A. Krasznahorkay, A. C. Larsen, T. Renstrøm, S. J. Rose, S. Siem, and G. M. Tveten, Level density and γ-ray strength function in the odd-odd ^{238}Np nucleus, Phys. Rev. C **89**, 044323 (2014).

[23] H. Uhrenholt, S. Åberg, A. Dobrowolski, T. Døssing, T. Ichikawa, and P. Möller, Combinatorial nuclear level-density model, Nucl. Phys. A **913**, 127 (2013).

[24] D. M. Brink, Doctoral thesis, some aspects of the interaction of fields with matter, Oxford University, 1955.

[25] P. Axel, Electric dipole ground-state transition width strength function and 7-MeV photon interactions, Phys. Rev. **126**, 671 (1962).

[26] F. Zeiser, G. M. Tveten, F. L. Bello Garrote, M. Guttormsen, A.-C. Larsen, V. W. Ingeberg, A. Görgen, and S. Siem, The γ-ray energy response of the Oslo Scintillator Array OSCAR, Nucl. Instrum. Methods Phys. Res., Sect. A **985**, 164678 (2021).

[27] M. Guttormsen, A. Bürger, T. E. Hansen, and N. Lietaer, Nucl. Instrum. Methods Phys. Res., Sect. A **648**, 168 (2011).

[28] M. Guttormsen, T. Tveter, L. Bergholt, F. Ingebretsen, and J. Rekstad, The unfolding of continuum γ-ray spectra, Nucl. Instrum. Methods Phys. Res., Sect. A **374**, 371 (1996).

[29] M. Guttormsen, T. Ramsøy, and J. Rekstad, The first generation of γ-rays from hot nuclei, Nucl. Instrum. Methods Phys. Res., Sect. A **255**, 518 (1987).

[30] A. Schiller, L. Bergholt, M. Guttormsen, E. Melby, J. Rekstad, and S. Siem, Extraction of level density and γ strength function from primary γ spectra, Nucl. Instrum. Methods Phys. Res., Sect. A **447**, 498 (2000).

[31] F. Zeiser and G. M. Tveten, oslocyclotronlab/OCL_GEANT4: Geant4 model of OSCAR, 2020, https://doi.org/10.5281/zenodo.4018494.

[32] A. C. Larsen, M. Guttormsen, M. Krtička, E. Běták, A. Bürger, A. Görgen, H. T. Nyhus, J. Rekstad, A. Schiller, S. Siem, H. K. Toft, G. M. Tveten, A. V. Voinov, and K. Wikan, Analysis of possible systematic errors in the Oslo method, Phys. Rev. C **83**, 034315 (2011).

[33] P. A. M. Dirac, The quantum theory of the emission and absorption of radiation, Proc. R. Soc. London, Ser. A **114**, 243 (1927).

[34] E. Fermi, *Nuclear Physics* (The University of Chicago Press, Chicago, US, 1950).

[35] G. A. Bartholomew, E. D. Earle, A. J. Ferguson, J. W. Knowles, and M. A. Lone, Gamma-ray strength functions, in *Advances in Nuclear Physics*, edited by M. Baranger and E. Vogt (Springer US, Boston, MA, 1973), Vol. 7, pp. 229–324.

[36] J. M. Blatt and V. F. Weisskopf, *Theoretical Nuclear Physics*, 1st ed. (Springer, New York, 1952), p. 389.

[37] J. Kopecky and M. Uhl, Test of gamma-ray strength functions in nuclear reaction model calculations, Phys. Rev. C **41**, 1941 (1990).

[38] National Nuclear Data Center, information extracted from the NuDat database.

[39] S. F. Mughabghab, *Atlas of Neutron Resonances: Resonance Properties and Thermal Cross Sections Z=1–100* (Elsevier, Amsterdam, 2018), Vol. 2.

[40] T. von Egidy and D. Bucurescu, Systematics of nuclear level density parameters, Phys. Rev. C **72**, 044311 (2005).

[41] T. von Egidy and D. Bucurescu, Erratum: Systematics of nuclear level density parameters [Phys. Rev. C **72**, 044311 (2005)], Phys. Rev. C **73**, 049901(E) (2006).

[42] A. Gilbert and A. G. W. Cameron, A composite nuclear-level density formula with shell corrections, Can. J. Phys. **43**, 1446 (1965).

[43] T. Ericson, The statistical model and nuclear level densities, Adv. Phys. **9**, 425 (1960).

[44] T. Von Egidy, H. Schmidt, and A. Behkami, Nuclear level densities and level spacing distributions: Part II, Nucl. Phys. A **481**, 189 (1988).

[45] M. Guttormsen, M. Aiche, F. L. Bello Garrote, L. A. Bernstein, D. L. Bleuel, Y. Byun, Q. Ducasse, T. K. Eriksen, F. Giacoppo, A. Görgen, F. Gunsing, T. W. Hagen, B. Jurado, M. Klintefjord, A. C. Larsen, L. Lebois, B. Leniau, H. T. Nyhus, T. Renstrøm, S. J. Rose *et al.*, Experimental level densities of atomic nuclei, Eur. Phys. J. A **51**, 170 (2015).

[46] F. Pogliano, A. C. Larsen, F. L. Bello Garrote, M. M. Bjørøen, T. K. Eriksen, D. Gjestvang, A. Görgen, M. Guttormsen, K. C. W. Li, M. Markova, E. F. Matthews, W. Paulsen, L. G. Pedersen, S. Siem, T. Storebakken, T. G. Tornyi, and J. E. Vevik, Indirect measurement of the $(n, \gamma)^{127}$Sb cross section, Phys. Rev. C **106**, 015804 (2022).

[47] A. Konig, S. Goriely, and S. Hilaire, TALYS-1.9, A nuclear reaction program, user manual, Techical Report, 2017.

[48] A. Koning, D. Rochman, J.-C. Sublet, N. Dzysiuk, M. Fleming, and S. van der Marck, Tendl: Complete nuclear data library for innovative nuclear science and technology, Nucl. Data Sheets **155**, 1 (2019), Special Issue on Nuclear Reaction Data.

[49] A. C. Larsen, M. Guttormsen, M. Krtička, E. Běták, A. Bürger, A. Görgen, H. T. Nyhus, J. Rekstad, A. Schiller, S. Siem, H. K. Toft, G. M. Tveten, A. V. Voinov, and K. Wikan, Erratum: Analysis of possible systematic errors in the Oslo method [Phys. Rev. C **83**, 034315 (2011)], Phys. Rev. C **97**, 049901(E) (2018).

[50] M. N. Harakeh and A. van der Woude, *Giant Resonances* (Oxford University, Oxford, 2001).

[51] S. S. Dietrich and B. L. Berman, Atlas of photoneutron cross sections obtained with monoenergetic photons, At. Data Nucl. Data Tables **38**, 199 (1988).

[52] D. Savran, T. Aumann, and A. Zilges, Experimental studies of the pygmy dipole resonance, Prog. Part. Nucl. Phys. **70**, 210 (2013).

[53] A. Bracco, E. Lanza, and A. Tamii, Isoscalar and isovector dipole excitations: Nuclear properties from low-lying states and from the isovector giant dipole resonance, Prog. Part. Nucl. Phys. **106**, 360 (2019).

[54] S. Goriely, S. Hilaire, S. Péru, and K. Sieja, Gogny-HFB+QRPA dipole strength function and its application to radiative nucleon capture cross section, Phys. Rev. C **98**, 014327 (2018).

[55] B. L. Berman, M. A. Kelly, R. L. Bramblett, J. T. Caldwell, H. S. Davis, and S. C. Fultz, Giant resonance in deformed nuclei: Photoneutron cross sections for Eu^{153}, Gd^{160}, Ho^{165}, and W^{186}, Phys. Rev. **185**, 1576 (1969).

[56] R. Bergère, H. Beil, and A. Veyssière, Photoneutron cross sections of La, Tb, Ho and Ta, Nucl. Phys. A **121**, 463 (1968).

[57] V. V. Varlamov, A. I. Davydov, and V. D. Kaidarova, Evaluation of reliable cross sections of photoneutron reactions on ^{103}Rh and ^{165}Ho nuclei, Phys. At. Nucl. **82**, 212 (2019).

[58] M. Martini, S. Péru, S. Hilaire, S. Goriely, and F. Lechaftois, Large-scale deformed quasiparticle random-phase approximation calculations of the γ-ray strength function using the Gogny force, Phys. Rev. C **94**, 014304 (2016).

[59] S. Goriely, P. Dimitriou, M. Wiedeking, T. Belgya, R. Firestone, J. Kopecky, M. Krticka, V. Plujko, R. Schwengner, S. Siem, H. Utsunomiya, S. Hilaire, S. Péru, Y. S. Cho, D. M. Filipescu, N. Iwamoto, T. Kawano, V. Varlamov, and R. Xu, Reference database for photon strength functions, Eur. Phys. J. A **55**, 172 (2019).

[60] K. L. Malatji, K. S. Beckmann, M. Wiedeking, S. Siem, S. Goriely, A. C. Larsen, K. O. Ay, F. L. Bello Garrote, L. C. Campo, A. Görgen, M. Guttormsen, V. W. Ingeberg, P. Jones, B. V. Kheswa, P. von Neumann-Cosel, M. Ozgur, G. Potel, L. Pellegri, T. Renstrøm, G. M. Tveten, and F. Zeiser, Statistical properties of the well deformed ^{153,155}Sm nuclei and the scissors resonance, Phys. Rev. C **103**, 014309 (2021).

[61] K. Malatji (private communication).

[62] A. Simon, M. Guttormsen, A. C. Larsen, C. W. Beausang, P. Humby, J. T. Harke, R. J. Casperson, R. O. Hughes, T. J. Ross, J. M. Allmond, R. Chyzh, M. Dag, J. Koglin, E. McCleskey, M. McCleskey, S. Ota, and A. Saastamoinen, First observation of low-energy γ-ray enhancement in the rare-earth region, Phys. Rev. C **93**, 034303 (2016).

[63] M. Guttormsen, K. O. Ay, M. Ozgur, E. Algin, A. C. Larsen, F. L. Bello Garrote, H. C. Berg, L. Crespo Campo, T. Dahl-Jacobsen, F. W. Furmyr, D. Gjestvang, A. Görgen, T. W. Hagen, V. W. Ingeberg, B. V. Kheswa, I. K. B. Kullmann, M. Klintefjord, M. Markova, J. E. Midtbø, V. Modamio *et al.*, Evolution of the γ-ray strength function in neodymium isotopes, Phys. Rev. C **106**, 034314 (2022).

[64] W. Ziegler, C. Rangacharyulu, A. Richter, and C. Spieler, Orbital Magnetic Dipole Strength in ^{148,150,152,154}Sm and Nuclear Deformation, Phys. Rev. Lett. **65**, 2515 (1990).

[65] E. Lipparini and S. Stringari, Sum rules and giant resonances in nuclei, Phys. Rep. **175**, 103 (1989).

[66] B. Pritychenko, M. Birch, B. Singh, and M. Horoi, Tables of E2 transition probabilities from the first 2^+ states in even–even nuclei, At. Data Nucl. Data Tables **107**, 1 (2016).

[67] P. Möller, A. Sierk, T. Ichikawa, and H. Sagawa, Nuclear ground-state masses and deformations: FRDM(2012), At. Data Nucl. Data Tables **109-110**, 1 (2016).

85

Paper III

Experimentally constrained ^{165,166}Ho(n,γ) rates and implications for the s process

III

Experimentally constrained ^{165,166}Ho(n, γ) rates and implications for the s process

F. Pogliano [1],[*] A. C. Larsen [1],[†] S. Goriely [2] L. Siess,[2] M. Markova [1] A. Görgen [1] J. Heines [1] V. W. Ingeberg [1]
R. G. Kjus,[1] J. E. L. Larsson [1] K. C. W. Li [1] E. M. Martinsen [1] G. J. Owens-Fryar [3,4] L. G. Pedersen [1] S. Siem [1]
G. S. Torvund [1] and A. Tsantiri [3,4]

[1]*Department of Physics, University of Oslo, N-0316 Oslo, Norway*
[2]*Institut d'Astronomie et d'Astrophysique, Université Libre de Bruxelles, CP 226, B-1050 Brussels, Belgium*
[3]*Department of Physics and Astronomy, Michigan State University, East Lansing, Michigan 48824, USA*
[4]*Facility for Rare Isotope Beams, Michigan State University, East Lansing, Michigan 48824, USA*

The γ-ray strength function and the nuclear level density of ^{167}Ho have been extracted using the Oslo method from a ^{164}Dy($\alpha, p\gamma$)^{167}Ho experiment carried out at the Oslo Cyclotron Laboratory. The level density displays a shape that is compatible with the constant temperature model in the quasicontinuum, while the strength function shows structures indicating the presence of both a scissors resonance and a pygmy dipole resonance. Using our present results as well as data from a previous ^{163}Dy($\alpha, p\gamma$)^{166}Ho experiment, the ^{165}Ho(n, γ) and ^{166}Ho(n, γ) eellian-averaged cross section (MACS) uncertainties have been constrained. The possible influence of the low-lying, long-lived 6 keV isomer ^{166}Ho in the s process is investigated in the context of a $2M_{\odot}$, [Fe/H] $= -0.5$ asymptotic giant branch star. We show that the newly obtained ^{165}Ho(n, γ) MACS affects the final ^{165}Ho abundance, while the ^{166}Ho(n, γ) MACS only impacts the enrichment of ^{166,167}Er to a limited degree due to the relatively rapid β decay of the thermalized ^{166}Ho at typical s-process temperatures.

I. INTRODUCTION AND MOTIVATION

The two main mechanisms responsible for the creation of elements heavier than iron in the universe are the s and the r processes, standing for slow and rapid neutron-capture process, respectively [1,2]. The r process lasts for a few seconds and involves neutron densities of $N_n \gtrsim 10^{20}$ cm^{-3} (see, e.g., Ref. [3]). Such extremely high neutron densities will create very exotic, neutron-rich nuclei close to the neutron drip line, and will eventually β decay to stability when the neutron flux is exhausted.

In contrast, the s process involves neutron densities of $N_n \leqslant 10^{10}$ cm^{-3} and may last for thousands of years during the asymptotic giant branch (AGB) phase of low-mass stars [4]. At these low neutron densities, neutron captures usually take place on stable or very long-lived nuclei, as the neutron-capture timescale is longer than the one for the β decay for most of the unstable nuclei. This means that s-process nucleosynthesis follows a relatively narrow path along the valley of β stability up to Pb and Bi. However, some β-unstable neutron-rich nuclei have longer lifetimes than others, and if their lifetimes are comparable to the average timescale for neutron capture, they become so-called branching points along the s-process path. In these cases, astrophysical conditions such as neutron density and temperature may influence the specific path the s process takes, and a precise knowledge

of the nuclear properties of the involved nuclei is paramount for the correct description of the nucleosynthesis flow [4]. Examples of s-process branching points include ^{85}Kr and ^{151}Sm, where their location in the nuclear chart in between two stable nuclei gives separable branches that the reaction flow may follow (see Ref. [4] and references therein).

One case of interest is the odd-odd ^{166}Ho. As ^{165}Ho is the only stable isotope of this element, ^{166}Ho is made during the s process. Although its ground state β decays to ^{166}Er rather fast ($T_{1/2} \approx 26$ h), ^{166}Ho has a very low-lying ($E_x \approx 6$ keV) 7^- isomeric state that also β decays to ^{166}Er, but with a much longer half-life of about 1200 years [5]. This half-life is on the same timescale as the s process, which means that this branching could affect the final abundance of ^{165}Ho as well as the isotopic abundance ratio of ^{166}Er / ^{167}Er.

Assuming ^{166}Ho to be thermalized under typical s-process conditions (which should be a valid assumption according to Misch *et al.* [6]), the correct estimate of its impact requires knowledge of various nuclear properties, such as the ^{165}Ho(n, γ) reaction rate, the ^{166}Ho(n, γ) reaction rate, and the ^{166}Ho β-decay rate. While the latter has been estimated by Takahashi and Yokoi [7], the ^{165}Ho(n, γ) cross section has been measured directly [8]. In addition, both neutron-capture rates can be indirectly derived from experimentally extracted nuclear level densities and γ-strength functions for ^{166}Ho and ^{167}Ho using the Hauser-Feshbach formalism [9–11].

In this work, we aim at clarifying the impact of ^{166}Ho on the s process by using experimentally constrained ^{165}Ho(n, γ) and ^{166}Ho(n, γ) rates in s-process simulations. In Sec. II we present the results of the ^{164}Dy($\alpha, p\gamma$)^{167}Ho experiment

[*]francesco.pogliano@fys.uio.no
[†]a.c.larsen@fys.uio.no

carried out at the Oslo Cyclotron Laboratory. Using the Oslo method, we are able to extract the level density and γ strength function, which are used as input to calculate the ^{166}Ho(n, γ) Maxwellian-averaged cross sections as described in Sec. III. In Sec. IV, *s*-process calculations in AGB stars are performed, and the impact of the newly derived neutron-capture rates on the final abundances is discussed.

II. EXTRACTION OF THE NUCLEAR LEVEL DENSITY AND THE γ-RAY STRENGTH FUNCTION

While nuclear energy levels and reduced transition probabilities can be measured within the discrete region using spectroscopy methods, this task becomes increasingly difficult when going higher up in excitation energy. Here, levels become so close to each other that it is very difficult to distinguish them experimentally. When the mean level spacing D becomes so small that $D^{-1} \geqslant 50\text{--}200$ MeV^{-1}, the nuclear properties are better described in terms of average statistical quantities: the nuclear level density (NLD) and the γ-ray strength function (GSF). These two quantities, apart from being essential ingredients to calculate neutron-capture rates within the Hauser-Feshbach framework [9], may also reveal collective effects in the nucleus of interest for nuclear structure. The total NLD for all spins and both parities is usually written as $\rho(E_x)$ and gives information on the number of energy levels per excitation-energy bin. The GSF, written as f^{XL}, gives information on the electromagnetic response of the nucleus and the probabilities for γ decay of electric or magnetic character X and multipolarity L. The GSF is defined as [12]

$$f^{XL}(E_x, E_\gamma, J, \pi) = \frac{\langle \Gamma_\gamma^{XL}(E_x, E_\gamma, J, \pi) \rangle}{D(E_x, E_\gamma, J, \pi) E_\gamma^{2L+1}}, \quad (1)$$

where E_x is the initial excitation energy, E_γ is the transition energy, J is the angular momentum, π is the parity, $\langle \Gamma_\gamma^{XL} \rangle$ is the average partial γ-decay width, and D is the mean level spacing for the specific class of quantum levels considered in the average. The partial width $\langle \Gamma_\gamma^{XL} \rangle$ can be related to the transmission coefficient $\mathcal{T}^{XL}$ by [13]

$$\langle \Gamma_\gamma^{XL}(E_x, E_\gamma, J, \pi) \rangle = \mathcal{T}^{XL}(E_x, E_\gamma, J, \pi) \frac{D(E_x, E_\gamma, J, \pi)}{2\pi}. \quad (2)$$

By joining Eqs. (1) and (2), the transmission coefficient $\mathcal{T}^{XL}$ and the GSF f^{XL} can be related through

$$f^{XL}(E_x, E_\gamma, J, \pi) = \frac{\mathcal{T}^{XL}(E_x, E_\gamma, J, \pi)}{2\pi E_\gamma^{2L+1}}. \quad (3)$$

Here, E_x, J, and π may be averaged out using the generalized Brink-Axel hypothesis [14,15], shown to hold for Dy nuclei [16], and it is usually sufficient to consider dipole radiations $E1$ and $M1$ that dominate in the quasicontinuum region (see, e.g., Ref. [17]). These two assumptions simplify Eq. (3) to

$$f(E_\gamma) = \frac{\mathcal{T}(E_\gamma)}{2\pi E_\gamma^3}. \quad (4)$$

The NLD and the GSF can be extracted from experimental data using the Oslo method. In the following we go through the experimental setup, the experiment itself and a brief description of the data analysis method.

A. Experimental setup

The experiment was carried out at the Oslo Cyclotron Laboratory in October 2022 and aimed at measuring p-γ coincidences from the ^{164}Dy$(\alpha, p\gamma)^{167}$Ho reaction. A beam of α particles with ≈ 1.3 nA intensity was accelerated to 26 MeV by the MC-35 Scanditronix cyclotron, and the beam impinged on a ^{164}Dy self-supporting target, 1.73 mg/cm^2 thick and with 98.5% enrichment. The target was placed in the center of the Oslo SCintillator ARray (OSCAR) and the Silicon Ring (SiRi) detector arrays, which recorded particle-γ coincidences. OSCAR [18,19] is an array of 30 cylindrical (3.5 in. $\times$ 8.0 in.) LaBr$_3$(Ce) scintillator detectors mounted on a truncated icosahedron frame, with an energy resolution of 2.7% full-width half maximum at $E_\gamma = 662$ keV and a prompt timing peak with time resolution of ≈ 1.8 ns (standard deviation) for this experiment. SiRi [20] is a ΔE-E particle telescope array, which consists of eight silicon-telescope modules in a ring configuration covering 126°–140° (corresponding to about 6% of 4π) in backward angles. Each module consists of a thick (1550 μm) E back detector and a thin (130 μm) ΔE front detector. Each front detector is segmented in eight strips covering about 2° each, while the back detector is not segmented. The different energies deposited in the E and ΔE detectors allow us to discriminate between different ejectiles, so that the data from the (α, p) channel could be selected. The specific reaction kinematics allows us to calculate the excitation energy E_x the residual nucleus is left in, and associate this to its corresponding γ spectrum. By plotting the detected γ rays against E_x we obtain a matrix called the coincidence matrix, which is the starting point for extracting the NLD and the GSF using the Oslo method.

B. The Oslo method and normalization details

The γ rays measured with OSCAR will inevitably be convoluted with the detector response [19]. The *unfolding* procedure [25] helps us correct for this convolution, and obtain a γ-ray spectrum for the full-energy peaks only. From the unfolded spectra we can obtain the first-generation γ rays using the weighted subtraction technique by Guttormsen *et al.* [26].

By inspection of the first-generation matrix, we may select the region coinciding with the quasicontinuum, in this case between $E_x = 4.5$ and 7.0 MeV, and limiting the γ rays to $E_\gamma > 1.2$ MeV. From Fermi's golden rule [27,28], we may express the γ-decay probability $P(E_\gamma, E_x)$ for a nucleus at excitation energy E_x to emit a γ ray of energy E_γ as [29]

$$P(E_\gamma, E_x) \propto \mathcal{T}(E_\gamma)\rho(E_x - E_\gamma). \quad (5)$$

Using a global χ^2 minimization technique described in Ref. [29], we are then able to extract the functional shape

TABLE I. Parameters used for the ^{167}Ho NLD and GSF normalizations. The parameters E_0 and T_{CT} are determined from a fit to our data points at high E_x together with the calculated $\rho(S_n)$ value. The D_0 and $\langle \Gamma_\gamma \rangle$ values are taken from Ref. [21], but with an uncertainty estimation as described in the text. The two values for the spin-cutoff parameter $\sigma_I^2(S_n)$ are from the FG formula [22] and from the RMI formula [23] (see text and Ref. [24]).

E_0 (MeV)	T_{CT} (MeV)	D_0 (eV)	I_t	σ_I^2(FG)	σ_I^2(RMI)	σ_d^2	$\langle \Gamma_\gamma \rangle$ (meV)
−1.836	0.620	2.32(77)	7	5.68	7.10	2.96	89(9)

of the NLD and the GSF from the selected region in the first-generation matrix. Thus we obtain the solutions

$$\tilde{\rho}(E_x - E_\gamma) = A e^{\alpha(E_x - E_\gamma)} \rho(E_x - E_\gamma), \quad (6a)$$

$$\tilde{\mathcal{T}}(E_\gamma) = B e^{\alpha E_\gamma} \mathcal{T}(E_\gamma), \quad (6b)$$

where A, B, and α are free parameters, and any choice of them gives an equally good fit to the first-generation matrix. To determine these parameters, we must make use of the known discrete energy levels at low E_x and the level density at the neutron separation energy S_n for the level density, and the average total radiative width $\langle \Gamma_\gamma \rangle$ for the strength function [30].

The discrete energy levels are readily available at NUDAT [31], while the value of $\rho(S_n)$ can be calculated from the measured level spacing D_0 of s-wave neutron resonances and the spin-cutoff parameter σ_I^2 at S_n by [29]

$$\rho(S_n) = \frac{2\sigma_I^2}{D_0 \left[(I_t + 1) e^{-(I_t+1)^2/2\sigma_I^2} + I_t e^{-I_t^2/2\sigma_I^2} \right]}, \quad (7)$$

where I_t is the spin of the $A - 1$ isotope that is the target in the neutron-resonance experiment.

As our level-density data points do not reach $\rho(S_n)$ due to the lower limit on E_γ, the data has to be extrapolated up to S_n. The choice of extrapolation function is usually not important given that the lower E_γ is not too large. Typically the extrapolation is done with either the back-shifted Fermi gas (BSFG) model [22,32],

$$\rho_{FG}(E_x) = \frac{\exp(2\sqrt{aU})}{12\sqrt{2} a^{1/4} U^{5/4} \sigma_I}, \quad (8)$$

or the constant-temperature (CT) model [22,33],

$$\rho_{CT}(E_x) = \frac{1}{T_{CT}} \exp\left(\frac{E_x - E_0}{T_{CT}} \right), \quad (9)$$

where $U = E_x - E_1$. Here a, E_1, E_0, and T_{CT} are fitting parameters. For ^{167}Ho, the CT model was observed to fit the data at higher E_x better than the BSFG one, and the values for E_0 and T_{CT} were found to be −1.836 MeV and 0.620 MeV, respectively.

The value of D_0 can be retrieved from the *Atlas of Neutron Resonances* [21], where a calculated value of $D_0 = 2.32$ eV is provided using the long-lived 7^- isomer as target for thermal neutron capture. The only unknown left to calculate the level density at S_n using Eq. (7) is the spin-cutoff parameter at S_n. For this reason the normalization procedure used for ^{167}Ho closely resembles the one used for ^{166}Ho in Ref. [24] except for the fact that the CT model was used instead of the BSFG.

The choice of σ_I^2 is model dependent, as there is no experimental data on the spin distribution for all accessible spins at

S_n for these nuclei. Two widely used models are the rigid body of inertia formula as applied by von Egidy and Bucurescu [23] (here labeled RMI), or the Gilbert and Cameron approach [22] (here labeled FG). We have no reason to prefer one against the other, so we let σ_I^2 vary between the FG value of $\sigma_I = 5.68$ and the RMI value of $\sigma_I = 7.10$. We assume that the error in $\rho(S_n)$ is evenly distributed between the two σ_I^2 values, and otherwise decided by the uncertainty associated to the D_0 value. Unfortunately, the *Atlas of Neutron Resonances* [21] does not provide an uncertainty to its recommended value. Considering that there are three measured neutron resonances, $N_r = 3$, the uncertainty was estimated to be 33% using the $\Delta D_0/D_0 = 1/N_r$ formula from RIPL3 [34]. For the σ_I^2 dependence on excitation energy, we follow Refs. [34,35] and assume $\sigma^2(E_x)$ to be linearly dependent with respect to the excitation energy:

$$\sigma^2(E_x) = \sigma_d^2 + \frac{E_x - E_d}{S_n - E_d} [\sigma_I^2 - \sigma_d^2], \quad (10)$$

where σ_d^2 is the spin-cutoff parameter at a low excitation energy E_d. In our case, σ_d^2 was found to be 2.96 at $E_d = 0.220$ MeV. The fit of the NLD to the discrete levels is done in a similar way as in Refs. [24,36], where we chose the E_x interval with the most complete level scheme.
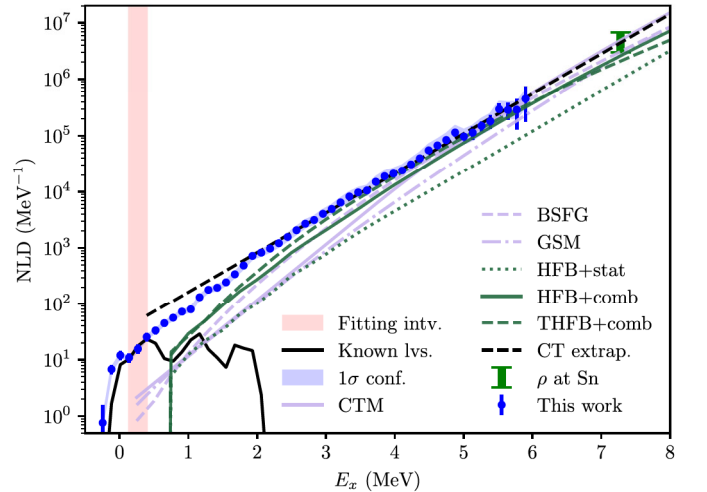
FIG. 1. The normalized NLD compared to the theoretical models used in TALYS 1.96 [10]. For an overview of the models and references, see text. The error bars indicate the statistical and systematic uncertainties from the Oslo method, and the uncertainty band shows the systematic errors from the normalization procedure. The vertical, pink-shaded band (light grey) indicates the region used for fitting the extracted NLD to the known levels of ^{167}Ho from Ref. [31].
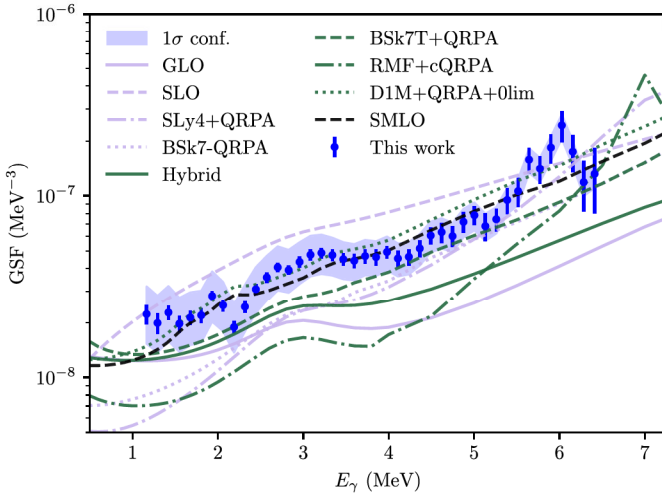
FIG. 2. The normalized GSF compared to the theoretical models used in TALYS 1.96 [10]. For all the $E1$ models listed in the plot, the $M1$ SMLO [37] was added, except for the D1M+QRPA-0lim $E1$ model, where the corresponding D1M+QRPA-0lim $M1$ was used [38]. See text for an overview of the models and their references. Uncertainties are as in Fig. 1.

For the normalization of the GSF we use the average, total radiative width $\langle\Gamma_\gamma\rangle$ [30], also available in the *Atlas of Neutron Resonances*, where it is given as 88.5 meV [21]. Again, the uncertainty in this quantity is not provided, but the value of $\langle\Gamma_\gamma\rangle$ is quite similar for neighboring rare-earth nuclei; from systematics of these $\langle\Gamma_\gamma\rangle$ values we estimate the uncertainty to be 10%, therefore we have used $\langle\Gamma_\gamma\rangle = 89(9)$ meV. We use the same method as in Refs. [24,36] in order to propagate the systematic and statistical uncertainties from the fitting parameters to the normalized GSF. An overview of all the values used for the NLD and GSF normalizations can be found in Table I, and the normalized NLD and GSF are displayed in Figs. 1 and 2 respectively.

C. Level density and strength function

The normalized level density is compared with TALYS [10] models in Fig. 1. The models used in the comparison are

(1) The constant-temperature plus Fermi gas model (CTM) [22].
(2) The back-shifted Fermi gas model (BSFG) [22,32].
(3) The generalised superfluid model (GSM) [39,40].
(4) The Skyrme-Hartree-Fock-Bogolyubov plus statistical model (HFB+Stat), tables from Ref. [41].
(5) The Hartree-Fock-Bogoluybov plus combinatorial model (HFB+comb), tables from Ref. [42].
(6) The temperature-dependent Gogny-Hartree-Fock-Bogolyubov model (THFB+comb) [43].

In general, the models do not agree very well with the data at low excitation energies, but the agreement improves somewhat for $E_x \gtrsim 5$ MeV.

The comparison between the extracted GSF and the TALYS models can be seen in Fig. 2. The models here include both $E1$ and $M1$ radiation. The $E1$ models used are

(1) The Kopecky-Uhl generalized Lorentzian (GLO) [17].
(2) The Brink-Axel standard Lorentzian (SLO) [15,44].
(3) The Hartree-Fock-BCS plus QRPA (quasiparticle random-phase approximation) tables based on the SLy4 interaction (SLy4+QRPA) [45].
(4) The HFB plus QRPA calculation based on the BSk7 interaction (BSk7+QRPA) [46].
(5) The hybrid model (Hybrid) [47].
(6) The BSk7+QRPA model with T-dependent width (BSk7T+QRPA) [46].
(7) The relativistic mean field plus continuum QRPA calculation with T-dependent width (RMF+cQRPA) [48].
(8) The Gogny-HFB plus QRPA calculation complemented by low-energy enhancement (D1M+QRPA+0lim) [38].
(9) The simplified modified Lorentzian (SMLO) [37].

For the $M1$ strength component, the default $M1$ SMLO model [37] with upbend was used, except for D1M+QRPA where the corresponding $M1$ strength was used [38].

We note that most models predict a structure centered at ≈ 3 MeV on the tail of the giant electric dipole resonance (GEDR) compatible with an $M1$ scissors resonance (SR) [49], although our experimental results do not match their predicted magnitude. The structure at ≈ 6 MeV can be interpreted as the $E1$ pygmy dipole resonance [50,51] (PDR), but here we should be careful as the poor statistics from the experiment leads to rather big statistical uncertainties. The D1M+QRPA model [38] and the simplified modified Lorentzian [37] do the best job at predicting the GSF as they have the correct magnitude, although none of them reproduce the two observed resonancelike structures.

The Oslo method does not allow to distinguish between $E1$ and $M1$ radiation. Therefore, to extract, e.g., the SR integrated strength, the GSF is modeled using empirical functions and data from neighboring nuclei. The giant dipole resonance (GEDR) is known to be of $E1$ character and expected to be double-peaked for a deformed nucleus [52,53]. We therefore model the GEDR with two Lorentzian-type functions using the generalized Lorentzian (GLO) function by Kopecky and Uhl [17]:

$$f^{\text{GLO}}(E_\gamma)$$
$$= \sum_{i=1}^{2} \frac{\sigma_{0,i}\Gamma_{0,i}}{3\pi^2\hbar^2c^2}\left(\frac{E_\gamma\Gamma_K(E_\gamma, T_f)}{\left(E_\gamma^2 - E_{0,i}^2\right)^2 + E_\gamma^2\Gamma_K^2} + 0.7\frac{\Gamma_K(0, T_f)}{E_{0,i}^3}\right),$$
$$\tag{11}$$

where

$$\Gamma_K(E_\gamma, T_f) = \frac{\Gamma_{0,i}}{E_{0,i}^2}\left(E_\gamma^2 + 4\pi^2T_f^2\right) \tag{12}$$

and $\Gamma_{K,0} = \Gamma_K(0, T_f)$. Here $E_{0,i}$, $\Gamma_{0,i}$, $\sigma_{0,i}$ and T_f are parameters representing the energy centroid, the width, the peak cross section of each peak ($i = 1, 2$), and the temperature of the final levels, respectively. The functions are fitted to the neighboring ^{165}Ho GEDR data, as this is the closest nucleus with experimental GEDR data available, measured by Berman

TABLE II. The parameters used in the fit functions shown in Fig. 3.

Function	T_f (MeV)	$E_{0,s}$ (MeV)	$\Gamma_{0,s}$ (MeV)	$\sigma_{0,s}$ (mb)	B_{SR} (μ_I^2)
GEDR1	0.72(1)	12.34(1)	3.17(3)	337(1)	–
GEDR2	–	14.78(1)	1.85(3)	196(2)	–
PDR	–	6.11(5)	1.20(3)	8.0(6)	–
SR_{SLO}	–	3.19(5)	0.87(11)	0.72(7)	6.3(10)
SR_{exp}	–	–	–	–	4.0(7)

et al. [54] and Bergere *et al.* [55]. However, we chose to apply the more recent reanalysis and evaluation of the two experiments from Varlamov *et al.* [56].

The PDR and the SR are fitted by a standard Lorentzian (SLO), defined as

$$f^{SLO}(E_\gamma) = \frac{1}{3\pi^2\hbar^2c^2}\frac{\sigma_s\Gamma_s^2 E_\gamma}{\left(E_\gamma^2 - E_s^2\right)^2 + E_\gamma^2\Gamma_s^2}, \quad (13)$$

where E_s, Γ_s, and σ_s are the resonance parameters representing the energy centroid, the width, and the peak cross section. We see that the data are modeled relatively well, considering the above-mentioned big uncertainties concerning the pygmylike structure at $E_\gamma \approx 6$ MeV. The fit to the data allows for a clear separation between the contributions from the scissors and the pygmylike structures from the GEDR tail, and determining their respective strengths. The spin-flip $M1$ resonance is also probably present, but its expected contribution centered around 8 MeV has likely a magnitude far below the $E1$ contribution, so that we did not include it in the fit. All the fitting parameters are listed in Table II.

Of certain interest is the integrated *upward* SR strength B_{SR} that can be expressed as

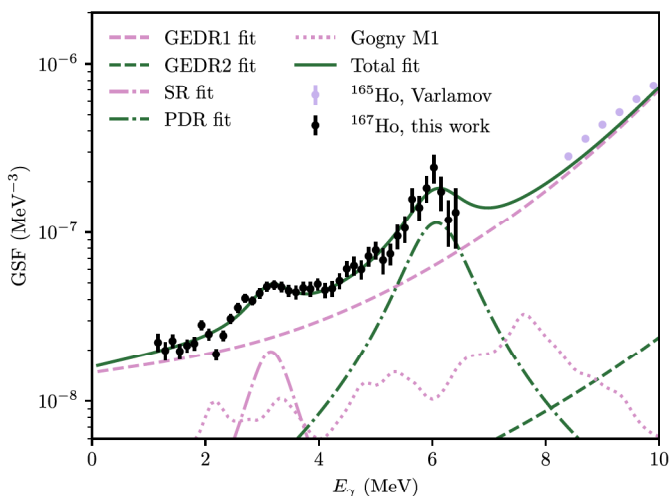$$B_{SR} = \frac{(3\hbar c)^3}{16\pi}\int f_{SR}(E_\gamma)dE_\gamma, \quad (14)$$

FIG. 3. The normalized GSF and the fit to the data using the empirical functions described in the text. The ^{165}Ho GEDR data from Varlamov *et al.* [56] are used fit the GEDR. The dotted line shows the theoretical QRPA predictions for the $M1$ GSF from Ref. [57].
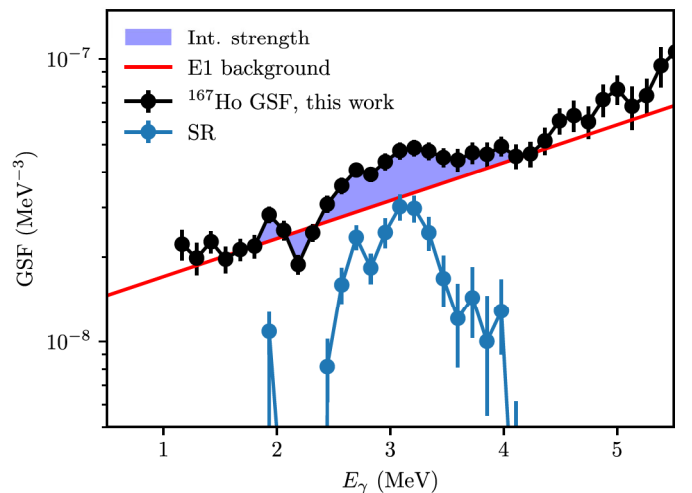

FIG. 4. Estimation of the $E1$ strength using a simple exponential passing through two points of the GSF (see text). Data points from this work are shown as black points, while the red line is the modeled $E1$ strength, and the blue area shows the residual strength.

where f_{SR} is the function describing the SR. This function could, for example, be the SLO function fitting the broad structure at $E_\gamma \approx 3$ MeV. To obtain a lower bound for the integrated strength, the $E1$ tail can be modeled as a simple exponential function going through two data points that are considered to be the E_γ limits of the SR. Such an approach has been used by Agvaanluvsan *et al.* [58], Nyhus *et al.* [59], Malatji *et al.* [60], and referred to as Method 3 in Pogliano *et al.* [24]. By choosing $E_\gamma = 1.804$ and 4.236 MeV as the limiting points, we calculate an integrated strength $B_{SR} = 4.0(7)\mu_N^2$, see Fig. 4. This is to be compared to the B_{SR} calculated by integrating the SLO fit of the SR using the parameters in Table II between 0 and 10 MeV, giving a value of $6.3(10)\mu_N^2$. The latter value assumes the $E1$ contribution stemming from the GEDR tail to be smaller than for the former value, and is comparable to values obtained for ^{163,164}Dy by Renstrøm *et al.* [16].

III. NEUTRON-CAPTURE RATES

With our experimental data on the NLD and the GSF, and by using a neutron optical-model potential (OMP), we can employ the Hauser-Feshbach formalism [9,11] in order to calculate the (n,γ) cross section for the $N-1$ isotope. Here, we use the ^{166}Ho data from Ref. [24] and the present NLD and GSF of ^{167}Ho from this work to calculate the ^{165}Ho(n,γ) and ^{166}Ho(n,γ) cross sections, respectively. The cross sections are calculated using the nuclear reaction code TALYS 1.96 [10]. Information on the OMP cannot be extracted using the Oslo method, and we here rely on the OMP models implemented in TALYS. We use the phenomenological model by Koning and Delaroche [61] for both nuclei, where OMP parameters from experimental data are given for ^{165}Ho, as well as the semimicroscopic Jeukenne-Lejeune-Mahaux (JLM) model by Bauge *et al.* [62].

Our calculated ^{165}Ho(n,γ) cross section is compared with directly measured neutron-capture data from the literature in
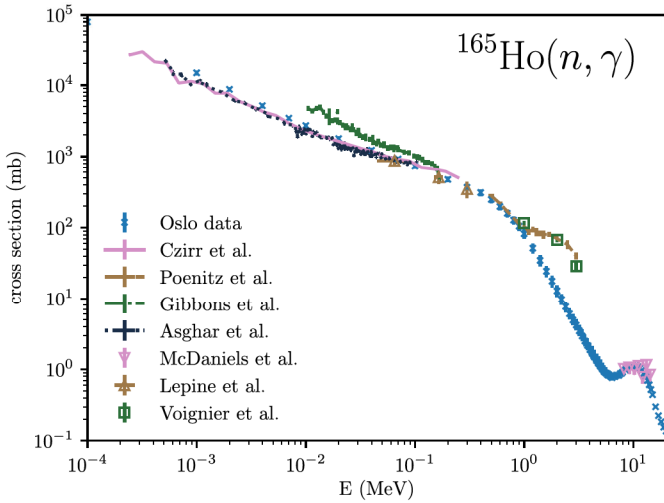
FIG. 5. The ^{165}Ho(n, γ) cross section calculated with the experimentally extracted NLD and GSF for ^{166}Ho compared to data from Czirr *et al.* [63], Poenitz *et al.* [66], Gibbons *et al.* [67], McDaniels *et al.* [65], Asghar *et al.* [64], Voignier *et al.* [68], and Lepine *et al.* [69].

Fig. 5. We observe that our experimentally-constrained cross section calculation agrees rather well with the data sets of Czirr *et al.* [63], Asghar *et al.* [64], Lepine *et al.* [69], and McDaniels *et al.* [65]. On the other hand, the other neutron-capture measurements seem to be significantly higher. The reason for this discrepancy in the directly measured cross sections as well as our result is not clear, and it would be desirable to perform new (n, γ) measurements on ^{165}Ho to understand and resolve this issue.

The radiative neutron-capture cross section is a crucial ingredient to the neutron-capture rate $N_A \langle \sigma v \rangle (T)$ as seen from the reactivity equation (see, e.g., Ref. [3])

$$N_A \langle \sigma v \rangle (T) = \left(\frac{8}{\pi \tilde{m}} \right)^{1/2} \frac{N_A}{(k_B T)^{3/2} G_t(T)} \int_0^\infty \sum_\mu \frac{2J_t^\mu + 1}{2J_t^0 + 1}$$

$$\times \sigma_{n\gamma}^\mu(E) E \exp\left[-\frac{E + E_x^\mu}{k_B T} \right] dE, \quad (15)$$

where N_A is Avogadro's number, $\tilde{m}$ the reduced target mass, k_B is Boltzmann's constant, T the temperature in the astrophysical environment, and J_t^0 and J_t^μ are the ground state and the μth excited energy level spins respectively, E_x^μ the excitation energy of the μth energy level, E the relative kinetic energy between the neutron and the target nucleus, $\sigma_{n\gamma}^\mu$ the (n, γ) cross section for the target nucleus excited to the μth state, and $G_t(T)$ the partition function given by

$$G_t(T) = \sum_\mu \frac{2J_t^\mu + 1}{2J_t^0 + 1} \exp\left[\frac{-E_x^\mu}{k_B T} \right]. \quad (16)$$

From the radiative neutron-capture rate we can calculate the Maxwellian-averaged cross section $N_A \langle \sigma \rangle_T$ (MACS):

$$N_A \langle \sigma \rangle_T = \frac{N_A \langle \sigma v \rangle}{v_T}, \quad (17)$$

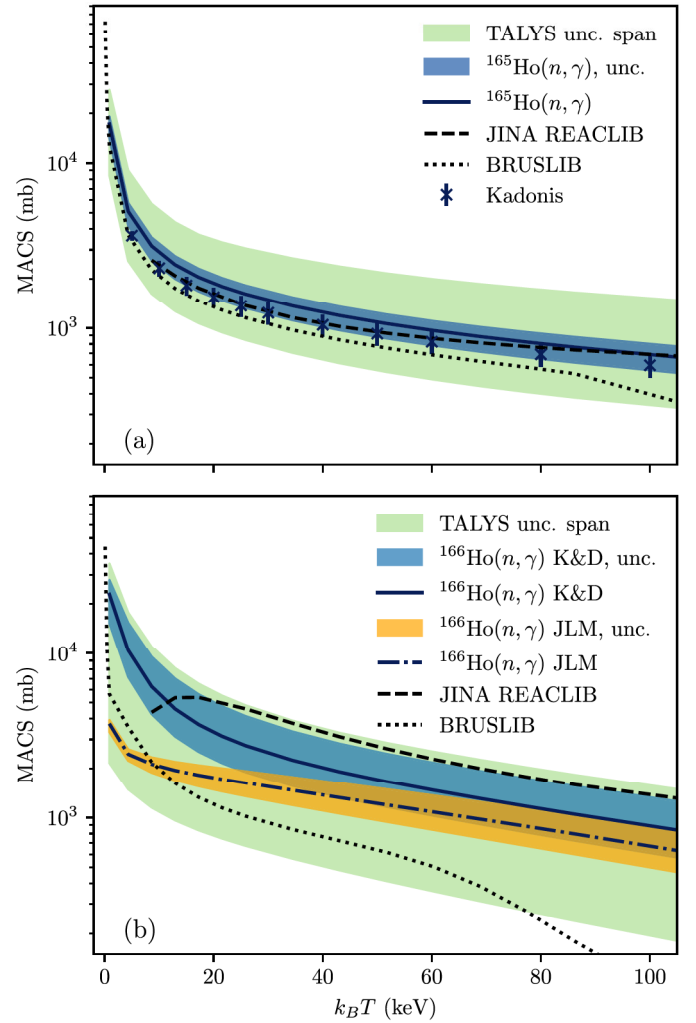where $v_T = \sqrt{2 k_B T / \tilde{m}}$ is the thermal velocity.

FIG. 6. The Maxwellian-averaged cross sections for (a) ^{165}Ho(n, γ) and (b) ^{166}Ho(n, γ) using our data as input compared to the TALYS uncertainty range as well as JINA REACLIB [70] and BRUSLIB [71] (see text).

The ^{165}Ho and ^{166}Ho calculated MACS values are shown in Fig. 6(a) and 6(b), respectively. The error propagation from the systematic and statistical errors of the NLD and GSF is done with the same procedure as in Ref. [36]. For both cases we compare our results with the range covered by the TALYS models and two selected libraries used for astrophysical network calculations: JINA REACLIB [70], and BRUSLIB [71]. For ^{165}Ho, we also compare our derived data with the ones provided in the KADoNiS database [72]. In the KADoNiS database, it is specified that the MACS measurements for this nucleus fall in two groups, one where the MACS at 30 keV is $\approx$1380 mb [73] and one providing cross sections $\approx$15% lower at $\approx$1200 mb [63,74,75]. The KADoNiS value of 1237 ± 183 mb is calculated as an average of the two groups, which falls slightly below (but still close to) the previous value from the compilation by Bao *et al.* [8] of 1280 ± 100 mb. Our derived MACS agrees quite well with the JINA REACLIB rates and the recommended KaDoNiS values, both of which fall within the MACS confidence interval, although this cannot be said for the BRUSLIB values. At

30 keV we obtained a MACS of 1494^{+193}_{-272} mb, slightly above the KaDoNiS recommended value, but still compatible with our findings.

For ^{166}Ho we show both the rates calculated using the global phenomenological OMP model from Koning and Delaroche [61] and the JLM model by Bauge *et al.* [62] as these give considerably different predictions for the temperature ranges relevant to the *s* process due to different significant contributions of the inelastic channel. In particular, the 30 keV MACS is estimated to be 2505^{+1257}_{-769} mb using the Koning and Delaroche OMP, and 1550^{+297}_{-275} mb using the JLM model.

IV. APPLICATION TO THE *s* PROCESS IN AGB STARS

The newly derived ^{165}Ho(n, γ) MACS may directly impact the *s*-process production of Ho. Assuming a local equilibrium [4], the $A = 165$ isotopic abundance $N_s(^{165}\text{Ho})$ can be approximated by $N_s(^{165}\text{Ho}) = \langle \sigma_{164} \rangle / \langle \sigma_{165} \rangle \times N_s(^{164}\text{Dy})$, where $\langle \sigma_{164} \rangle$ is the ^{164}Dy MACS and $N_s(^{164}\text{Dy})$ its *s*-process abundance. Therefore, a change of the ^{165}Ho(n, γ) MACS directly affects the *s*-process abundance of Ho. Such an impact is illustrated for the *s* process in AGB stars, as detailed below.

AGB nucleosynthesis predictions have been computed using the STAREVOL code [76] with an extended reaction network of 414 species linked by 637 nuclear reactions. Details on the nuclear network and input physics can be found in Goriely and Siess [77]. The solar abundances are taken from Asplund *et al.* [78], and correspond to a metallicity of $Z = 0.0134$. The Reimers [79] mass loss rate with $\eta_R = 0.4$ is used from the main sequence up to the end of core helium burning and the Vassiliadis and Wood [80] prescription during the AGB phase. Dedicated models with an initial mass of $2M_\odot$ and a metallicity of [Fe/H] $= -0.5$[1] have been computed as explained below.

In the present calculations, a diffusion equation is used to model the partial mixing of protons in the C-rich layers at the time of the third dredge-up. We follow Eq. (9) of Goriely and Siess [77] and use the corresponding diffusive mixing parameters, i.e., $f_{\text{env}} = 0.10$, $D_{\min} = 10^9$ cm^2 s^{-1} and $p = 5$, where f_{env} controls the extent of the mixing, $D_{\min}$ the value of the diffusion coefficient at the base of the envelope, and p is a free parameter describing the shape of the diffusion profile.

The elemental surface overabundances [X/Fe] at the end of the AGB phase after the occurrence of 11 thermal pulses are shown in Fig. 7 for the elements ranging between Sm ($Z = 62$) and Re ($Z = 75$). On the basis of the initial large TALYS uncertainties corresponding to a variation of the ^{165}Ho(n, γ) MACS by a factor of 3.5 [see Fig. 6(a)], an uncertainty of ± 0.20 dex is obtained on the surface overabundance of Ho. With the newly constrained MACS, this uncertainty is reduced to ± 0.07 dex.
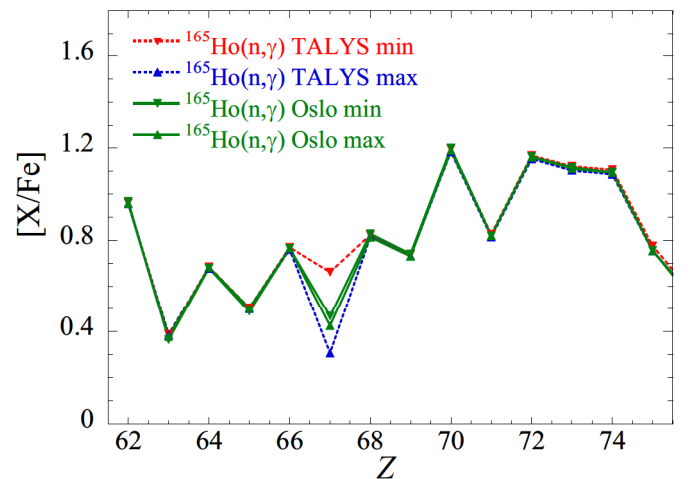

FIG. 7. Elemental surface overabundances [X/Fe] at the end of the AGB evolution of our $2M_\odot$ [Fe/H] $= -0.5$ model star as a function of the charge number Z for different values of the ^{165}Ho(n, γ) MACS, namely the upper and lower limits spanned by TALYS systematics and those constrained by the present Oslo experiment. The Oslo-constrained ^{166}Ho(n, γ) MACS obtained with the JLM OMP is adopted in all cases.

While the ^{165}Ho(n, γ) reaction directly affects the neutron capture along the radiative *s*-process path, the ^{166}Ho(n, γ) reaction comes into play only if a non-negligible amount of neutrons is produced. For the conditions considered here, i.e. an *s* process during the interpulse phase at a temperature of about 10^8 K, ^{166}Ho can be regarded as thermalized [6], i.e., its ground state and excited states are in thermal equilibrium, diminishing the potential impact of the 1200 yr isomer. The thermalized ^{166}Ho half-life of $T_{1/2} \simeq 9.8$ d at $T = 10^8$ K [7] is fast enough for this branching not to be affected by the ^{166}Ho(n, γ) reaction for interpulse neutron densities of $N_n \simeq 10^7$–10^8 cm^{-3}. Neutron densities larger than typically 3×10^9 cm^{-3} would be required for this channel to become relevant. Interestingly, during the convective thermal pulse, a large neutron burst may be produced by ^{22}Ne(α, n) and, despite a low neutron-to-seed ratio, may impact some relative isotopic abundances at the branching points. During the convective pulse, temperatures of $T = (3$–$3.5) \times 10^8$ K and neutron densities of 10^{10}–10^{11} cm^{-3} are found. These latter neutron densities are high enough to activate the ^{166}Ho(n, γ) channel, despite the relatively fast β decay of ^{166}Ho ($T_{1/2} \simeq 1.4$ d at $T = 3.5 \times 10^8$ K). The final isotopic surface overabundances are shown in Fig. 8 for different ^{166}Ho(n, γ) rates (adopting the ^{165}Ho(n, γ) rate from Bao *et al.* [8]). A lower value of ^{166}Ho MACS is seen to give rise to an increase of the ^{166}Er and ^{167}Er abundances, hence of the Er elemental overabundance by 0.04 dex, if we consider the large uncertainties spanned by TALYS calculations [see Fig. 6(b)]. This uncertainty is significantly reduced to below 0.01 dex, when using the Oslo-constrained rates, despite the remaining uncertainty stemming from the OMP. We aslo remark that if the neutron density is large enough to branch the ^{166}Ho neutron channel, the ^{167}Ho branching may also be slightly activated although its β-decay half-life is shorter than 3.1 h. This result

---

[1]The abundance of element X is defined as $[X/Y] = \log_{10}(n_X/n_Y)_* - \log_{10}(n_X/n_Y)_\odot$ where n_i is the number density of element i, and Y is a normalizing element, generally Fe.
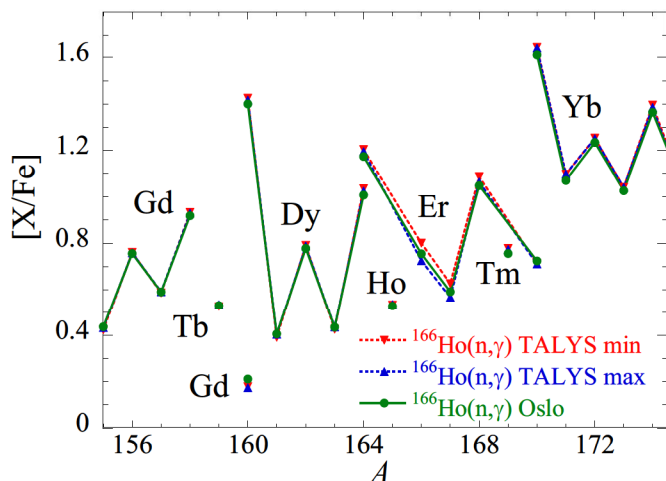
FIG. 8. Isotopic surface overabundances [X/Fe] at the end of the AGB evolution of our $2M_\odot$ [Fe/H] = −0.5 model star as a function of the atomic mass A for different values of the ^{166}Ho(n, γ) MACS, namely the upper and lower limits spanned by TALYS systematics and those constrained by the present Oslo experiment using the JLM OMP.

method. The NLD is shown to behave consistently to the constant-temperature model, and the GSF shows typical features for a rare-earth, neutron-rich, deformed nucleus showing structures compatible with the $M1$ scissors mode and the PDR. The ^{166,167}Ho NLDs and GSFs were used to constrain the ^{165,166}Ho(n, γ) MACS uncertainties. The MACS results were further applied to investigate the role of these two nuclei in the s process. Of particular interest is the behavior of ^{166}Ho, whose ground state has a half-life of about 26 h, while its 6 keV first excited state has instead a half-life of 1200 yr against β decay. This was studied in the context of a $2M_\odot$, [Fe/H] = −0.5 AGB star.

The obtained ^{165}Ho(n, γ) MACS was shown to be lower than several of the previous experimental results, which led to a higher production of ^{165}Ho in the s-process final abundances. With the assumption of thermalization of ^{166}Ho in typical s-process interpulse conditions, the impact on the relative ^{166}Er and ^{167}Er enrichments is small. Only during convective thermal pulses were the neutron densities high enough to activate the ^{167}Ho branch, and consequently influence the Er abundances.

clearly depends on the adopted TALYS rate for the ^{167}Ho(n, γ) reaction.

In summary, while the ^{165}Ho(n, γ) reaction directly affects the production of Ho, the ^{166}Ho(n, γ) reaction only plays a non-negligible role if the neutron density is high enough to activate the temperature-dependent branching at ^{166}Ho. In this case, the relative enrichment of the ^{166,167}Er isotopes may be affected. Through the newly derived rates, the uncertainty affecting the s-process abundances of Ho and Er can be significantly reduced. These remain much smaller than those stemming from stellar evolution modeling.

V. SUMMARY

In this work, we have presented the newly obtained NLD and GSF for rare-earth, odd-even ^{167}Ho from the ^{164}Dy$(\alpha, p\gamma)^{167}$Ho experimental data analyzed with the Oslo

[1] E. M. Burbidge, G. R. Burbidge, W. A. Fowler, and F. Hoyle, Synthesis of the elements in stars, Rev. Mod. Phys. **29**, 547 (1957).

[2] A. G. W. Cameron, Nuclear reactions in stars and nucleogenesis, Publ. Astron. Soc. Pac. **69**, 201 (1957).

[3] M. Arnould, S. Goriely, and K. Takahashi, The r-process of stellar nucleosynthesis: Astrophysics and nuclear physics achievements and mysteries, Phys. Rep. **450**, 97 (2007).

[4] F. Käppeler, R. Gallino, S. Bisterzo, and W. Aoki, The *s* process: Nuclear physics, stellar models, and observations, Rev. Mod. Phys. **83**, 157 (2011).

[5] K. Faler, Determination of the half-life of the longer-lived 166ho isomer, J. Inorg. Nucl. Chem. **27**, 25 (1965).

[6] G. W. Misch, T. M. Sprouse, M. R. Mumpower, A. J. Couture, C. L. Fryer, B. S. Meyer, and Y. Sun, Sensitivity of neutron-rich nuclear isomer behavior to uncertainties in direct transitions, Symmetry **13**, 1831 (2021).

[7] K. Takahashi and K. Yokoi, Beta-decay rates of highly ionized heavy atoms in stellar interiors, At. Data Nucl. Data Tables **36**, 375 (1987).

[8] Z. Bao, H. Beer, F. Käppeler, F. Voss, K. Wisshak, and T. Rauscher, Neutron cross sections for nucleosynthesis studies, At. Data Nucl. Data Tables **76**, 70 (2000).

[9] W. Hauser and H. Feshbach, The inelastic scattering of neutrons, Phys. Rev. **87**, 366 (1952).

[10] A. Koning, S. Hilaire, and S. Goriely, TALYS: modeling of nuclear reactions, Eur. Phys. J. A **59**, 131 (2023).

[11] T. Rauscher and F.-K. Thielemann, Astrophysical reaction rates from statistical model calculations, At. Data Nucl. Data Tables **75**, 1 (2000).

[12] G. A. Bartholomew, E. D. Earle, A. J. Ferguson, J. W. Knowles, and M. A. Lone, Gamma-ray strength functions, in *Advances in Nuclear Physics: Volume 7*, edited by M. Baranger and E. Vogt (Springer US, 1973), pp. 229–324.

[13] J. M. Blatt and V. F. Weisskopf, *Theoretical Nuclear Physics* (Wiley, New York, 1952).

[14] D. M. Brink, Some aspects of the interaction of fields with matter, Doctoral thesis, Oxford University, 1955.

[15] P. Axel, Electric dipole ground-state transition width strength function and 7-MeV photon interactions, Phys. Rev. **126**, 671 (1962).

[16] T. Renstrøm, H. Utsunomiya, H. T. Nyhus, A. C. Larsen, M. Guttormsen, G. M. Tveten, D. M. Filipescu, I. Gheorghe, S. Goriely, S. Hilaire, Y.-W. Lui, J. E. Midtbø, S. Péru, T. Shima, S. Siem, and O. Tesileanu, Verification of detailed balance for γ absorption and emission in Dy isotopes, Phys. Rev. C **98**, 054310 (2018).

[17] J. Kopecky and M. Uhl, Test of gamma-ray strength functions in nuclear reaction model calculations, Phys. Rev. C **41**, 1941 (1990).

[18] V. W. Ingeberg (unpublished).

[19] F. Zeiser, G. M. Tveten, F. L. Bello Garrote, M. Guttormsen, A.-C. Larsen, V. W. Ingeberg, A. Görgen, and S. Siem, The γ-ray energy response of the Oslo Scintillator Array OS-CAR, Nucl. Instrum. Methods Phys. Res., Sect. A **985**, 164678 (2021).

[20] M. Guttormsen, A. Bürger, T. E. Hansen, and N. Lietaer, Nucl. Instrum. Methods Phys. Res., Sect. A **648**, 168 (2011).

[21] S. F. Mughabghab, *Atlas of Neutron Resonances: Resonance Parameters and Thermal Cross Sections Z=1–102* (Elsevier, Amsterdam, 2018).

[22] A. Gilbert and A. G. W. Cameron, A composite nuclear-level density formula with shell corrections, Can. J. Phys. **43**, 1446 (1965).

[23] T. von Egidy and D. Bucurescu, Systematics of nuclear level density parameters, Phys. Rev. C **72**, 044311 (2005); Erratum: Systematics of nuclear level density parameters [Phys. Rev. C **72**, 044311 (2005)], **73**, 049901 (2006).

[24] F. Pogliano, F. L. Bello Garrote, A. C. Larsen, H. C. Berg, D. Gjestvang, A. Görgen, M. Guttormsen, V. W. Ingeberg, T. W. Johansen, K. L. Malatji, E. F. Matthews, M. Markova, J. E. Midtbø, V. Modamio, L. G. Pedersen, E. Sahin, S. Siem, T. G. Tornyi, and A. S. Voyles, Observation of a candidate for the $M1$ scissors resonance in odd-odd ^{166}Ho, Phys. Rev. C **107**, 034605 (2023).

[25] M. Guttormsen, T. Tveter, L. Bergholt, F. Ingebretsen, and J. Rekstad, The unfolding of continuum γ-ray spectra, Nucl. Instrum. Methods Phys. Res., Sect. A **374**, 371 (1996).

[26] M. Guttormsen, T. Ramsøy, and J. Rekstad, The first generation of γ-rays from hot nuclei, Nucl. Instrum. Methods Phys. Res., Sect. A **255**, 518 (1987).

[27] P. A. M. Dirac, The quantum theory of the emission and absorption of radiation, Proc. R. Soc. London, Ser. A **114**, 243 (1927).

[28] E. Fermi, *Nuclear Physics* (University of Chicago Press, Chicago, 1950).

[29] A. Schiller, L. Bergholt, M. Guttormsen, E. Melby, J. Rekstad, and S. Siem, Extraction of level density and γ strength function from primary γ spectra, Nucl. Instrum. Methods Phys. Res., Sect. A **447**, 498 (2000).

[30] A. C. Larsen, M. Guttormsen, M. Krtička, E. Běták, A. Bürger, A. Görgen, H. T. Nyhus, J. Rekstad, A. Schiller, S. Siem, H. K. Toft, G. M. Tveten, A. V. Voinov, and K. Wikan, Analysis of possible systematic errors in the Oslo method, Phys. Rev. C **83**, 034315 (2011); Erratum: Analysis of possible systematic errors in the Oslo method [Phys. Rev. C **83**, 034315 (2011)] **97**, 049901 (2018).

[31] National Nuclear Data Center, information extracted from the NuDat database.

[32] T. Von Egidy, H. Schmidt, and A. Behkami, Nuclear level densities and level spacing distributions: Part II, Nucl. Phys. A **481**, 189 (1988).

[33] T. Ericson, The statistical model and nuclear level densities, Adv. Phys. **9**, 425 (1960).

[34] R. Capote, M. Herman, P. Obložinský, P. Young, S. Goriely, T. Belgya, A. Ignatyuk, A. Koning, S. Hilaire, V. Plujko, M. Avrigeanu, O. Bersillon, M. Chadwick, T. Fukahori, Z. Ge, Y. Han, S. Kailas, J. Kopecky, V. Maslov, G. Reffo *et al.*, RIPL–Reference Input Parameter Library for calculation of nuclear reactions and nuclear data evaluations, Nucl. Data Sheets **110**, 3107 (2009).

[35] M. Guttormsen, S. Goriely, A. C. Larsen, A. Görgen, T. W. Hagen, T. Renstrøm, S. Siem, N. U. H. Syed, G. Tagliente, H. K. Toft, H. Utsunomiya, A. V. Voinov, and K. Wikan, Quasicontinuum γ decay of ^{91,92}Zr: Benchmarking indirect (n, γ) cross section measurements for the s process, Phys. Rev. C **96**, 024313 (2017).

[36] F. Pogliano, A. C. Larsen, F. L. Bello Garrote, M. M. Bjørøen, T. K. Eriksen, D. Gjestvang, A. Görgen, M. Guttormsen, K. C. W. Li, M. Markova, E. F. Matthews, W. Paulsen, L. G. Pedersen, S. Siem, T. Storebakken, T. G. Tornyi, and J. E. Vevik, Indirect measurement of the (n, γ) ^{127}Sb cross section, Phys. Rev. C **106**, 015804 (2022).

[37] S. Goriely and V. Plujko, Simple empirical $E1$ and $M1$ strength functions for practical applications, Phys. Rev. C **99**, 014303 (2019).

[38] S. Goriely, S. Hilaire, S. Péru, and K. Sieja, Gogny-HFB+QRPA dipole strength function and its application to radiative nucleon capture cross section, Phys. Rev. C **98**, 014327 (2018).

[39] A. V. Ignatyuk, K. K. Istekov, and G. N. Smirenkin, Collective effects in the level density and the nuclear fission probability, Yad. Fiz. **30**, 1205 (1979).

[40] A. V. Ignatyuk, J. L. Weil, S. Raman, and S. Kahane, Density of discrete levels in ^{116}Sn, Phys. Rev. C **47**, 1504 (1993).

[41] S. Goriely, F. Tondeur, and J. Pearson, A Hartree–Fock nuclear mass table, At. Data Nucl. Data Tables **77**, 311 (2001).

[42] S. Goriely, S. Hilaire, and A. J. Koning, Improved microscopic nuclear level densities within the Hartree-Fock-Bogoliubov plus combinatorial method, Phys. Rev. C **78**, 064307 (2008).

[43] S. Hilaire, M. Girod, S. Goriely, and A. J. Koning, Temperature-dependent combinatorial level densities with the D1M Gogny force, Phys. Rev. C **86**, 064317 (2012).

[44] D. Brink, Individual particle and collective aspects of the nuclear photoeffect, Nucl. Phys. **4**, 215 (1957).

[45] S. Goriely and E. Khan, Large-scale QRPA calculation of E1-strength and its impact on the neutron capture cross section, Nucl. Phys. A **706**, 217 (2002).

[46] S. Goriely, E. Khan, and M. Samyn, Microscopic HFB+QRPA predictions of dipole strength for astrophysics applications, Nucl. Phys. A **739**, 331 (2004).

[47] S. Goriely, Radiative neutron captures by neutron-rich nuclei and the r-process nucleosynthesis, Phys. Lett. B **436**, 10 (1998).

[48] I. Daoutidis and S. Goriely, Large-scale continuum random-phase approximation predictions of dipole strength for astrophysical applications, Phys. Rev. C **86**, 034328 (2012).

[49] K. Heyde, P. von Neumann-Cosel, and A. Richter, Magnetic dipole excitations in nuclei: Elementary modes of nucleonic motion, Rev. Mod. Phys. **82**, 2365 (2010).

[50] D. Savran, T. Aumann, and A. Zilges, Experimental studies of the pygmy dipole resonance, Prog. Part. Nucl. Phys. **70**, 210 (2013).

[51] A. Bracco, E. Lanza, and A. Tamii, Isoscalar and isovector dipole excitations: Nuclear properties from low-lying states and from the isovector giant dipole resonance, Prog. Part. Nucl. Phys. **106**, 360 (2019).

[52] S. S. Dietrich and B. L. Berman, Atlas of photoneutron cross sections obtained with monoenergetic photons, At. Data Nucl. Data Tables **38**, 199 (1988).

[53] M. N. Harakeh and A. van der Woude, *Giant Resonances* (Oxford University Press, Oxford, 2001).

[54] B. L. Berman, M. A. Kelly, R. L. Bramblett, J. T. Caldwell, H. S. Davis, and S. C. Fultz, Giant resonance in deformed nuclei: Photoneutron cross sections for Eu^{153}, Gd^{160}, Ho^{165}, and W^{186}, Phys. Rev. **185**, 1576 (1969).

[55] R. Bergère, H. Beil, and A. Veyssière, Photoneutron cross sections of La, Tb, Ho and Ta, Nucl. Phys. A **121**, 463 (1968).

[56] V. V. Varlamov, A. I. Davydov, and V. D. Kaidarova, Evaluation of reliable cross sections of photoneutron reactions on ^{103}Rh and ^{165}Ho nuclei, Phys. At. Nucl. **82**, 212 (2019).

[57] M. Martini, S. Péru, S. Hilaire, S. Goriely, and F. Lechaftois, Large-scale deformed quasiparticle random-phase approximation calculations of the γ-ray strength function using the Gogny force, Phys. Rev. C **94**, 014304 (2016).

[58] U. Agvaanluvsan, A. Schiller, J. A. Becker, L. A. Bernstein, P. E. Garrett, M. Guttormsen, G. E. Mitchell, J. Rekstad, S. Siem, A. Voinov, and W. Younes, Level densities and γ-ray strength functions in ^{170,171,172}Yb, Phys. Rev. C **70**, 054611 (2004).

[59] H. T. Nyhus, S. Siem, M. Guttormsen, A. C. Larsen, A. Bürger, N. U. H. Syed, G. M. Tveten, and A. Voinov, Radiative strength functions in ^{163,164}Dy, Phys. Rev. C **81**, 024325 (2010).

[60] K. L. Malatji, K. S. Beckmann, M. Wiedeking, S. Siem, S. Goriely, A. C. Larsen, K. O. Ay, F. L. Bello Garrote, L. C. Campo, A. Görgen, M. Guttormsen, V. W. Ingeberg, P. Jones, B. V. Kheswa, P. von Neumann-Cosel, M. Ozgur, G. Potel, L. Pellegri, T. Renstrøm, G. M. Tveten *et al.*, Statistical properties of the well deformed ^{153,155}Sm nuclei and the scissors resonance, Phys. Rev. C **103**, 014309 (2021).

[61] A. Koning and J. Delaroche, Local and global nucleon optical models from 1 keV to 200 MeV, Nucl. Phys. A **713**, 231 (2003).

[62] E. Bauge, J. P. Delaroche, and M. Girod, Lane-consistent, semimicroscopic nucleon-nucleus optical model, Phys. Rev. C **63**, 024607 (2001).

[63] J. B. Czirr and M. L. Stelts, Measurement of the neutron capture cross section of holmium-165 and gold-197, Nucl. Sci. Eng. **52**, 299 (1973).

[64] M. Asghar, C. Chaffey, and M. Moxon, The neutron resonance parameters and average capture cross section of 165Ho, Nucl. Phys. A **108**, 535 (1968).

[65] D. McDaniels, P. Varghese, D. Drake, E. Arthur, A. Lindholm, I. Bergqvist, and J. Krumlinde, Radiative capture of fast neutrons by ^{165}Ho and ^{238}U, Nucl. Phys. A **384**, 88 (1982).

[66] W. Poenitz, Radiative capture of fast neutrons in ^{165}Ho and ^{181}Ta, Argonne National Laboratory Technical Report, 1975 (unpublished).

[67] J. H. Gibbons, R. L. Macklin, P. D. Miller, and J. H. Neiler, Average radiative capture cross sections for 7- to 170-keV neutrons, Phys. Rev. **122**, 182 (1961).

[68] J. Voignier, S. Joly, and G. Grenier, Capture cross sections and gamma-ray spectra from the interaction of 0.5- to 3.0-MeV neutrons with nuclei in the mass range A = 45 to 238, Nucl. Sci. Eng. **112**, 87 (1992).

[69] J. R. D. Lépine, R. Douglas, and H. Maia, Fast neutron capture cross-section measurements of rare-earth nuclei, Nucl. Phys. A **196**, 83 (1972).

[70] R. H. Cyburt, A. M. Amthor, R. Ferguson, Z. Meisel, K. Smith, S. Warren, A. Heger, R. D. Hoffman, T. Rauscher, A. Sakharuk, H. Schatz, F. K. Thielemann, and M. Wiescher, The JINA REACLIB database: Its recent updates and impact on type-I x-ray bursts, Astrophys. J. Suppl. Ser. **189**, 240 (2010).

[71] Y. Xu, S. Goriely, A. Jorissen, G. L. Chen, and M. Arnould, Databases and tools for nuclear astrophysics applications - BRUSsels nuclear LIBrary (BRUSLIB), Nuclear Astrophysics Compilation of REactions II (NACRE II) and Nuclear NETwork GENerator (NETGEN), Astron. Astrophys. **549**, A106 (2013).

[72] KADoNiS, data extracted using the KADoNiS On-Line Data Service, accessed 2023-03-05.

[73] R. L. Macklin and R. R. Winters, Stable isotope capture cross sections from the oak ridge electron linear accelerator, Nucl. Sci. Eng. **78**, 110 (1981).

[74] *Nuclear Data for Science and Technology*, *Proceedings of an International Conference, Jülich, 13–17 May 1991*, edited by S. M. Qaim (Springer, Berlin, 1992).

[75] N. Yamamuro, K. Saito, T. Emoto, T. Wadam, Y. Fujita, and K. Kobayashi, Neutron capture cross section measurements of Nb-93, I-127, Ho-165, Ta-181 and U-238 between 3.2 and 80keV, J. Nucl. Sci. Technol. **17**, 582 (1980).

[76] L. Siess and M. Arnould, Production of ^{26}Al by super-AGB stars, Astron. Astrophys. **489**, 395 (2008).

[77] S. Goriely and L. Siess, Sensitivity of the s-process nucleosynthesis in AGB stars to the overshoot model, Astron. Astrophys. **609**, A29 (2018).

[78] M. Asplund, N. Grevesse, A. J. Sauval, and P. Scott, The Chemical Composition of the Sun, Annu. Rev. Astron. Astrophys. **47**, 481 (2009).

[79] D. Reimers, Circumstellar absorption lines and mass loss from red giants, Mém. Soc. R. Sci. Liège **8**, 369 (1975).

[80] E. Vassiliadis and P. R. Wood, Evolution of low- and intermediate-mass stars to the end of the asymptotic giant branch with mass loss, Astrophys. J. **413**, 641 (1993).

98

Impact of level densities and γ-strength functions on r-process simulations

IV

Impact of level densities and γ-strength functions on r-process simulations

F. Pogliano[1, *] and A. C. Larsen[1, †]

[1]*Department of Physics, University of Oslo, N-0316 Oslo, Norway*
(Dated: August 3, 2023)

Studies attempting to quantify the sensitivity of the r-process abundances to nuclear input have to cope with the fact that the theoretical models they rely on, rarely come with confidence intervals. This problem has been dealt with by either estimating these intervals and propagating them statistically to the final abundances using reaction networks within simplified astrophysical models, or by running more realistic astrophysical simulations using different nuclear-physics models consistently for all the involved nuclei. Both of these approaches have their strengths and weaknesses. In this work, we use the reaction network code SkyNet [1] to run r-process calculations for five trajectories using 49 different neutron-capture rate models. Our results shed light on the importance of taking into account shell effects and pairing correlations in the network calculations.

I. INTRODUCTION

The origin of elements heavier than iron in the solar system can be attributed to three main production mechanisms, the p, the s and the r processes [2, 3]. While the first one is only responsible for the creation of some few, proton-rich nuclei, the latter two are each responsible for about 50% of the final solar abundances. The r process stands for *rapid* neutron-capture process, involves very high neutron densities ($\gtrsim 10^{20}$ cm^{-3}) and the neutron flux lasts for less than a second. Within the timescale of the r process, the neutron-capture rate is usually higher than the β-decay rate, making it possible to reach very exotic and neutron-rich nuclei up to the neutron drip line. During the r process, material will pile up at $A \approx 80$, 130 and 195 due to the high neutron flux as well as the neutron closed shells at $N = 50, 82, 126$.

The r-process sites have been a mystery for many years. The recent observation of the GW170817 gravitational waves event [4] from a neutron star merger (NSM) followed by its electromagnetic counterpart (e.g., Ref. [5]) provided observational evidence that heavy elements indeed are produced in these cataclysmic astrophysical events. Many other sites have been proposed over the years, such as prompt core-collapse supernovae, collapsars and the reheating of supernova ejecta by neutrinos (neutrino-driven wind, NDW), see e.g. Ref. [6] for a review.

The r process may happen under different astrophysical conditions and can be categorized as either hot or cold. The hot r process happens in environments with temperatures above a few GK. When temperatures exceed ≈ 2.0 GK the photo-disintegration rate wins over the β-decay rate and one reaches an $(n, \gamma) \leftrightarrows (\gamma, n)$ equilibrium, where only temperature, neutron abundance and irradiation time, the neutron separation energy S_n of the involved nuclei, their β-delayed neutron emissions and β decay rates are important for the final abundances [7].

If the r process instead happens mostly at colder temperatures, then other nuclear properties such as fission properties and neutron-capture reaction rates will also be crucial for the nucleosynthesis flow.

In order to model the r process in a realistic way, we need both the correct astrophysical conditions and the right nuclear input [8]. Radioactive-beam facilities and new experimental techniques may allow us to study the properties of some of the involved, exotic nuclei such as masses, β-decay rates and (n, γ)-rates (see e.g. the reviews in Refs. [9, 10] and references therein). Nevertheless, simulations are still heavily reliant on the predictions of theoretical models.

Sensitivity studies are a tool that can help us figure out the properties of which nuclei or nuclear regions have the biggest impact on the final abundances, and are thus of vital importance for planning and conducting experiments. These studies usually focus on one specific quantity (such as β-decay rates, masses or neutron-capture rates) by varying this quantity within some confidence interval or range of uncertainty, and then analyze the impact this variation has on the final abundances [7, 9]. Although all of these quantities are important, in this work we will focus on the neutron-capture rates.

The lack of confidence intervals in theoretical neutron-capture rates predictions poses a great problem when trying to estimate the uncertainties in the final abundances stemming from the uncertainties in the nuclear models. In addition to the need for realistic simulations of the astrophysical environment(s), this lack is posing a significant challenge for sensitivity studies in the attempt to nail down which nuclei or regions in the nuclear chart that influence the r-process abundances the most.

Several sensitivity studies for neutron-capture rates can be found in the literature. These studies may be divided into two categories, depending on the approach used to address these astrophysical and nuclear aspects of the uncertainties. We label the first category the "statistical approach". Here, a particular set of initial conditions for the r process is chosen so that the network simulation reproduces some known abundances (e.g. the solar r-process abundances, or the ones from a more sophisti-

---

* francesco.pogliano@fys.uio.no
† a.c.larsen@fys.uio.no

cated astrophysical simulation). The abundance yields from this simulation are referred as the "baseline". The neutron-capture rates of a set of the involved nuclei are then modified individually, and for every rate variation the r-process simulation is run again with the same initial conditions, and every new output is compared to the baseline. The nuclei whose variation will lead to the biggest change in abundances with respect to the baseline, are identified as the most interesting to study experimentally. The capture rates are varied either by multiplying and dividing the baseline rates by a constant factor [11–14], by assuming the rate uncertainty to have a log-normal distribution about the baseline value [9] or by assuming the distribution to be flat within the predictions of a set of theoretical models, and log-normal outside [15]. In the last two cases, the probability distributions are used to pick the variations using a Monte Carlo technique, and the results are then analyzed statistically [9, 16, 17].

The statistical approach is a powerful tool when trying to estimate model prediction uncertainties, and it allows to study the impact of individual nuclear properties. However, it has two drawbacks. Firstly, by varying rates individually, one does not properly account for well-known nuclear properties such as pairing effects. It is well known that in general, neutron-odd nuclei will have a higher neutron-capture rate than neighboring neutron-even nuclei, as long as they are not close to a neutron magic number. In Fig. 1, using the Sb isotopic chain as an example, we see how the rates and Q-values gradually decrease the more neutrons are present in the nucleus. We also observe how odd-even effects (neutron pairing) lead to a higher capture rate and Q-value for isotopes with an odd number of neutrons, compared to their even neighbors. Such correlations might get lost if the multiplicative factor is bigger than the typical difference between neighboring isotopes.

Secondly, the statistical-approach simulations of the r process are relying on one-zone models for the astrophysical conditions, meaning that the final abundances are reproduced by only one set of initial conditions. This is usually not the case in a real astrophysical scenario, where many zones with different initial conditions contribute to the final abundances. This means that while the variation of the neutron-capture rate in a nucleus in the statistical approach may lead to a significant change in the final abundances, this change might become insignificant when mixed together with the resulting abundances from the other "zones". In short, by disregarding the correlations between neighboring nuclei one may overestimate uncertainties in the final abundances, and the one-zone approach may point to single nuclei being important, while this importance could be averaged out when doing multi-zone calculations.

We label the second category of sensitivity studies the "model-consistent approach". Here, the problems with the statistical approach are addressed by simulating the full astrophysical event where the r process takes place
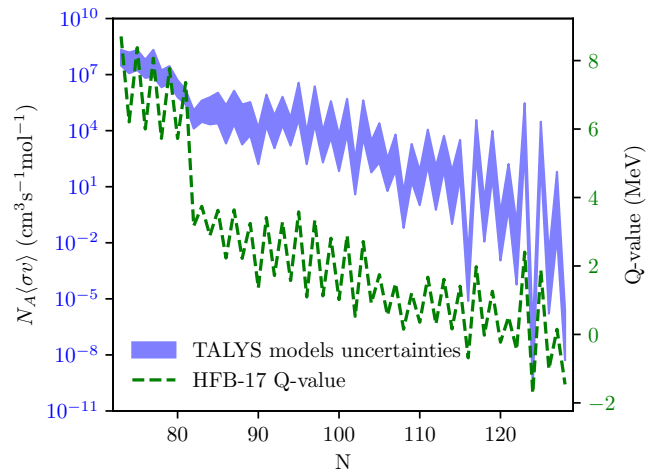

FIG. 1. The evolution of the neutron-capture rate $N_A\langle\sigma v\rangle$ evaluated at $T = 1.0$ GK and the (n,γ) Q-value along the Sb isotopic chain for all 48 theoretical TALYS models explained in Section III, calculated with the HFB-17 [18] mass model (see text).

(many trajectories with different physical parameters) and by employing the same nuclear models consistently for the whole nuclear chart. The nuclear uncertainties are propagated to the final abundances by repeating the simulation with different theoretical models of the quantity under consideration. This means that the final abundances represent the weighted sum of the abundances from different "zones". Furthermore, when it comes to neutron-capture rates, correlations between neighboring isotopes are accounted for as these are changed model-consistently. Although there are no studies for the r process neutron-capture rates to date, one may find mass and β-decay sensitivity studies in the context of neutron star mergers by Kullmann et al. [19] or for neutron-capture rates in the intermediate neutron-capture process by Goriely et al. [20]. However, also this approach comes with some drawbacks. First, potential errors and uncertainties in the theoretical models themselves are not accounted for (such as the choice of the interaction and its parameter uncertainties in a mean-field calculation), and this may lead to a significant underestimation of the actual uncertainties in the final abundances. Second, models may give reliable predictions of nuclei in a certain mass region, but not so in another, and this may lead to apparently confident but wrong abundance predictions.

In this work, we will investigate the impact of varying neutron-capture rates for the r process using a model-consistent approach for five different trajectories. A trajectory represents the time evolution of density and temperature in the expanding "bubble" simulating material from e.g. a supernova or NSM. A single trajectory is equivalent to a one-zone simulation, and is therefore not necessarily representative for the actual nucleosynthesis outcome in the specific astrophysical sites. Nevertheless,

the results can be compared to the predicted abundance uncertainties from the sensitivity studies using the statistical approach, and hopefully cast light on systematic and methodical sources of biases and errors in both methods. The details on the astrophysical simulations are described in Section II, while the choice of nuclear inputs is discussed in Section III. In Section IV the results are shown and discussed, and a summary of the main findings is given in V.

II.   NETWORK CALCULATIONS

In this work we make use of the five trajectories considered in Mumpower *et al.* [9]. When not given directly by the multizone simulation, the initial entropy S, the electron fraction Y_e and the dynamical timescale τ for the trajectories are provided below:

a) A "hot" r process with low entropy: $S = 30\ k_B$, $Y_e = 0.20$, $\tau = 70$ ms.

b) A "hot" r process with high entropy: $S = 100\ k_B$, $Y_e = 0.25$, $\tau = 80$ ms.

c) A "cold" r process from a neutrino-driven wind (NDW) scenario modeled after Arcones *et al.* [21], with artificially reduced Y_e to 0.31.

d) A neutron-rich NSM trajectory modeled after Goriely *et al.* [22].

e) A "hot" r process with very high entropy: $S = 200$ k_B, $Y_e = 0.30$, $\tau = 80$ ms.

Here, we have labeled the trajectory "hot" when the $(n,\gamma) \Leftrightarrow (\gamma,n)$ equilibrium is the dominant mechanism ($T \gtrsim 1$ GK until freezeout), and "cold" when the trajectories fall out of the $(n,\gamma) \Leftrightarrow (\gamma,n)$ equilibrium before the neutron flux is exhausted (see Fig. 1 in Mumpower et al. [9] for a plot of the temperature time evolution of the a) and c) trajectories). These trajectories are used to run one-zone r-process simulations using SkyNet [1] for a time of 1 Gy. The reaction network includes electron screening and uses the JINA REACLIB library rates [23] for all nuclear reactions except for neutron capture, as discussed in the following section. Spontaneous and neutron-induced fission was modeled with the rates of Panov *et al.* [24], with zero outgoing neutrons. Although we expect neutrons to be emitted during fission, results with two and four emitted neutrons per fission event did not yield appreciable differences in the final abundances for the region considered.

III.   NUCLEAR INPUT

We calculate neutron-capture rates for every unstable neutron-rich nucleus using the nuclear reaction code TALYS 1.95 [25, 26]. The code exploits the compound nucleus picture and uses the Wolfenstein-Hauser-Feshbach [27, 28] (WHB) formalism to calculate the neutron-capture rate. The main nuclear ingredients to the rate calculations are three nuclear statistical quantities: the optical-model potential (OMP), the nuclear level density (NLD) and the γ-ray strength function (GSF).

The neutron-capture rate $N_A\langle\sigma v\rangle(T)$ is calculated from the (n,γ) cross section $\sigma_{n\gamma}$ as [7]

$$N_A\langle\sigma v\rangle(T) = N_A \left(\frac{8}{\pi\widetilde{m}}\right)^{1/2} \frac{1}{(k_B T)^{3/2}\,G(T)} \times$$
$$\int_0^\infty \sum_\mu \frac{2J_t^\mu + 1}{2J_t^0 + 1}\sigma_{n\gamma}^\mu(E)E \exp\left[-\frac{E + E_\mu}{k_B T}\right]\mathrm{d}E, \quad (1)$$

where N_A is Avogadro's number, $\widetilde{m}$ the reduced mass of the target nucleus, k_B Boltzmann's constant, T the temperature, J_t the target's spin, E the relative energy between target and neutron, and $G(T)$ is the partition function defined as:

$$G(T) \equiv \sum_\mu \frac{(J_\mu + 1)}{(J_0 + 1)}e^{-E_\mu k_B}. \quad (2)$$

The suffixes μ and 0 represent the μ-excited states and the ground state, respectively, and $\sigma_{n\gamma}^\mu$ represent thus the neutron-capture cross section when the nucleus is excited at a certain energy level μ. In the WHF formalism, the neutron-capture cross section is calculated as

$$\sigma_{n,\gamma}(E_x) = \sum_{J,\pi} \sigma_n^{\mathrm{CN}}(E_x, J, \pi)P_\gamma(E_x, J, \pi), \quad (3)$$

where $\sigma_n^{\mathrm{CN}}(E_x, J, \pi)$ is the probability that a free neutron ends up forming an excited compound nucleus of excitation energy E_x, spin J and parity π, and $P_\gamma(E_x, J, \pi)$ the probability of the compound nucleus to γ-decay, effectively capturing the neutron. The first factor is described by the OMP, while the second can be expressed as

$$P_\gamma(E_x, J, \pi) = \frac{\mathcal{T}_\gamma(E_x, J, \pi)}{\mathcal{T}_{\mathrm{tot}}(E_x, J, \pi)}, \quad (4)$$

where $\mathcal{T}_\gamma(E_x, J, \pi)$ is the γ-transmission coefficient, and $\mathcal{T}_{\mathrm{tot}} = \mathcal{T}_\gamma + \mathcal{T}_n$ is the total transmission coefficient (where γ-decay and neutron emission usually are the only two allowed decay channels). Here, $\mathcal{T}_\gamma(E_x, J, \pi)$ may be expressed as

$$\mathcal{T}_\gamma(E_x, J, \pi) = 2\pi \sum_{X,L} \int_0^{E_x} E_\gamma^{2L+1}f^{XL}(E_\gamma) \times$$
$$\rho(E_x - E_\gamma, J, \pi)\mathrm{d}E_\gamma, \quad (5)$$

where X and L represent the electromagnetic mode (electric E or magnetic M), L the multipolarity, E_γ the transition energy, and f and ρ the GSF and the NLD, respectively.

TALYS 1.95 provides six different NLD models and eight GSF models. The NLD models with their respective TALYS keyword in parenthesis are:

- The constant-temperature + Fermi gas model (CTM, keyword `ldmodel 1`) [29]

- The Back-shifted Fermi gas model (BSFG, keyword `ldmodel 2`) [29, 30]

- The Generalised Superfluid model (GSM, keyword `ldmodel 3`) [31, 32]

- The Hartree-Fock plus Bardeen-Cooper-Schrieffer statistical model (HFB+Stat, keyword `ldmodel 4`), tables from Ref. [33]

- The Hartree-Fock-Bogoliubov + combinatorial model (HFB+comb, keyword `ldmodel 5`), tables from Ref. [34]

- The temperature-dependent Gogny-Hartree-Fock-Bogoliubov model (THFB+comb, keyword `ldmodel 6`) [35]

where the first three are phenomenological models where fitting parameters are adjusted to reproduce known experimental data. The last three models are semi-microscopic, meaning that their predictions are based on a more fundamental treatment of the nuclear many-body problem. However, we note that even these models are subject to adjustments through fit parameters in order for them to reproduce measured data such as known, discrete levels and s-wave neutron-resonance spacings.

Correspondingly, the TALYS GSF models are:

- The Kopecky-Uhl generalized Lorentzian (GLO, keyword `strength 1`) [37]

- The Brink-Axel standard Lorentzian (SLO, keyword `strength 2`) [38, 39]

- The Hartree-Fock-BCS + QRPA tables based on the SLy4 interaction (SLy4+QRPA, keyword `strength 3`) [40]

- The HFB + QRPA calculation based on the BSk7 interaction (BSk7+QRPA, keyword `strength 4`) [41]

- The hybrid model (Hybrid, keyword `strength 5`) [42]

- The BSk7 + QRPA model with T-dependent width (BSk7T+QRPA, keyword `strength 6`) [41]

- The relativistic mean field + continuum QRPA calculation with T-dependent width (RMF+cQRPA, keyword `strength 7`) [43]

- The Gogny-HFB + QRPA calculation complemented by low-energy enhancement (D1M+QRPA+0lim, keyword `strength 8`) [44]

where the first two again are phenomenological models, and the last six are semi-microscopic models. From TALYS 1.96 [45], a ninth GSF model was introduced, namely the simplified modified Lorentzian (SMLO) [46]. Although not included in the present study, this has now become the default choice of GSF model in TALYS. This exclusion is not expected to influence the results of the study, as the neutron-capture rate predictions using this model usually fall within the extremes of the other model combinations.

While TALYS provides different OMP models, the choice of one model over another becomes gradually less significant when the temperature increases; for typical r-process temperatures the OMP is considered to be of minor importance[1]. For this reason we only apply the Koning & Delaroche OMP model [48].

Not part of the compound nucleus picture is the direct capture (DC) mechanism for neutron capture (see, e.g., Refs. [49, 50] and references therein). This mechanism is expected to contribute with a small cross section, so that for many cases compound capture cross section completely dominates the total cross section. However, near the neutron drip line, close to and at neutron shell closures, the compound capture cross section becomes small enough so that the DC contribution may become appreciable and even the dominant part. We have chosen to not include DC this study, as its model predictions are rather uncertain, and we want to focus on the rates calculated via the compound nucleus picture, as these can be constrained with experimental data from Oslo-type experiments.

For the mass model, we use the FRDM-2012 model by Möller *et al.* [36] (TALYS keyword `massmodel 1`) and the Skyrme-Hartree-Fock-Bogoliubov model [18] (HFB-17), corresponding to the TALYS keyword `massmodel 2`. Apart from being readily available in TALYS, these two mass models (or similar, updated versions of them) have been shown to produce comparable abundances in mass sensitivity studies, see e.g. [19, 51].

By combining the six NLD models and the eight GSF models we obtain 48 different neutron-capture rate models for each chosen mass model. These were calculated for all elements from Fe ($Z = 26$) up to Sg ($Z = 106$), from the first neutron-rich unstable isotope up to the drip line. Although the Q-value for neutron capture on N-even nuclei may already become negative before the drip line (see e.g. Fig. 1), the neutron-capture rates were nevertheless included for completeness, as they can become relevant for trajectories with high neutron densities.

We note that TALYS provides different settings to modify and customize the input; nevertheless, we decided to keep these to the default ones, as the scope of the study is not necessarily to give an accurate description of the r process, but to analyze the qualitative

————

[1] This is not true if the isovector part of the potential is strongly enhanced, see Ref. [47].
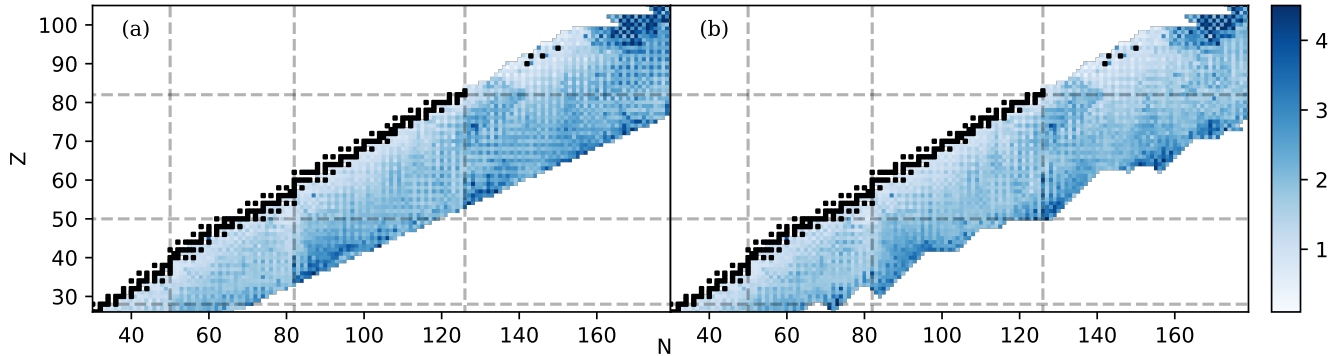
FIG. 2. (Color online) Differences (in orders of magnitude) between the highest and lowest predicted neutron-capture rate at $T = 1.0$ GK for all the 48 models using (a) the FRDM-2012 [36] mass model (an updated version of what the JINA REACLIB rates [23] are based on) and (b) the HFB-17 [18] mass model. The plotted differences $\Delta(Z, N)$ have been calculated as $\Delta(Z, N) = \log_{10}(N_A \langle \sigma v \rangle_{\max}) - \log_{10}(N_A \langle \sigma v \rangle_{\min})$, where $N_A \langle \sigma v \rangle_{\max,\min}$ represent the maximum and minimum predicted rates, respectively. The different mass models predict different neutron drip lines, and this is the reason for the different shapes.
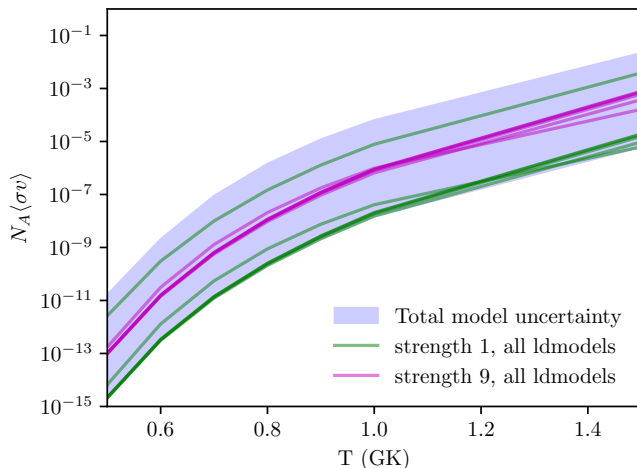

FIG. 3. (Color online) Neutron-capture rate predictions for different choices of GSF while varying the NLD models, using ^{182}Xe as an exemplary case (see text).
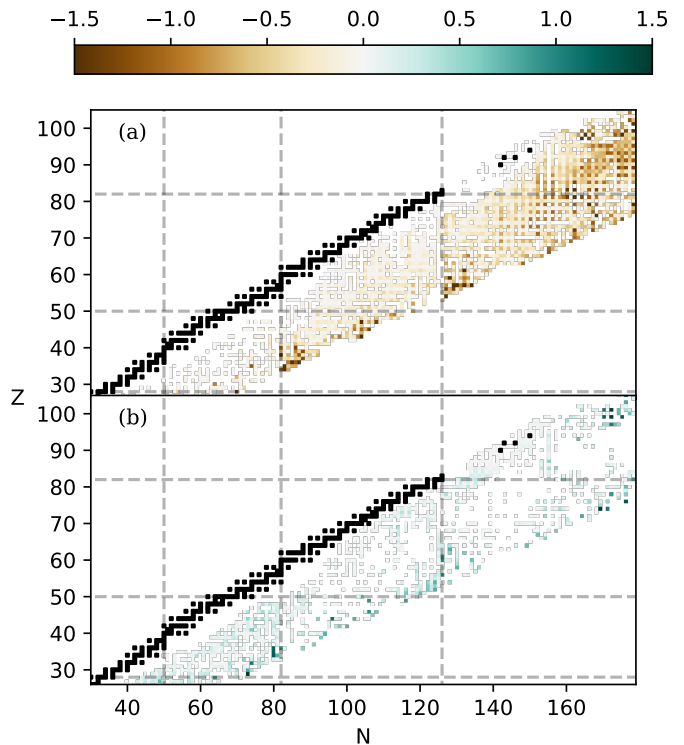

FIG. 4. (Color online) Difference between Figs. 2(b) and 2(a), showing which mass model generates the biggest spread in predicted neutron capture rates, for all the 48 combinations of NLD and GSF models. The negative differences (i.e. where the FDRM-2012 model predicts larger uncertainties) are shown in the top panel, while the positive ones (where the HFB-17 predicts the larger uncertainties) in the bottom panel.

change in the predicted abundances when using the same neutron-capture rate model consistently throughout the nuclear chart. Starting from TALYS 1.96 [45], new default NLD and GSF models were introduced, where a new `strength 9` (the SMLO model introduced above) replaced the GLO as default GSF, and where $M1$ components such as a parametrized upbend and scissors mode were added to all GSFs. Although these structures in the GSF are observed experimentally for some nuclei, there are still significant challenges in our understanding of these structures that make it highly questionable to add them to all nuclei on a general basis. For example, the scissors resonance is difficult to reproduce correctly, as models still overestimate or underestimate its strength
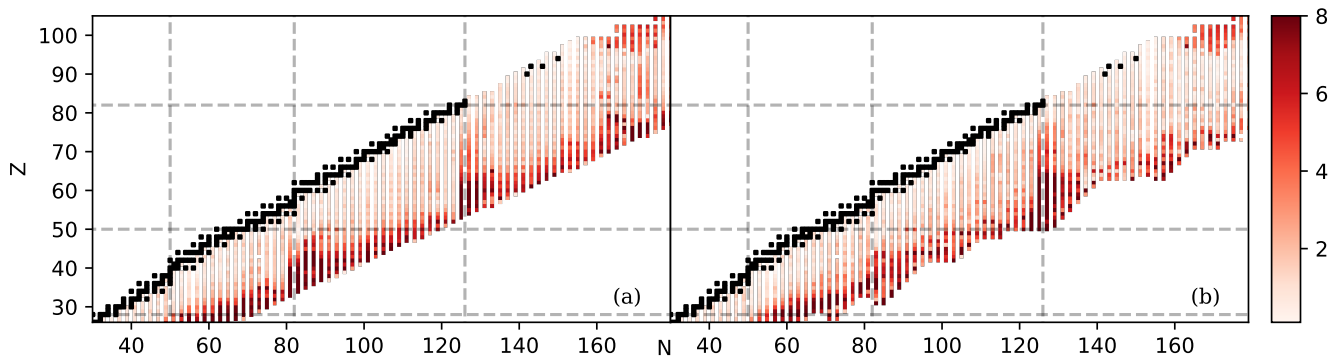
FIG. 5. (Color online) The biggest difference for each of the 48 models for the neutron-capture rate at $T = 1.0$ GK of an N-odd nucleus (Z, N) and its N-even neighbors $(Z, N - 1)$ and $(Z, N + 1)$. The difference (in orders of magnitude) is plotted against (Z, N) for (a) the FRDM-2012 [36] mass model and (b) the HFB-17 [18] mass model. The differences were calculated in a similar fashion as for those in Fig. 2.
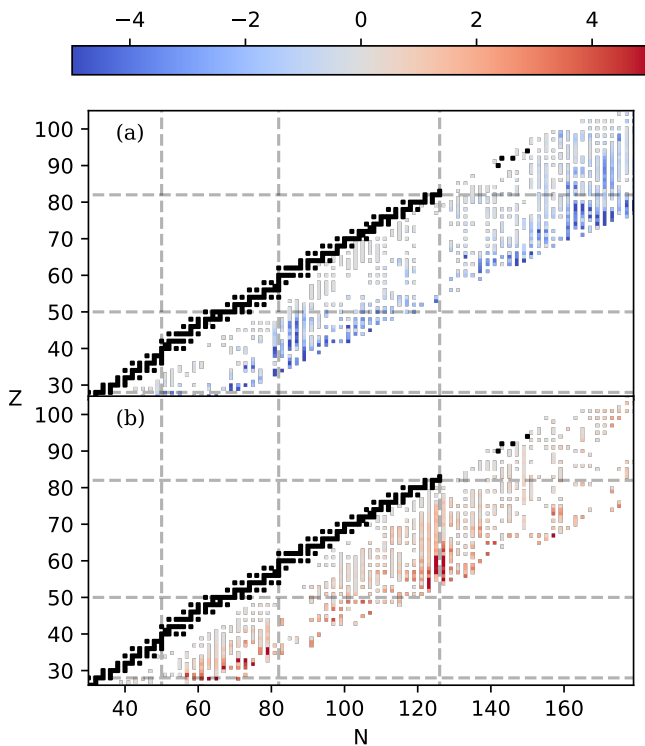

FIG. 6. (Color online) Difference between Figs. 5(b) and 5(a), showing which mass model generates the highest staggering (see text). The negative differences are plotted in the top panel, while the positive ones in the bottom panel.

when compared to experimental data (see e.g. Ref. [52]). For the upbend, we still do not have reliable systematics or even confirmed its presence throughout the nuclear chart even for stable nuclei, let alone exotic neutron-rich ones. It has so far mainly been observed in lighter nuclei (see e.g. Ref. [53]), and it is still not clear whether this

feature is actually due to $M1$ transitions, or $E1$ transitions, or a mix of both [54]. Nevertheless, there is no doubt that its presence could indeed impact the neutron-capture rates [55]. We deem that a thorough study of the $M1$ scissors mode and the upbend would be highly important, but would also be outside the scope of the present study. Considering also that the SMLO model usually yields neutron-capture rates within the extremes produced by other model combinations, we decided that the use of TALYS 1.95 instead of 1.96 was both satisfactory with respect to the objective of the study, and gave us better control on the different models, parameters and features included.

All other nuclear reactions rates are described using the JINA REACLIB library [23]. This library is based on the NON-SMOKER theoretical rates [56]. For every neutron-capture rate model we substitute the default JINA REACLIB neutron-capture rates (and those for their inverse reaction) with the TALYS-calculated ones. These, together with the default JINA REACLIB rates, are the 49 neutron-capture models used in the reaction network calculations in this work.

In Fig. 2, we show the differences between the highest and the lowest predicted neutron-capture rate out of the 48 TALYS calculations taken at temperature 1.0 GK in the astrophysical environment for the two mass models.[2] We calculate this difference as

$$\Delta(Z, N) = \log_{10}(N_A \langle \sigma v \rangle_{\text{max}}) - \log_{10}(N_A \langle \sigma v \rangle_{\text{min}}) \quad (6)$$

where $N_A \langle \sigma v \rangle_{\text{max,min}}$ represent the maximum and minimum predicted rates, respectively. As can be seen, the deviations can be very large, in particular in the regions

_____

[2] Because of a bug in TALYS, the rates using `strength 6` were not used for the isotopes of Tm ($Z = 69$) between $A = 215$ and 248. For these few affected nuclei, the JINA REACLIB rates were used instead.

close to the neutron drip line and in the regions near the neutron magic numbers $N = 82, 126$.

It is unfortunately difficult to investigate if such large uncertainties are due to the deviations in NLD or GSF model predictions, since, as seen in Eq. (5), the two quantities are convoluted with each other in such a way that it is difficult to isolate the contribution of one of the two quantities. This means that, e.g., we could hold a GSF model constant, vary the six NLD models and obtain a large variation in the calculated neutron-capture rate predictions. This would lead us to believe that the choice of NLD model is responsible for such large uncertainties, until we try again by holding a different GSF model constant while varying the NLD models, and obtain more similar predictions for all employed GSF models. This effect is shown in Fig. 3. Even if some choices for the GSF model will yield a large variation in the predicted neutron-capture rates when changing the NLD model, others may instead yield rather similar predictions, here exemplified in the context of ^{182}Xe(n,γ) by using the GLO (`strength 1`, [37]) and the SMLO (`strength 9`, [46]) models for the GSF, respectively.

Another consideration when using NLD and GSF models to calculate neutron-capture rates in the context of the r process, is the fact that for very exotic nuclei with low (or even negative) (n,γ) Q-values, the neutron-capture cross section becomes very sensitive to levels (or rather, resonances) at very low excitation energies and their decay properties. However, the low-lying levels are experimentally unknown for the very neutron-rich region of the r process. Moreover, the choice of bin size may also play a significant role for the neutron-capture rate calculation. When also considering that the NLD models are typically tested against neutron-resonance data at high excitation energies, it suggests that the level density at low E_x in the exotic, neutron-rich mass region is particularly poorly constrained and, thus, the neutron-capture rate may be even more uncertain than what models predict.

We note that there is a large difference in the rate predictions for very heavy nuclei around $Z = 100$ for both mass models. This might not be surprising as there is no or very little data in this region, due to the fusion-evaporation reactions used to produce very heavy and super-heavy nuclei that favor production channels with (multiple) neutron emission(s). We also remark that the general trends of the two mass models applied here are very similar. Fig. 2 shows that, for both mass models, the 48 predicted neutron capture rates tend to agree more when close to the valley of stability, than close to the drip line, as expected. In Fig. 4, we show the difference between Figs. 2(b) and 2(a) as a way to quantify the difference in the predicted spread for the two mass models. Fig. 4(a) shows for example that the FRDM-2012 overall generates larger uncertainties, especially for neutron-rich, $N > 126$ nuclei, and right after neutron shell closures for $Z \approx 35, 55$ close to the drip line. Fig. 4(b) shows that the HFB-17 model has larger uncertainties for light nu-

clei ($50 < N < 82$) and again near the drip line right before the $N = 126$ isotone.

As a way to quantify the odd-even effects in each model, we would also like to investigate how the predicted neutron-capture rate changes when going from an N-odd nucleus (Z, N) and its N-even neighbors $(Z, N - 1)$ and $(Z, N + 1)$. This is shown in Fig. 5, where the biggest difference between the neutron-capture rate of an N-odd nucleus and each of its neighbors is chosen and plotted. The differences are calculated in the same way as for Fig. 2, where a difference value of e.g. 6 means a 6-orders-of-magnitude difference in neutron-capture rate between an N-odd nucleus and one of its N-even neighbors, within the same model. Unsurprisingly, the biggest staggering is shown to be around N-shell closures, and near the drip line.

In order to investigate how the two mass models compare, we show in Fig. 6 the difference between 5(b) and 5(a), again in orders of magnitude. The lower plot indicates where the HFB-17 mass model [18] generates the higher staggering in neutron-capture rates, and the upper plot for the FRDM mass model [36], correspondingly. We observe how the FRDM-2012 model (blue squares in Fig. 6(a)) predicts a larger staggering for neutron-rich nuclei around the $N = 82$ isotone, and for the $N > 160$ region, while the HFB-17 model (red squares in Fig. 6(b)) instead predicts larger staggering close to the $N = 126$ isotone and generally for the $82 < N < 126$ region, again for neutron rich nuclei.

IV. RESULTS

The abundance yields obtained from the five trajectories using SkyNet can be seen in Fig. 7[3]. We observe a marked staggering effect especially in the rare-earth peak. This may be mostly due to the choice of mass model, as the HFB-17 predicts strong odd-even effects in the nuclide chart region that would eventually β-decay to the rare-earth elements, see Fig. 6. This staggering in fact disappears for trajectories (c) and (d) when the JINA REACLIB rates are used, which are calculated with the NON-SMOKER formula [56], using the FRDM mass model [36]. Interestingly, the effect is preserved in all simulations for trajectory (e), including the one using JINA REACLIB. This is to be compared to the final abundances uncertainty band plotted in Fig. 11b from Mumpower *et al.* [9], where the same trajectory was employed with the same mass model (HFB-17), but by varying the neutron-capture rates using the statistical approach. Here the staggering is almost non-present, showing how the impact of shell effects and pairing correlations may indeed be washed out, if the assumed model uncertainties are large enough to hide them.

---

[3] The data used for the figure can be found in Ref. [57].

Another noticeable result is the relatively small uncertainties we obtain from using different neutron-capture models as compared to Fig. 11b in Mumpower *et al.* [9]. The same can be concluded when comparing to the uncertainty bands of Fig. 13 in Nikas *et al.* [15] for different trajectories. The uncertainties we obtain here are of course underestimated, because we have not considered parameter uncertainties in the input models used to calculate the neutron-capture reaction rates. Even so, we find that the difference between the neutron-capture rate models used in this work may be of several orders of magnitude as shown in Fig. 2, similar to what the typical magnitude of the assumed rate errors are in the statistical approach. This suggests that the inclusion of shell effects and pairing correlations does play an important and non-negligible role in reducing prediction uncertainties in the calculated abundances.

Finally, in all the five different abundance yields in Fig. 7, one can see how the $A \approx 186$ region has a bigger relative uncertainty compared to the rest. This is because it originates from the most neutron-rich region close to the $N = 126$ isotone, above the (possibly) doubly-magic ^{176}Sn and around the "dark blue" regions in Fig. 2(b). This region is extremely neutron-rich and exotic, with very large uncertainties in the predicted neutron-capture rates, which are again reflected in the final abundance predictions.

Unfortunately, the region around the $N = 126$ isotones, is very difficult to study experimentally. However, although not reaching ^{176}Sn, new and upcoming experimental facilities like FRIB [59], FAIR [60] and the $N = 126$ factory [61], might provide data in the region $Z = 70$-80, $N \approx 126$, which would help constrain the theoretical mass models. Moreover, methods for measuring neutron-capture cross sections in inverse kinematics as suggested by e.g. Reifarth *et al.* [62] and Dillmann *et al.* [63] would be extremely valuable to get experimental information on neutron-capture rates of neutron-rich nuclei. Moreover, methods for measuring neutron-capture cross sections in inverse kinematics as suggested by e.g. Reifarth *et al.* [62] would be extremely valuable to get experimental information on neutron-capture rates of neutron-rich nuclei. Also indirect techniques like the Oslo method (Ref. [10] and references therein), the surrogate method (see Ref. [64] and references therein), the β-Oslo method [65], the shape method [66, 67] and the inverse-kinematics Oslo method [68] would provide useful information to constrain the neutron-capture rates.

V. SUMMARY

The lack of confidence intervals in theoretical neutron-capture rates predictions poses a great problem for the correct quantification of final abundances errors of the r process. This in turn makes the task of performing sensitivity studies difficult, and the conclusions on which nuclear properties have the biggest impact po-
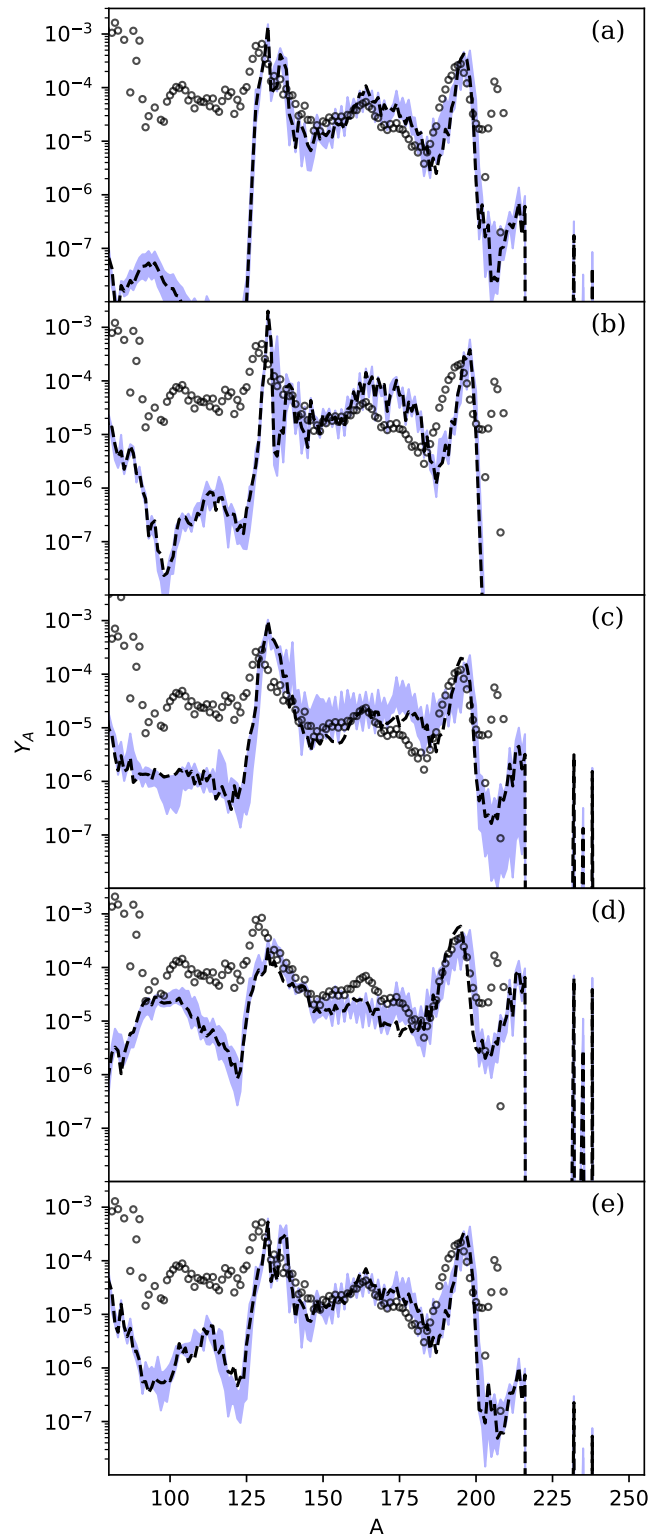

FIG. 7. The abundances from the five trajectories after 1 Gy evolution. In blue is the span of the final abundance predictions calculated from the 48 neutron-capture rate models. The black dashed line represents the abundances obtained using JINA REACLIB rates [23], while the black dots are the r solar abundances [58] scaled down to fit the third peak at $A \approx 195$.

tentially questionable. In this work we have discussed the strengths and weaknesses of two different approaches found in the literature, dubbed here as the "statistical" and the "model-consistent" approach. While the former tries to quantify the statistical errors in model predictions and attempts to propagate these using one-zone astrophysical models and interpret the results statistically, the latter sticks to one or few models and use them consistently for all the involved nuclei in more sophisticated, multi-zone simulations.

We have presented the results of network calculations using five different r-process trajectories, each having different inputs and representing different astrophysical scenarios. For each of these, 48 different neutron-capture rate models (plus the JINA REACLIB rates) were employed in order to estimate the sensitivity of the final abundances to these reaction rates. Although these are not meant to be interpreted as realistic representations of the r process in these sites, this study provides some insights on the different strengths and weaknesses of the two approaches mentioned above.

A staggering effect was observed especially for the rare-earth region in all trajectories, a feature that cannot be explained solely by the choice of mass model. The fact that this does not appear in similar studies using the statistical approach [9, 15], even using the same mass model, suggests that the assumption of uncorrelated statistical errors in these studies may indeed mask the shell effects and pairing correlations, and probably overestimate the uncertainties. This is also corroborated by the fact that our uncertainties are markedly smaller than those obtained in the above mentioned studies, even though the rate uncertainties are of similar magnitude.

We do remark that the obtained uncertainties in this study are probably underestimated with regard to the real uncertainties, as uncertainties in the model parameters are not taken into account. A detailed investigation including these uncertainties is beyond the scope of this work, but would be highly desirable to pursue in the future. We also note that experimental information for neutron-rich nuclei, especially near the $N = 126$ closed shell, would be extremely valuable to better constrain the models in this mass region.

VI. ACKNOWLEDGMENTS

[1] J. Lippuner and L. F. Roberts, Skynet: A modular nuclear reaction network library, The Astrophysical Journal Supplement Series 233, 18 (2017).

[2] E. M. Burbidge, G. R. Burbidge, W. A. Fowler, and F. Hoyle, Synthesis of the elements in stars, Rev. Mod. Phys. 29, 547 (1957).

[3] A. G. W. Cameron, Nuclear reactions in stars and nucleogenesis, Publications of the Astronomical Society of the Pacific 69, 201 (1957).

[4] B. P. Abbott et al. (LIGO Scientific Collaboration and Virgo Collaboration), GW170817: Observation of gravitational waves from a binary neutron star inspiral, Physical Review Letters 119, 161101 (2017).

[5] I. Arcavi, G. Hosseinzadeh, D. A. Howell, C. McCully, D. Poznanski, D. Kasen, J. Barnes, M. Zaltzman, S. Vasylyev, D. Maoz, and S. Valenti, Optical emission from a kilonova following a gravitational-wave-detected neutron-star merger, Nature (London) 551, 64 (2017).

[6] T. Kajino, W. Aoki, A. Balantekin, R. Diehl, M. Famiano, and G. Mathews, Current status of r-process nucleosynthesis, Progress in Particle and Nuclear Physics 107, 109 (2019).

[7] M. Arnould, S. Goriely, and K. Takahashi, The r-process of stellar nucleosynthesis: Astrophysics and nuclear physics achievements and mysteries, Physics Reports 450, 97–213 (2007).

[8] G. Martínez-Pinedo and K. Langanke, Nuclear quests for the r-process, The European Physical Journal A 59, 67 (2023).

[9] M. Mumpower, R. Surman, G. McLaughlin, and A. Aprahamian, The impact of individual nuclear properties on r-process nucleosynthesis, Progress in Particle and Nuclear Physics 86, 86 (2016); Corrigendum to "the impact of individual nuclear properties on r-process nucleosynthesis" [j. prog. part. nucl. phys. 86c (2015) 86–126], Progress in Particle and Nuclear Physics 87, 116 (2016).

[10] A. Larsen, A. Spyrou, S. Liddick, and M. Guttormsen, Novel techniques for constraining neutron-capture rates relevant for r-process heavy-element nucleosynthesis, Progress in Particle and Nuclear Physics 107, 69 (2019).

[11] R. Surman, J. Beun, G. C. McLaughlin, and W. R. Hix, Neutron capture rates near $A = 130$ that effect a global change to the r-process abundance distribution, Phys. Rev. C 79, 045809 (2009).

[12] M. R. Mumpower, G. C. McLaughlin, and R. Surman, Influence of neutron capture rates in the rare earth region on the r-process abundance pattern, Phys. Rev. C 86, 035803 (2012).

[13] R. Surman, M. Mumpower, R. Sinclair, K. L. Jones, W. R. Hix, and G. C. McLaughlin, Sensitivity studies for the weak r process: neutron capture rates, AIP Advances 4, 10.1063/1.4867191 (2014).

[14] D. Vescovi, R. Reifarth, S. Cristallo, and A. Couture, Neutron-capture measurement candidates for the r-process in neutron star mergers, Frontiers in Astronomy

and Space Sciences **9**, 10.3389/fspas.2022.994980 (2022).

[15] S. Nikas, G. Perdikakis, M. Beard, R. Surman, M. R. Mumpower, and P. Tsintari, Propagation of hauser-feshbach uncertainty estimates to r-process nucleosynthesis: Benchmark of statistical property models for neutron rich nuclei far from stability (2020), arXiv:2010.01698 [nucl-th].

[16] Mumpower, M., Surman, R., and Aprahamian, A., The impact of global nuclear mass model uncertainties on r-process abundance predictions, EPJ Web of Conferences **93**, 03003 (2015).

[17] M. Mumpower, R. Surman, and A. Aprahamian, Variances in r-process predictions from uncertain nuclear rates, Journal of Physics: Conference Series **599**, 012031 (2015).

[18] S. Goriely, N. Chamel, and J. M. Pearson, Skyrme-Hartree-Fock-Bogoliubov nuclear mass formulas: Crossing the 0.6 MeV accuracy threshold with microscopically deduced pairing, Phys. Rev. Lett. **102**, 152503 (2009).

[19] I. Kullmann, S. Goriely, O. Just, A. Bauswein, and H.-T. Janka, Impact of systematic nuclear uncertainties on composition and decay heat of dynamical and disc ejecta in compact binary mergers, Monthly Notices of the Royal Astronomical Society **523**, 2551 (2023).

[20] S. Goriely, L. Siess, and A. Choplin, The intermediate neutron capture process, A&A **654**, A129 (2021).

[21] Arcones, A., Janka, H.-Th., and Scheck, L., Nucleosynthesis-relevant conditions in neutrino-driven supernova outflows - I. Spherically symmetric hydrodynamic simulations, A&A **467**, 1227 (2007).

[22] S. Goriely, A. Bauswein, and H.-T. Janka, r-process nucleosynthesis in dynamically ejected matter of neutron star mergers, The Astrophysical Journal Letters **738**, L32 (2011).

[23] R. H. Cyburt, A. M. Amthor, R. Ferguson, Z. Meisel, K. Smith, S. Warren, A. Heger, R. D. Hoffman, T. Rauscher, A. Sakharuk, H. Schatz, F. K. Thielemann, and M. Wiescher, THE JINA REACLIB DATABASE: ITS RECENT UPDATES AND IMPACT ON TYPE-i x-RAY BURSTS, The Astrophysical Journal Supplement Series **189**, 240 (2010).

[24] Panov, I. V., Korneev, I. Yu., Rauscher, T., Martínez-Pinedo, G., Kelic-Heil, A., Zinner, N. T., and Thielemann, F.-K., Neutron-induced astrophysical reaction rates for translead nuclei*, A&A **513**, A61 (2010).

[25] A. Koning, S. Goriely, and S. Hilaire, *TALYS-1.9, A nuclear reaction program, user manual*, Tech. Rep. (2017).

[26] A. Koning, D. Rochman, J.-C. Sublet, N. Dzysiuk, M. Fleming, and S. van der Marck, Tendl: Complete nuclear data library for innovative nuclear science and technology, Nuclear Data Sheets **155**, 1 (2019), special Issue on Nuclear Reaction Data.

[27] L. Wolfenstein, Conservation of angular momentum in the statistical theory of nuclear reactions, Physical Review **82**, 690 (1951).

[28] W. Hauser and H. Feshbach, The inelastic scattering of neutrons, Physical Review **87**, 366 (1952).

[29] A. Gilbert and A. G. W. Cameron, A composite nuclear-level density formula with shell corrections, Canadian Journal of Physics **43**, 1446 (1965).

[30] T. Von Egidy, H. Schmidt, and A. Behkami, Nuclear level densities and level spacing distributions: Part II, Nuclear Physics A **481**, 189 (1988).

[31] A. Ignatyuk, K. Istekov, and G. Smirenkin, Collective effects in the level density and the nuclear fission probability, Yadernaya Fizika **30**, 1205 (1979).

[32] A. V. Ignatyuk, J. L. Weil, S. Raman, and S. Kahane, Density of discrete levels in ^{116}Sn, Phys. Rev. C **47**, 1504 (1993).

[33] P. Demetriou and S. Goriely, Nuclear Physics A **695**, 95 (2001).

[34] S. Goriely, S. Hilaire, and A. J. Koning, Improved microscopic nuclear level densities within the Hartree-Fock-Bogoliubov plus combinatorial method, Phys. Rev. C **78**, 064307 (2008).

[35] S. Hilaire, M. Girod, S. Goriely, and A. J. Koning, Temperature-dependent combinatorial level densities with the D1M Gogny force, Phys. Rev. C **86**, 064317 (2012).

[36] P. Möller, A. Sierk, T. Ichikawa, and H. Sagawa, Nuclear ground-state masses and deformations: FRDM(2012), Atomic Data and Nuclear Data Tables **109-110**, 1 (2016).

[37] J. Kopecky and M. Uhl, Test of gamma-ray strength functions in nuclear reaction model calculations, Phys. Rev. C **41**, 1941 (1990).

[38] D. Brink, Individual particle and collective aspects of the nuclear photoeffect, Nuclear Physics **4**, 215 (1957).

[39] P. Axel, Electric dipole ground-state transition width strength function and 7-MeV photon interactions, Phys. Rev. **126**, 671 (1962).

[40] S. Goriely and E. Khan, Large-scale QRPA calculation of E1-strength and its impact on the neutron capture cross section, Nuclear Physics A **706**, 217 (2002).

[41] S. Goriely, E. Khan, and M. Samyn, Microscopic HFB + QRPA predictions of dipole strength for astrophysics applications, Nuclear Physics A **739**, 331 (2004).

[42] S. Goriely, Radiative neutron captures by neutron-rich nuclei and the r-process nucleosynthesis, Physics Letters B **436**, 10 (1998).

[43] I. Daoutidis and S. Goriely, Large-scale continuum random-phase approximation predictions of dipole strength for astrophysical applications, Phys. Rev. C **86**, 034328 (2012).

[44] S. Goriely, S. Hilaire, S. Péru, and K. Sieja, Gogny-HFB+QRPA dipole strength function and its application to radiative nucleon capture cross section, Phys. Rev. C **98**, 014327 (2018).

[45] Koning, Arjan, Hilaire, Stephane, and Goriely, Stephane, Talys: modeling of nuclear reactions, Eur. Phys. J. A **59**, 131 (2023).

[46] S. Goriely and V. Plujko, Simple empirical E1 and M1 strength functions for practical applications, Phys. Rev. C **99**, 014303 (2019).

[47] S. Goriely and J.-P. Delaroche, The isovector imaginary neutron potential: A key ingredient for the r-process nucleosynthesis, Physics Letters B **653**, 178 (2007).

[48] A. Koning and J. Delaroche, Local and global nucleon optical models from 1 keV to 200 MeV, Nuclear Physics A **713**, 231 (2003).

[49] H. Oberhummer and G. Staudt, Direct reaction mechanism in astrophysically relevant processes, in *Nuclei in the Cosmos*, edited by H. Oberhummer (Springer Berlin Heidelberg, Berlin, Heidelberg, 1991) pp. 29–59.

[50] K. Sieja and S. Goriely, Eur. Phys. J. A **57**, 110 (2021).

[51] X. F. Jiang, X. H. Wu, and P. W. Zhao, Sensitivity study of r-process abundances to nuclear masses, The Astro-

physical Journal **915**, 29 (2021).

[52] F. Bello Garrote, A. Lopez-Martens, A. Larsen, I. Deloncle, S. Péru, F. Zeiser, P. Greenlees, B. Kheswa, K. Auranen, D. Bleuel, D. Cox, L. Crespo Campo, F. Giacoppo, A. Görgen, T. Grahn, M. Guttormsen, T. Hagen, L. Harkness-Brennan, K. Hauschild, G. Henning, R.-D. Herzberg, R. Julin, S. Juutinen, T. Laplace, M. Leino, J. Midtbø, V. Modamio, J. Pakarinen, P. Papadakis, J. Partanen, T. Renstrøm, K. Rezynkina, M. Sandzelius, J. Sarén, C. Scholey, S. Siem, J. Sorri, S. Stolze, and J. Uusitalo, Experimental observation of the M1 scissors mode in 254No, Physics Letters B **834**, 137479 (2022).

[53] J. E. Midtbø, A. C. Larsen, T. Renstrøm, F. L. Bello Garrote, and E. Lima, Consolidating the concept of low-energy magnetic dipole decay radiation, Phys. Rev. C **98**, 064321 (2018).

[54] M. D. Jones, A. O. Macchiavelli, M. Wiedeking, L. A. Bernstein, H. L. Crawford, C. M. Campbell, R. M. Clark, M. Cromaz, P. Fallon, I. Y. Lee, M. Salathe, A. Wiens, A. D. Ayangeakaa, D. L. Bleuel, S. Bottoni, M. P. Carpenter, H. M. Davids, J. Elson, A. Görgen, M. Guttormsen, R. V. F. Janssens, J. E. Kinnison, L. Kirsch, A. C. Larsen, T. Lauritsen, W. Reviol, D. G. Sarantites, S. Siem, A. V. Voinov, and S. Zhu, Examination of the low-energy enhancement of the γ-ray strength function of ^{56}Fe, Phys. Rev. C **97**, 024327 (2018).

[55] A. C. Larsen and S. Goriely, Impact of a low-energy enhancement in the γ-ray strength function on the neutron-capture cross section, Phys. Rev. C **82**, 014318 (2010).

[56] T. Rauscher and F.-K. Thielemann, Astrophysical reaction rates from statistical model calculations, Atomic Data and Nuclear Data Tables **75**, 1 (2000).

[57] F. Pogliano and A.-C. Larsen, Final abundances used in "Impact of level densities and gamma-strength functions on r-process simulations", 10.5281/zenodo.8108946 (2023).

[58] S. Goriely, Uncertainties in the solar system r-abundance distribution, A&A **342**, 881 (1999).

[59] Facility for Rare Isotope Beams.

[60] Facility for Antiproton and Ion Research.

[61] The N=126 Factory, Argonne National Lab.

[62] R. Reifarth, K. Göbel, T. Heftrich, M. Weigand, B. Jurado, F. Käppeler, and Y. A. Litvinov, Spallation-based neutron target for direct studies of neutron-induced reactions in inverse kinematics, Phys. Rev. Accel. Beams **20**, 044701 (2017).

[63] I. Dillmann, O. Kester, R. Baartman, A. Chen, T. Junginger, F. Herwig, D. Kaltchev, A. Lennarz, T. Planche, C. Ruiz, and N. Vassh, Measuring neutron capture cross sections of radioactive nuclei, The European Physical Journal A **59**, 105 (2023).

[64] J. E. Escher, J. T. Harke, R. O. Hughes, N. D. Scielzo, R. J. Casperson, S. Ota, H. I. Park, A. Saastamoinen, and T. J. Ross, Constraining neutron capture cross sections for unstable nuclei with surrogate reaction data and theory, Phys. Rev. Lett. **121**, 052501 (2018).

[65] A. Spyrou, S. N. Liddick, A. C. Larsen, M. Guttormsen, K. Cooper, A. C. Dombos, D. J. Morrissey, F. Naqvi, G. Perdikakis, S. J. Quinn, T. Renstrøm, J. A. Rodriguez, A. Simon, C. S. Sumithrarachchi, and R. G. T. Zegers, Novel technique for constraining r-process (n, γ) reaction rates, Phys. Rev. Lett. **113**, 232502 (2014).

[66] M. Wiedeking, M. Guttormsen, A. C. Larsen, F. Zeiser, A. Görgen, S. N. Liddick, D. Mücher, S. Siem, and A. Spyrou, Independent normalization for γ-ray strength functions: The shape method, Phys. Rev. C **104**, 014311 (2021).

[67] D. Mücher, A. Spyrou, M. Wiedeking, M. Guttormsen, A. C. Larsen, F. Zeiser, C. Harris, A. L. Richard, M. K. Smith, A. Görgen, S. N. Liddick, S. Siem, H. C. Berg, J. A. Clark, P. A. DeYoung, A. C. Dombos, B. Greaves, L. Hicks, R. Kelmar, S. Lyons, J. Owens-Fryar, A. Palmisano, D. Santiago-Gonzalez, G. Savard, and W. W. von Seeger, Extracting model-independent nuclear level densities away from stability, Phys. Rev. C **107**, L011602 (2023).

[68] V. W. Ingeberg, S. Siem, M. Wiedeking, *et al.*, Eur. Phys. J. A. **56**, 68 (2020).

Appendices

Appendix A

Data tables: Experimental Maxwellian-averaged cross sections

Listed here are the tabulated Maxwellian-averaged cross section (MACS) data calculated from the three experiments described in Papers I, II and III, as plotted in Figs. 6.1 and 6.3, complete with errors and TALYS uncertainties.
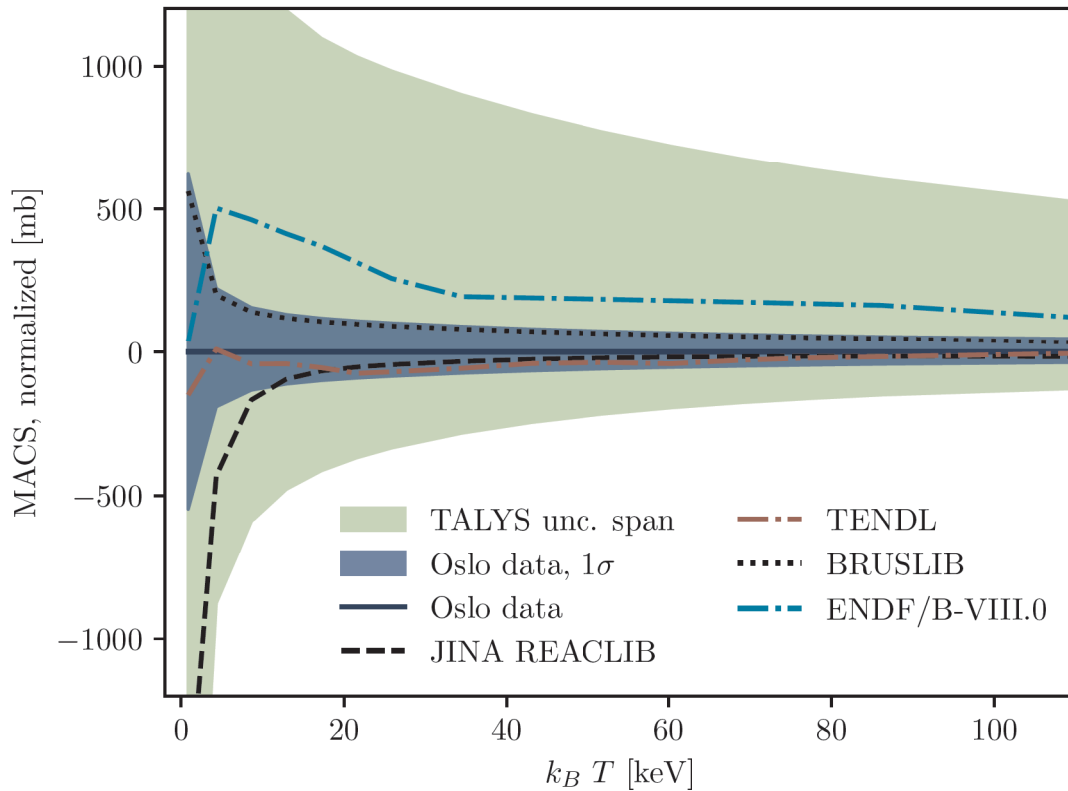
A.1 ^{126}Sb MACS

Figure A.1: MACS of ^{126}Sb, normalized to the new recommended values. Similar plot as for Fig. 6.1.

T	$k_B T$	MACS	Lower error	Upper error	TALYS unc. low	TALYS unc. high
(GK)	(keV)	(mb)	(mb)	(mb)	(mb)	(mb)
0.01	0.862	3842	3295	4464	1274	8478
0.05	4.31	1278	1087	1502	402	3175
0.10	8.62	858	725	1015	268	2238
0.15	12.9	696	584	829	218	1889
0.20	17.2	602	503	722	189	1699
0.25	21.5	538	446	648	169	1571
0.30	25.9	488	403	591	154	1471
0.40	34.5	412	338	504	130	1313
0.50	43.1	357	291	439	112	1189
0.60	51.7	315	256	390	98.5	1088
0.70	60.3	282	229	351	88.0	1004
0.80	68.9	256	207	319	79.6	933
0.90	77.6	235	189	294	72.7	873
1.0	86.2	217	174	272	67.0	821
1.5	129	158	126	201	48.4	619
2.0	172	124	98.3	158	37.8	427
2.5	215	97.8	77.6	126	30.3	345
3.0	259	75.8	60.0	97.9	21.1	271
3.5	302	56.2	44.4	72.9	10.3	204
4.0	345	39.2	30.8	51.2	5.61	143
5.0	431	16.6	13.0	22.0	2.25	61.3
6.0	517	6.95	5.42	9.33	1.19	27.8
7.0	603	3.26	2.54	4.44	0.755	13.4
8.0	689	1.74	1.36	2.41	0.503	6.11
9.0	776	1.03	0.809	1.45	0.350	3.09
10.0	862	0.648	0.515	0.919	0.258	1.78

Table A.1: Calculated data for the ^{126}Sb MACS as in Fig. 6.1.
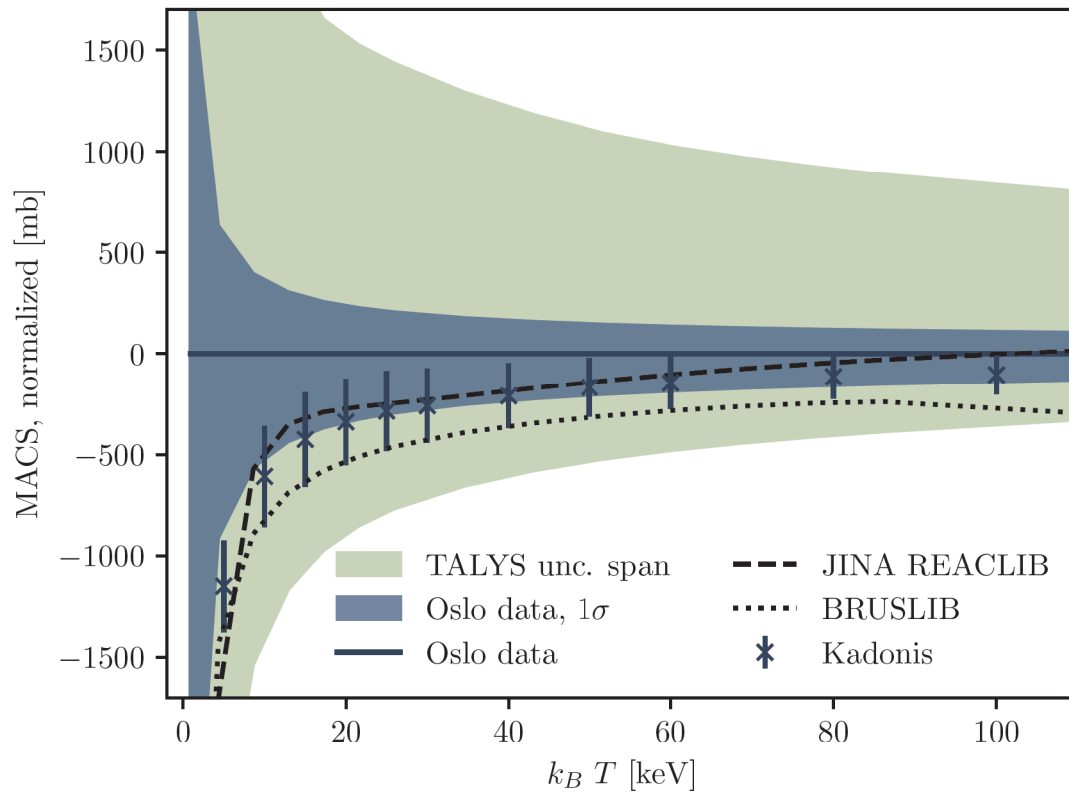
A.2 ^{165}Ho MACS

Figure A.2: MACS of ^{165}Ho, normalized to the new recommended values. Similar plot as for Fig.

T	$k_B T$	MACS	Lower error	Upper error	TALYS unc. low	TALYS unc. high
(GK)	(keV)	(mb)	(mb)	(mb)	(mb)	(mb)
0.01	0.862	17244	14249	19149	8429	27746
0.05	4.31	5113	4201	5745	2567	9018
0.10	8.62	3160	2598	3556	1625	5668
0.15	12.9	2433	1999	2739	1267	4386
0.20	17.2	2044	1677	2302	1071	3697
0.25	21.5	1794	1471	2022	942	3321
0.30	25.9	1615	1322	1822	846	3053
0.40	34.5	1363	1113	1542	708	2659
0.50	43.1	1191	969	1350	612	2374
0.60	51.7	1063	864	1210	542	2156
0.70	60.3	965	783	1101	488	1989
0.80	68.9	887	717	1015	445	1857
0.90	77.6	821	663	943	410	1747
1.0	86.2	765	617	882	380	1651
1.5	129	556	445	653	276	1288
2.0	172	390	308	468	208	1008
2.5	215	253	197	313	160	777
3.0	259	156	119	198	109	589
3.5	302	93.9	70.3	125	63.7	438
4.0	345	57.0	41.7	79.2	37.8	315
5.0	431	22.1	15.5	34.0	14.1	141
6.0	517	8.88	6.00	15.0	5.54	49.2
7.0	603	2.58	1.71	4.74	1.61	14.8
8.0	689	0.337	0.220	0.669	0.214	4.89
9.0	776	0.037	0.024	0.078	0.024	2.36
10.0	862	0.005	0.003	0.012	0.003	1.23

Table A.2: Calculated data for the ^{165}Ho MACS as in Fig. 6.3(a).
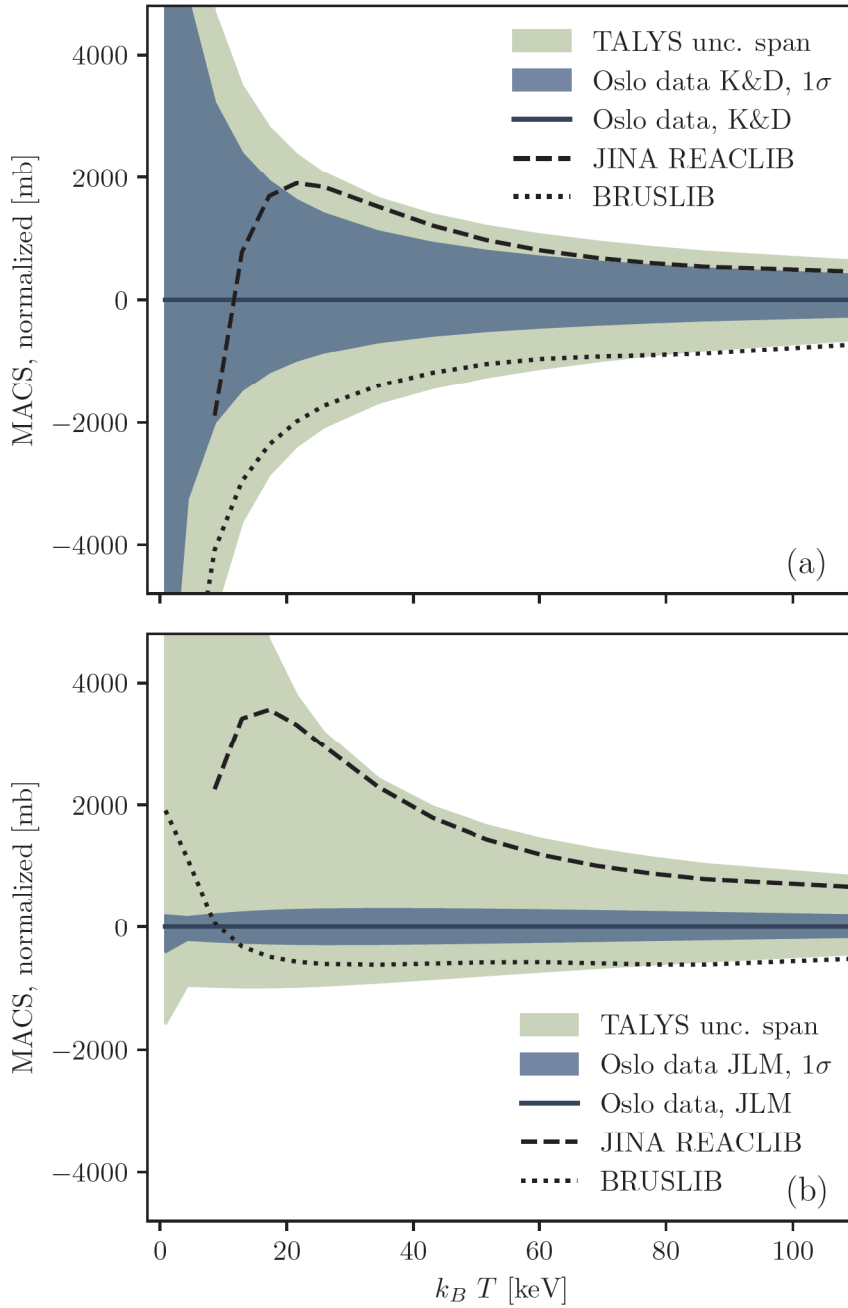
A.3   ¹⁶⁶Ho MACS

Figure A.3: MACS of ¹⁶⁶Ho, normalized to the new recommended values. Similar plot as for Fig. 6.3(b). In the upper panel the values are normalized to the values calculated with the K&D OMP model [122], while in the lower panel to the ones calculated with the JLM OMP model [123].

T	k_BT	MACS	Lower error	Upper error	TALYS unc. low	TALYS unc. high
(GK)	(keV)	(mb)	(mb)	(mb)	(mb)	(mb)
0.01	74.3	22826	15290	27878	2161	35048
0.05	371	10406	7157	15359	1484	17718
0.10	743	6267	4267	9493	1151	10960
0.15	1114	4585	3122	6987	962	8085
0.20	1485	3690	2522	5617	838	6510
0.25	1856	3134	2153	4751	747	5512
0.30	2228	2750	1899	4147	675	4815
0.40	2970	2240	1560	3346	565	3889
0.50	3713	1906	1333	2826	481	3288
0.60	4456	1661	1163	2452	414	2856
0.70	5198	1467	1026	2163	358	2523
0.80	5941	1307	911	1926	312	2252
0.90	6683	1170	812	1727	273	2024
1.0	7426	1050	725	1555	239	1827
1.5	11139	632	425	955	126	1141
2.0	14852	396	260	613	69.7	753
2.5	18565	255	164	405	39.7	548
3.0	22278	167	104	272	23.3	412
3.5	25990	110	67.1	184	14.0	315
4.0	29703	72.6	43.3	125	8.79	238
5.0	37129	32.3	18.3	59.7	3.88	121
6.0	44555	13.4	7.18	26.4	1.77	49.4
7.0	51981	2.97	1.52	6.26	0.456	16.9
8.0	59407	0.312	0.153	0.701	0.056	5.36
9.0	66833	0.035	0.017	0.085	0.007	1.66
10.0	74258	0.005	0.002	0.014	0.001	0.703

Table A.3: Calculated data for the ^{166}Ho MACS as in Fig. 6.3(b), using the K&D OMP model [122].

T	$k_B T$	MACS	Lower error	Upper error	TALYS unc. low	TALYS unc. high
(GK)	(keV)	(mb)	(mb)	(mb)	(mb)	(mb)
0.01	74.3	3734	3327	3932	2161	35048
0.05	371	2439	2231	2610	1484	17718
0.10	743	2120	1887	2333	1151	10960
0.15	1114	1943	1689	2189	962	8085
0.20	1485	1817	1551	2087	838	6510
0.25	1856	1717	1443	2002	747	5512
0.30	2228	1627	1351	1921	675	4815
0.40	2970	1466	1193	1767	565	3889
0.50	3713	1324	1059	1621	481	3288
0.60	4456	1197	944	1487	414	2856
0.70	5198	1082	843	1362	358	2523
0.80	5941	978	753	1246	312	2252
0.90	6683	884	672	1137	273	2024
1.0	7426	797	600	1036	239	1827
1.5	11139	469	340	633	126	1141
2.0	14852	276	195	382	69.7	753
2.5	18565	164	114	232	39.7	548
3.0	22278	99.5	67.5	145	23.3	412
3.5	25990	61.8	40.8	93.1	14.0	315
4.0	29703	39.7	25.2	62.8	8.79	238
5.0	37129	18.1	10.5	32.3	3.88	121
6.0	44555	8.33	4.43	16.7	1.77	49.4
7.0	51981	2.11	1.04	4.74	0.456	16.9
8.0	59407	0.253	0.117	0.631	0.056	5.36
9.0	66833	0.032	0.014	0.091	0.007	1.66
10.0	74258	0.006	0.002	0.019	0.001	0.703

Table A.4: Calculated data for the ^{166}Ho MACS as in Fig. 6.3(b), using the JLM OMP model [123].

Bibliography

[1] Lodders, K. "Solar system abundances and condensation temperatures of the elements". In: *The Astrophysical Journal* vol. 591, no. 2 (2003), p. 1220. DOI: **10.1086/375492**.

[2] Görgen, A. et al. "The Oslo Cyclotron Laboratory". In: *The European Physical Journal Plus* vol. 136, no. 2 (2021), p. 181. DOI: **10.1140/epjp/s13360-021-01150-3**.

[3] Miernik, K. *Chart of nuclides drawer*. https://github.com/kmiernik/Chart-of-nuclides-drawer. Accessed on April 3rd, 2023. (2019).

[4] Audi, G. et al. "The NUBASE2016 evaluation of nuclear properties". In: *Chinese Physics C* vol. 41, no. 3 (2017), p. 030001. DOI: **10.1088/1674-1137/41/3/030001**.

[5] Pauli, W. "Über das Wasserstoffspektrum vom Standpunkt der neuen Quantenmechanik". In: *Zeitschrift für Physik A Hadrons and nuclei* vol. 36, no. 5 (1926), pp. 336–363. DOI: **10.1007/BF01450175**.

[6] Schrödinger, E. "An Undulatory Theory of the Mechanics of Atoms and Molecules". In: *Physical Review* vol. 28 (1926), pp. 1049–1070. DOI: **10.1103/PhysRev.28.1049**.

[7] Dirac, P. A. M. and Fowler, R. H. "The quantum theory of the electron". In: *Proceedings of the Royal Society of London. Series A, Containing Papers of a Mathematical and Physical Character* vol. 117, no. 778 (1928), pp. 610–624. DOI: **10.1098/rspa.1928.0023**.

[8] Mayer, M. G. "On Closed Shells in Nuclei". In: *Physical Review* vol. 74 (1948), pp. 235–239. DOI: **10.1103/PhysRev.74.235**.

[9] Mayer, M. G. "On Closed Shells in Nuclei. II". In: *Physical Review* vol. 75 (1949), pp. 1969–1970. DOI: **10.1103/PhysRev.75.1969**.

[10] Haxel, O., Jensen, J. H. D., and Suess, H. E. "On the "Magic Numbers" in Nuclear Structure". In: *Physical Review* vol. 75 (1949), pp. 1766–1766. DOI: **10.1103/PhysRev.75.1766.2**.

[11] Thomson, W. and Kelvin, L. "On the age of the Sun's heat". In: *Popular Lectures and Addresses*. Vol. 1. Cambridge Library Collection - Physical Sciences. Cambridge University Press, (2011), p. 349. DOI: **10.1017/CBO9780511997242.013**.

[12] Harkins, W. D. and Wilson, E. D. "LXXVI. Energy relations involved in the formation of complex atoms". In: *The London, Edinburgh, and Dublin Philosophical Magazine and Journal of Science* vol. 30, no. 179 (1915), pp. 723–734. DOI: **10.1080/14786441108635449**.

[13]   Perrin, Jean. "Matière et lumière - Essai de synthèse de la mécanique chimique". In: *Annales de Physique* vol. 9, no. 11 (1919), pp. 5–108. DOI: 10.1051/anphys/191909110005.

[14]   Wesemael, F. "Harkins, Perrin and the Alternative Paths to the Solution of the Stellar-Energy Problem, 1915–1923". In: *Journal for the History of Astronomy* vol. 40, no. 3 (2009), pp. 277–296. DOI: 10.1177/0021828609004000302.

[15]   Rutherford, E. "Collision of α particles with light atoms. IV. An anomalous effect in nitrogen". In: *Philosophical Magazine* vol. 90, no. sup1 (1919, reprint 2010), pp. 31–37. DOI: 10.1080/14786431003659230.

[16]   Bethe, H. A. "Energy Production in Stars". In: *Physical Review* vol. 55 (1939), pp. 434–456. DOI: 10.1103/PhysRev.55.434.

[17]   Gamow, G. "The Creation of the Universe". In: *The Sewanee Review* vol. 66, no. 3 (1958), pp. 413–422.

[18]   Alpher, R. A., Bethe, H., and Gamow, G. "The origin of chemical elements". In: *Physical Review* vol. 73 (1948), pp. 803–804. DOI: 10.1103/PhysRev.73.803.

[19]   Hoyle, F. "On nuclear reactions occuring in very hot stars. I. The synthesis of elements from carbon to nickel". In: *The Astrophysical journal. Supplement series* vol. 1 (1954), p. 121. DOI: 10.1086/190005.

[20]   Merrill, P. W. "Spectroscopic observations of stars of class S". In: *The Astrophysical Journal* vol. 116 (1952), p. 21. DOI: 10.1086/145589.

[21]   Dunbar, D. N. F. et al. "The 7.68-Mev State in C^{12}". In: *Physical Review* vol. 92 (1953), pp. 649–650. DOI: 10.1103/PhysRev.92.649.

[22]   Suess, H. E. and Urey, H. C. "Abundances of the elements". In: *Reviews of Modern Physics* vol. 28 (1956), pp. 53–74. DOI: 10.1103/RevModPhys.28.53.

[23]   Burbidge, E. M. et al. "Synthesis of the elements in stars". In: *Reviews of Modern Physics* vol. 29 (1957), pp. 547–650. DOI: 10.1103/RevModPhys.29.547.

[24]   Cameron, A. G. W. "Nuclear reactions in stars and nucleogenesis". In: *Publications of the Astronomical Society of the Pacific* vol. 69, no. 408 (1957), p. 201. DOI: 10.1086/127051.

[25]   Arnould, M., Goriely, S., and Takahashi, K. "The r-process of stellar nucleosynthesis: Astrophysics and nuclear physics achievements and mysteries". In: *Physics Reports* vol. 450, no. 4-6 (2007), pp. 97–213. DOI: 10.1016/j.physrep.2007.06.002.

[26]   Arnould, M. and Goriely, S. "The p-process of stellar nucleosynthesis: astrophysics and nuclear physics status". In: *Physics Reports* vol. 384, no. 1 (2003), pp. 1–84. DOI: 10.1016/S0370-1573(03)00242-4.

[27]   Pogliano, F. and Larsen, A.-C. *Impact of level densities and γ-strength functions on r-process simulations.* 2023. arXiv: 2305.03664 [nucl-th].

[28] Fields, B. D. "The Primordial Lithium Problem". In: *Annual Review of Nuclear and Particle Science* vol. 61, no. 1 (2011), pp. 47–68. DOI: 10.1146/annurev-nucl-102010-130445.

[29] Penzias, A. A. and Wilson, R. W. "A measurement of excess antenna temperature at 4080 Mc/s." In: *The Astrophysical Journal* vol. 142 (1965), p. 419. DOI: 10.1086/148307.

[30] Iliadis, C. *Nuclear physics of stars.* pp. 54,553–559. Weinheim, (2015).

[31] Beringer, J. et al. "Review of particle physics". In: *Physical Review D* vol. 86 (2012), p. 010001. DOI: 10.1103/PhysRevD.86.010001.

[32] Miralda-Escudé, J. "The Dark Age of the Universe". In: *Science* vol. 300, no. 5627 (2003), pp. 1904–1909. DOI: 10.1126/science.1085325.

[33] Schlaufman, K. C., Thompson, I. B., and Casey, A. R. "An Ultra Metal-poor Star Near the Hydrogen-burning Limit*". In: *The Astrophysical Journal* vol. 867, no. 2 (2018), p. 98. DOI: 10.3847/1538-4357/aadd97.

[34] Iliadis, C. *Nuclear physics of stars.* Chapters 1 and 5. Weinheim, (2015).

[35] Arnett, W. D. and Thielemann, F. K. "Hydrostatic nucleosynthesis. I - Core helium and carbon burning." In: *The Astrophysical Journal* vol. 295 (1985), pp. 589–619. DOI: 10.1086/163402.

[36] Thielemann, F. K. and Arnett, W. D. "Hydrostatic Nucleosynthesis. II - Core neon to silicon burning and presupernova abundance yields of massive stars". In: *The Astrophysical Journal* vol. 295 (1985), p. 604. DOI: 10.1086/163403.

[37] Chieffi, A., Limongi, M., and Straniero, O. "The Evolution of a 25 $M_\odot$ Star from the Main Sequence up to the Onset of the Iron Core Collapse". In: *The Astrophysical Journal* vol. 502, no. 2 (1998), pp. 737–762. DOI: 10.1086/305921.

[38] Woosley, S. E., Heger, A., and Weaver, T. A. "The evolution and explosion of massive stars". In: *Reviews of Modern Physics* vol. 74 (4 2002), pp. 1015–1071. DOI: 10.1103/RevModPhys.74.1015.

[39] Arnould, M. and Goriely, S. "Astronuclear Physics: A tale of the atomic nuclei in the skies". In: *Progress in Particle and Nuclear Physics* vol. 112 (2020), p. 103766. DOI: 10.1016/j.ppnp.2020.103766.

[40] Busso, M., Gallino, R., and Wasserburg, G. J. "Nucleosynthesis in Asymptotic Giant Branch Stars: Relevance for Galactic Enrichment and Solar System Formation". In: *Annual Review of Astronomy and Astrophysics* vol. 37, no. 1 (1999), pp. 239–309. DOI: 10.1146/annurev.astro.37.1.239.

[41] Karakas, A. I. and Lattanzio, J. C. "The Dawes Review 2: Nucleosynthesis and Stellar Yields of Low- and Intermediate-Mass Single Stars". In: *Publications of the Astronomical Society of Australia* vol. 31, e030 (2014), e030. DOI: 10.1017/pasa.2014.21.

[42] Reifarth, R., Lederer, C., and Käppeler, F. "Neutron reactions in astrophysics". In: *Journal of Physics G: Nuclear and Particle Physics* vol. 41, no. 5 (2014), p. 053101. DOI: 10.1088/0954-3899/41/5/053101.

[43] Käppeler, F. et al. "The *s* process: Nuclear physics, stellar models, and observations". In: *Reviews of Modern Physics* vol. 83 (1 2011), pp. 157–193. DOI: 10.1103/RevModPhys.83.157.

[44] Pogliano, F. et al. "Experimentally constrained ^{165,166}Ho(n, γ) rates and implications for the *s* process". In: *Physical Review C* vol. 107 (2023), p. 064614. DOI: 10.1103/PhysRevC.107.064614.

[45] Kajino, T. et al. "Current status of r-process nucleosynthesis". In: *Progress in Particle and Nuclear Physics* vol. 107 (2019), pp. 109–166. DOI: 10.1016/j.ppnp.2019.02.008.

[46] Cowan, J. J. et al. "Origin of the heaviest elements: The rapid neutron-capture process". In: *Reviews of Modern Physics* vol. 93 (2021), p. 015002. DOI: 10.1103/RevModPhys.93.015002.

[47] Abbott, B. P. et al. "GW170817: Observation of gravitational waves from a binary neutron star inspiral". In: *Physical Review Letters* vol. 119 (2017), p. 161101. DOI: 10.1103/PhysRevLett.119.161101.

[48] Arcavi, I. et al. "Optical emission from a kilonova following a gravitational-wave-detected neutron-star merger". In: *Nature (London)* vol. 551, no. 7678 (2017), pp. 64–66. DOI: 10.1038/nature24291.

[49] Goriely, S. et al. "New Fission Fragment Distributions and *r*-Process Origin of the Rare-Earth Elements". In: *Physical Review Letters* vol. 111 (24 2013), p. 242502. DOI: 10.1103/PhysRevLett.111.242502.

[50] Thielemann, F.-K., Wehmeyer, B., and Wu, M.-R. "r-Process Sites, their Ejecta Composition, and their Imprint in Galactic Chemical Evolution". In: *Journal of Physics: Conference Series* vol. 1668, no. 1 (2020), p. 012044. DOI: 10.1088/1742-6596/1668/1/012044.

[51] Qian, Y.-Z. and Woosley, S. E. "Nucleosynthesis in Neutrino-Driven Winds. I. The Physical Conditions". In: *The Astrophysical Journal* vol. 471, no. 1 (1996), p. 331. DOI: 10.1086/177973.

[52] Surman, R., McLaughlin, G. C., and Hix, W. R. "Nucleosynthesis in the Outflow from Gamma-Ray Burst Accretion Disks". In: *The Astrophysical Journal* vol. 643, no. 2 (2006), p. 1057. DOI: 10.1086/501116.

[53] Hampel, M. et al. "The intermediate neutron-capture process and carbon-enhanced metal-poor stars". In: *The Astrophysical Journal* vol. 831, no. 2 (2016), p. 171. DOI: 10.3847/0004-637x/831/2/171.

[54] Lugaro, M. et al. "The s-process in asymptotic giant branch stars of low metallicity and the composition of carbon-enhanced metal-poor stars". In: *The Astrophysical Journal* vol. 747, no. 1 (2012), p. 2. DOI: 10.1088/0004-637X/747/1/2.

[55] Cowan, J. J. and Rose, W. K. "Production of ^{14}C and neutrons in red giants." In: *The Astrophysical Journal* vol. 212 (1977), pp. 149–158. DOI: **10.1086/155030**.

[56] Choplin, A., Siess, L., and Goriely, S. "The intermediate neutron capture process - I. Development of the i-process in low-metallicity low-mass AGB stars". In: *Astronomy & Astrophysics* vol. 648 (2021), A119. DOI: **10.1051/0004-6361/202040170**.

[57] Cristallo, S. et al. "Constraints of the physics of low-mass AGB stars from CH and CEMP stars". In: *The Astrophysical Journal* vol. 833, no. 2 (2016), p. 181. DOI: **10.3847/1538-4357/833/2/181**.

[58] Herwig, F. et al. "Convective–reactive proton–12C combustion in Sakurai's object (V4334 Sagittarii) and implications for the evolution and yields from the first generations of stars". In: *The Astrophysical Journal* vol. 727, no. 2 (2011), p. 89. DOI: **10.1088/0004-637X/727/2/89**.

[59] Clarkson, O. and Herwig, F. "Convective H–He interactions in massive population III stellar evolution models". In: *Monthly Notices of the Royal Astronomical Society* vol. 500, no. 2 (2020), pp. 2685–2703. DOI: **10.1093/mnras/staa3328**.

[60] Cruz, M. A., Serenelli, A., and Weiss, A. "S-process in extremely metal-poor, low-mass stars". In: *Astronomy & Astrophysics* vol. 559 (2013), A4. DOI: **10.1051/0004-6361/201219513**.

[61] Denissenkov, P. A. et al. "The i-process yields of rapidly accreting white dwarfs from multicycle He-shell flash stellar evolution models with mixing parametrizations from 3D hydrodynamics simulations". In: *Monthly Notices of the Royal Astronomical Society* vol. 488, no. 3 (2019), pp. 4258–4270. DOI: **10.1093/mnras/stz1921**.

[62] Goriely, S. "Uncertainties in the solar system r-abundance distribution". In: *Astronomy & Astrophysics* vol. 342 (1999), pp. 881–891.

[63] Mumpower, M. et al. "The impact of individual nuclear properties on r-process nucleosynthesis". In: *Progress in Particle and Nuclear Physics* vol. 86 (2016), pp. 86–126. DOI: **10.1016/j.ppnp.2015.09.001**.

[64] Goriely, S. and Siess, L. "Sensitivity of the s-process nucleosynthesis in AGB stars to the overshoot model". In: *Astronomy & Astrophysics* vol. 609 (2018), A29. DOI: **10.1051/0004-6361/201731427**.

[65] Goriely, S., Siess, L., and Choplin, A. "The intermediate neutron capture process". In: *Astronomy & Astrophysics* vol. 654 (2021), A129. DOI: **10.1051/0004-6361/202141575**.

[66] Surman, R. et al. "Sensitivity studies for the weak r process: Neutron capture rates". In: *AIP Advances* vol. 4, no. 4 (2014), p. 041008. DOI: **10.1063/1.4867191**.

[67] Vescovi, D. et al. "Neutron-capture measurement candidates for the r-process in neutron star mergers". In: *Frontiers in Astronomy and Space Sciences* vol. 9 (2022). DOI: **10.3389/fspas.2022.994980**.

[68] McKay, J. E. et al. "The impact of (n,γ) reaction rate uncertainties on the predicted abundances of i-process elements with $32 \leq Z \leq 48$ in the metal-poor star HD94028". In: *Monthly Notices of the Royal Astronomical Society* vol. 491, no. 4 (2019), pp. 5179–5187. DOI: 10.1093/mnras/stz3322.

[69] Denissenkov, P. A. et al. "The impact of (n,γ) reaction rate uncertainties of unstable isotopes on the i-process nucleosynthesis of the elements from Ba to W". In: *Monthly Notices of the Royal Astronomical Society* vol. 503, no. 3 (2021), pp. 3913–3925. DOI: 10.1093/mnras/stab772.

[70] Kullmann, I. et al. "Impact of systematic nuclear uncertainties on composition and decay heat of dynamical and disc ejecta in compact binary mergers". In: *Monthly Notices of the Royal Astronomical Society* vol. 523, no. 2 (2023), pp. 2551–2576. DOI: 10.1093/mnras/stad1458.

[71] Wolfenstein, L. "Conservation of angular momentum in the statistical theory of nuclear reactions". In: *Physical Review* vol. 82 (1951), pp. 690–696. DOI: 10.1103/PhysRev.82.690.

[72] Hauser, W. and Feshbach, H. "The Inelastic Scattering of Neutrons". In: *Physical Review* vol. 87 (1952), pp. 366–373. DOI: 10.1103/PhysRev.87.366.

[73] Bethe, H. A. "An attempt to calculate the number of energy levels of a heavy nucleus". In: *Physical Review* vol. 50 (1936), pp. 332–341. DOI: 10.1103/PhysRev.50.332.

[74] Gilbert, A. and Cameron, A. G. W. "A composite nuclear-level density formula with shell corrections". In: *Canadian Journal of Physics* vol. 43, no. 8 (1965), pp. 1446–1496. DOI: 10.1139/p65-139.

[75] Ericson, T. "The statistical model and nuclear level densities". In: *Advances in Physics* vol. 9, no. 36 (1960), pp. 425–511. DOI: 10.1080/00018736000101239.

[76] Von Egidy, T., Schmidt, H., and Behkami, A. "Nuclear level densities and level spacing distributions: Part II". In: *Nuclear Physics A* vol. 481, no. 2 (1988), pp. 189–206. DOI: 10.1016/0375-9474(88)90491-5.

[77] Von Egidy, T. and Bucurescu, D. "Systematics of nuclear level density parameters". In: *Physical Review C* vol. 72 (2005), p. 044311. DOI: 10.1103/PhysRevC.72.044311.

[78] Von Egidy, T. and Bucurescu, D. "Erratum: Systematics of nuclear level density parameters [Physical Review C 72, 044311 (2005)]". In: *Physical Review C* vol. 73 (2006), p. 049901. DOI: 10.1103/PhysRevC.73.049901.

[79] Ericson, T. and Strutinski, V. "On angular distributions in compound nucleus processes". In: *Nuclear Physics* vol. 8 (1958), pp. 284–293. DOI: 10.1016/0029-5582(58)90156-1.

[80] Guttormsen, M. et al. "Quasicontinuum γ decay of ^{91,92}Zr: Benchmarking indirect (n,γ) cross section measurements for the s process". In: *Physical Review C* vol. 96 (2017), p. 024313. DOI: 10.1103/PhysRevC.96.024313.

[81] Goriely, S., Tondeur, F., and Pearson, J. "A Hartree-Fock nuclear mass table". In: *Atomic Data and Nuclear Data Tables* vol. 77, no. 2 (2001), pp. 311–381. DOI: 10.1006/adnd.2000.0857.

[82] Goriely, S., Hilaire, S., and Koning, A. J. "Improved microscopic nuclear level densities within the Hartree-Fock-Bogoliubov plus combinatorial method". In: *Physical Review C* vol. 78 (2008), p. 064307. DOI: 10.1103/PhysRevC.78.064307.

[83] Hilaire, S. et al. "Temperature-dependent combinatorial level densities with the D1M Gogny force". In: *Physical Review C* vol. 86 (2012), p. 064317. DOI: 10.1103/PhysRevC.86.064317.

[84] Koning, Arjan, Hilaire, Stephane, and Goriely, Stephane. "TALYS: modeling of nuclear reactions". In: *The European Physical Journal A* vol. 59, no. 6 (2023), p. 131. DOI: 10.1140/epja/s10050-023-01034-3.

[85] Pogliano, F. et al. "Indirect measurement of the $(n,\gamma)^{127}$Sb cross section". In: *Physical Review C* vol. 106 (2022), p. 015804. DOI: 10.1103/PhysRevC.106.015804.

[86] Pogliano, F. et al. "Observation of a candidate for the $M1$ scissors resonance in odd-odd ^{166}Ho". In: *Physical Review C* vol. 107 (2023), p. 034605. DOI: 10.1103/PhysRevC.107.034605.

[87] Bartholomew, G. A. et al. "Gamma-ray strength functions". In: *Advances in Nuclear Physics: Volume 7*. Ed. by Baranger, M. and Vogt, E. Boston, MA: Springer US, 1973, pp. 229–324. DOI: 10.1007/978-1-4615-9044-6_4.

[88] Kopecky, J. and Uhl, M. "Test of gamma-ray strength functions in nuclear reaction model calculations". In: *Physical Review C* vol. 41 (1990), pp. 1941–1955. DOI: 10.1103/PhysRevC.41.1941.

[89] Brink, D. M. *Doctoral thesis.* (1955).

[90] Axel, P. "Electric dipole ground-state transition width strength function and 7-MeV photon interactions". In: *Physical Review* vol. 126 (1962), pp. 671–683. DOI: 10.1103/PhysRev.126.671.

[91] Guttormsen, M. et al. "Validity of the Generalized Brink-Axel Hypothesis in ^{238}Np". In: *Physical Review Letters* vol. 116 (2016), p. 012502. DOI: 10.1103/PhysRevLett.116.012502.

[92] Campo, L. C. et al. "Test of the generalized Brink-Axel hypothesis in ^{64,65}Ni". In: *Physical Review C* vol. 98 (2018), p. 054303. DOI: 10.1103/PhysRevC.98.054303.

[93] Larsen, A. C. et al. "Low-energy enhancement and fluctuations of γ-ray strength functions in 56,57Fe: test of the Brink–Axel hypothesis". In: *Journal of Physics G: Nuclear and Particle Physics* vol. 44, no. 6 (2017), p. 064005. DOI: 10.1088/1361-6471/aa644a.

[94]   Renstrøm, T. et al. "Verification of detailed balance for γ absorption and emission in Dy isotopes". In: *Physical Review C* vol. 98 (2018), p. 054310. DOI: 10.1103/PhysRevC.98.054310.

[95]   Harakeh, M. N. and van der Woude, A. *Giant resonances*. Oxford: Oxford University Press, (2001).

[96]   Dietrich, S. S. and Berman, B. L. "Atlas of photoneutron cross sections obtained with monoenergetic photons". In: *Atomic Data and Nuclear Data Tables* vol. 38, no. 2 (1988), pp. 199–338. DOI: 10.1016/0092-640X(88)90033-2.

[97]   Heyde, K., von Neumann-Cosel, P., and Richter, A. "Magnetic dipole excitations in nuclei: Elementary modes of nucleonic motion". In: *Reviews of Modern Physics* vol. 82 (2010), pp. 2365–2419. DOI: 10.1103/RevModPhys.82.2365.

[98]   Savran, D., Aumann, T., and Zilges, A. "Experimental studies of the pygmy dipole resonance". In: *Progress in Particle and Nuclear Physics* vol. 70 (2013), pp. 210–245. DOI: 10.1016/j.ppnp.2013.02.003.

[99]   Bracco, A., Lanza, E., and Tamii, A. "Isoscalar and isovector dipole excitations: Nuclear properties from low-lying states and from the isovector giant dipole resonance". In: *Progress in Particle and Nuclear Physics* vol. 106 (2019), pp. 360–433. DOI: 10.1016/j.ppnp.2019.02.001.

[100] Markova, M. *Experimental study of the pygmy dipole resonance in the (p,p'γ) reaction on 124Sn and its evolution in the Sn isotopic chain.* (2020).

[101] Voinov, A. et al. "Large Enhancement of Radiative Strength for Soft Transitions in the Quasicontinuum". In: *Physical Review Letters* vol. 93 (2004), p. 142504. DOI: 10.1103/PhysRevLett.93.142504.

[102] Midtbø, J. E. et al. "Consolidating the concept of low-energy magnetic dipole decay radiation". In: *Physical Review C* vol. 98 (2018), p. 064321. DOI: 10.1103/PhysRevC.98.064321.

[103] Bohr, N. "Neutron capture and nuclear constitution". In: *Nature* vol. 137, no. 3461 (1936), pp. 344–348. DOI: 10.1038/137344a0.

[104] Misch, G. W. et al. "Sensitivity of neutron-rich nuclear isomer behavior to uncertainties in direct transitions". In: *Symmetry* vol. 13, no. 10 (2021). DOI: 10.3390/sym13101831.

[105] Cyburt, R. H. et al. "The JINA REACLIB database: Its recent updates and impact on type-I X-ray bursts". In: *The Astrophysical Journal Supplement Series* vol. 189, no. 1 (2010), pp. 240–252. DOI: 10.1088/0067-0049/189/1/240.

[106] Rauscher, T. and Thielemann, F.-K. "Astrophysical reaction rates from statistical model calculations". In: *Atomic Data and Nuclear Data Tables* vol. 75, no. 1 (2000), pp. 1–351. DOI: 10.1006/adnd.2000.0834.

[107] Xu, Y. et al. "Databases and tools for nuclear astrophysics applications - BRUSsels Nuclear LIBrary (BRUSLIB), Nuclear Astrophysics Compilation of REactions II (NACRE II) and Nuclear NETwork GENerator (NETGEN)". In: *Astronomy & Astrophysics* vol. 549 (2013), A106. DOI: 10.1051/0004-6361/201220537.

[108] Guttormsen, M. et al. "The SiRi particle-telescope system". In: *Nuclear Instruments and Methods in Physical Research section A* vol. 648 (2011), p. 168. DOI: 10.1016/j.nima.2011.05.055.

[109] Zeiser, F. et al. "The γ-ray energy response of the Oslo Scintillator Array OSCAR". In: *Nuclear Instruments and Methods in Physics Research Section A* vol. 985 (2021), p. 164678. DOI: 10.1016/j.nima.2020.164678.

[110] Guttormsen, M. et al. "The unfolding of continuum γ-ray spectra". In: *Nuclear Instruments and Methods in Physics Research Section A* vol. 374, no. 3 (1996), pp. 371–376. DOI: 10.1016/0168-9002(96)00197-0.

[111] Guttormsen, M., Ramsøy, T., and Rekstad, J. "The first generation of γ-rays from hot nuclei". In: *Nuclear Instruments and Methods in Physics Research Section A* vol. 255, no. 3 (1987), pp. 518–523. DOI: 10.1016/0168-9002(87)91221-6.

[112] Dirac, P. A. M. "The quantum theory of the emission and absorption of radiation". In: *Proceedings of the Royal Society of London. Series A, Containing papers of a mathematical and physical character* vol. 114, no. 767 (1927), pp. 243–265.

[113] Fermi, E. *Nuclear physics.* Chicago, (1950).

[114] Midtbø, J. E. *The low-energy enhancement: an experimental and theoretical study of nuclear level densities and γ-ray strength functions.* Oslo, (2019).

[115] Schiller, A. et al. "Extraction of level density and γ strength function from primary γ spectra". In: *Nuclear Instruments and Methods in Physics Research Section A* vol. 447, no. 3 (2000), pp. 498–511. DOI: 10.1016/S0168-9002(99)01187-0.

[116] Mughabghab, S. F. *Atlas of neutron resonances.* Amsterdam, Netherlands, (2018).

[117] Capote, R. et al. "RIPL – Reference Input Parameter Library for calculation of nuclear reactions and nuclear data evaluations". In: *Nuclear Data Sheets* vol. 110, no. 12 (2009). Special Issue on Nuclear Reaction Data, pp. 3107–3214. DOI: 10.1016/j.nds.2009.10.004.

[118] Guttormsen, M. et al. "Experimental level densities of atomic nuclei". In: *The European Physical Journal A* vol. 51, no. 12 (2015), p. 170. DOI: 10.1140/epja/i2015-15170-4.

[119] V. W. Ingeberg, S. Siem, M. Wiedeking, et al. In: *The European Physical Journal A* vol. 56 (2020), p. 68. DOI: 10.1140/epja/s10050-020-00070-7.

[120] Spyrou, A. et al. "Novel technique for Constraining r-Process (n, γ) Reaction Rates". In: *Physical Review Letters* vol. 113 (23 2014), p. 232502. DOI: 10.1103/PhysRevLett.113.232502.

[121] Midtbø, J. E. et al. "A new software implementation of the Oslo method with rigorous statistical uncertainty propagation". In: *Computer Physics Communications* vol. 262 (2021), p. 107795. DOI: 10.1016/j.cpc.2020. 107795.

[122] Koning, A. and Delaroche, J. "Local and global nucleon optical models from 1 keV to 200 MeV". In: *Nuclear Physics A* vol. 713, no. 3 (2003), pp. 231–310. DOI: 10.1016/S0375-9474(02)01321-0.

[123] Bauge, E., Delaroche, J. P., and Girod, M. "Lane-consistent, semimicroscopic nucleon-nucleus optical model". In: *Physical Review C* vol. 63 (2001), p. 024607. DOI: 10.1103/PhysRevC.63.024607.

[124] Koning, A. et al. "TENDL: Complete Nuclear Data Library for Innovative Nuclear Science and Technology". In: *Nuclear Data Sheets* vol. 155 (2019). Special Issue on Nuclear Reaction Data, pp. 1–55. DOI: 10.1016/j.nds. 2019.01.002.

[125] Brown, D. et al. "ENDF/B-VIII.0: The 8th major release of the nuclear reaction data library with CIELO-project cross sections, new standards and thermal scattering data". In: *Nuclear Data Sheets* vol. 148 (2018). Special Issue on Nuclear Reaction Data, pp. 1–142. DOI: 10.1016/j.nds. 2018.02.001.

[126] Lippuner, J. and Roberts, L. F. "SkyNet: A Modular Nuclear Reaction Network Library". In: *The Astrophysical Journal Supplement Series* vol. 233, no. 2 (2017), p. 18. DOI: 10.3847/1538-4365/aa94cb.

[127] Koning, A., Goriely, S., and Hilaire, S. *TALYS-1.9, A nuclear reaction program, user manual*. Tech. rep. 2017.